Modelling dry granular flows over topography

Jonathan Michael Foonlan Tsang
Queens' College, University of Cambridge

12 April 2019

This dissertation is submitted for the degree of
Doctor of Philosophy.

Declaration

This dissertation is submitted for the degree of Doctor of Philosophy.

This dissertation is the result of my own work and includes nothing which is the outcome of work done in collaboration except as declared in the preface and specified in the text.

It is not substantially the same as any that I have submitted, or, is being concurrently submitted for a degree or diploma or other qualification at the University of Cambridge or any other University or similar institution except as declared in the Preface and specified in the text. I further state that no substantial part of my dissertation has already been submitted, or, is being concurrently submitted for any such degree, diploma or other qualification at the University of Cambridge or any other University or similar institution except as declared in the Preface and specified in the text. It does not exceed the prescribed word limit for the relevant Degree Committee.

Abstract

Modelling dry granular flows over topography
Jonathan Michael Foonlan Tsang

Dry granular flows are common and important in the environment and industry, and yet their behaviour is very poorly understood. The dynamics of individual grains are governed by the simple and well-known laws of Newtonian mechanics, but how do these 'microscopic' particle-level laws translate into the 'macroscopic' collective motion of thousands or millions of grains, which flow like a liquid?

Various rheological models of granular flows have been developed to facilitate a continuum approach, but hitherto they have only been applied to flows in very simple geometries such as parallel shear flow. In these applications, the flows are assumed to be quasi-steady and to vary only over very long distances in the streamwise direction. This approximation, related to the 'shallow water' model of hydraulics, greatly simplifies the equations of motion. However, the assumption is inappropriate for modelling flows interacting with basal features that vary over lengthscales comparable to the depth of the current, or for flows with abrupt time-dependence that cannot be assumed to be quasi-steady. We refer to these spatial and temporal inhomogeneities collectively as *topography*.

In this thesis, we apply a common rheological model to problems involving various types of spatial or temporal topography. One problem that we shall particularly study concerns a flow down a chute that experiences a sudden increase in basal roughness, either spatially or in time. This change induces an evolution of the depthwise velocity profile that begins near the base but eventually spreads throughout the current. We introduce an adaptation of the $\mu(I)$ rheology and find the velocity profile that this rheological model predicts, using a technique similar to the Blasius boundary layer theory for Newtonian fluids flowing past an aerofoil.

We validate the predictions of the rheological model by comparing them against the results of discrete particle model (DPM) simulations. We review existing techniques for DPM, and present a number of novel ways of employing these techniques. These methods allow us to reduce the computational cost of simulations while maintaining their realism.

The internal profile of a granular flow, and its response to a change in basal conditions, are difficult to observe in experiments or in real life, since grains are opaque. However, the models studied here can help to make predictions about the depth and speed of the flows, or conversely to make inferences about the nature of the base, given measurements on the surface of the flow.

Acknowledgements

All things are without self.

Buddhist concept of *anatta*

I could not have attempted this work without the devoted and generous guidance of my supervisors, Stuart Dalziel and Nathalie Vriend. My other contemporaries at Cambridge have been very helpful colleagues and friends, and in particular I should thank the rest of the Granular Group: Josh Caplan, Matt Arran, Amalia Thomas, Paul Jarvis, Binbin Jin, Stéphanie Riber, Ben Young and Karol Bacik have all given me very useful ideas to think about. Outside of the Granular Group, Stephen Cowley gave me advice on asymptotics and boundary layer theory, John Hinch taught me plenty of things about non-Newtonian fluid mechanics, Colmcille Caulfield provided some consultation on stability theory, and John Willis gave me helpful pointers on solid mechanics and contact theory. The Maths Computer Officers have given very valuable assistance and much patience with my heavy use of the DAMTP computers.

I must also thank the other MercuryDPM developers, especially Anthony Thornton, Thomas Weinhart, Deepak Tunuguntla, Irana Denissen and Marnix van Schrojenstein Lantman, for all their support with the MercuryDPM code, from teaching me the basics to welcoming me into the development team, as well as their hospitality during my visits to Twente.

I would like to acknowledge the financial support of EPSRC, DAMTP and Queens' College.

Finally, on a personal level, I would like to thank the numberless family, friends, neighbours and organisations who have supported me and given me the emotional and spiritual, and sometimes physical, strength to persist over the last few years. I am particularly grateful to my close friends Mary, Sara and Benjamin, who, besides their personal support, have helped to proofread parts of this thesis.

Contents

1. Introduction

> Now, the five grains are the people's mainstay and the source of the ruler's revenue. When all the five grains are gathered, all the five tastes will be offered the ruler; when not all gathered, the five tastes will not be all offered. Failure of one grain is called dearth; failure of two grains is called scarcity; failure of three grains is called calamity; failure of four grains is called want; and failure of all five grains is called famine. When famine and dearth visit a country, [...] the scholars will not go to school. [...] And this is the sign of extreme scarcity.
>
> Mo Tzu, *The Seven Causes of Anxiety*, 5th century BCE

The efficient transportation and transfer of granular materials has been an important process since antiquity. These materials include staple foods, including the 'five grains' (wheat, oat, rice, millet and salt), as well as construction materials such as sand and gravel, all of which continue to be important commodities today. Granular flows also occur in geophysical settings in much more uncontrolled ways: phenomena such as avalanches and rockslides kill thousands of people each year (Petley 2012, Perkins 2012) and cause economic and social disruption. It is therefore desirable to understand the physics of such flows and to develop models for predicting their behaviour.

Although granular flows are common in everyday life, accurate mathematical models of their behaviour are surprisingly difficult to develop. A recurrent difficulty is the interaction between the grain-scale ('microscopic') properties of the material and the 'macroscopic' features of the entire flow (Andreotti et al. 2015). The flow behaviour of grains is in contrast to flows of liquids and gases, in which there is a clear separation of lengthscales between the molecular size and the flow lengthscale: for example, a water molecule's diameter is about 100 pm, while even the smallest bacteria are at least 100 nm wide (Staley 1999), and the smallest animal *Myxozoa shekel* at least 8.5 μm (Kaur and Singh 2011). For granular flows, the lack of a separation of lengthscales means that, in contrast to liquids and gases, the material cannot necessarily be treated as a continuum, and some thought must be paid to the interactions between individual grains. Nonetheless, given the extremely large numbers of grains in typical flows of interest, it is highly desirable to develop continuum models that can capture the collective, macroscopic dynamics, since the microscopic dynamics are unnecessarily detailed and not directly comparable to real-life measurements. One problem when creating continuum models is that, collectively, grains 'can behave like a solid, a liquid or a gas' (Andreotti et al. 2015, p. 13): figure 1.1 demonstrates all three states in a single current (see also Jaeger et al. (1996, figure 1)). The different states have irreconcilably different rheological properties (Forterre and Pouliquen 2008). In the present work, we focus almost exclusively on modelling the 'liquid', flowing state. In this regime, grain-to-grain contacts are frequent but not permanent (as opposed to the solid state), grains simultaneously engage in multiple contacts (as opposed to the gaseous state), and the mean free path is proportional to the typical grain size.

There are other difficulties in modelling granular flows and comparing their predictions against real flows. A major obstacle is that, in contrast to common liquids and gases, samples of granular

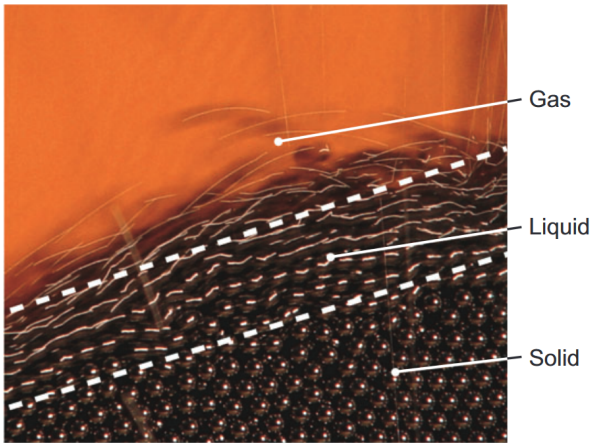

Figure 1.1.: A granular material can behave like a solid, a liquid or a gas. From Forterre and Pouliquen (2008, figure 1).

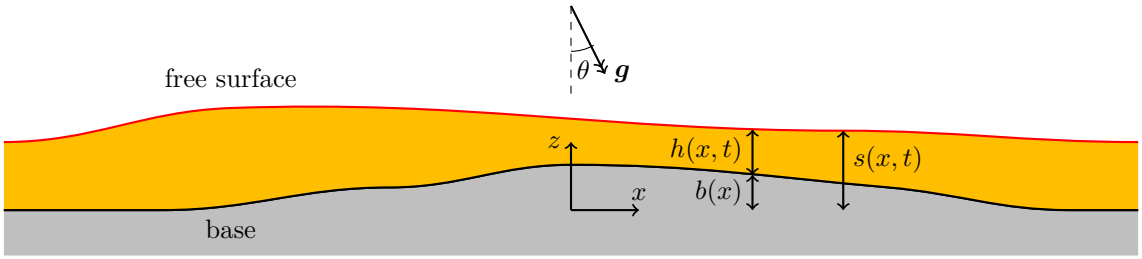

Figure 1.2.: Definition of coordinates.

materials may differ greatly in their properties, depending on the nature of the constituent grains: this variability makes it difficult to compare experimental results between different authors, who use different grains. A sample of grains could even evolve over time, as grains could break down or become rounded due to chipping or abrasion. Another issue is that grains tend to be opaque, so experimental techniques such as particle image velocimetry (Lueptow et al. 2000) can measure only the surface velocity of a flow, not the internal velocity profile.

1.1. Models of granular flows

We adopt the coordinate system shown in figure 1.2. The flow is over a surface inclined at an angle θ to the horizontal. The streamwise direction is x and the perpendicular direction is z. The shape of the surface is described by the equation $z = b(x)$. Throughout this thesis, we consider flows that are quasi-two-dimensional, so that there is no flow and no variation in the cross-stream direction y. This assumption greatly simplifies the governing equations of all models. However, care must be taken in interpreting a two-dimensional model, and the validity of the two-dimensional assumption must be returned to (§14.1).

Models of granular flow can be divided into the broad categories of *continuum models* and *discrete particle models* (or simply *discrete models*). Under a continuum model, the flow is assumed to completely occupy a region in space. One describes the state of the granular flow within this region in terms of continuum fields such as density ρ, velocity $\boldsymbol{u}$ and pressure p.

These fields represent local averages of the positions, velocities and stresses of individual grains. As in classical continuum mechanics, these fields are governed by a system of partial differential equations that express mass continuity and momentum balance. The material properties of the granular medium are described through a constitutive relationship between the dynamics and the kinematics of the medium.

Continuum models may be further subdivided into two categories. In a *rheological model*, one is concerned with the values of these continuum fields everywhere within a flow: a field such as a velocity $\boldsymbol{u}$ is treated as a function $\boldsymbol{u}(\boldsymbol{x}, t)$, defined at every position $\boldsymbol{x}$ within the flow and at all times t. These fields are then governed by a system of partial differential equations, which are generalisations of the Navier–Stokes equations for classical Newtonian fluids. In a *depth-averaged model*, one is not concerned with the interior of a flow, only on depth-averages of these quantities. The depth-averaged fields are also governed by systems of partial differential equations, but now there is only one spatial coordinate x. Depth-averaged models are generalisations of the Saint-Venant shallow water equations that are widely used in hydraulics (Chow 1959). Depth-averaged models are mathematically more tractable than continuum models, as there is only one spatial dimension in their governing equations. They are also more directly relatable to experiments, since experimental techniques such as particle image velocimetry (Lueptow et al. 2000) can measure only the surface velocity of a flow, not the internal velocity profile. However, depth-averaged models must make certain assumptions about this internal profile, as we shall discuss in Chapter 5. In Chapters 11 and 12, we shall study problems for which such assumptions give incorrect predictions about a flow.

In contrast to continuum models, discrete particle models (DPM) of granular flows retain the notion that a granular medium is a system of particles, whose trajectories are to be calculated by integrating Newton's equations of motion on each particle i to find its position $\boldsymbol{x}_i$ and velocity $\boldsymbol{u}_i$ as a function of time. This is a system of ordinary differential equations, in contrast to the partial differential equations of continuum models. This approach is similar to that of smoothed particle hydrodynamics (Liu and Liu 2010) for modelling classical fluid flows. Discrete particle models idealise many of the features of the constituent particles and their interactions with each other. Particles are taken to have regular shapes, such as discs (in 2D) or spheres (in 3D); and the number of particles in a DPM simulation is many orders of magnitude smaller than the number of grains in the real flow that it models. The forces on each particle consist of an external gravitational force, plus *contact forces* from particle-to-particle interactions, which are calculated based on a specified contact model (see Chapter 7). In this thesis, we focus on dry systems, and assume that particles do not experience any resistive or cohesive forces from any interstitial fluid.

Except in the most simple situations, DPM are conducted as computer simulations, and are therefore referred to also as *DPM simulations*.[1] In this work, the term 'simulation' shall refer exclusively to DPM simulations. Although we shall use computational methods to solve some of the equations from continuum models, we shall refer to these simply as 'numerical solutions'. Discrete particle models are also referred to as 'discrete element methods' (DEM), which must not be confused with 'finite element methods' (FEM) or 'boundary element methods' (BEM), which are techniques for solving partial differential equations (Iserles 2008) and are hence relevant to continuum models, not to discrete models. We shall also use the term 'grain' to refer to the constituents of a real flow, and 'particle' to refer to those of a DPM: this distinction emphasises that particles in a DPM are idealisations of real grains, and should not be interpreted

[1] Two-body problems are often solvable by hand, and can be used as test cases for a DPM code.

as having a one-to-one relationship.

The direct output of a DPM simulation consists of information about each particle's properties, such as position, velocity and angular velocity, at each timestep. In order to compare this output with the predictions of continuum models, the process of *coarse-graining* is used to convert these data into continuum fields for density ρ and velocity $\boldsymbol{u}$, by taking local averages. One may then perform depth-averaging on these continuum fields, if desired.

Discrete particle models have an advantage over continuum models because DPM retain the fundamentally discrete nature of granular media. Continuum models of granular flows rely on the validity of the 'continuum assumption', postulating that the flow should be infinitely divisible so that it is appropriate to talk about infinitesimal 'fluid elements'. This assumption becomes invalid when considering flows with characteristic lengthscales comparable to the grain size or the main free path, such as the flow through a narrow orifice undergoing granular jamming (To et al. 2001). Likewise, the phenomenon of granular segregation (see *e.g.* Gray and Thornton (2005)) is caused by the finite size or irregular shapes of constituent grains in a mixture, and is poorly described by existing continuum models (van der Vaart et al. 2018).

There is no criterion to definitively judge whether a fundamentally discrete material such as a granular material can be treated as a continuum: a single grain cannot be treated as a continuum, and adding or removing a single grain of sand does not change whether the continuum assumption is valid, so does it not follow that the continuum assumption is invalid for any number of grains? This is the sorites paradox, attributed to Eubulides of Miletus (4th century BCE). Despite this philosophical issue, continuum models are nonetheless much more useful than discrete particle models for systems with an extremely large number of grains, and in particular when flow lengthscales are many orders of magnitude greater than the typical grain size. In such systems, DPM would be computationally infeasible. Continuum models also emphasise the statistical properties of a flow, rather than the trajectories of individual grains: the latter tend to be very sensitive to initial conditions and to grain properties, while the former are more reproducible and directly comparable to experimental or observational results.

1.2. Topography

In recent years, a number of rheological models of granular flows have been developed (Andreotti et al. 2015). An important example is the $\mu(I)$ rheology (Jop et al. 2006), a commonly-used model that has successfully given partial descriptions of some granular phenomena (*e.g.* Riber et al. (2015), Baker et al. (2016a), Gray and Edwards (2014)), despite some mathematical difficulties (Barker et al. 2015). Although previous studies have compared numerical solutions to the $\mu(I)$ rheology against empirical results (from experiments or DPM simulations), mathematically analytical solutions to the $\mu(I)$ equations have been obtained only for flows that may be treated as quasi-steady and quasi-uniform. Some of these flow geometries are shown in GDR MiDi (2004). In other words, although rheological models in principle give velocity fields governed by partial differential equations (PDE), in practice most analytical applications of these PDE neglect the effects of the $\partial/\partial t$ and $\partial/\partial x$ terms. This approach is similar to the lubrication approximation for thin fluid flows (Acheson 1990, Batchelor 2000), in which a balance is made between the fluid viscosity and a streamwise pressure gradient, with effects from inertial terms neglected.

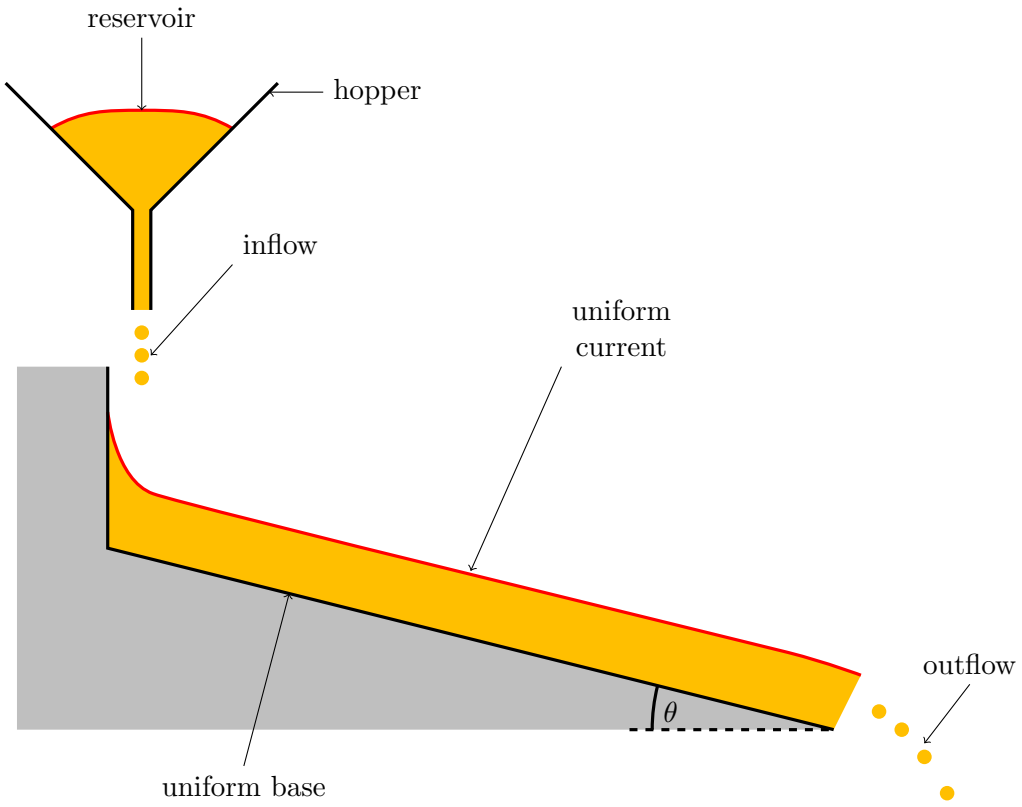

Figure 1.3.: The basic structure of an experimental chute flow. Side walls are not shown. The chute shown in this figure has no topographical features, and in the steady state a uniform current develops.

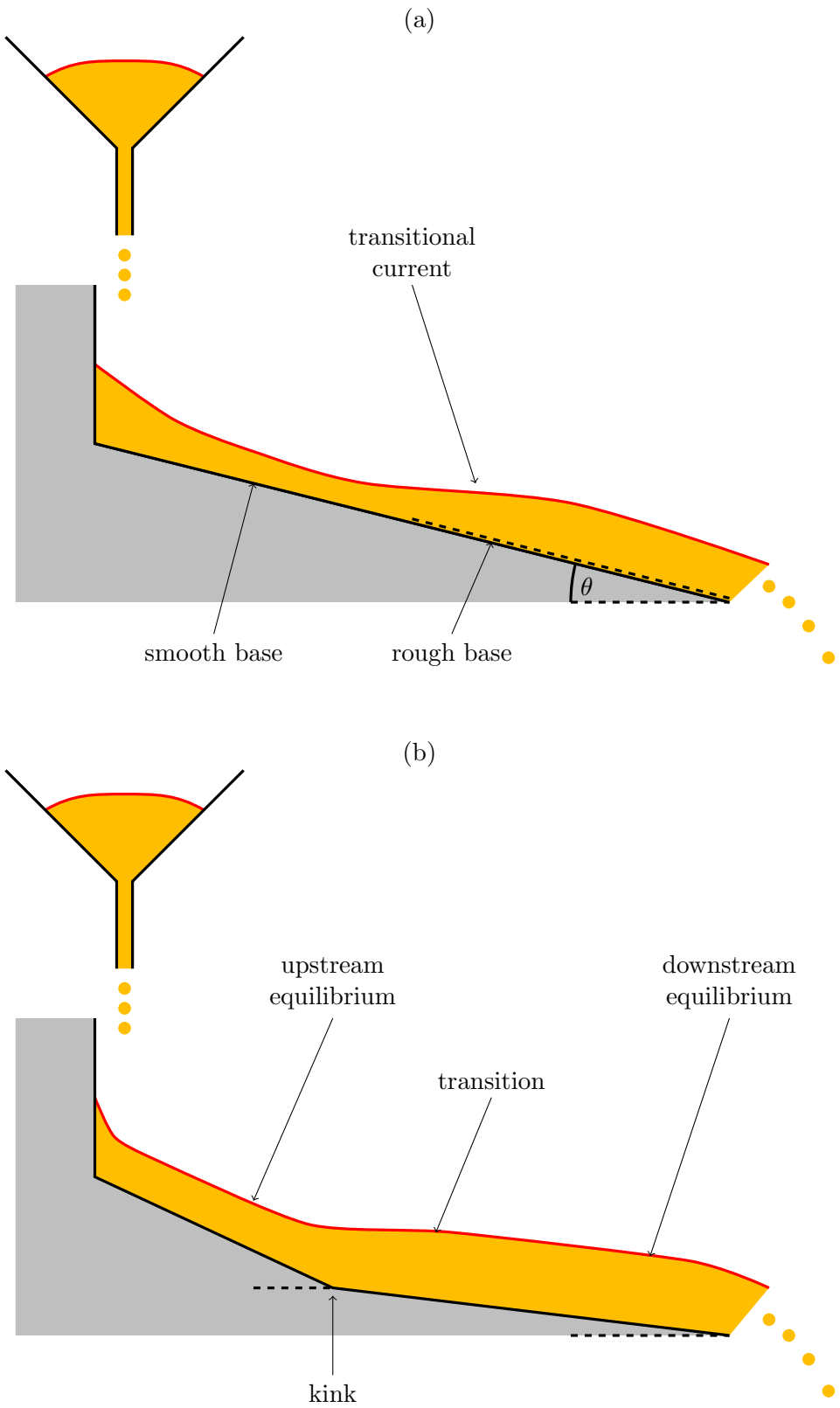

Figure 1.4.: Examples of chutes with streamwise topographical features. The flows that develop in the steady states have transitional behaviours around the topographical features.

The present work shall attempt to apply the $\mu(I)$ rheology to problems where dependencies on x and t are important, at least in particular regimes. In these problems, the dependencies shall be triggered by externally-imposed inhomogeneities in the governing equations or boundary conditions. We shall use the term *topography* to refer to these inhomogeneities. Our focus shall be on *chute flows*, that is, free surface flows down an inclined surface. A simple chute flow is shown in figure 1.3. This chute has no streamwise variation except at its upstream and downstream ends. Figure 1.4 shows two examples of chutes that have streamwise variation. Although 'topography' is usually understood to refer to inhomogeneities in space, we shall also use the term to encompass situations with time-dependent conditions; Chapter 12 shall discuss such problems.

1.3. Outline of thesis

Part I will review existing continuum models of granular flows, which may be divided into rheological models and depth-averaged models. We begin by describing and reviewing the $\mu(I)$ rheology (Jop et al. 2006) in Chapter 2. Much of the present work shall use the $\mu(I)$ rheology but we shall outline some other rheological models, which address some shortcomings of the $\mu(I)$ rheology, in Chapter 3. Although we shall not work with these models in detail, they will introduce some of the language needed to describe some observed phenomena outside of the dense flow regime. Alongside the choice of a rheology, one must also specify boundary conditions on a flow (Chapter 4): these are very similar to boundary conditions on classical fluids, but their physical interpretation requires some thought. We finish Part I by reviewing depth-averaged models (Chapter 5, introducing in particular the model of Gray and Edwards (2014).

Part II shall be a discussion of discrete particle models. After reviewing the basic ideas (Chapter 6), we will discuss methods of contact modelling (Chapter 7), and initial and boundary conditions on DPM (Chapter 8). While a significant body of work has been published on this, we note some issues that have been neglected by existing work, and propose some novel techniques for overcoming these issues. We also discuss the relationship between continuum models and DPM, and investigate the effects of particle-level parameters on the bulk rheology of the flow, in Chapter 9. A recurrent theme will be the trade-off between improving the physical realism of a DPM, and minimising the computational cost of a simulation. Some technicalities that arise when implementing a DPM simulation are discussed in Appendix A.

Part III will apply both continuum and discrete particle models to model problems involving flows subject to topography. Two such problems are sketched in figure 1.4: the chute in panel (a) has an abrupt change in basal roughness, while the chute in panel (b) is kinked. Our main focus shall be on the former, although (as we shall argue) there are similarities between the two problems, as both involve abrupt changes. Chapter 10 shall consider these problems using a depth-averaged approach. Chapter 11 shall study the setup in figure 1.4(a) using the $\mu(I)$ rheology, to consider more carefully the evolving velocity profile within this flow. As we shall see, this problem has many similarities to the classical Blasius boundary layer problem (Schlichting and Gersten 2017), and we term the present setup the 'granular Blasius problem'. We shall show that the predictions of the $\mu(I)$ equations match the results of DPM simulations. While Chapters 10 and 11 focus on steady flows with streamwise evolution, Chapter 12 shall apply the $\mu(I)$ rheology to a streamwise-independent but unsteady flow, in which basal boundary

conditions or the flow angle (or equivalently, the direction of gravity) are abruptly changed in time rather than in space: these are examples of temporal topography. Although a perfectly streamwise-independent flow is impossible to implement in a lab experiment, such a geometry is rather common in DPM; but we shall see that there are important differences between time-dependent and streamwise-dependent problems.

Part IV will summarise the work of the previous three parts (Chapter 13), and propose further work to investigate the interactions between topographical features and several phenomena of granular flows that are outside the scope of this thesis (Chapter 14). The final chapter, Chapter 15, restates the motivations for this work and the main conclusions.

Part I.

Continuum models

This part of the thesis describes the $\mu(I)$ rheology (Chapter 2), and briefly reviews some alternative rheological models that address some of the shortcomings of the $\mu(I)$ rheology (Chapter 3). We then discuss the boundary conditions on continuum fields (Chapter 4). Finally, we review a depth-averaged model of granular flows (Chapter 5).

2. The $\mu(I)$ rheology

> There are some [...] who think that the number of the sand is infinite in multitude; and I mean by the sand not only that which exists about Syracuse and the rest of Sicily but also that which is found in every region whether inhabited or uninhabited. Again there are some who, without regarding it as infinite, yet think that no number has been named which is great enough to exceed its magnitude. And it is clear that they who hold this view, if they imagined a mass made up of sand in other respects as large as the mass of the Earth, including in it all the seas and the hollows of the Earth filled up to a height equal to that of the highest of the mountains, would be many times further still from recognizing that any number could be expressed which exceeded the multitude of the sand so taken. But I will try to show you by means of geometrical proofs [...] that, of the numbers named by me [...], some exceed not only the number of the mass of sand equal in magnitude to the Earth filled up in the way described, but also that of the mass equal in magnitude to the universe.
>
> Archimedes, *The Sand Reckoner*

2.1. The $\mu(I)$ equations

As a rheological model, the $\mu(I)$ rheology describes a flow in terms of continuum fields, and specifies a system of partial differential equations and boundary conditions that governs them. For a granular flow, we introduce the density field $\rho(\boldsymbol{x}, t)$ and the velocity field $\boldsymbol{u}(\boldsymbol{x}, t)$, which can be interpreted as local averages of individual particles' masses and velocities. The relationship between continuum fields and individual particles' properties is defined in Weinhart et al. (2013) and described further in §9.1, but for the purpose of continuum modelling the exact definition is not important. We note that the density field ρ refers to the bulk density of the granular flow. This is distinct from the intrinsic density ρ_* of the material, and the two are related by the packing fraction $\phi(\boldsymbol{x}, t) = \rho(\boldsymbol{x}, t)/\rho_*$.

All continua are governed by the conservation of mass,

$$\frac{\partial \rho}{\partial t} + \boldsymbol{\nabla} \cdot (\rho \boldsymbol{u}) = 0. \tag{2.1a}$$

In an inertial frame of reference, momentum balance is expressed as Cauchy momentum equation,

$$\rho \left(\frac{\partial \boldsymbol{u}}{\partial t} + \boldsymbol{u} \cdot \boldsymbol{\nabla}\, \boldsymbol{u} \right) = \rho \boldsymbol{g} + \boldsymbol{\nabla} \cdot \boldsymbol{\sigma}, \tag{2.1b}$$

with no body forces other than gravity $\rho \boldsymbol{g}$. In the internal forces term, $\boldsymbol{\sigma}$ is the Cauchy stress tensor (Acheson 1990), and the divergence of a rank 2 tensor is given, in index notation, by

$$(\boldsymbol{\nabla} \cdot \boldsymbol{\sigma})_i = \frac{\partial \sigma_{ij}}{\partial x_j}\,.$$

Each rheological model then closes the system (2.1) by giving a *constitutive relation* that allows us to express $\boldsymbol{\sigma}$ in terms of ρ and $\boldsymbol{u}$. These constitutive relations can sometimes be derived from kinetic theory, but for many materials they must be experimentally determined.

The $\mu(I)$ rheology (Jop et al. 2006) is based on a series of experiments and DPM simulations from previous works. Firstly, simulations by da Cruz et al. (2005) established that the packing fraction ϕ of a dense flow remains approximately constant, so that (2.1a) may be replaced with the incompressibility condition,

$$\boldsymbol{\nabla} \cdot \boldsymbol{u} = 0, \tag{2.2}$$

provided that the intrinsic density ρ_* is the same for all particles.[1, 2]

The stress tensor is then decomposed into an isotropic and a deviatoric part by writing

$$\boldsymbol{\sigma} = -p\mathbf{1} + \boldsymbol{\tau},$$

where p is defined as the pressure, and $\mathbf{1}$ is the identity tensor, $(\mathbf{1})_{ij} = \delta_{ij}$. As in classical fluid dynamics, the pressure field is determined by imposing (2.2) as a condition on $\boldsymbol{u}$ when solving (2.1b).

In classical continuum mechanics, the stress tensor $\boldsymbol{\sigma}$ and therefore the tensor $\boldsymbol{\tau}$ are assumed to be symmetric, $\sigma_{ij} = \sigma_{ji}$. This follows from a standard argument that states that the torques on an infinitesimal volume element must balance (Acheson 1990). Most rheological models of granular flows take this assumption as well. However, the argument is not physically justified as it is not meaningful to consider 'infinitesimal' volumes, or indeed any lengthscales smaller than the grain size d.

To study the shear stress $\boldsymbol{\tau}$, GDR MiDi (2004) and da Cruz et al. (2005) conducted experiments and simulations in simple shear geometries at steady state. (These geometries are illustrated in figure 1 of GDR MiDi (2004)). Under simple shear, the shear stress tensor $\boldsymbol{\tau}$ takes a value only along the direction of shear, and its magnitude τ may be measured. For simple shear, GDR MiDi (2004) noted the significance of the *inertial number*,

$$I = \frac{d\dot{\gamma}}{\sqrt{p/\rho}}, \tag{2.3}$$

where d is the mean grain diameter and $\dot{\gamma}$ is the shear rate. The inertial number is therefore nondimensional. Testing a variety of granular media at different imposed shear rates, GDR MiDi (2004) found that the shear stress obeys the relationship

$$\frac{\tau}{p} = \mu(I), \tag{2.4}$$

where the function $\mu(I)$ is specific to a given species of grains, and must be empirically determined (§§2.3, 9.2). We note the similarity between (2.4) and Coulomb's law of dry friction, with the difference being that the coefficient of friction here is variable, being dependent on the shear rate and pressure through I. A basic property of the function $\mu(I)$ is that it must be non-decreasing in I, since τ must increase with $\dot{\gamma}$ (when the pressure is fixed). This is a

[1] Incompressibility (2.2) implies that the advective derivative $\partial\phi/\partial t + \boldsymbol{u} \cdot \boldsymbol{\nabla}\phi = 0$, so that ϕ is constant along streamlines. This is a weaker statement than the assertion that ϕ is constant.

[2] We shall sometimes refer to the rheology discussed in this chapter specifically as the 'incompressible $\mu(I)$ rheology', to contrast it against a compressible version that will be introduced in §3.1. Without any qualifiers, the '$\mu(I)$ rheology' shall assume incompressibility.

necessary condition for well-posedness (in the sense of Hadamard; see *e.g.* Barker et al. (2015, p. 798), Evans (2010)); if μ were allowed to decrease with I then the Cauchy momentum equation (2.1b) would be unstable to perturbations at arbitrarily small wavelengths.

The results of GDR MiDi (2004) came from steady flows in simple shear. To arrive at the $\mu(I)$ rheology, Jop et al. (2006) made the extrapolation that the result (2.4) may hold in more general velocity fields in multiple dimensions, with $\dot{\gamma}$ replaced by the local shear rate, and the shear stress τ acting in a direction that opposes the shear rate. Accordingly, one defines the shear rate tensor

$$\boldsymbol{D} = \frac{1}{2}\left(\boldsymbol{\nabla}\,\boldsymbol{u} + (\boldsymbol{\nabla}\,\boldsymbol{u})^T\right) = \operatorname{Sym}\boldsymbol{\nabla}\,\boldsymbol{u}, \tag{2.5}$$

and its magnitude

$$||\boldsymbol{D}|| = \sqrt{\frac{1}{2}\operatorname{trace}\left(\boldsymbol{D}^2\right)} = \sqrt{\frac{1}{2}D_{ij}D_{ij}}.$$

The inertial number is then defined as

$$I = \frac{2d||\boldsymbol{D}||}{\sqrt{p/\rho}}. \tag{2.6}$$

The extra factor of 2 in (2.6), not present in (2.3), is due to the factor of $1/2$ in the formula for $||\boldsymbol{D}||$, which is the definition of the magnitude of a rank 2 tensor (Gray and Edwards 2014). To arrive at the $\mu(I)$ rheology, Jop et al. (2006) proposes

$$\boldsymbol{\tau} = \mu(I)p\frac{\boldsymbol{D}}{||\boldsymbol{D}||}, \tag{2.7}$$

extrapolating (2.4) to multiple dimensions. In this work, we shall refer to

$$\boldsymbol{s} = \frac{\boldsymbol{D}}{||\boldsymbol{D}||} \tag{2.8}$$

as the *strain rate direction tensor*.

Although high inertial number flows can be interpreted as 'fast' flows, we note that I does not depend directly on the magnitude of velocity, but rather on the strain rate $||\boldsymbol{D}||$; the inertial number and the $\mu(I)$ equations are invariant under Gallilean boosts. Therefore, a 'fast' flow relative to a fixed chute could have a low inertial number, depending on the velocity profile. A better interpretation of the inertial number is as the ratio between two timescales,

$$I = \frac{t_{\text{micro}}}{t_{\text{macro}}}, \quad \text{where} \quad t_{\text{micro}} = \frac{d}{\sqrt{p/\rho}}, \quad t_{\text{macro}} = \frac{1}{2||\boldsymbol{D}||}. \tag{2.9}$$

Here, the microscopic timescale t_{micro} is the timescale over which particles rearrange around each other, which increases with d and decreases with the pressure p. The macroscopic timescale t_{macro} is the timescale associated with the shear rate (Andreotti et al. 2015).[3]

Having defined this constitutive relation, the Cauchy momentum equation (2.1b) may now be written as

$$\rho\left(\frac{\partial \boldsymbol{u}}{\partial t} + \boldsymbol{u}\cdot\boldsymbol{\nabla}\,\boldsymbol{u}\right) = \rho\boldsymbol{g} - \boldsymbol{\nabla}\,p + \boldsymbol{\nabla}\cdot\left(\mu(I)p\boldsymbol{s}\right). \tag{2.10}$$

The mass and momentum equations must be further supplemented by boundary conditions. Appropriate boundary conditions for granular flows shall be discussed in Chapter 4.

[3] In this scaling argument, the factor of 2 could be placed into the definition of t_{micro}, rather than that of t_{macro}.

2.2. Steady uniform flows and the Bagnold velocity profile

A particularly important class of solutions to the incompressible $\mu(I)$ equations is a family of steady solutions that are uniform in x, so that $\partial/\partial t = \partial/\partial x = 0$. The depth h is constant and the velocity takes the form $\boldsymbol{u} = (u, w) = (U(z), 0)$. Under these conditions, there is no acceleration on any element, so the stresses on each element must balance. In particular, the friction coefficient $\mu(I)$ must be equal to $\tan\theta$. Hence, the inertial number I is given by

$$I = \mu^{-1}(\tan\theta) = I(\theta),$$

defining the new function $I(\theta)$ for convenience. With $\partial/\partial x = \partial/\partial t = 0$, the flow is entirely streamwise and the pressure must be hydrostatic, so

$$p = g(h - z)\cos\theta. \tag{2.11}$$

We can then solve for $U(z)$ from the definition of the inertial number (2.6), obtaining

$$U(z) = u_b + \frac{2}{3}\frac{I(\theta)\sqrt{g\cos\theta}}{d}\left[h^{3/2} - (h-z)^{3/2}\right], \tag{2.12}$$

where $U(0) = u_b$ is the *slip velocity*. If the no-slip condition is applied at $z = 0$ then $u_b = 0$, and (2.12) is referred to as a *Bagnold velocity profile*

$$U(z) = \frac{2}{3}\frac{I(\theta)\sqrt{g\cos\theta}}{d}\left[h^{3/2} - (h-z)^{3/2}\right]. \tag{2.13}$$

The general form (2.12) shall be called a *Bagnold-with-slip profile*. We discuss whether the no-slip condition actually applies in Chapter 4.

In the above, we have assumed that the inverse $\mu^{-1}(\tan\theta)$ exists. Whether this be the case depends on the function $\mu(I)$ for this species of grains. If $\mu^{-1}(\tan\theta)$ does not exist, then no steady uniform flow is possible: the slope angle is either so steep that the flow accelerates indefinitely, or so shallow that the flow comes to a halt.

Even if $\mu^{-1}(\tan\theta)$ does exist and therefore the steady uniform solution (2.13) is admissible, this solution may not be attractive, but may be subject to instabilities. Instabilities shall be discussed in more detail in §14.2, but it can be shown that, in two dimensions, if time-dependence is suppressed ($\partial/\partial t = 0$) then a steady flow evolves towards (2.13) as $x \to \infty$ (§10.1.3); likewise, if streamwise-dependence is suppressed ($\partial/\partial x = 0$) then any initial velocity profile evolves towards (2.13) as $t \to \infty$; we show this (§12.2).

Given the depth of a flow $\mathcal{H}$, it is helpful to define the Bagnoldian velocity scale $\mathcal{U}_{\mathrm{Bag}}$ and the relative grain size δ by the formulae

$$\mathcal{U}_{\mathrm{Bag}} = \frac{\sqrt{g\mathcal{H}^3}}{d} = \frac{\sqrt{g\mathcal{H}}}{\delta}, \quad \delta = d/\mathcal{H}. \tag{2.14}$$

These shall be used in scaling arguments later.

2.3. Experimental calibration of the $\mu(I)$ rheology

The function $\mu(I)$ is found experimentally using the simple shear flow geometries described in GDR MiDi (2004). For chute flows, a long chute is inclined at an angle θ and a steady stream of grains at a prescribed flow rate q is allowed to flow down it. Eventually the flow develops into a state that is statistically steady and uniform in the streamwise direction. Assuming that the internal velocity of this flow has the Bagnold profile (2.13), then the depth of the current h and the flow rate q may be measured. From these, I may be calculated, according to the formula

$$I = \frac{5dq}{2(gh^5 \cos\theta)^{1/2}}, \tag{2.15}$$

which appears as equation (19) in GDR MiDi (2004). Meanwhile, in a steady state, the friction coefficient is $\mu = \tan\theta$, giving a relationship between θ, μ and I. In Chapter 9, we shall use a similar procedure to calibrate discrete particle models.

All experimental results agree that for dry granular flows $\mu(I)$ increases with I. This is to be expected, or else the final term on the right-hand side of (2.10) would act like a problematic 'backwards diffusion' term (Evans 2010). However, there is no consensus on whether the function $\mu(I)$ has a certain functional form for different species of granular materials. It can be shown that the $\mu(I)$ rheology is well-posed only if the function $\mu(I)$ satisfies certain conditions, such as $\mu'(I) > 0$ (§2.4, Barker et al. (2015)).

The $\mu(I)$ rheology applies to granular materials in a dense flowing state. It is known that at low slope angle θ, a steady current on the chute does not develop. Instead, the grains form a pile that intermittently collapses. Meanwhile, at high values of θ, the chute-perpendicular component of gravity is not strong enough to keep the grains in a dense state: consider, for example, the ultimate case $\theta = 90°$: gravity points entirely in the streamwise direction, so that grains are driven forward without making contact with the base. Motivated by these observations, Jop et al. (2005) proposed the form

$$\mu(I) = \mu_1 + \frac{\mu_2 - \mu_1}{I_0/I + 1}, \tag{2.16}$$

where μ_1, μ_2 and I_0 are fitted parameters. The function $\mu(I)$ then takes values within the range $[\mu_1, \mu_2)$, and the equation $\mu(I) = \tan\theta$ has a (unique) solution for I if and only if $\theta \in [\theta_1, \theta_2)$, where $\theta_1 = \arctan\mu_1$ and $\theta_2 = \arctan\mu_2$.

This captures the fact that a steady flow is not supported in chutes at high inclinations, but there is no experimental evidence to support the presence of an abrupt cutoff like this. 'Those functional forms have not been tested for large values of the inertial number I' (Forterre and Pouliquen 2008). In Chapter 11, we shall see that this asymptotic behaviour is important for determining the behaviour of boundary layers, *i.e.* flow regions with high shear rate and therefore high inertial number. In particular, the asymptotic behaviour of (2.16) is not consistent with the growth of boundary layers observed from DPM simulations (§11.4). We therefore contend that the form (2.16) must eventually be replaced with some other expression, at least for $I \gg 1$.

We also propose fitting functions of the power-law form

$$\mu(I) = \mu_s + mI^\alpha \tag{2.17}$$

where μ_s, m and the exponent α are experimentally fitted constants, with $\alpha m > 0$ to ensure that $\mu(I)$ increases with I; indeed,

$$I \frac{\mathrm{d}\mu}{\mathrm{d}I} = \alpha m I^\alpha > 0. \tag{2.18}$$

Under the (2.17), the derivative $\mathrm{d}\mu/\,\mathrm{d}I$ has a power-law dependence on I, which may allow self-similar behaviours to be found: this behaviour shall be useful in Chapters 11 and 12. If $\alpha < 0$, then the form (2.17) is singular at $I = 0$; nonetheless, (2.17) could be a useful form for $\mu(I)$ in a region of I away from $I = 0$. For example, in Chapters 11 and 12, we shall consider high shear rate flows, for which $I \gg 1$; we shall suppose that $\mu(I)$ takes the form (2.17) *asymptotically*. For example, the Jop fit (2.16) has the asymptotic form (2.17) by taking $\alpha = -1$, $m = -(\mu_2 - \mu_1)I_0 < 0$, and $\mu_s = \mu_2$.

Experimental techniques for measuring the depth h of a current, used in the experimental formula (2.15), include laser triangulators, which have accuracy and precision far tighter than the particle size d.[4] As we have said already, continuum models take the view that a granular flow wholly occupies a particular region, which may be bounded above clearly, as sketched in figures 1.2–1.4. In reality, '[c]are must be taken when defining the height of the surface as saltating particles can obscure the dense region below' (Holyoake and McElwaine 2012): the limiting factor on the precision of h therefore comes from the definition of h itself, not from experimental equipment. The difficulty of defining a free surface shall be a recurrent one in other rheological models (§3.1), as well as in DPM (§9.1.2).

2.4. Shortcomings of the $\mu(I)$ rheology

While the $\mu(I)$ rheology appears to be a good model for grains in a state of dense flow (Jop 2015), there are some aspects of granular flows that this model is not able to describe.

As discussed in the introduction (§1.1), all continuum models, including the $\mu(I)$ rheology, rely on the central assumption that the granular material may be treated as a continuum. This assumption fails when the particle size d or the mean free path are not sufficiently small compared to other lengthscales, such as the typical depth of a current or the aperture of a nozzle. The $\mu(I)$ rheology therefore cannot capture granular phenomena that are caused by the discrete nature of grains and by the fact that they have a nonzero size. These phenomena include granular phase transitions, in which a granular material ceases to be in a dense flowing state and either becomes static, known as a jamming transition (To et al. 2001), or 'dissociated', entering a kinetic regime (Lun 1991). Jamming and dissociation correspond respectively to the cases of very low and very high inertial numbers. In accordance with this, Barker et al. (2015) showed that the $\mu(I)$ rheology can be locally ill-posed, in the sense of Hadamard (Evans 2010), at extreme inertial numbers, depending on the form of the function $\mu(I)$.

As we mentioned in §2.3, simple laboratory experiments on chute flows as well as similar DPM simulations (to be introduced in Chapter 9) indicate that, at high slopes θ, grains are not in a state of dense flow but are mostly dissociated from each other. With few grain-to-grain

[4] For example, Holyoake and McElwaine (2012) measured the depth of their flows using 'a Micro Epsilon LLT2800-100 laser triangulator. This equipment [...] gives the surface height at a resolution of around 1 mm between points', and gives precision 'within 0.2 mm which is significantly less than the median grain diameter'.

interactions, little energy is dissipated from inelastic collisions or frictional contacts, and a steady uniform flow does not develop, at least over the timescales or lengthscales practical to consider in an experiment or simulation. (In the limiting case of $\theta = 90^\circ$, particles are in freefall and have no interactions at all, either with each other or with the base.)

At low inertial numbers, a necessary condition for the well-posedness of the $\mu(I)$ rheology is that $\mu(I) \to 0$ as $I \to 0$: without this condition, the shear stress would be discontinuous when the shear rate $\boldsymbol{D}$ changes direction (since the shear direction tensor $\boldsymbol{s}$ is discontinuous at $||\boldsymbol{D}|| = 0$). The requirement that $\lim_{I \to 0} \mu(I) = 0$ is at odds with experimental fits such as (2.16) and (2.17), although, as mentioned in §2.3, these forms can be interpreted as applying away from $I = 0$.

* * *

A number of alternative rheological models of granular media have been proposed in response to the difficulties faced by the $\mu(I)$ rheology, which we now review in Chapter 3. Any rheological model, including the $\mu(I)$ rheology, must be supplemented with boundary conditions, which we shall consider in Chapter 4. Chapter 5 shall review a depth-averaged model derived from the $\mu(I)$ rheology. Finally, we shall study how the function $\mu(I)$ is affected by the microscopic properties of the constituent particles of a flow in Chapter 9.

3. Other rheological models

> And so these men of Indostan
> Disputed loud and long,
> Each in his own opinion
> Exceeding stiff and strong,
> Though each was partly in the right
> And all were in the wrong!
>
> John Godfrey Saxe, *The Blind Men and the Elephant*

This chapter reviews some alternative models of granular flows, which attempt to describe flow phenomena that the incompressible $\mu(I)$ rheology is not able to capture (§2.4). We first describe rheological models that are based on the friction law (2.4) but incorporating compressibility, so that the packing fraction ϕ is allowed to be non-constant (§3.1). Models based on kinetic theory (§3.2) apply to very sparse flows $\phi \ll 1$. Finally, nonlocal models (§3.3) offer a description of how the flow behaviour depends on the grain size d when d becomes comparable to other flow lengthscales such as the depth of a current.

3.1. Compressibility

The assumption that a granular flow is incompressible (2.2) is incompatible with the phenomenon of Reynolds dilatation (Andreotti et al. 2015), which is the tendency for static grains to be packed in a more dense configuration (higher ϕ) than grains under shearing. This reflects the physical fact that, contrary to the continuum assumption, grains do not fully occupy a space but can move apart from each other. If ϕ is allowed to vary significantly, then the more general mass conservation equation (2.1a) must be used instead of the incompressibility condition (2.2). Jop et al. (2006) used the incompressibility assumption for the $\mu(I)$ rheology, arguing that the DPM simulations of da Cruz et al. (2005) showed that variations in ϕ are small.[1]

When compressibility is introduced, the system (2.1) must be supplemented by an equation of state that relates the new variable ϕ to the quantities u, w and p. One approach (see *e.g.* Forterre and Pouliquen (2008), Heyman et al. (2017)) is to introduce a 'coupled-ϕ' rheology, using the equation of state

$$\phi = \phi(I),$$

with $\phi'(I) \leq 0$. This captures the notion that ϕ decreases as the rate of shearing is increased, while ϕ increases with pressure (since a higher pressure reduces I). Empirically, $\phi(I)$ is approximately a linear function of I (da Cruz et al. 2005). Under this dependence, ϕ is not introduced as a new dynamic variable, as it remains coupled to the velocity field. The mass conservation

[1] da Cruz et al. (2005) presented this data as their figure 2 and discussed it briefly in their section V.A; they refer to the packing fraction as the 'solid fraction' and use the symbol ν.

equation (2.1a) becomes

$$\frac{\mathrm{d}\phi}{\mathrm{d}I}\left(\frac{\partial I}{\partial t} + \boldsymbol{u}\cdot\boldsymbol{\nabla} I\right) + \phi\,\boldsymbol{\nabla}\cdot\boldsymbol{u} = 0,$$

which gives an equation relating $\boldsymbol{u}$ and p.

More recently, Barker et al. (2017) introduced the 'compressible I-dependent rheology' (CIDR). Under CIDR, the packing fraction ϕ is promoted to a separate dynamical variable, governed by (2.1a), rather than coupled with I. A new constitutive relation is proposed, in which the stress tensor has a separate dependence on ϕ.

When ϕ is allowed to be non-constant, the definition of the inertial number (2.6) must be revisited: since the bulk density $\rho = \rho_*\phi$ depends on the packing fraction, (2.6) implies an implicit, coupled dependence between I and ϕ. The coupled-ϕ rheology as it has been presented above is therefore difficult to apply in practice. Heyman et al. (2017) 'chose to retain the usual incompressible definition of the inertial number' by replacing ρ with ρ_* in the definition of I, thereby making the coupling one-way rather than two-way.[2] Thomas Barker (pers. comm., 21 September 2018) agreed, arguing that 'we have also opted to use only the intrinsic grain density in the inertial number definition [...] using the intrinsic grain density makes it easier to distinguish between the effects of packing density and of the strain-rate in the constitutive equations'.

As before (§2.3), the notion of a 'free surface' in a continuum model is an abstraction, since there is no canonical way of defining such as surface in terms of the positions of individual grains. When compressibility is introduced, an additional complication arises. An incompressible model takes $\phi = \text{constant} > 0$ within a flow and $\phi = 0$ without, and supposes a strict cutoff. But when compressibility is introduced and ϕ is allowed to vary within a flow, an additional boundary condition is required on ϕ. Although various authors have applied compressible rheologies to chute flows, none have explicitly stated any such free surface boundary condition (Forterre and Pouliquen 2008, Heyman et al. 2017, Barker et al. 2017). Given that the packing fraction ϕ is lower in a layer near the free surface than within the body of the flow (Barker et al. 2017), it is likely that compressible modifications of the $\mu(I)$ rheology break down there, and that the flow in that layer is governed instead by kinetic theory, which we now describe.

3.2. Kinetic theoretical models

Even if the $\mu(I)$ rheology is modified as in the previous section to allow compressibility, it still becomes inappropriate at very low packing fractions. In such a regime, particles have a relatively long mean free path compared to their size, and particle-to-particle interactions become mostly binary. Dissipation in such a system is caused by inelasticity in individual collisions, not by the trapping of a particle between several others or by the friction of individual grain-to-grain contacts. It is also no longer meaningful to speak of a 'microscopic rearrangement' timescale, or to interpret the inertial number as a characterisation of this timescale (2.9): in this regime, particles move around each other ballistically, not due to pressure.

Several alternative models have been developed to describe the rheology of a granular material in this 'kinetic regime' (Andreotti et al. 2015), including those of Haff (1983), Lun and Savage (1986), and Lun (1991): historically, these precede the development of the $\mu(I)$ rheology. These

[2] Heyman et al. (2017) use the notation ϱ and ρ to correspond with our ρ and ρ_*, respectively.

studies still talk of the velocity field $\boldsymbol{u}(\boldsymbol{x}, t)$, the pressure $p(\boldsymbol{x}, t)$ and the packing fraction $\phi(\boldsymbol{x}, t)$, but they also introduce the new concept of *granular temperature*, $T(\boldsymbol{x}, t)$, which characterises the local *variance* of particles' velocities, defined in analogy with classical gases. As a variance of velocities, T has dimensions of $(\text{length})^2(\text{time})^{-2}$. Most authors (Andreotti et al. 2015, p. 170) define T as the local spatial average, over individual particles, of the temporal variances of their velocities. On the other hand, Weinhart et al. (2013) defines T as the local spatial variance of the velocities of individual particles, taken as a snapshot in time. These definitions are subtly different but can be expected to be approximately equivalent provided that the microscopic dynamics may be assumed to be ergodic (Birkhoff 1931).

Different kinetic theoretical models of granular flows agree that the temperature field T is governed by an equation of the general form

$$\phi\left(\frac{\partial T}{\partial t} + \boldsymbol{u}\cdot\boldsymbol{\nabla} T\right) = \boldsymbol{\nabla}\cdot(D_T\,\boldsymbol{\nabla} T) + \boldsymbol{\sigma} : \boldsymbol{D} - \Delta_T,$$

an advection-diffusion-reaction equation. Here, D_T is the diffusivity of temperature, and Δ_T is the rate of temperature dissipation. These are functions of ϕ, $\boldsymbol{u}$, T, p and their derivatives, as well as material properties of the constituent grains, all of which are to be specified by the individual models. Moreover, the momentum equation (2.1b) retains its general form, but the stress tensor $\boldsymbol{\sigma}$ may now depend on T as well; again, the particular constitutive relation for $\boldsymbol{\sigma}$ varies from model to model.

The term $\boldsymbol{\sigma} : \boldsymbol{D}$ represents the generation of temperature from shearing, which is familiar from classical fluid dynamics (Batchelor 2000). The dissipation term Δ_T represents the effects of inelastic collisions, which conserve total momentum but reduce the relative velocities of particles, and therefore the variance. While Haff (1983) and Lun et al. (1984) disagree on the exact functional form of Δ_T, they agree on the scaling

$$\Delta_T \propto \frac{(1-e^2)}{d} T^{3/2} f(\phi), \tag{3.1}$$

where e is the coefficient of restitution between two colliding particles, and d is the particle diameter as before. The scalings by T and d follow from dimensional considerations, and the coefficient $1 - e^2$ is the proportion of kinetic energy dissipated in a collision with restitution coefficient e. The unspecified remaining (nondimensional) coefficient of proportionality $f(\phi)$ is related to the rate of collisions between particles, which increases with ϕ.

In the language of the above, the limit of high packing fraction and low temperature restores the dense flow regime for which the $\mu(I)$ rheology is suitable. However, the two rheologies arise from different approaches, and kinetic theoretical models are invalid for high ϕ. It is not clear how to formally relate the concepts of inertial number and granular temperature, and there is currently no model of granular materials that reconciles the dense and kinetic regimes (Andreotti et al. 2015).

Although we shall focus on dense flows in this work, we mention these kinetic models not just for the sake of completeness, but because the role of the restitution coefficient will become important when we come to look at discrete particle models in Part II. The formula (3.1) has been developed for the kinetic regime, but we shall seek a similar formula for dense flows. This will have computational advantages, as we shall see in §7.5.

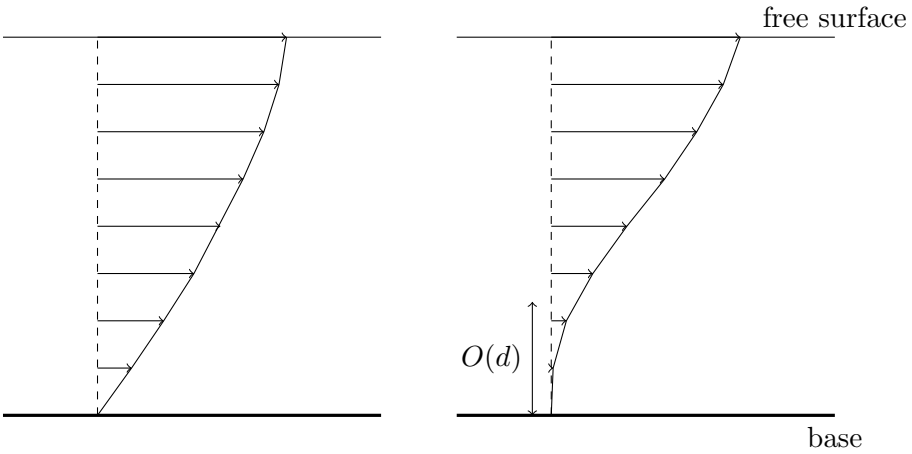

Figure 3.1.: Left: The Bagnold velocity profile, the velocity profile predicted by the $\mu(I)$ rheology for a steady uniform chute flow. Right: A velocity profile with low fluidity near the base, observed in flows of large grains and predicted by nonlocal models. The profile on the right has a shape factor $\chi > 5/4$. The basal boundary layer is proportional to d.

3.3. Nonlocal models

The $\mu(I)$ rheology also faces difficulties at dense packings and very low inertial numbers. The $\mu(I)$ rheology is a 'local' rheological model, in the sense that the stress tensor $\boldsymbol{\sigma}$ at a point depends only on the local values of pressure and shear rate, and not on their derivatives. Perhaps unsurprisingly, experimental work has shown that this approach is unsatisfactory when there are velocity gradients over lengthscales that are comparable to the particle diameter d (Kamrin and Henann 2015), or equivalently if d is comparable to other lengthscales in a flow. For example, it is well-established (see *e.g.* Pouliquen (1999), Jop (2015)) that no flow occurs if the depth of a current h is below a certain threshold $h_{\text{stop}}(\theta) = O(d)$. This stopping is not predicted by the $\mu(I)$ rheology, but has motivated a number of 'nonlocal' constitutive relations, including the *cooperative model* (Henann and Kamrin 2013, Kamrin and Henann 2015) and the *gradient model* (Bouzid et al. 2013). Both of these modify the local $\mu(I)$ rheology by generalising the constitutive relation (2.7) so that the stress $\boldsymbol{\sigma}$ depends not only on the strain rate (2.5), but also on further gradients of the velocity field. The correction terms containing these gradients are multiplied by coefficients proportional to the particle size d, so that these terms are small except for gradients over short distances, which are $O(1/d)$. The relationship between local and nonlocal models is similar to the relationship between the Euler equations and the Navier–Stokes equations at high Reynolds number: the latter includes a term for viscosity that is small except when there are velocity gradients over small lengthscales.

Figure 3.1 contrasts the Bagnold velocity profile with a sketch of the modified velocity profile predicted by nonlocal rheology. The nonlocal profile matches will with experimental evidence on two-dimensional large photoelastic discs, in both a shear cell geometry (Tang et al. 2018) and a chute flow geometry (Thomas and Vriend 2019), the latter of which being of more relevance to the present work.

For DPM simulations, in §9.4 we shall conduct calibration tests examining the effects of particle

size on rheological parameters. As we shall see, changing d appears to have only minor effects on the bulk rheology provided that d is smaller than about 1/20th of the depth.

* * *

In this chapter, we have reviewed a number of rheological models of granular materials that have been proposed. Each of these attempt to describe a particular regime of a granular material, but at present, there is no 'universal' theory that unifies all of these models and is applicable to granular materials in all regimes (Andreotti et al. 2015). It is unlikely that any such continuum model will ever exist, given the fundamentally discrete nature of granular materials (§1.1).

This thesis shall focus largely on the $\mu(I)$ rheology, which we shall use to study the problems in Part III. Therefore, we shall not make much use of these alternative rheologies outside of this chapter, but the language of these models will be important when we analyse discrete particle models in Part II, or study applications in Part III.

4. Boundary conditions

Whether one uses the $\mu(I)$ rheology (Chapter 2) or an alternative rheological model (Chapter 3), it is necessary to supplement the equations of motions with boundary conditions on the fields at the base $z = b(x)$ and the free surface $z = s(x, t)$. As in classical continuum mechanics, these boundary conditions may be divided into *kinematic boundary conditions* (§4.1) and *dynamic boundary conditions* (§4.2). We also need boundary conditions at the upstream and downstream ends of the flow domain (§4.3). For unsteady flows, we must also specify initial conditions.

Boundary conditions in continuum models are rather different from boundary conditions in discrete particle models. The latter shall be discussed in Chapter 8, but the difference between may be summarised thus: boundary conditions in a continuum model apply to fields, while boundary conditions in a discrete particle model govern individual particles.

Many continuum boundary conditions are expressed in terms of discontinuities of fields across boundaries. Throughout this chapter, we use the notation $[f]$ to mean the change in a quantity f across either side of a boundary, with the sign convention $[f] = f_+ - f_-$, where $f_\pm$ are the values of f on either side of the boundary, with the positive side defined by the direction of the normal $\boldsymbol{n}$ to the boundary. The equation $[f] = 0$ asserts that f is continuous across the boundary.

4.1. Kinematic boundary conditions

At any boundary, the kinematic boundary conditions are a consequence of the condition of mass continuity (2.1a). If the velocity field $\boldsymbol{u}$ satisfies incompressibility (2.2), then the normal component of the relative velocity of the continuum to the boundary must be continuous across the boundary:

$$[(\boldsymbol{u} - \boldsymbol{U}) \cdot \boldsymbol{n}] = 0. \tag{4.1}$$

In (4.1), $\boldsymbol{n}$ is the normal to the boundary and $\boldsymbol{U}$ is the velocity of the boundary, In particular, at a stationary rigid boundary $\boldsymbol{U} = \boldsymbol{0}$, we obtain from (4.1) the *no-penetration condition* $\boldsymbol{u} \cdot \boldsymbol{n} = 0$. If the rigid base is at $z = 0$, the boundary condition becomes

$$w = 0 \qquad \text{at } z = 0.$$

More generally, if the base is given by the curve $z = b(x)$, then the boundary condition is

$$-b'(x)u + w = 0 \qquad \text{at } z = b(x), \tag{4.2}$$

assuming that b is smooth. Similarly, at the free surface $z = s(x, t)$, it can be shown that (4.1) implies the *kinematic free surface boundary condition*

$$\frac{\partial h}{\partial t} + u\,\frac{\partial s}{\partial x} = w \qquad \text{at } z = s(x, t). \tag{4.3}$$

The kinematic boundary condition (4.1) applies for any incompressible continuum, regardless of any other rheological properties.

4.2. Dynamic boundary conditions

In continuum mechanics, the dynamic boundary conditions on a surface arise from considering stress balances on a surface element. The appropriate dynamic boundary conditions depend on the particular nature of the continuum and the surface. For granular flows, there is the complication that the continuum treatment is not valid across small scales. At the top of a flow, the position of a free surface cannot be defined precisely in terms of the positions of individual grains (§§8.6, 9.1.2). Basal dynamics are governed by the geometric effects of individual grains being constrained by the bumpiness of a surface.

4.2.1. Dynamic boundary conditions at the free surface

Under classical continuum mechanics, the stresses on a thin surface element on a free surface must balance, giving the condition

$$[\boldsymbol{\sigma} \cdot \boldsymbol{n}] + \left((\mathbf{1} - \boldsymbol{nn}) \cdot \boldsymbol{\nabla}\right) \boldsymbol{\sigma}_{\mathrm{surf}} = \mathbf{0} \quad \text{at } z = s(x,t), \tag{4.4}$$

where $\boldsymbol{\sigma}_{\mathrm{surface}}$ is the surface stress, proportional to surface tension and mean curvature. In the absence of surface tension, (4.4) becomes $[\boldsymbol{\sigma} \cdot \boldsymbol{n}] = 0$. Assuming that the fluid is immersed in a vacuum or a material of very low viscosity, the stress outside of the flow is equal to zero, and so the *dynamic free surface boundary condition* (4.4) implies the two conditions

$$\boldsymbol{n} \cdot (\boldsymbol{\sigma} \cdot \boldsymbol{n}) = 0 \quad \text{and} \quad \boldsymbol{n} \times (\boldsymbol{\sigma} \cdot \boldsymbol{n}) = \mathbf{0} \qquad \text{at } z = s(x,t), \tag{4.5}$$

where $\times$ denotes the cross product. We assume that the boundary conditions (4.5) are also applicable for the $\mu(I)$ rheology, so that both the pressure p and the shear rate $||\boldsymbol{D}||$ vanish at the free surface. However, the derivation of (4.4) relies on the ability to take a surface element with limitingly small thickness. In fact, the notion of a 'free surface' is an abstraction made by continuum models: at the level of individual grains, there can be no meaningful or canonical definition of a surface that divides a granular current from the void above it.

4.2.2. Dynamic boundary conditions at the base

In the previous section we discussed the kinematic condition (4.2) on the normal component of the velocity at the base. In classical fluid dynamics, for a viscous fluid, one also imposes the *no-slip boundary condition*

$$u_s = \left| (\boldsymbol{u} - \boldsymbol{U}) - \left((\boldsymbol{u} - \boldsymbol{U}) \cdot \boldsymbol{n}\right) \boldsymbol{n} \right| = 0, \tag{4.6}$$

indicating that there should be no relative tangential velocity to the motion of the surface. But this condition does not follow from geometric principles in the same way that (4.2) does from the incompressibility assumption; rather, (4.6) is an empirical assertion, and Acheson (1990) notes that early fluid dynamicists were hesitant to impose this condition for high Reynolds numbers flows. Indeed, a dilute viscous gas being sheared against a sufficiently smooth wall has been shown to exhibit a slip velocity

$$u_s \propto \dot{\gamma} l_{\mathrm{mf}}, \tag{4.7}$$

where $\dot{\gamma}$ is the shear rate and l_{mf} is the mean free path of a gas molecule (Morris et al. 1992). Lauga and Squires (2005) identify l_{mf} as a lengthscale below which the continuum assumption

itself becomes inappropriate. To generalise the condition (4.7), they advocated the use of a mixed (Robin) boundary condition,

$$u_s = \lambda \frac{\partial u}{\partial z} = \mathrm{Kn} \frac{\partial u}{\partial n}, \tag{4.8}$$

which appears as equation (1) in their paper. Here, the *Knudsen number* Kn is a constant $0 \leq \mathrm{Kn} \leq \infty$, with $\mathrm{Kn} = 0$ corresponding to the no-slip condition and $\mathrm{Kn} = \infty$ to a free-slip condition. Lauga and Squires (2005) interpret Kn as the ratio $\lambda/\mathcal{L}$, where the 'slip length' λ is the lengthscale over which an individual fluid particle (such as a molecule) may freely travel before encountering any interactions, and $\mathcal{L}$ is a representative lengthscale of the physical system, such as the depth of a current. Then (4.8) is equivalent to (4.7), with λ playing the role of l_{mf}.[1]

The aforementioned works culminating in (4.8) considered Newtonian flows, for which the tractional stress can be written as $\tau = \eta\dot{\gamma}$, where η is the dynamic viscosity, and so (4.8) can be interpreted as

$$u_s = \frac{\lambda}{\eta}\tau. \tag{4.9}$$

We propose that the form (4.9) could be generalised and applied to non-Newtonian flows, such as the $\mu(I)$ rheology, for which $\tau = \mu p$ and $\mu = \mu(I)$. We interpret the lengthscale λ as a dimensional characterisation of the roughness of a base, while the 'viscosity' η defines a timescale $\eta/\tau = \lambda/u_s$.

For a granular flow, whether or not the no-slip condition (4.6) holds on the base depends both on the geometric roughness of the base and on the intrinsic coefficient of friction between the base and a particle moving against it. The latter is due to asperities at the microscopic level that provide a frictional resistance to sliding motions between any two materials, and we shall discuss its effects when we later discuss contact modelling in Chapter 7. In this work, by 'roughness' and 'smoothness' we shall refer to asperities on a base that are comparable to the grain size, giving a geometric constraint on the motion of the grains.

The motion of a single grain moving against a geometrically smooth but frictional wall was considered in Artoni et al. (2009). In that work, the grain was subject to random applied tangential forces that represent the effect of all the other grains in the system. It was shown that the motion of the grain depends on whether the average magnitude of these applied tangential force exceeds a certain threshold, which is proportional to the friction between the grain and the wall (which is equal to the normal force times a coefficient of friction). It was shown that if the applied tangential force does not exceed this threshold, then the particle does not move at all; otherwise, the particle translates intermittently with a positive mean velocity, exhibiting a stick-slip behaviour.

The analyses in Artoni et al. (2009) and Morris et al. (1992) considered only geometrically smooth walls with intrinsic friction. When the walls have geometric roughness, the amplitude of this roughness is an extra parameter that may determine whether grains may slip or not. If the roughness is sufficiently angular, then it may effect a no-slip condition by confining grains from rolling or sliding along the surface, even in the absence of intrinsic friction. There has been much recent work into the dynamics of flows over geometrically rough bases, with a major difficulty being to statistically characterise a randomly-generated rough base.

[1] Lauga and Squires (2005) further note that the term 'mean free path' is not directly applicable to liquids.

Recent DPM simulations by Bharathraj and Kumaran (2017) on steady streamwise-uniform flows have shown that the no-slip condition suddenly begins to apply when the amplitude of the roughness is increased beyond a certain critical value that is proportional to the grain size. Again for steady uniform flows, Jing et al. (2016) proposed a quantification of the roughness of a frozen-particle base, defining the roughness indicator' R_a of a base in terms of the size and arrangement of the basal particles, and the intrinsic coefficient of friction between particles. However, neither of these works are directly applicable to streamwise non-uniform flows, in which grains have inertia relative to the base, and may temporarily violate the no-slip condition when flowing over a base that would otherwise impose a no-slip condition: such a case shall be demonstrated in figure 11.9.

4.3. Domain boundary conditions

As well as the kinematic and dynamic boundary conditions on the top and bottom of a flow, it is also necessary to specify streamwise boundary conditions for the governing equations.

The simplest case is that of a flow that is completely streamwise-independent, with $\partial/\partial x = 0$. If the flow is also steady, $\partial/\partial t = 0$, then we return to the case of §2.2. For unsteady flows, the incompressibility condition (2.2) implies that $w = 0$, so that h is nonetheless constant, and the evolution of $u(z,t)$ is given simply by the x-component of (2.10). This case shall be studied in Chapter 12.

An alternative streamwise boundary condition is to take a domain $0 \leq x \leq \mathcal{L}$ of finite length $\mathcal{L}$ and periodic boundary conditions at $x = 0$ and $x = \mathcal{L}$. A flow in a periodic domain can have some level of streamwise-dependence, but assuming that such dependence is small, a periodic domain predicts approximately the same behaviour as a streamwise-independent model, when quantities such as a component of the velocity field, or the depth $h(x,t)$, are averaged over x. In this thesis, we shall not make use of periodic domains in the context of continuum models, but we shall discuss a closely related concept of periodicity in DPM in §8.1.1.

In reality, flows can be neither perfectly streamwise-independent nor perfectly periodic, because they take place on chutes of finite length (figure 1.3), and will inevitably be affected by endpoint dynamics. But assuming that topographical features are localised and that the endpoints are far, the precise details of the endpoints dynamics can be neglected, or the far-field flow may be assumed to be uniform: we shall take this approach in Chapters 10 and 11.

5. Depth-averaged models

> Everything changes and nothing remains still [and] you cannot step twice into the same stream.
>
> Adapted from Heraclitus' words, as recorded in Plato's *Cratylus*

Rheological models such as the $\mu(I)$ rheology (Chapter 2) consider a continuum approximation to the flow velocity everywhere within a granular material. In most cases, it is impossible to obtain an analytically exact solution, and the numerical solution of (2.10) may be computationally intense, depending on the domain size and shape. One therefore resorts to approximations.

Flows of interest in industrial or environmental contexts (see Chapter 1) often extend over lengthscales $\mathcal{L}$ that are orders of magnitudes larger than their characteristic depth $\mathcal{H}$. As before, we assume homogeneity in the cross-stream direction, and that there is no flow in this direction. The *shallowness assumption*,

$$\epsilon = \mathcal{H}/\mathcal{L} \ll 1, \tag{5.1}$$

gives a separation of lengthscales that we can exploit by working with *depth-averaged quantities*. Using $z = s(x,t)$ as the position of the free surface and $z = b(x)$ as the position of a rigid base, the depth-average of any field $f = f(x,z,t)$ is defined as

$$\overline{f}(x,t) = \frac{1}{h(x,t)} \int_{b(x)}^{s(x,t)} f(x,z,t)\,\mathrm{d}z, \tag{5.2}$$

where the depth-averaging operation is denoted by an overline, and the depth of the flow is $h(x,t) = s(x,t) - b(x)$.

Most depth-averaged models are extensions of the shallow water equations

$$\frac{\partial h}{\partial t} + \frac{\partial}{\partial x}\left(h\overline{u}\right) = 0, \tag{5.3a}$$

$$\frac{\partial}{\partial t}\left(h\overline{u}\right) + \frac{\partial}{\partial x}\left(h\overline{u}^2 + \frac{1}{2}gh^2\right) = 0, \tag{5.3b}$$

originally proposed by Saint-Venant (1871) for shallow water flows (Chow 1959) on a flat base $b = 0$. The system (5.3) is an expression of conservation of mass (5.3a) and momentum balance (5.3b), which are obtained by depth-averaging the incompressibility condition (2.2) and the Euler equations respectively, combined with the shallowness assumption (5.1) and the assumption that the depthwise velocity profile is uniform (*i.e.* that of a plug flow). We shall return to this assumption in §5.2.

5.1. Depth-averaged $\mu(I)$ equations

Gray and Edwards (2014) depth-averaged the incompressible $\mu(I)$ equations to produce a pair of equations for mass and momentum balance along a granular flow, analogous to the derivation of (5.3) from the Euler equations. In this section, we outline their main results, but using the notation of the present work.

The depth-averaging operation (5.2) is applied to the governing equations (2.2) and (2.10). Assuming that the flow is incompressible and that ρ and ϕ are constant, then depth-averaging the incompressibility condition (2.2) using the formula (5.2) gives

$$\frac{\partial h}{\partial t} + \frac{\partial}{\partial x}\left(h\overline{u}\right) = 0, \tag{5.4a}$$

an equation for conservation of mass, identical to (5.3a). The boundary values of w have been eliminated using the kinematic boundary conditions at the base and the free surface (§4.1). Note that this equation holds for any incompressible fluid, irrespective of its rheology. Depth-averaging the momentum balance equation gives a second equation

$$\frac{\partial}{\partial t}\left(h\overline{u}\right) + \frac{\partial}{\partial x}\left(h\overline{u^2} + \frac{1}{2}gh^2\cos\theta\right) = gh\cos\theta\left(\tan\theta - \overline{\mu} - b'(x)\right) + \frac{\partial}{\partial x}\left(\nu h^{3/2}\frac{\partial \overline{u}}{\partial x}\right), \tag{5.4b}$$

which appears (in different notation) as (4.14) of Gray and Edwards (2014). This is an extension of (5.3b), and has additional terms accounting for streamwise driving (for a sloped surface $\theta > 0$), friction $\overline{\mu}$, diffusive internal stresses ν, as well as basal slope $b'(x)$.

The derivations of (5.3b) and (5.4b) both use the shallowness assumption (5.1). Under this assumption, the incompressibility condition (2.2) implies a scaling

$$\frac{|u|}{\mathcal{L}} \sim \frac{|w|}{\mathcal{H}}, \quad \text{so} \quad |w|/|u| \ll 1. \tag{5.5}$$

Since the perpendicular velocity w is small compared to the streamwise velocity u, perpendicular accelerations are small, and the pressure p within the flow is approximately hydrostatic (2.11). This gives

$$\frac{\partial p}{\partial x} \sim \rho g \frac{\partial s}{\partial x}\cos\theta,$$

where $s = b + h$ is the position of the free surface. This pressure gradient results in the $gh^2/2$ terms on the left-hand sides of (5.3b) and (5.4b). The original shallow water equation (5.3b) further assumes that $b = 0$, while the more general form (5.4b) has the additional term $b'(x)$, which represents basal topography.

An important difference between the Saint-Venant model and the depth-averaged $\mu(I)$ model is in the advective acceleration terms on the left-hand sides of their momentum equations: (5.3b) contains the term $\overline{u}^2$, while (5.4b) contains the term $\overline{u^2}$. The difference arises because the shallow water model makes the assumption that the depthwise velocity profile is uniform. The depth-averaged $\mu(I)$ rheology does not make this assumption.[1] We discuss the relationship between $\overline{u}^2$ and $\overline{u^2}$ initially in §5.2, and a major purpose of the problems studied in Part III shall be to understand the behaviour of this relationship in response to topographical features.

[1] If we write $u' = u - \overline{u}$, then

$$\overline{u^2} = \overline{u}^2 + \overline{(u')^2} \geq \overline{u}^2,$$

with equality if and only if $u' = 0$ identically.

profile name	profile function $S(\zeta)$	χ
plug	1	1
Poiseuille	$6\zeta(1-\zeta)$	$6/5$
Nusselt	$\frac{3}{2}\zeta(2-\zeta)$	$6/5$
Bagnold	$\frac{5}{3}(1-(1-\zeta)^{3/2})$	$5/4$
Couette	2ζ	$4/3$

Table 5.1.: The shape factors for some common velocity profiles.

The depth-averaged coefficients of friction $\overline{\mu}$ and diffusivity ν are to be expressed as functions of h and $\overline{u}$, and should be related to the function $\mu(I)$ from the local rheology. Gray and Edwards (2014) find these by integrating the streamwise component of (2.10), but the formula for $\overline{\mu}$ may be found heuristically as

$$\overline{\mu}(h,\overline{u}) = \mu(I) = \mu\left(\frac{5d\overline{u}}{2(gh^3\cos\theta)^{1/2}}\right),$$

with I given by the experimental formula (2.15), writing $q = h\overline{u}$ for the flow rate q. The coefficient of diffusivity ν appears as (4.16) in Gray and Edwards (2014), and is equal to $g^{1/2}$ multiplied by a lengthscale that is a material property. Although the final term in (5.4b), which represents the viscosity-like effects of friction, is a nonlinear diffusion term, the diffusivity coefficient ν does not have dimensions of kinematic viscosity.

5.2. The shape factor

The $\overline{u^2}$ term that appears in (5.4b) cannot *a priori* be expressed in terms of h and $\overline{u}$, so (5.4a) and (5.4b) do not yet form a closed system of equations. Instead of working with $\overline{u^2}$ directly, we define the *shape factor*

$$\chi = \frac{\overline{u^2}}{\overline{u}^2} = \frac{h\displaystyle\int_0^h u^2\,\mathrm{d}z}{\left(\displaystyle\int_0^h u\,\mathrm{d}z\right)^2}, \tag{5.6}$$

a dimensionless number that quantifies the variance of velocity within the current (Gray and Edwards 2014). The shape factor is equal to 1 for a plug flow, and greater than 1 for any other profile. In particular, the shape factor is equal to 5/4 for the Bagnold velocity profile (2.13).

Gray and Edwards (2014) report that a common approach in the depth-averaged modelling literature is to close the system by assuming that the internal velocity profile takes a self-similar form: in our notation, writing

$$u(x,z,t) = \overline{u(x,t)}S\left(\frac{z}{h(x,t)}\right), \tag{5.7}$$

where the profile function $S(\zeta)$ satisfies $\int_0^1 S(\zeta)\,\mathrm{d}\zeta = 1$. Having chosen a profile $S(\zeta)$, the shape factor is

$$\chi = \int_0^1 S(\zeta)^2\,\mathrm{d}\zeta, \tag{5.8}$$

which is constant.

From the point of view of the depth-averaged system (5.4), the profile $S(\zeta)$, or the value of the shape factor (5.6), are externally specified. In both the granular flows and the shallow water literature, a common choice is to assume a plug flow profile so that $S(\zeta) = 1$ and $\chi = 1$ (Gray and Edwards 2014, Baker et al. 2016b, Hogg and Pritchard 2004). This assumption was used in the original shallow water equations by Saint-Venant (1871). Taking $\chi = 1$ is the simplest model, but this is valid only if the no-slip condition does not apply (§4.2.2), and there is no shear within the flow. These assumptions are unsatisfactory for granular flows, and a more general choice of $S(\zeta)$ should be informed by the internal dynamics of a flow as well as the basal boundary conditions. For gravity currents, Hogg and Pritchard (2004) further note that the value of χ 'may have a significant effect on the nature of the predicted flows', specifically on the frontal dynamics of a spreading current; however, such currents are not within the scope of the present work.

In the small grain limit $d \ll \mathcal{H}$ and the absence of any other external lengthscales or timescales, the assertion that $\chi = \overline{u^2}/\overline{u}^2$ be constant follows from dimensional analysis. Therefore, sufficiently far from any inhomogeneities, the internal profile at a given (x, t) can be approximated as that of a steady uniform flow, and the shape factor chosen accordingly (provided that such a flow can exist). We will justify this approximation more mathematically in Part III, as well as exploring the rate of convergence of a velocity profile towards a self-similar profile (5.7).

For steady uniform flows, the $\mu(I)$ rheology with the no-slip condition predicts a Bagnold velocity profile with $\chi = 5/4$, while alternative rheologies (Chapter 3) or boundary conditions (§4.2.2) predict alternative profiles and different values of χ. For example, the Bagnold-with-slip profile (2.12) has $1 < \chi < 5/4$, while nonlocal models (§3.3) predict profiles with $\chi > 5/4$ for large values of δ, consistent with experimental results (Thomas and Vriend 2019).

5.3. Error analysis for the shape factor

In practice, the velocity field $u(x, z, t)$, and therefore the averages $\overline{u}$ and $\overline{u^2}$, cannot be measured exactly. DPM simulations and real flows always exhibit some variance from their initial conditions, and experimental results will have measurement errors. Moreover, nominally steady (resp. streamwise-uniform) flows usually exhibit some time-dependence (resp. streamwise evolution), and so the measured value of u must have some variance. In addition, the data from DPM simulations and laboratory experiments always exhibit some variance from their initial conditions; experimental results may also have measurement errors or imprecisions.

In this section, we consider the robustness of the definition (5.6) to errors in u, assuming that the depth h may be measured exactly. Let $u = u_0 + u'$, where u_0 is the 'true' value of u and u' is the error; similarly, write $\chi = \chi_0 + \chi'$. We seek an estimate for the magnitude of χ'.

The expression (5.6) gives

$$\frac{1}{h}\left(\chi_0+\chi'\right)=\frac{\int_0^h\left(u_0^2+2u_0u'+u'^2\right)\,\mathrm{d}z}{\left(\int_0^h u_0\,\mathrm{d}z\right)^2+2\left(\int_0^h u_0\,\mathrm{d}z\right)\left(\int_0^h u'\,\mathrm{d}z\right)+\left(\int_0^h u'\,\mathrm{d}z\right)^2} \tag{5.9}$$

$$=\frac{\int_0^h u_0^2\,\mathrm{d}z}{\left(\int_0^h u_0\,\mathrm{d}z\right)^2}+2\frac{\int_0^h u_0u'\,\mathrm{d}z}{\left(\int_0^h u_0\,\mathrm{d}z\right)^2}-2\frac{\left(\int_0^h u_0^2\,\mathrm{d}z\right)\left(\int_0^h u'\,\mathrm{d}z\right)}{\left(\int_0^h u_0\,\mathrm{d}z\right)^3}+o\left(\frac{||u'||}{h||u_0||}\right), \tag{5.10}$$

$$\chi'=\frac{2h\int_0^h u_0u'\,\mathrm{d}z}{\left(\int_0^h u_0\,\mathrm{d}z\right)^2}-\frac{2h\left(\int_0^h u_0^2\,\mathrm{d}z\right)\left(\int_0^h u'\,\mathrm{d}z\right)}{\left(\int_0^h u_0\,\mathrm{d}z\right)^3}+o\left(\frac{||u'||}{||u_0||}\right), \tag{5.11}$$

giving the relative error χ'/χ_0 as

$$\frac{\chi'}{\chi_0}=\frac{2\int_0^h u_0u'\,\mathrm{d}z}{\int_0^h u_0^2\,\mathrm{d}z}-\frac{2\int_0^h u'\,\mathrm{d}z}{\int_0^h u_0\,\mathrm{d}z}+o\left(\frac{||u'||}{||u_0||}\right). \tag{5.12}$$

In the above, the norm of a function is defined as the square-integral

$$||f||=\left[\int_0^h f(z)^2\,\mathrm{d}z\right]^{1/2}.$$

Note that $||f||$ does not have the same dimensions as f, but has an additional dimension of $[\text{length}]^{1/2}$ from the $\mathrm{d}z$.

If the final correction term in (5.12) is ignored, then an estimate of the maximum error $||\chi'||$ may be obtained using the calculus of variations, maximising χ' over possible perturbation functions $u'(z)$, given that the relative error is

$$R=\frac{||u'||}{||u_0||}.$$

It can be shown that the maximal value of $||\chi'||$ is attained by the function

$$u'(z)=R||u_0||\frac{u_0(z)-M}{||u_0-M||},\qquad\text{where}\qquad M=\frac{\int_0^h u_0^2\,\mathrm{d}z}{\int_0^h u_0\,\mathrm{d}z}. \tag{5.13}$$

(Note that the prime u' in (5.13) does not denote a derivative.) Putting (5.13) into (5.12) gives the maximum relative error

$$\left|\frac{\chi'}{\chi_0}\right|_{\max}=2(\chi_0-1)^{1/2}R+o(R). \tag{5.14}$$

In particular, if the base flow u_0 is Bagnoldian, then $\chi_0=5/4$ and so $|\chi'/\chi_0|_{\max}\sim R$. Informally, χ depends quadratically on u so one would expect χ to have a relative error of $2R$, but in fact the minus sign in (5.12) allows for some cancellation between the two terms.

In the above, we assumed that h could be measured exactly, but a similar perturbation analysis could be performed for errors in h, by writing $h=h_0+h'$ and using Leibniz's rule

$$\int_0^{h_0+h'}f(z)\,\mathrm{d}z=\int_0^{h_0}f(z)\,\mathrm{d}z+f(h_0)h'+o(h')$$

to estimate the errors in each integral. From this we arrive at an estimate of the sensitivity of χ on h, *viz.*

$$\frac{\chi'}{\chi_0} = \left[1 - 2\frac{u_{\mathrm{surf}}}{\overline{u}} + \frac{u_{\mathrm{surf}}^2}{\overline{u^2}}\right]\frac{h'}{h_0} + o(|h'/h_0|), \tag{5.15}$$

where u_{surf} is the surface velocity.[2]

The estimates (5.14, 5.15) give some guarantees over the robustness of χ to variations in the depth h and the velocity profile u. We note again that although we have used the term 'error' in the above calculation, h' and u' do not necessarily refer to measurement errors or uncertainties. It may also refer to variance in measurements due to time-fluctuations, or to different results across experiments or simulations. In the context of DPM, (5.14) could also refer to the sensitivity of the shape factor to the precise method by which continuum fields are constructed from discrete data (§9.1).

5.4. Initial and boundary conditions

The system (5.4) must be supplemented by initial and boundary conditions on h and $\overline{u}$. These conditions depend on the specific problem being studied, but we make some general remarks below.

The shallow water equations (5.3) form a hyperbolic system (Evans 2010, Iserles 2008, Billingham and King 2001), and can be analysed using the method of characteristics. It can be shown that the 'Riemann invariants' $J_{C\pm} = \overline{u} \pm 2c$ are conserved along the $C_\pm$ 'characteristic curves' $x_{C\pm}(t)$ satisfying $x'_{C\pm}(t) = \overline{u} \pm c$ respectively, where $c = (gh)^{1/2}$ is the wave speed (García-Navarro et al. 2008). Informally, the solution for h and $\overline{u}$ at a given point (x, t) can be determined by following the characteristic curves backwards in time to find the values of $J_{C\pm}$ from the initial or boundary conditions.

The additional diffusivity term in the granular depth-averaged equations (5.4b) turns (5.4) into a parabolic system.[3] The quantities $\overline{u} \pm 2c$ are not exactly conserved along the characteristics, due to diffusion.[4] However, in the small grain limit $d \ll \mathcal{H}$, the diffusivity ν is small, the Riemann invariants are still approximately conserved along the characteristics, and the above discussion continues to apply.

In Chapter 10, we shall apply the above depth-averaged model to steady flows. Dropping the $\partial/\partial t$ terms converts (5.4) into a system of ordinary, rather than partial, differential equations, which are easier to analyse, but the evolution towards a steady state, and the interpretation of boundary conditions, shall require further consideration (§10.1).

* * *

The depth-averaged equations (5.4) have one less spatial dimension than the full equations of motion (2.10), and are therefore more amenable to analysis. However, they tell us nothing

[2] The surface velocity may be taken either at $z = h_0$ or at $z = h_0 + h'$; the resulting difference is absorbed into the $o(|h'/h_0|)$ term.

[3] A PDE is characterised according to its highest-order derivatives (David Baker and Owen Petrie, pers. comm., 6 February 2019).

[4] Strictly speaking, the term 'characteristics' does not apply to non-hyperbolic systems.

about the internal profile of a flow; instead, the shape factor χ has to be specified externally.

We shall use the depth-averaged model (5.4) to study the abrupt roughness transition shown in figure 1.4(a) and compare the predictions against those of the $\mu(I)$ rheology (Chapter 11) and a time-dependent analogue (Chapter 12). We shall see that the depth-averaged model can be mathematically analysed to produce qualitatively correct behaviour over long distances, but also that the assumption of a self-similar velocity profile $\chi =$ constant is not justified in the presence of a roughness change.

Part II.

Discrete particle models

This part of the thesis will begin by recounting basic concepts about DPM (Chapter 6). The following few chapters will deal with contact modelling (Chapter 7), initial and boundary conditions (Chapter 8), and the relationship between DPM and continuum models (Chapter 9). In each of these chapters, we review existing techniques for each of these steps and discuss their usage. We also introduce some novel techniques that can be used for more realistic models or more efficient simulations.

Our discussion shall focus on physical aspects of discrete particle modelling, although we shall need to consider computational costs when constructing a DPM. Details about the *implementation* of DPM simulations are discussed briefly in Appendix A. The simulations in this work were conducted using the software package MercuryDPM (Weinhart et al. 2012, Thornton et al. 2013, Weinhart et al. 2013). A wide range of applications of MercuryDPM towards a number of problems are reviewed in Weinhart et al. (2017). A broad survey of DPM techniques and implementation can be found in O'Sullivan (2014).

6. Fundamental ideas

> The whole is greater than the sum of its parts.
>
> Aristotle

In a system of N grains, the individual grains are governed by Newton's laws of motion. Let $\boldsymbol{x}_i(t) = (x_i, y_i, z_i)$ be the position of the centre of mass of the ith particle and let $\boldsymbol{u}_i(t) = \dot{\boldsymbol{x}}_i(t)$ be the velocity. Then Newton's second law states that

$$\frac{\mathrm{d}}{\mathrm{d}t}(m_i \boldsymbol{u}_i) = \boldsymbol{f}_i = \boldsymbol{f}_i^{\mathrm{ext}} + \sum_{j \neq i} \boldsymbol{f}_{ij}^{\mathrm{c}} + \boldsymbol{f}_i^{\mathrm{walls}}, \quad i = 1, \ldots, N, \tag{6.1a}$$

where the force $\boldsymbol{f}_i$ on the ith grain consists of an external force $\boldsymbol{f}_i^{\mathrm{ext}}$ on the grain, the forces $\sum_{j \neq i} \boldsymbol{f}_{ij}^{\mathrm{c}}$ from other grains, and the contact forces $\boldsymbol{f}_i^{\mathrm{walls}}$ from fixed objects such as walls and obstacles. Moreover, if the ith grain has moment of inertia tensor $\boldsymbol{I}_i$ and angular velocity $\boldsymbol{\omega}_i$, then these satisfy

$$\frac{\mathrm{d}}{\mathrm{d}t}(\boldsymbol{I}_i \cdot \boldsymbol{\omega}_i) = \boldsymbol{\tau}_i^{\mathrm{ext}} + \sum_{j \neq i} \boldsymbol{\tau}_{ij} + \boldsymbol{\tau}_i^{\mathrm{walls}}, \quad i = 1, \ldots, N, \tag{6.1b}$$

where $\boldsymbol{\tau}_i^{\mathrm{ext}}$ is an external torque, $\boldsymbol{\tau}_{ij}$ is the torque on particle i from particle j, and $\boldsymbol{\tau}_i^{\mathrm{walls}}$ is the torque from contacts with fixed objects.

In this thesis, we assume that the external force on a particle $\boldsymbol{f}_i^{\mathrm{ext}} = m_i \boldsymbol{g}$ is the weight of that particle in a gravitational field, while the external torque vanishes. Usually, $\boldsymbol{g}$ will be taken as constant, but in Chapter 12 we shall study the effects of a time-dependent (but spatially uniform) gravitational field $\boldsymbol{g}$ (in an inertial frame, so that there are no other fictitious forces). By taking no other external forces than the weight, we neglect any effects of air or water resistance. We also assume that the forces $\boldsymbol{f}_{ij}^{\mathrm{c}}$ between particles are contact forces, which are nonzero if and only if particles are in contact; we exclude long-range forces such as cohesion due to an interstitial fluid. Thus, our simulations are limited to dry flows. There has been work to couple discrete particle models with simulations of hydrodynamic flows, but at present these face significant computational difficulties (O'Sullivan 2014).

In practice, the system (6.1) is not useful for describing the dynamics of granular media, even if there were no computational difficulties from solving the large system of coupled equations for $N \gg 1$. The contact forces and torques between grains all depend on the mechanical properties of the grains as well as their shapes and orientations. The moment of inertia also depends on the shape and orientation of each grain. In a sample of sand, grains typically have very irregular shapes, and the mechanical properties may vary from grain to grain, or even within a single grain. Only with all of this information would it be possible to solve (6.1).

A *discrete particle model* of a granular flow attempts to strip away all of these details about individual grains, while retaining realistic 'bulk' or 'statistical' behaviour, as defined by appropriate averages over particles. There are three steps when designing a discrete particle model.

We first suppose that the constituent grains all have a regular shape. All of the DPM in the present work are two-dimensional and use particles that are circular discs: these assumptions are discussed in §6.1 and §6.2 respectively. Next, we must specify a *contact model* that governs the interactions between two particles in terms of their relative positions, velocities and rotations. Doing so closes the system (6.1) by giving explicit expressions for the moments of inertia and the contact forces and torques. Contact modelling will be discussed in Chapter 7. Finally, we must specify initial and boundary conditions, which govern the introduction and removal of particles, and their interactions with the boundaries of a simulation domain; these are discussed in Chapter 8.

After specifying the particle shapes and sizes, the contact models for particle interactions, and initial and boundary conditions, we may then integrate (6.1) to find the functions $\boldsymbol{x}_i(t)$, $\boldsymbol{u}_i(t)$ and $\boldsymbol{\omega}_i(t)$, allowing us to trace the motion of each particle from a given set of initial conditions. This information by itself is not useful: a system of $N \gg 1$ particles is likely to be chaotic, so these solutions are extremely sensitive to initial conditions as well as numerical errors. However, we can construct local averages of particles' positions and velocities, which are much more robust to noise. This averaging process is called *coarse-graining*, which we define in §9.1. Coarse-graining produces a set of continuum fields describing the bulk behaviour of the flow, and the results may be compared against continuum models or lab experiments. In Chapter 9, we describe the coarse-graining process, as well as the calibration of a DPM against the $\mu(I)$ rheology.

Discrete particle models are realised as computer simulations, and some computational issues faced by these simulations are discussed briefly in Appendix A. But experimentalists also use the principle of studying systems of particles with regular shapes and contact properties as models for more general granular flows. Notably, McElwaine and Nishimura (2000) performed experiments in which up to 550,000 ping-pong balls were released down a ski jump in Sapporo, Japan. On a smaller scale, studies of force transmission inside granular materials using photoelastic discs, such as Shukla (1991), Owens and Daniels (2011), Tang et al. (2018), Thomas and Vriend (2019), are based on the same principle.

6.1. Two-dimensionality

The discrete particle models to be discussed in this thesis are all *two-dimensional* (2D), which means that all particles are constrained to a single layer on the (x, z) plane; in other words, $y_i = v_i = 0$ for all particles. The angular velocity vectors $\boldsymbol{\omega}_i$ all lie in the y-direction so that rotation occurs only in the (x, z) plane. This is the modelling approach used in the photoelasticity community (*e.g.* Shukla (1991), Owens and Daniels (2011), Tang et al. (2018)), where the imaging technique requires that the particles lie in a single layer. Our motivation here is computational. The running time of a simulation of N particles grows somewhere between $O(N)$ and $O(N^2)$ (Appendix A). By taking only one layer of particles in the cross-stream direction, a two-dimensional simulation can cover a much longer and deeper domain compared to a three-dimensional simulation with the same number of particles.

Some care should be taken in interpreting two-dimensional DPM. A 2D continuum model merely states that *statistically* (in the sense of §9.1) particles have no motion or variation in the cross-stream y-direction: we refer to such flows as *quasi-two-dimensional*. On the other hand, a 2D discrete model makes the stronger statement that the entire flow is only one particle wide, with

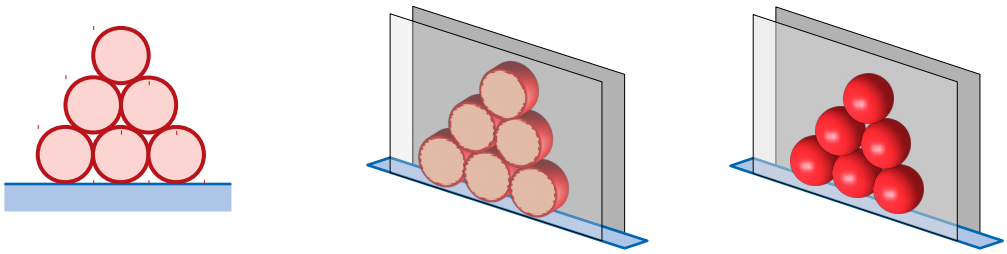

Figure 6.1.: Circular particles in a 2D DPM (left) can be interpreted as discs or cylinders with line contacts (middle), or as spheres with point contacts (right). Particles are confined to a single channel with zero sidewall friction.

all the particles aligned on a single plane in the y-direction and having no velocity component out of this plane. Furthermore, a 2D DPM cannot necessarily be compared directly to lab experiments on discs: for example, in experiments, discs may have out-of-plane particle rotation, and may be affected by sidewall drag (Owens and Daniels 2011).

Two-dimensional DPM are therefore fundamentally phenomenological, but they are nonetheless able to model many aspects of quasi-2D flows at a fraction of the computational cost of a 3D DPM (Deluzarche and Cambou 2006, O'Sullivan 2014). However, there are certain behaviours that are poorly captured in 2D DPM: for example, discs packed in two dimensions have a much larger packing fraction than spheres in three dimensions. Discs cannot move around each other as easily as out-of-plane motion is prohibited, so that granular segregation is slower in 2D. Moreover, circular particles in a 2D DPM can be in contact with fewer neighbours than monodisperse spheres in 3D.[1]

6.2. Particle shapes and sizes

In our simulations, we use circular particles. As shown in figure 6.1, such particles could represent discs (or cylinders) or spheres, confined to a single channel with no other sidewall effects. In both cases, particles may not move around each other in the cross-stream direction, so the distinction between discs and spheres has no effect on the inter-particle kinematics. The difference between spheres and discs may inform our choice of contact model, but as we shall discuss in Chapter 7 there are other considerations that we account for when choosing a contact model. Therefore, the distinction shown in figure 6.1 is largely immaterial for two-dimensional DPM simulations. For definiteness, we shall mostly refer to our particles as discs: this allows more direct comparison with the work of the photoelasticity community, which solely uses discs rather than spheres (Owens and Daniels 2011, Thomas and Vriend 2019).

A contact between two circular particles has exactly one contact point, which lies on the line connecting their centres. The contact point and normal may be computed exactly, and the

[1] For perfectly monodisperse discs, each disc has at most six neighbours, while perfectly monodisperse spheres can have up to twelve. Fitting seven small discs around a larger central disc needs a size dispersity of around 13%, as defined in §6.2; the simulations used in this thesis have a size dispersity of 10%.

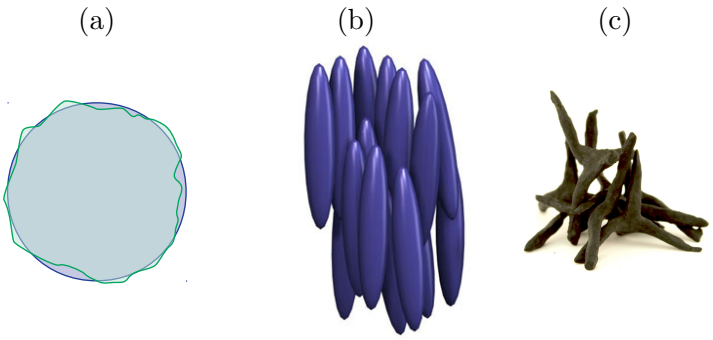

Figure 6.2.: (a) An grain with small-scale asperities (green) can be modelled as a circular particle (blue), if appropriate rolling resistance is added. (b) A system of prolate grains can exhibit nematic alignment, which is not possible with circular particles. (c) Caltrops can strongly interlock with each other, which cannot happen with spheres.

theory of elastic contacts between discs or spheres is well-established (Johnson 1985). There are therefore computational and modelling advantages to using circular particles. As we shall note in §7.4.2, a modified contact model with rolling resistance may be used to capture some of the properties of grains that are approximately round (figure 6.2(a)). However, a model using circular particles cannot handle granular phenomena that are caused by shape effects, such as shape segregation, the nematic effects of prolate particles (figure 6.2(b)), or jamming of highly nonconvex materials (figure 6.2(c)).[2]

In most samples of granular materials, such as sand or gravel, there will be some variation in the sizes of grains, even if the material is nominally monodisperse. Any discrete particle model of these materials should retain this property. If not, a system of discs or spheres that are all of the same size may develop locally into unrealistically ordered or 'crystalline' structures, in which forces may be transmitted over much longer distances than they would be in a disordered arrangement. It is therefore necessary to introduce some size dispersity in a DPM to break up these structures, but not so much dispersity that size segregation may occur.

In our simulations, size dispersity is provided by particles having diameters d_i with $\pm 10\%$ variation about a mean particle diameter. Using periodic domain tests (Chapter 9), we found that this size dispersity did not result in a significant amount of size segregation, which justifies the description of the particles as being nominally monodisperse.[3]

The process by which one creates a sample of particles with size dispersity in a discrete particle model shall be given in §8.2.

[2]Panel (b) is from Kevin Yager, Barrett Research Group, `http://barrett-group.mcgill.ca/tutorials/liquid_crystal/LC01.htm`. Panel (c) is from Philadelphia History Museum at the Atwater Kent, Historical Society of Pennsylvania Collection, photograph by Sara Hawken, `http://philadelphiaencyclopedia.org/archive/artifact-caltrops/caltrops07/`.

[3]Specifically, no correlation was found between the sizes d_i and the depthwise positions z_i or velocities w_i of the particles.

7. Contact models

> There is happiness in life;
> Inevitably, there are often also tears.
> But as we meet each other below the Lion Rock,
> At least we find more joy than sorrow.
>
> *Below the Lion Rock*

A discrete particle model requires a law that governs particle-to-particle interactions. In a granular flow in a dense state, each particle may be in continuous contact with multiple different particles, forming force chains that transmit forces over long distances (Mueth et al. 1998, Peters et al. 2005, Thomas and Vriend 2019). This is in contrast to a granular 'gas' in the kinetic regime (§3.2), in which particles have a mean free path that is much longer than the typical particle diameter, so that interactions between particles are mostly binary collisions, and multiple contacts are rare. In a DPM, we assume that when a particle is involved in many contacts, each contact may be treated independently. This assumption, which is commonly used in Hertzian contact modelling (Johnson 1985), can be reasonably applied to real grains, provided that a contact force on one side of a grain does not cause a large enough deformation on the other side of the grain to affect contacts on that other side. To enforce this condition in a simulation, the particles must be made sufficiently 'stiff' so that the amount of overlap between two particles remains small compared to the particle size.

In this chapter, we first define some basic concepts in §7.1, and state some general guidelines for choosing a contact model. As sketched in figure 7.1, the contact force between two two-dimensional particles can be divided into a component f_n normal to the contact line, and a tangential component f_t, and most contact models assume that these may be treated separately. We discuss the normal component in §§7.2, 7.3, first stating some classical results about elastic contacts in §7.2, and reviewing some of the recent literature on dissipative contacts in §7.3. As for tangential contacts, §7.4 will discuss models of friction between two bodies.

Although contact models are informed by theoretical and experimental results on contacts between real materials, we must also consider computational limitations when choosing a contact model for a DPM simulation. In §7.5, we shall discuss some techniques by which the computational cost of a simulation may be reduced by adjusting a contact model appropriately, possibly at the expense of realism.

7.1. Definitions

Assuming that the binary contacts treatment is appropriate, a contact model should give the force between two particles as a function of the relative displacement and velocity of the particles. Two circular particles with positions $\boldsymbol{x}_1$ and $\boldsymbol{x}_2$ are said to interact if their distance $|\boldsymbol{x}_1 - \boldsymbol{x}_2| < R_1 + R_2$, where $R_i = d_i/2$ are the radii of the particles. We say that the *overlap* between the

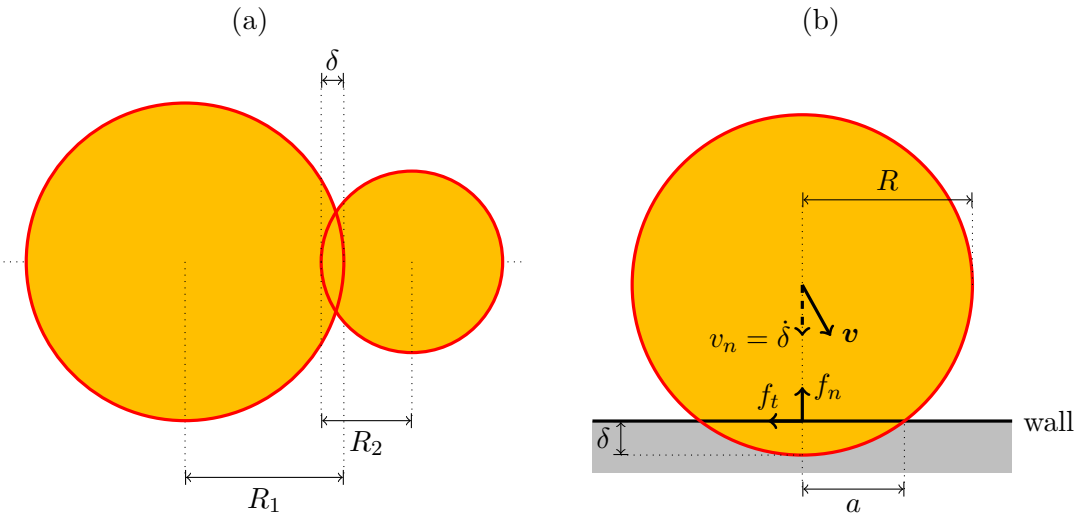

Figure 7.1.: A contact between particles of radii R_1 and R_2 (panel (a)) is equivalent to a contact between a particle of radius R and a wall (panel (b)), where R and m are given by (7.1) and (7.2). As in figure 6.1, the circles shown here can represent either cylinders or spheres.

two particles is $\delta = R_1 + R_2 - |\boldsymbol{x}_1 - \boldsymbol{x}_2|$. Instead of considering a contact between two discs, it is often easier to consider an equivalent problem of a disc of radius R interacting with a half-space (or 'wall'), where the reduced radius (or effective radius) of the collision

$$R = \frac{R_1 R_2}{R_1 + R_2} \tag{7.1}$$

is half the harmonic mean of the radii of the two original discs. This equivalence is illustrated in figure 7.1. The mass m of the new particle is likewise taken to be the reduced mass

$$m = \frac{m_1 m_2}{m_1 + m_2}. \tag{7.2}$$

A contact force consists of a normal component f_n and a tangential component f_t. The normal component usually consists of a repulsive reaction force as well as damping forces.[1] The tangential component usually represents a frictional traction between the two particles that resists relative tangential motion.

We shall discuss friction in §7.4, but for now we focus solely on the normal component. The value of f_n is to be a function of the overlap δ and the normal component of the relative velocity $\dot{\delta}$. The force may be decomposed into conservative and dissipative components, *viz.*

$$f_n(\delta, \dot{\delta}) = f_{\text{elastic}}(\delta) + f_{\text{dissipative}}(\delta, \dot{\delta}), \tag{7.3}$$

where the conservative force $f_{\text{elastic}}(\delta)$ represents elastic forces and $f_{\text{dissipative}}$ represents forces that are responsible for the dissipation of energy in a collision. By assumption, $f_{\text{dissipative}}$ must

[1] A DPM could use attractive forces to model adhesive or charged particles. We shall not consider attractive normal forces in this work.

have a dependence on $\dot{\delta}$, or it would not be a dissipative force. By Newton's second law, δ satisfies the differential equation

$$m\ddot{\delta} = -f_n. \tag{7.4}$$

We must now choose the forms of the functions f_{elastic} and $f_{\text{dissipative}}$ by specifying a contact model. The choice of one contact model over another, as well as the parameters within that model, is motivated both by considerations on the material properties of the physical grains and by computational limitations such as numerical stability. We shall discuss computational considerations in §7.5.

A basic condition is that both f_{elastic} and $f_{\text{dissipative}}$ should vanish if $\delta < 0$. This assumption asserts that particles may affect each other only through contact forces. Another condition is that $f_{\text{elastic}} > 0$, so that the elastic force is always repulsive. In principle, there is no problem with including non-contact forces into a DPM, but in this work we shall only consider finite-range forces. These assumptions are reasonable for modelling dry grains that are sufficiently large that electrostatic or cohesive forces may be neglected, but not for very fine powders. The restriction to finite-range forces brings significant computational advantages (§A.1).

7.2. Linear elasticity

Suppose that particles and walls are made of a linearly elastic material, and that dissipation is negligible. The normal repulsion force $f_{\text{elastic}}(\delta)$ can be computed using the well-established Hertzian contact theory (Johnson 1985, Owens and Daniels 2011). The full calculations, which may be found in Johnson (1985), are complicated, but the key results can be obtained by simple scaling arguments, given below. The arguments depend on whether the two-dimensional particle represents a cylinder or a sphere (figure 6.1).

7.2.1. For a cylinder

Consider a cylinder of length L interacting with a wall, as figure 7.1(b). Assuming that the overlap satisfies $0 < \delta \ll R$, then the contact length

$$a = \sqrt{R^2 - (R-\delta)^2} \sim \sqrt{2R\delta} \sim \sqrt{R\delta},$$

and the contact area

$$A = aL \sim L\sqrt{R\delta}.$$

The strains in both the particle and the wall scale as

$$\epsilon \sim \frac{\delta}{a} \sim \sqrt{\frac{\delta}{R}}.$$

Meanwhile, the stress on the contact is

$$\sigma \sim \frac{f_{\text{elastic}}}{A} \sim \frac{f_{\text{elastic}}}{L\sqrt{R\delta}},$$

and Hooke's law states that $\sigma \sim E\epsilon$, where E is the Young's modulus of the material. After some rearrangement, one obtains

$$f_{\text{elastic}} \sim EL\delta,$$

showing that f_n grows in direct proportion to δ. We therefore say that

$$f_{\text{elastic}}(\delta) = \begin{cases} k\delta, & \delta > 0, \\ 0, & \delta \leq 0, \end{cases} \tag{7.5}$$

where k, the *geometric stiffness*, is proportional to EL.

Note that in this chapter, 'stress' refers to the mechanical state within a particle, not to the 'bulk' stress of a flow; likewise with 'strain' and 'strain rate'.

For a perfectly elastic collision, so that $f_{\text{dissipative}} = 0$, one easily solves (7.4) to give

$$\delta(t) = v_0 \sqrt{\frac{m}{k}} \sin\left(t\sqrt{\frac{k}{m}}\right),$$

using the initial conditions $\delta(0) = 0$ and $\dot{\delta}(0) = v_0$, where v_0 is the incident velocity of the collision. We say that the *contact time* is

$$t_c = \pi\sqrt{\frac{m}{k}}, \tag{7.6}$$

the time at which δ becomes zero again. Note that t_c decreases against increasing k. We note that the final velocity

$$v_f = -\dot{\delta}(t_c) = v_0,$$

showing that the coefficient of restitution

$$e = \frac{v_f}{v_0} \tag{7.7}$$

is equal to 1, as expected. We also find the maximum penetration as

$$\delta_{\max} = v_0\sqrt{m/k}. \tag{7.8}$$

7.2.2. For a sphere

A similar scaling argument may be made if we instead suppose that the circular particles shown in figure 7.1 represent spheres rather than cylinders. In this case, the contact area A scales as

$$A = \pi a^2 \sim R\delta,$$

but the expressions for stress and strain otherwise remain the same, and we find that

$$f_{\text{elastic}}(\delta) = \begin{cases} K\delta^{3/2}, & \delta > 0, \\ 0, & \delta \leq 0, \end{cases} \tag{7.9}$$

where K is proportional to $ER^{1/2}$. As with the cylindrical case, we still refer to $k = K\delta^{1/2}$ as the geometric stiffness, but k now increases with δ and is no longer a constant. With the

force law (7.9), it is not possible to solve (7.4) to find an analytic solution for $\delta(t)$, but it can be shown that

$$t_c = 2\int_0^{\delta_{\max}} \frac{\mathrm{d}\delta}{\left(v_0^2 - \frac{4K}{5m}\delta^{5/2}\right)^{1/2}} \tag{7.10}$$

$$= \frac{2\delta_{\max}}{v_0}\int_0^1 \frac{\mathrm{d}s}{(1-s^{5/2})^{1/2}} \tag{7.11}$$

$$\approx 2.94 \times \frac{\delta_{\max}}{v_0}, \tag{7.12}$$

where

$$\delta_{\max} = \left(\frac{5mv_0^2}{4K}\right)^{2/5} \tag{7.13}$$

is the *maximum penetration* of the collision. We note that $t_c \propto v_0^{-1/5}$, so the contact time decreases with increasing impact velocity.

The $\delta^{3/2}$ law (7.9) is sometimes referred to (*e.g.* by Bharathraj and Kumaran (2017)) as '*the* Hertzian contact law', to the exclusion of the linear law (7.5). In fact, both laws are consistent with Hertz's theory of elastic contacts, but for differently-shaped particles (Johnson 1985). As discussed in §6.1 and shown in figure 6.1, the distinction is not important in a two-dimensional DPM, but must be made if a contact model is supposed to correspond directly to a system of real discs, for example, in photoelasticity experiments (Tang et al. 2018, Thomas and Vriend 2019).

7.3. Linear viscoelasticity

While Hertzian contact theory between two elastic bodies is well-established, models of the effects of dissipative forces in a DPM have been more *ad hoc*, and in the literature there exist conflicting expressions for the proper form of the dissipative term $f_{\text{dissipative}}(\delta, \dot{\delta})$. A large problem is that there are several mechanisms by which a contact may be dissipative: amongst these, Kuwabara and Kono (1987) identify plastic deformation, dry friction and viscoelasticity, and Andreotti et al. (2015, p. 30) also list radiative elastic loss. These mechanisms are described by different expressions for $f_{\text{dissipative}}(\delta, \dot{\delta})$. The mechanics within a particle are not directly important when using a DPM, but should be considered if a contact model is to be realistic. In this section, we review a simple model of viscoelasticity and use it to derive expressions for $f_{\text{dissipative}}$ using scaling arguments analogous to those of §7.2, again distinguishing between the cylindrical and the spherical cases. However, we shall describe in §7.5 other models that have been proposed because they are easier to interpret or specify in a DPM. These models are possibly less physical, but they capture the qualitative effects of a dissipative contact.

Supposing that particles are made of a viscoelastic material, a common model for such materials is the Kelvin–Voight spring-dashpot model (Roylance 2001). Under this model, the stress on a material is a linear combination of the strain and the strain rate. The first component is conservative, and we have already discussed it in §7.2. In the second component, the assertion that the dissipative stress is directly proportional to the strain rate is equivalent to Newton's law of viscosity,

$$\sigma_{\text{dissipative}} \sim \eta\dot{\epsilon},$$

where η is the dynamic viscosity. The strain rate $\dot{\epsilon} \sim \dot{\delta}/a$, where a is the contact width. As in §7.2, converting this into a contact law between two particles depends on whether these particles are cylinders or spheres.

7.3.1. For a cylinder

For a cylinder, $A \sim L\sqrt{R\delta}$ and $a \sim \sqrt{R\delta}$ as in §7.2.1, so that the force scales as

$$f_{\text{dissipative}} \sim \eta L \dot{\delta}.$$

Therefore,

$$f_{\text{dissipative}}(\delta, \dot{\delta}) = \begin{cases} \gamma\dot{\delta}, & \delta > 0, \\ 0, & \delta \leq 0, \end{cases}$$

where $\gamma \sim \eta L$ is called the *dissipation coefficient*.

For $\delta > 0$, the combined effects of (7.5) and (7.3.1) turn the equation of motion (7.4) into the linear equation

$$m\ddot{\delta} + \gamma\dot{\delta} + k\delta = 0, \tag{7.14}$$

with initial conditions $\delta(0) = 0$ and $\dot{\delta}(0) = v_0$ as before. This is referred to as the linear spring-dashpot model (O'Sullivan 2014).

Supposing that $\gamma < 2\sqrt{mk}$, then the equation (7.14) is an underdamped system, and so

$$\delta(t) = \frac{2mv_0}{4mk - \gamma^2} \exp\left(\frac{-\gamma t}{2m}\right) \sin\left(\frac{\sqrt{4mk - \gamma^2}}{2m}\, t\right). \tag{7.15}$$

With the nonzero dissipation, the contact time is now

$$t_c = \frac{2\pi m}{\sqrt{4mk - \gamma^2}}. \tag{7.16}$$

The final velocity v_f and coefficient of restitution e are given by

$$e = \frac{v_f}{v_0} = \exp\left(\frac{-\gamma t_c}{2m}\right) = \exp\left(\frac{-\pi\gamma}{\sqrt{4mk - \gamma^2}}\right), \tag{7.17}$$

with $0 < e \leq 1$. In practice, the quantities t_c and e are easier to interpret than the material properties k and γ. These latter two can be calculated from the former two according to the formulae

$$\gamma = \frac{m}{t_c} \log(1/e), \qquad k = \frac{1}{2} m \left[\left(\pi/t_c\right)^2 + \left(\gamma/m\right)^2\right].$$

If instead $\gamma \geq 2\sqrt{mk}$, then the equation (7.14) is critically damped or overdamped; the two colliding particles do not eventually separate from each other: in this case, the collision time can be said to be infinite, and the coefficient of restitution to be 0; they would not be given by the formulae (7.16) and (7.17).

7.3.2. For a sphere

For a sphere, geometric arguments similar to those of §7.2.2 give

$$f_{\text{dissipative}} \sim \eta R^{1/2} \delta^{1/2} \dot{\delta}.$$

Analogously to §7.3.1, we can combine this dissipative force with the elastic force from §7.2.2 to construct a nonlinear spring-dashpot model,

$$m\ddot{\delta} + \Gamma \delta^{1/2} \dot{\delta} + K \delta^{3/2} = 0, \qquad \delta(0) = 0, \qquad \dot{\delta}(0) = v_0, \tag{7.18}$$

where the dissipation coefficient $\Gamma \propto \eta R^{1/2}$. This model was proposed by Kuwabara and Kono (1987), who derive it from first principles rather than these scaling arguments, and relate the K and Γ to fundamental material constants. They also show that (7.18) matches well with experimental results on collisions of hard spheres.

Unlike the cylindrical case (§7.3.1), the system (7.18) cannot be solved analytically in terms of simple functions.

7.4. Tangential forces

Our discussion in this chapter so far has been concerned with only the normal component f_n of forces in a contact. We now discuss the tangential component f_t, which resists relative motion in a direction tangential to a particle. For circular particles, once the value of f_t determined, the torque that such a force exerts on a particle is simply $\tau = f_t(d/2)$, the force multiplied by the radius of the particle. In contrast, normal forces act through the centre of mass of a rotation, and do not exert a torque on a circular particle. For noncircular particles, both the normal component and the tangential component of a contact force could exert a torque, depending on the point of contact and its relationship to the centre of mass of the particle.

A contact model must give the tangential force f_t in terms of the relative tangential motion between particles. In two dimensions, there are two different types of tangential motion between two bodies: *sliding* and *rolling* (O'Sullivan 2014, Johnson 1985). Sliding is the presence of a relative linear velocity at the contact between the two bodies, while rolling is the presence of a relative angular velocity when the two bodies' angular velocities are aligned. In three dimensions, it is also possible to have *torsional* motion and forces between two spheres, when their angular velocities are not aligned (O'Sullivan 2014). This is not possible in the two-dimensional models discussed in this thesis, in which the angular velocity vectors of all particles are parallel to each other.

Assuming that the tangential forces due to sliding and rolling may be treated independently, we write

$$f_t = f_{ts} + f_{tr},$$

where f_{ts} and f_{tr} resist sliding and rotational motion respectively. Each force must act in the direction that opposes the corresponding motion. Various models, with varying degrees of complexity, have been proposed for the forms of f_{ts} and f_{tr}, but there is no consensus between different authors (O'Sullivan 2014). As with dissipative normal forces (discussed in §7.3), part of the problem is the variety of physical mechanisms that a frictional contact might represent.

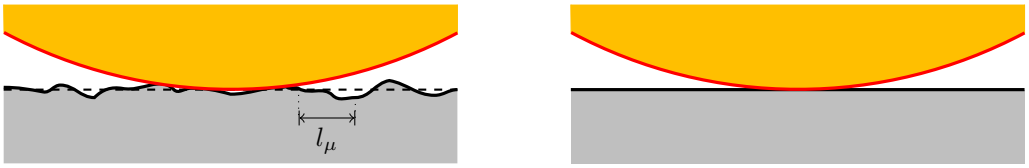

Figure 7.2.: When surface asperities occur over a lengthscale that is much smaller than the grain size (left), a DPM may treat the surface as geometrically smooth (right), with the resistance to motion being represented through a friction model. The grain itself may also have asperities, not shown in this diagram.

The tangential force f_t includes friction, which is dissipative, but f_t can also include conservative elastic forces that resist small deformations in the tangential direction.

Friction between two surfaces arises out of asperities on each surface, which resist tangential motion by locking on each other. All surfaces contain these asperities, but when these asperities occur over a lengthscale l_μ much smaller than the particle diameter d, a DPM treats the surface as being geometrically smooth, with the resistance to motion being represented through a frictional force f_t. This abstraction is shown in figure 7.2. It should be noted throughout this section that by 'friction' we refer to the intrinsic friction of contacts between individual particles: this is distinct from the 'bulk' friction observed at a macroscopic level resisting the motion of a current as a whole. As we shall see in Chapter 9, a system of particles exhibits a bulk friction even if individual contacts are frictionless: the dissipation is provided by the dissipative normal forces described in §7.3. The simulations that we shall describe in Part III in fact use frictionless contacts.

7.4.1. Sliding resistance

For small deformations in the tangential direction, many materials exhibit linear elastic or viscoelastic behaviour, just as with deformations in the normal direction (§§7.2, 7.3). We define the *tangential sliding displacement* δ_{ts} as the displacement of the particle along the wall relative to $\delta_{ts} = 0$, the position at the start of the contact. The force f_{ts} resisting this displacement can depend on δ_{ts} and its derivatives with respect to time. For cylindrical particles, scaling arguments similar to the ones used in §§7.2.1, 7.3.1 can be used to show that δ_{ts} can be modelled as a linear spring-dashpot system

$$f_{ts} = -m\ddot{\delta}_{ts} = k_{\mathrm{sl}}\delta_{ts} + \gamma_{\mathrm{sl}}\dot{\delta}_{ts}, \tag{7.19}$$

where the stiffness k_{sl} and dissipation coefficient γ_{sl} for sliding are proportional to, but not equal to, the coefficients k and γ, respectively, for normal forces from (7.14). The same analogy can be made for spherical particles.

But for large displacements (in particular, for sustained sliding), f_{ts} does not obey (7.19). Instead, its magnitude is bounded above, and the Coulomb friction model states that this bound is proportional to the normal force f_n,

$$|f_{ts}| \leq \mu_{\mathrm{sl}} f_n, \tag{7.20}$$

where μ_{sl} is the *coefficient of sliding friction*. Combining (7.19) and (7.20) gives the contact model

$$f_{ts} = \min\left(k_{\mathrm{sl}}\delta_{ts} + \gamma_{\mathrm{sl}}\dot{\delta}_{ts}, \mu_{\mathrm{sl}} f_n\right).$$

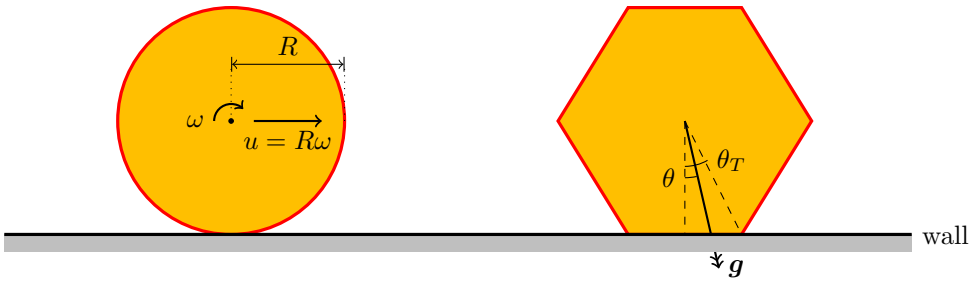

Figure 7.3.: Left: A circular particle rolling along a wall with velocity u and angular velocity ω experiences no sliding resistance if $u = R\omega$. Right: A non-circular particle on a wall does not roll if the slope θ is below a threshold angle θ_T.

Saturating the bound in (7.20) gives the elementary law of Coulomb friction.

7.4.2. Rolling resistance

Rolling resistance acts against relative angular velocities of two bodies in contact with each other. It is again useful to consider the prototypical problem of a circular particle[2] moving against a wall. We note two elementary facts about such a contact. Firstly, a circular particle may roll freely against the wall without slip, provided that $u = R\omega$, where u is the translational speed of the particle, ω is the angular velocity, and R is its radius. Under this condition, there is no relative linear motion between the particle and the wall at the contact point, so the sliding resistance described in §7.4.1 vanishes. Secondly, a circular particle resting on a wall inclined at a slope θ will start to roll down for any value of $\theta \neq 0$, as the weight of the circle exerts a torque on the point of contact. In contrast, an angular particle on a plane does not roll if $\theta < \theta_T$ for some threshold θ_T that depends on the shape and orientation of the particle. This is illustrated in the right-hand diagram in figure 7.3 for a regular hexagon. In general, for a regular polygon with n sides, the threshold slope is $\theta_T = \pi/n$.

A DPM with circular particles can capture this property of angular particles by introducing a rolling resistance

$$f_{tr} = \mu_{\mathrm{ro}} f_n \tag{7.21}$$

with *coefficient of rolling friction* μ_{ro}. Note that μ_{ro} is quite distinct from the coefficient of sliding friction μ_{sl}, and there is not necessarily any relationship between them.

As we have seen, if a circular particle is meant to represent a regular polygon with n sides, then the coefficient of rolling friction is given by $\mu_r = \tan\theta_r = \tan\pi/nT$. However, if the particle is meant to represent an irregular shape, as shown in figure 6.2(a), then μ_r is an abstract quantity that qualitatively, but not quantitatively, relates to the geometry of these asperities. Moreover, in a DPM, one typically uses a single value of μ_{ro} for all particles in the system, so the chosen value of μ_{ro} represents an average over multiple grains.

Estrada et al. (2011) compared simulations using frictionless regular n-gons against simulations using circular particles with an appropriate equivalent rolling fricion. Looking at statistical properties such as shear strength and packing fraction, they found that, for $n \geq 5$, the two sets of simulations gave remarkably similar results for bulk properties such as shear strength and

[2]The particle would be a sphere in 3D.

packing fraction. This justifies the idea that 'approximately circular' particles (in the sense of §6.2) can be treated as circles with rolling resistance.

Now, the simple rolling friction law (7.21) in fact gives only the limiting value of rolling friction. But consider a polygon resting on a flat surface. If the polygon is lifted and rotated slightly, it does not roll onto a different edge, but returns to its initial resting position. To model this behaviour using a circular particle, the rolling resistance may be proportional to the angular displacement. This is the idea behind the Iwashita–Oda rolling resistance model (Iwashita and Oda 1998), which is in common usage (O'Sullivan 2014). This model asserts that f_{tr} is given by

$$f_{tr} = \min\left(k_{\mathrm{ro}}\delta_r + \gamma_{\mathrm{ro}}\dot{\delta_r}, \mu_{\mathrm{ro}} f_n\right),$$

acting in the direction that opposes rolling. This is analogous to the linear viscoelastic friction model discussed in §7.4.1. Here, δ_r is the angular displacement and k_{ro} and γ_{ro} are material constants, with $\gamma_{\mathrm{ro}}\dot{\delta_r}$ representing dissipative resistance against rolling. When the angular displacement is large, representing a continuous rolling motion, then the rolling resistance is given by the simple expression (7.21).

7.5. Computational considerations

Although the models of Hertzian elasticity and viscoelasticity are believed to hold for many real materials, a discrete particle model is not directly concerned with the intrinsic material properties of particles, only with the particles' interactions with each other; we do not suppose a one-to-one relationship between particles in a model, and real grains. Indeed, we have already made simplifications about particles' shapes, sizes and dimensionality (Chapter 6). We therefore have some freedom when choosing a contact model and its parameters. We can exploit this freedom to reduce the computational cost of a simulation, or to make the results easier to interpret.

7.5.1. Elastic contacts

Consider, for example, the linear elasticity model for cylinders (§7.2.1). For this model, we must specify the geometric stiffness k, which is proportional to the Young's modulus E of the material. As we saw in (7.6), the contact time t_c in a collision is proportional to $k^{-1/2}$. Now, for a numerical solution to (7.4) to be accurate, the simulation timestep Δt should be small compared to t_c.[3] We may decrease k in order to increase t_c, allowing us to take larger timesteps. The particles in a DPM are typically much less stiff than the physical grains that they represent. For example, the true Young's modulus of glass is around 30 GPa. By comparison, the simulations of Jing et al. (2016) use a Young's modulus $E = 5\,\mathrm{MPa}$. Bharathraj and Kumaran (2017) give their simulation parameters in nondimensionalised form, but emphasise that their stiffness is at least 10^3 times smaller than that of real particles.[4] Reddy and Kumaran (2007)

[3] Anthony Thornton (pers. comm., 2016) recommends $\Delta t = t_c/50$, although $\Delta t = t_c/20$ may be small enough for testing purposes.

[4] Bharathraj and Kumaran (2017) give some values: 'Expressed in dimensionless form, [...] $k_n = 10^6$, [...] For real particles [...] the particle spring stiffness is in the range of [...] $10^9 - 10^10$ for the Hertzian contact model.' They also note for the Hertzian model that 'the computational time required for such simulations [...] scales as $k_n^{-1/2}$'.

report that '[t]he equivalent spring constant for materials such as sand or glass beads is of the order of 10^7 N/m or more, whereas most simulations are carried out with a spring constant of order 10^3 N/m for computational efficiency'. Bharathraj and Kumaran (2017) claimed that the simulations of Reddy and Kumaran (2010, figures 5 and 6) showed that the rheology is only weakly dependent on the stiffness parameter k provided that $k > 10^6 mg/d$; we note that this conclusion, while plausible and very useful, might not be justified given the wide error bars. However, the maximum penetration (7.8) also increases in proportion to $k^{-1/2}$: if k is brought too low, then particles may exhibit an extremely large overlap with each other, making particles unrealistically compressible, as well as violating the assumption of the Hertzian contact theory that the deformation of a material due to contact forces is small (Johnson 1985) and that each interaction on a particle may be treated separately. When we choose a value of k, we must make a balance between increasing t_c without making $\delta_{\max}$ unacceptably large.

Analogous considerations apply to other models involving elastic contacts, including the model (§7.2.2) for spherical particles, and the linear viscoelasticity model for cylinders and spheres (§7.3).

For 3D simulations of spherical particles, it may also be preferable to use the contact model (7.5) instead of (7.9), even though this contradicts the assumption that the spheres are made of a linearly elastic material. The contact model (7.5) allows a constant collision time (7.6) to be specified, rather than the collision time (7.12) which depends on the impact velocity. Specifying a constant t_c is useful because the timestep Δt may then be chosen *a priori* such that $\Delta t/t_c \ll 1$, regardless of the impact velocity v_0 of any contacts.

7.5.2. Dissipative contacts and the coefficient of restitution

The choice of a dissipative contact model and its parameters (a dissipation coefficient or a coefficient of restitution) merit particular discussion, because they demonstrate the issues discussed in this section.

Consider first the expression $f_{\text{dissipative}} \propto \Gamma \delta^{1/2} \dot{\delta}$ for the dissipative force on a sphere: this law arises from the assumption that the material of the spheres obey the Newtonian viscosity law, $\sigma_{\text{dissipative}} \sim \eta \dot{\epsilon}$, combined with geometric scaling arguments (§7.3.2). If this intrinsic constitutive relation is replaced by a different model in which the intrinsic viscous stress $\sigma_{\text{dissipative}}$ inside a particle depends nonlinearly on the strain ϵ and strain rate $\dot{\epsilon}$, the same scaling arguments lead to an alternative expression for the dissipative force $f_{\text{dissipative}}(\delta, \dot{\delta})$. It is widely agreed (for example, by Kuwabara and Kono (1987) and Antypov and Elliott (2011)) that the dissipative force should be directly proportional to $\dot{\delta}$, and have a power-law dependence on δ, so that

$$f_{\text{dissipative}} \propto \delta^{\alpha} \dot{\delta},$$

where the exponent α is a constant. However, there is no consensus on the appropriate value of α.

The Hertzian viscoelasticity model for a sphere (§7.3.2), corresponding to the case $\alpha = 1/2$, predicts a variable coefficient of restitution e that depends on the impact velocity v_0 (Kuwabara and Kono 1987). The experimental results of Marinack et al. (2013, figures 3 and 4) show that, although e does depend on v_0, for many materials the dependence is weak, and the variation of e is no more than 0.1. Therefore, in practice, it can be more intuitive and analytically attractive to specify a fixed coefficient of restitution e rather than fixing the dissipation coefficient Γ,

which is difficult to interpret physically. Antypov and Elliott (2011) showed that, when the elastic force is $f_{\text{elastic}} = K\delta^{3/2}$ (§7.2.2), a constant coefficient of restitution can be produced by taking a dissipative force proportional instead to $\delta^{1/4}\dot{\delta}$: this proportionality would arise from a constitutive relation of the form $\sigma_{\text{dissipative}} \propto \epsilon^{-1}\dot{\epsilon}$ in a spherical geometry.

Our simulations, being in two dimensions, sidestep the above discussion by using the contact law for cylinders (7.14), which are compatible with both the linear viscoelasticity constitutive relations and the requirement for a constant coefficient of restitution (7.17).

Choosing an appropriate value of e also requires some thought. We shall see in Chapter 9 that the coefficient of restitution between particles plays an important role in governing whether the particles form a dense flow, or become dissociated and accelerate indefinitely. This happens because the coefficient of restitution determines the amount of dissipation in a particle-to-particle contact. As we noted in §6.1, in general, circular particles in two dimensions have fewer contacts with neighbours than three-dimensional spheres would have; moreover, for computational reasons, one typically uses a much smaller number of particles than there would be grains in a real flow. To ensure that the proper amount of energy is dissipated despite the smaller number of contacts, each contact should be made more dissipative. Hence, the value of e in a simulation should be smaller than its value in a collision between real grains.

We shall discuss the rheological effects of e in more detail in Chapter 9. For now, we note that there is however a computational limitation on how low e may be brought. Consider again the linear viscoelasticity law for a cylinder. In the equation of motion (7.14) and its solution (7.15), there are two timescales: in addition to the contact time (7.16), there is also a *dissipative timescale* $t_d = 2m/\gamma$, where γ is the dissipation coefficient. When solving (7.14) numerically, the integration timestep must be small compared to t_d for an accurate solution. Therefore, although reducing the coefficient of restitution allows us to increase the particle size and decrease the total number of particles, it can also require us to take a smaller timestep.

7.5.3. Particle size

The most direct way of reducing the computational cost of a simulation is to reduce the number of particles in the system. This lowers the number of contacts and therefore the cost of contact detection, which is the most expensive process in a simulation (O'Sullivan 2014).[5] The number of particles may be reduced either by making the simulation domain smaller, or by increasing the particle diameter d relative to other lengthscales such as the characteristic depth $\mathcal{H}$. Provided that $d/\mathcal{H}$ remains sufficiently small, the continuum approximation continues to apply. The $\mu(I)$ rheology takes d as a merely passive parameter in the inertial number (2.6); increasing d slows a flow down by decreasing the Bagnoldian velocity scale (2.14), but has no other direct effects.[6]

When increasing the value of d, one can compensate for the reduced flow speed by decreasing both the coefficient of restitution and the intrinsic coefficient of friction (see §7.4) between particles. A lower coefficient of restitution increases the amount of energy dissipated in particle-to-particle interactions, and accounts for the reduction in the number of such in-

[5] For a simulation of N particles, the computational cost per timestep is between $O(N)$ and $O(N^2)$, depending on the contact detection algorithm (§A.1).

[6] Increasing d has the additional computational advantage that collisions can be resolved using a lower particle stiffness, allowing us to use a larger timestep.

teractions.[7] Similarly, a lower coefficient of friction allows particles to rearrange around each other more easily, counteracting the increased particle diameter d. To see this, recall from §2.1 the interpretation of the inertial number as the ratio between the microscopic rearrangement timescale $t_{\text{micro}} = d/\sqrt{p/\rho}$ and the macroscopic shearing timescale $t_{\text{macro}} = 1/\dot{\gamma}$. The microscopic timescale t_{micro} increases with d so that the value of I increases, but when the intrinsic coefficient of friction is reduced then the function $\mu(I)$ for the bulk friction is also lowered. If d and the intrinsic coefficient of friction are chosen appropriately, the value of $\mu(I)$ may be kept approximately constant for given values of $\dot{\gamma}$ and p.

However, as d is further increased and made comparable to other lengthscales in a problem, the $\mu(I)$ rheology eventually becomes invalid as nonlocal effects become increasingly important (§3.3). In fact, at very large values of d, the continuum approximation cannot be applied at all.

7.6. Summary

In this chapter, we have reviewed possible laws that govern the interactions between particles. These laws close the system (6.1) by giving expressions for the interaction forces $\boldsymbol{f}_{ij}^{\text{c}}$ and torques $\boldsymbol{\tau}_{ij}$ in (6.1b). Each force $\boldsymbol{f}_{ij}^{\text{c}}$ can be decomposed into a normal component, which represents the elastic repulsion between two bodies in contact with each other, and a tangential component, which arises in response to a relative sliding or rolling motion at the point of contact, representing either frictional resistance or nonsphericity. For circular particles, only the tangential component exerts a torque on a particle.

While much of our discussion has focused on the contact mechanics of real materials (§7.2 and §7.3), we also noted that certain features of contact models are favourable from a computational point of view (§7.5). Particles in a DPM are not made of real materials, and indeed we have already made some unrealistic assumptions about their shape and size distribution (§6.2).

In Chapter 9 we shall study the relationship between the parameters of contact models, and the bulk rheological properties of a flow, so that DPM simulations may be related to continuum models such as the $\mu(I)$ rheology. We shall see that bulk properties are often only weakly affected by the contact model parameters. This implies that we have some freedom to choose our contact models focusing mostly on computational issues.

We noted in §7.4 that a flow may exhibit a bulk friction even if there is no intrinsic friction in particle-to-particle interactions, because dissipation can be provided by the inelasticity of the normal interactions. The rheological effects of these two mechanisms shall be investigated separately in Chapter 9.

To close this chapter, we summarise the contact models that we shall use in the simulations presented in Part III. Particles shall be nominally monodisperse cylinders (§6.2), with a size dispersity of 10%. Normal interactions shall be governed by the linear viscoelastic model appropriate for cylinders (§7.3.1). There shall be no intrinsic friction between particles, neither sliding nor rolling friction; dissipation shall be provided by inelasticity. In each simulation, the coefficient of restitution shall be taken as $e = 0.1$. As discussed in §7.5.2, this is rather lower than that of most rigid materials.

[7] The kinetic theory of Haff (1983) and Lun (1991) predict that the rate of decay of granular temperature is $\mathrm{D}T/\mathrm{D}t = -\Gamma \propto -(1-e^2)d^{-1}T^{3/2}$. One can keep Γ unchanged by reducing e when d is increased.

8. Initial and boundary conditions in DPM

> People at birth are naturally kind-hearted. Their natures are similar, but their habits make them different. If, foolishly, they are not taught, their nature will deteriorate. The right way in teaching is to attach the utmost importance to thoroughness.
>
> The opening lines of the *Three Character Classic*

Having chosen the laws that govern the interactions between particles, we next need to specify the initial state of a simulation with initial conditions. Unless the simulation is to take place in an unbounded domain, it will also be necessary to give rules dictating the behaviour of the system at the edges of the simulation domain with boundary conditions. In the context of chute flows, these initial and boundary conditions govern the introduction of particles into the system at the start of a simulation, the removal of particles at the end of a chute, and the continual replenishing of particles if a steady flow is to be maintained.

In most discrete particle models, including the problems that we shall study in Part III, we must begin by introducing particles into a simulation domain. Particle introduction is performed as a preliminary process, before the simulation proper is said to begin. We describe this process in §8.2. If a simulation is run for a long time then the exact final microstate, such as the positions and velocities of individual particles, is likely to depend very sensitively on the initial microstate, especially if the number of particles is large. However, a granular flow composed of many particles is likely to be ergodic (Birkhoff 1931), in the sense that time-averages of the *statistical* properties of the flow, including the coarse-grained density and velocity fields (§9.1), are likely to be independent of the properties of the initial random microstate.[1, 2]

As for boundary conditions, the types of conditions that are appropriate depends heavily on the sort of flow that is being modelled (O'Sullivan 2014). In this work, we shall use two geometries, which we describe in more detail in §8.1. Note that in the DPM literature, the term 'boundary' is used to refer to regions in space in which the simulation not only evolves particle positions and velocities according to Newton's laws (6.1a, 6.1b) supplemented by contact models, but also performs some other task (O'Sullivan 2014, Thornton et al. 2013, Weinhart et al. 2017). Boundaries are contrasted with 'walls', such as the base at the bottom of a flow, which in the language of DPM interact with particles directly through the contact laws described in Chapter 7. Such an interaction is shown in figure 7.1(b). The term 'boundary' in discrete particle modelling therefore has rather different connotations from those in continuum modelling, which

[1] Certain initial conditions may produce special behaviours of the flow. For example, a system of perfectly monodisperse particles in an ordered, crystalline state (§6.2) does not flow as easily as a disordered collection of particles, or in fact may not flow at all. By making the ergodicity assumption, we assert that these special cases occur with negligibly small probability. For example, the particle generation process, to be described in §8.2, randomises the positions and diameters of particles.

[2] Ergodicity can be defined formally in terms of a probability measure on the space of microstates, and the time-evolution of this measure (Daniel Heydecker, pers. comm., 21 January 2019).

we discussed in Chapter 4; however, for our discussion in this chapter, we shall use the term 'boundary condition' (in the sense of DPM) to refer to the effects of both boundaries and walls.

The four basic types of boundaries relevant for the present work are *insertion boundaries* (§8.2), which add particles to a simulation, *deletion boundaries* (§8.4), which remove particles that move beyond the edge of a domain, *periodic boundaries* (§8.1.1), which move particles that cross one edge of a domain to an opposite edge, and *Masers* (§8.3.3, Denissen et al. (2019)), which are used to provide a continuous stream of particles at the upstream end of a flow. Walls shall be discussed in §8.5. Throughout, it is important to remember that boundary conditions in DPM act on individual particles, unlike boundary conditions in continuum models, which apply to the statistical motion of particles. In particular, free surfaces, which play a integral role in continuum models of chute flow, do not have a direct analogy in a DPM (§8.6).

As with all aspects of discrete particle modelling, as we develop solutions for carrying out the processes of particle generation, introduction and removal, we must bear in mind whether a solution would give reproducible results, whether it would be physically realistic, and whether it would be computationally efficient. For example, in a real experiment, grains would be introduced onto a chute from a reservoir in a hopper, as was shown in figures 1.3 and 1.4. While the hopper geometry could be reproduced in a DPM, it would not be computationally useful to simulate the behaviour of all of the particles in the reservoir, as its details can be expected not to affect the behaviour of the current on the chute. Provided that the introduced flow can faithfully reproduce statistical properties such as flow rate and steadiness, the hopper geometry could be replaced with an unrealistic but simpler device.

Henceforth, we shall consider only two-dimensional DPM, and suppose that the particles are discs. We discussed the implications of these assumptions in §6.1 and Chapter 7, where we noted that these assumptions are stronger than the assumption of two-dimensionality in a continuum model.

8.1. Geometry of DPM of chute flows

The chute flows studied throughout this work could be realised in a laboratory experiment using an inclined chute, as illustrated in figures 1.3 and 1.4. Grains are released from a hopper onto a chute; the resulting current flows down the chute and eventually flow off the end, where they are collected. To maintain the approximate two-dimensionality of the flow, the chute should be bounded by side walls, which prevent any significant cross-stream motion; these walls should be smooth to allow slip and produce no velocity gradient in the cross-stream direction. The flow rate q can be controlled by adjusting the aperture size of the hopper compared to the grain size (To et al. 2001). According to the Janssen effect (Bertho et al. 2003), this flow rate is approximately time-independent and does not depend on the volume of grains in the hopper (above a certain minimum volume), so that a steady flow may be maintained for an indefinitely long time by occasionally replenishing the reservoir.

A DPM of a chute flow should attempt to recreate the setups shown in figures 1.3 and 1.4, but some abstractions can be made. For example, the dynamics in the reservoir and the dynamics can be simplified, as our interest is on the chute itself.

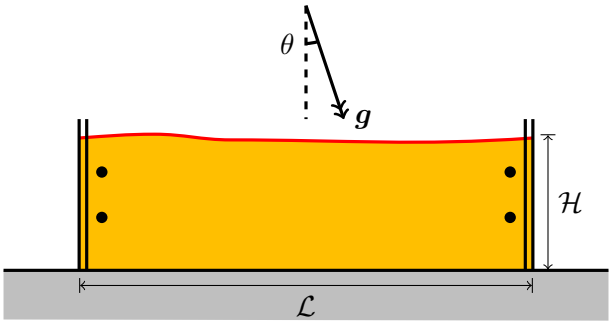

Figure 8.1.: A periodic domain for a DPM, denoted using repeat signs. Note that the free surface might not be perfectly level. The base could be bumpy (§8.5), but this is not shown here.

8.1.1. Periodic domains

A simple geometry that one can use in a DPM is a periodic domain, denoted in figure 8.1 using a pair of musical repeat signs. A particle that crosses one edge of the domain is moved to the other edge, and particles may interact with each other across those edges. The flow inside a periodic domain is approximately uniform in the streamwise direction, which makes it well-suited for studying streamwise-independent flows; using a periodic domain is analogous to setting $\partial/\partial x = 0$ in a continuum model. However, as we shall discuss later in this subsection, some caution must be taken when using this interpretation.

The number, mass, and intrinsic volume of particles within the periodic domain do not change with time. Periodic domain simulations are computationally useful, because the number of particles N within the domain is constant and can even be set directly, so that the computational cost of a periodic domain simulation can be estimated and controlled well.[3] However, although the intrinsic volume is fixed, the apparent volume, and the position of the free surface, may be time-dependent if a flow is compressible, due to Reynolds dilatation (§3.1).

A periodic domain is usually interpreted as a 'representative' sample of a long system that is (statistically) streamwise-uniform, ignoring endpoint effects (O'Sullivan 2014). Such an interpretation has been used to study granular materials in shear cells (see *e.g.* Thornton (2000)). In this thesis, we use periodic domains in the calibration tests of Chapter 9, which are analogous to the calibration tests used by GDR MiDi (2004). However, the interpretation of a periodic domain as a representative sample of a flow is not valid when there is streamwise topography, as in the application in Chapter 11. There are two other caveats that apply to this interpretation even in the absence of topography.

First, consider a steady flow on a long and frictionless chute: such a flow thins out in the streamwise direction as the flow accelerates, as sketched in figure 8.2.[4] In contrast, a flow in a periodic domain over a frictionless base has a constant depth due to conservation of volume; however, the flow does not attain a steady state, but accelerates with time. A periodic domain therefore cannot be used to represent chute flows that accelerate indefinitely.

Secondly, it is important to consider whether the periodic domain length $\mathcal{L}$, an unphysical

[3] The running time of a simulation of N particles grows approximately as $O(N)$ (§A.3).

[4] This is consistent with elementary Newtonian gravity currents (Simpson 2012), hydraulic open channel flow (Chow 1959), as well as the predictions of depth-averaged models (Chapter 10).

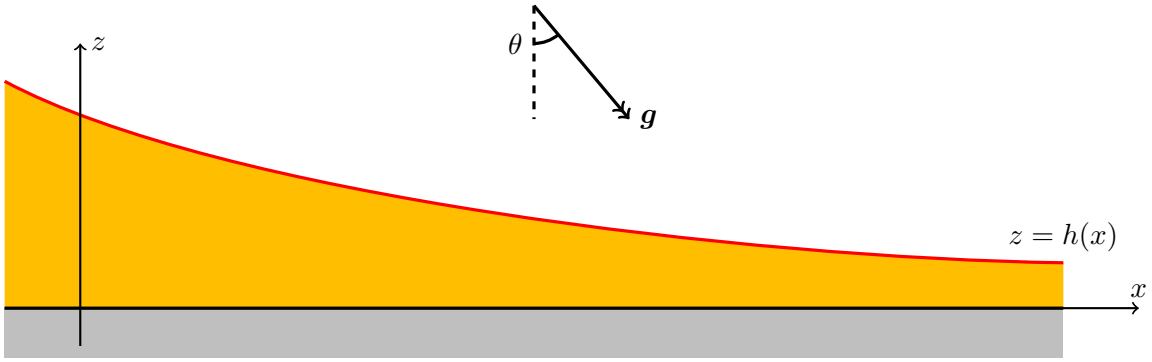

Figure 8.2.: If a chute is inclined too steeply, then the resulting current cannot be streamwise-uniform.

parameter that is chosen somewhat arbitrarily, has any significant effects on the properties of the flow. If $\mathcal{L}$ is so small that it becomes comparable to the particle size d, the periodicity creates an unrealistic, artificial crystalline structure in the streamwise direction, which affects the rheology of a flow by magnifying nonlocal effects (§3.3). On the other hand, if $\mathcal{L}$ is too large, then the assumption of streamwise-uniformity may be violated by the development of waves (§14.2.3). When we use periodic domains in this thesis in Chapter 9, we shall take $\mathcal{L} \approx \mathcal{H}$, where the typical flow depth $\mathcal{H} \gg d$; this intermediate choice for $\mathcal{L}$ can be expected to be long enough that it does not create artificial nonlocal effects, but short enough to suppress the formation of waves.[5]

8.1.2. Finite-length domains

To study streamwise-dependent flows in a DPM, one should use a finite-length domain instead of a periodic domain. Such a domain closely resembles a real experimental setup (figures 1.3 and 1.4). Particles are to be inserted into the simulation domain from a reservoir at the upstream end of the chute, from which they flow down, interacting with any topographical features of interest. When they reach the end of the chute, they are removed. However, in a DPM simulation it is usually advantageous to use unphysical conditions at the upstream and downstream ends of the chute. We shall discuss some options for inflow conditions in §8.3. As for outflow conditions, a simple solution is to place a 'deletion boundary' at the downstream end of the chute, which removes any particles that cross a position $x = x_{\max}$; we discuss deletion boundaries in §8.4.

We use a finite-length domain when we study the granular Blasius problem (Chapter 11), which considers a streamwise transitional flow.

8.2. Particle generation: Filling a domain with particles

We first consider the problem of filling a bounded domain with a static random dense packing of circular particles, where the particles may have a nontrivial size distribution (see §6.2). Such a packing will provide an initial condition for a simulation. The desire to randomise the packing and the size distribution means that a created packing cannot be precomputed, but must be

[5]The size of $\mathcal{L}$ is also limited by computational cost.

generated dynamically. As we noted at the start of the chapter, the generation process should be regarded as a preliminary step before the main part of a simulation.

For definiteness, suppose that the domain is rectangular and aligned with the coordinate axes, with opposite corners $(x, z) = (0, 0)$ and $(x, z) = (a, b)$, where $a, b > 0$; the area is ab. Gravity points in the negative-z direction. The domain is bounded below by a wall and on the sides either by walls or periodic boundaries. Our goal is to fill the domain with particles until the packing fraction exceeds a given goal ϕ_{goal}, that is,

$$\sum_i \pi(d_i/2)^2 \geq \phi_{\text{goal}} ab. \tag{8.1}$$

The requirement that the packing be static and dense also means that the particles should be allowed to settle, through their dissipative contacts with each other and the wall, until the total kinetic energy of the particles be smaller than a given threshold,

$$\sum_i \frac{1}{2} m_i \boldsymbol{u}_i^2 \leq E_{\text{threshold}}. \tag{8.2}$$

Guidance on the choices for ϕ_{goal} and $E_{\text{threshold}}$ will be given later in this section.

This particle generation process is supposed to be analogous to the experimental procedure of randomly filling a hopper with grains. The condition that the created packing should be stable under gravity means that particles must be allowed to settle as part of the generation process. No particles are to overlap with each other, except for the small amount of overlap allowed by a contact model (as discussed in Chapter 7), so we may not simply add particles to the system at random positions independently of each other. Finally, the condition that the packing should be random means that it is not acceptable to construct regular structures such as a square or hexagonal packing.

8.2.1. The insertion boundary algorithm

The procedure used to populate a region with a set of non-identical particles is as follows.[6] First, a 'prototypical' particle P_0 is defined, specifying its contact species but not its diameter. Then, at each timestep:

1. A counter n_f is set to 0.
2. A candidate particle P is defined, based on P_0 but with a diameter chosen from the uniform random distribution $\mathcal{U}(0.9d, 1.1d)$.
3. The simulation generates a random position (X, Z) inside the domain to be filled, with $X \sim \mathcal{U}(0, a)$ and $Z \sim \mathcal{U}(0, b)$, and tries to place P there.[7]

[6] This procedure, which is implemented as the `InsertionBoundary` class in MercuryDPM, is based on an algorithm by Dinant Krijgsman (Thornton et al. 2013). Krijgsman's original version performs steps 2 and 3 at the same time, so that a candidate particle's diameter and position are generated together. This led to a strong bias towards smaller particles. The present algorithm partially mitigates this bias, and is more readily generalised to polydisperse systems (see main text). As of February 2019, release version 0.11.1 of MercuryDPM continues to use the Krijgsman version; the algorithm presented here is in the Trunk and will be included in the next release.

[7] To fill a non-rectangular region, one would use an alternative distribution for the pair (X, Z). The ab on the right-hand side of (8.1) would be replaced with the area of that region.

4. The simulation checks if P, placed at (X, Z), would interact with any existing particles. If there would be no interactions, then the candidate particle P is added to the simulation. The counter n_f is reset to 0, and we return to step 2 in order to generate a new candidate particle. Otherwise, n_f is incremented by 1. If n_f now exceeds a chosen value $n_{\max}$, then the loop breaks for this timestep; if not, we return to step 3, to reattempt placing the particle at a different position.

Within a given timestep, the counter n_f is the number of consecutive times that the simulation has tried and failed to place a given candidate particle, while the parameter $n_{\max}$ is the maximum allowed value of this counter.

Optionally, when a particle is introduced into the simulation by the insertion boundary, it may be given a velocity according to some specified distribution. Moving particles away from an insertion boundary's region can help to reduce congestion and increase the rate at which particles are created. Giving newly-created particles a downwards initial velocity will help the system attain a static packing.

The above loop is then repeated at each time step until the conditions (8.1) and (8.2) are met, at which point the particles are judged to have reached a static dense packing. When these conditions are met, the insertion boundary is deactivated, and the state of the system is used as the initial state for the rest of the simulation. To do this, any bounding walls of this domain (other than the base) may be removed or replaced with periodic or Maser boundaries, the magnitude or direction of gravity may be changed to have a streamwise component: these represent the opening of a gate or the removal of an obstacle, which allows particles to flow. The simulation time is reset to zero.

The insertion boundary algorithm can be modified to create a bidisperse or polydisperse sample of particles, for example by specifying multiple prototypes $P_{0,i}$ and making a randomised choice over i in step 2. The algorithm can also easily generalised for noncircular particles or three-dimensional simulations. For nominally monodisperse particles, the insertion boundary algorithm has a slight bias towards creating smaller particles, which are less likely to fail the contact detection tests and more likely to be inserted. For our purposes, this bias away from a uniform distribution had no noticeable effects given that the 10% size dispersity was sufficiently small that the flow could be treated as essentially monodisperse.

8.2.2. Computational aspects

The parameters ϕ_{goal}, $E_{\text{threshold}}$ and $n_{\max}$ in the particle generation procedure should be chosen with computational efficiency in mind.

For ϕ_{goal}, we observe that as the domain fills with particles, the procedure above slows down the rate at which new particles are introduced to the system: that is, as ϕ increases, $\mathrm{d}\phi/\,\mathrm{d}t$ falls. This happens because, if a domain already has many particles, then new candidate particles are more likely to interact with existing particles. These candidates are therefore less likely to be inserted in step 3 in the algorithm. To avoid this, we may take a lower value of ϕ_{goal}, and compensate for this by increasing the domain size ab, so that the total volume of particles inserted, $\phi_{\text{goal}}ab$ remains the same. In our simulations, we use an insertion boundary of depth $b = 3\mathcal{H}$ and packing fraction goal $\phi_{\text{goal}} = 0.3$ to fill a region of approximate depth $\mathcal{H}$.[8] This value

[8]The maximum packing fraction for monodisperse circles in an unbounded domain is that of a hexagonal

of ϕ_{goal} gives a reasonable balance between the time taken to introduce the desired number of particles, and the time taken to dissipate all the energy that these particles would have. (Using a taller domain would create particles that fall down from a higher position.)

In principle, $E_{\text{threshold}}$ should be taken to be as small as possible, so that the final state should be very close to static. However, if $E_{\text{threshold}}$ is taken to be too small, the convergence towards this state could take a very long time, especially if contacts are not very dissipative. For example, under kinetic theoretical models (§3.2), the cooling law (3.1) predicts that the total kinetic energy should decay as t^{-2}, so that the time required until (8.2) be satisfied grows as $O(E_{\text{threshold}}^{-1/2})$ as $E_{\text{threshold}}$ is reduced.

The contact detection in step 3 is the most computationally costly process in the above loop, as the candidate particle must be tested against all existing particles in the system. Taking larger values of $n_{\max}$ will (on average) increase the number of particles inserted at each timestep, but the process becomes more computationally costly. In all of the simulations presented in this work, $n_{\max} = 0$, so that the loop within a timestep breaks as soon as a particle fails to be placed.

8.3. Particle introduction

To initialise a simulation in a periodic domain (§8.1.1, figure 8.1), one needs only to populate the domain with particles using the method described in §8.2. For a finite-length domain (§8.1.2), one must also continuously introduce a stream of particles at the upstream end of a chute flow. We would like to control the depth, flow rate and velocity profile of the incident stream, although these cannot necessarily be controlled independently of each other. For steady systems, we also desire that these properties be as statistically time-independent as possible. The methods that we describe here shall be of importance in Chapter 11.

8.3.1. An inefficient and poorly-controlled method: a persistent insertion boundary

In §8.2, we described the use of an insertion boundary to fill a region, by running the insertion boundary algorithm (§8.2.1) at each timestep until the packing fraction in that region exceeds a desired threshold, at which point the insertion boundary would be removed. In the present section, given our desire to introduce a steady stream of particles, it might seem reasonable to keep running the insertion boundary algorithm throughout a simulation, rather than removing it.

Unfortunately, this scheme is not computationally efficient. When candidate particles are produced, the costly contact detection step (step 3) in the insertion boundary algorithm will use much effort to test each candidate particle for interactions with existing particles, and this would be conducted throughout a simulation, not just in a preliminary setup stage. If the value of the 'maximum failures' $n_{\max}$ parameter (step 4) is high, then much of this effort will be wasted on candidate particles that fail to be introduced, while if $n_{\max}$ is low then it is difficult to maintain a high flow rate. Moreover, the stochastic nature of the insertion boundary algorithm (§8.2.1)

packing, $\phi_{\max} = \pi\sqrt{3}/6 \approx 0.9069$ (Weisstein 2018). This packing fraction is approximately attained with our parameters, since $3\mathcal{H} \times \phi_{\text{goal}} \approx \phi_{\max}\mathcal{H}$.

means that the rate at which particles are created and introduced cannot be controlled very well.

We therefore do not use a persistent insertion boundary for introducing a constant stream of particles. We use the insertion boundary algorithm only for generating particles in a preliminary process.

8.3.2. An inefficient method: a hopper

As an alternative to a persistent insertion boundary, it may seem sensible to use an insertion boundary to fill a 'hopper' and letting it drain out. This reflects the setup of a laboratory experiment, as shown in figure 1.3. Until the hopper runs out, the flow rate is time-independent to a very good approximation, according to the Janssen effect (Bertho et al. 2003); and an experimentalist can control the flow rate by adjusting the the aperture size of the hopper relative to the grain size d, provided that the aperture is large enough to avoid jamming (To et al. 2001).

DPM simulations of hoppers have been conducted (Thornton et al. 2013), and two-dimensional hoppers have been studied experimentally (To et al. 2001). But for the present work, the use of a hopper for particle introduction is a poor choice: it would be computationally wasteful to simulate the dynamics of particles in the hopper, most of which are almost stationary, when the focus is on the chute. A hopper also does not provide an indefinitely long supply of particles, unless replenished by the insertion boundary algorithm.

8.3.3. The Maser

The Maser ('Mercury laser'), developed by Denissen et al. (2019), is a mechanism for introducing a continuous stream of particles without the costly production process of the insertion boundary. The Maser consists of a periodic domain marked by a pair of periodic boundaries (§8.1.1). One of these boundaries is labelled as the 'outflow' boundary. As with a standard periodic domain, if a particle crosses the outflow boundary then it is moved to the other side of the domain. However, the Maser also makes a copy of that particle and introduces it into the flow.[9] In figure 8.3, we denote the Maser by a repetition sign with an arrow indicating the direction of outflow.

8.3.4. Controlling the flow from a Maser

The Maser offers two of the benefits of a periodic domain (§8.1.1). Firstly, the Maser generates a continuous flow regardless of how many particles it is initially populated with (using an insertion boundary). This property offers the user good control over the computational cost, and avoids the wastefulness of the hopper (§8.3.2). Moreover, the Maser offers excellent control over the depth and uniformity of the outflow: the periodicity of the Maser implies that if the Maser is

[9] The mechanics of the Maser are explained in Denissen et al. (2019, §C.5), who explain that 'the velocity inside the [M]aser boundary is influenced by the velocity in the outflow domain, since those particles do exert forces on particles inside the Maser boundary. Especially for subcritical flows, this influence can be substantial.' This shall not be of concern for us, since we shall artificially control the particles within a Maser (§8.3.4), and our application in Chapter 11 shall involve solely supercritical flows (see introduction to Part III).

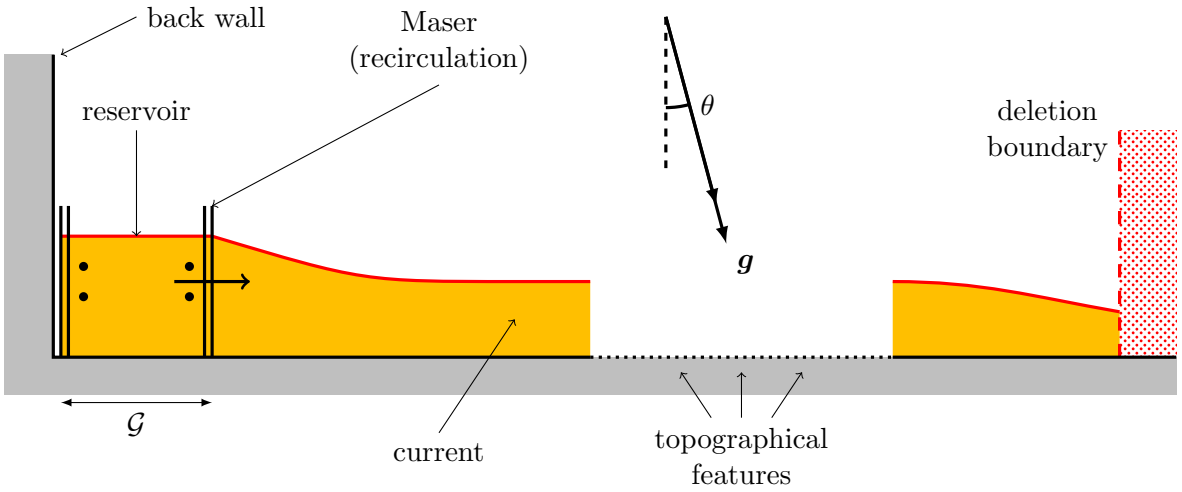

Figure 8.3.: Introducing particles onto a chute using a Maser (§8.3.3).

initially populated so that the free surface is approximately flat, then the outflow depth can be expected to remain approximately constant (see §8.1.1).

However, the caveats that apply to periodic domains (§8.1.1) also apply to the flow within the Maser. In particular, controlling the flow rate and the velocity profile of the outflow can be difficult. A steady flow rate q out of a Maser is possible only if the slope and the basal conditions inside the Maser admit a solution to $\tan\theta = \mu(I)$. If not, the flow within the Maser may indefinitely accelerate, or decelerate to a halt.

These behaviours can be corrected by applying additional, artificial forces on the particles within the Maser, to produce a desired velocity profile. In particular, to create a plug flow profile with a specified velocity $\mathcal{U}$, one may use a frictionless base within the Maser, and apply a drag force $mg\sin\theta \times u/\mathcal{U}$, where u is the streamwise speed, to counteract gravitational acceleration. Because of the frictionless base, the particles within the Maser collapse into a rigid body motion; then u, governed by

$$m\frac{\mathrm{d}u}{\mathrm{d}t} = mg\sin\theta(1 - u/\mathcal{U}),$$

will converge towards the desired value $\mathcal{U}$. We shall employ this technique in Chapter 11 to create a controlled plug flow.

The Maser employed by Denissen et al. (2019) also produces a steady flow without using this 'artificial drag' technique; their drag arises from the roughness of their basal topography within the Maser. This would be inappropriate for our application, since we shall need our outflow to have a plug profile.

In preliminary simulations, we attempted to control the flow out of a Maser by using a gate (figure 8.4). While the gate indeed prevented the particles within the Maser from accelerating indefinitely, the resulting outflow was not satisfactorily steady, but had large variations in time. These were caused by the buildup of a jammed region immediately behind the gate, which was occasionally released, producing a surge of particles. These surges did not appear to be periodic in time.

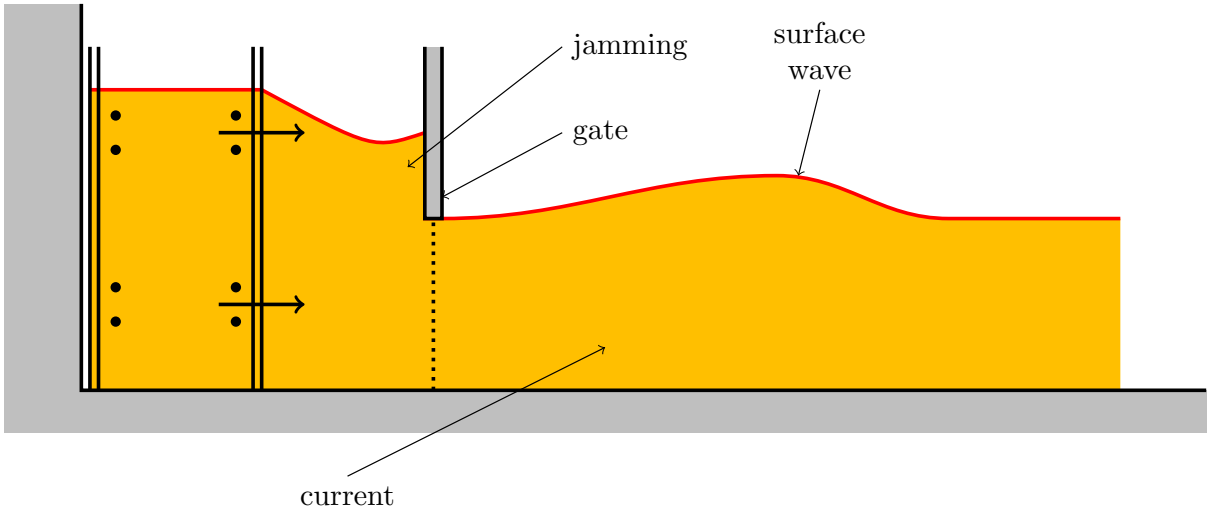

Figure 8.4.: A gate does not control the flow rate out of a Maser very well (§8.3.4). Particles occasionally form jammed regions just upstream of the gate, and the formation of breakup of these jammed regions is unpredictable and leads to large variations in the flow rate. This is most problematic for 2D simulations.

8.4. Deletion boundaries

A *deletion boundary* removes from the simulation any particles that enter a certain region, often a half-space defined by a line (in 2D) or plane (in 3D). A deletion boundary is placed at the downstream end of a chute in order to limit the number of particles in the simulation. Figure 8.5 shows some configurations in which this boundary could be placed. In panel (a), the deletion boundary is placed perpendicular to the chute at $x = x_{\max}$ and particles are removed as soon as they cross this position. In panels (b) and (c), the deletion boundary is horizontal (in the rotated coordinates), and particles are able to travel a little further beyond the end of the chute.

In each case, there is an disturbance to the flow upstream of $x = x_{\max}$, marked explicitly in panel (a). This disturbance arises because the end of the chute and the deletion boundary decrease the pressure in the flow. For example, in panel (a), particles at $x = x_{\max}$ experience no collisions with other particles to their right. For supercritical flows $\mathrm{Fr} = \mathcal{U}/\sqrt{g\mathcal{H}} > 1$, the upstream disturbance propagates a finite distance. In fact, it can be shown that, in the limit $\mathrm{Fr} \gg 1$, this distance is $O(\mathrm{Fr}^{-2}\mathcal{H}) = O(g\mathcal{H}^2/\mathcal{U}^2)$. This can be proved from the depth-averaged equations (Chapter 5), and the proof shall be given in §10.2.2.

Therefore, assuming that this endpoint $x = x_{\max}$ is sufficiently downstream of any topographical features that we are investigating, neither the exact position of $x_{\max}$ nor the configuration for the deletion boundary are important. Although configuration (c) in figure 8.5(c) is most similar to the experimental setup (figure 1.3), configuration (a) is marginally computationally cheaper, and we use this in practice.

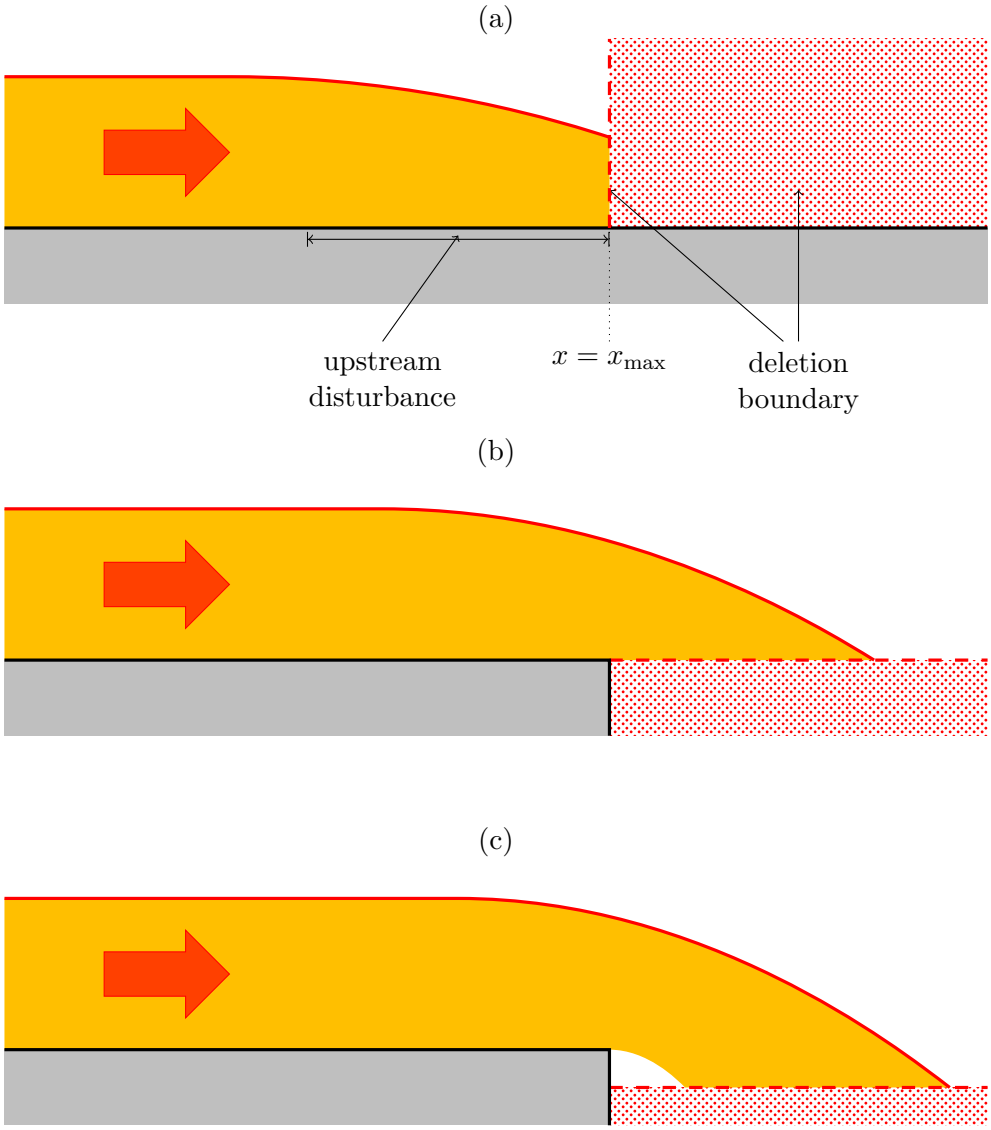

Figure 8.5.: Some possible configurations for the deletion boundary at the end of a chute. Deletion boundaries are marked as dotted red boxes bounded by dashed red lines. (The term ‘deletion boundary’ may refer to either.)

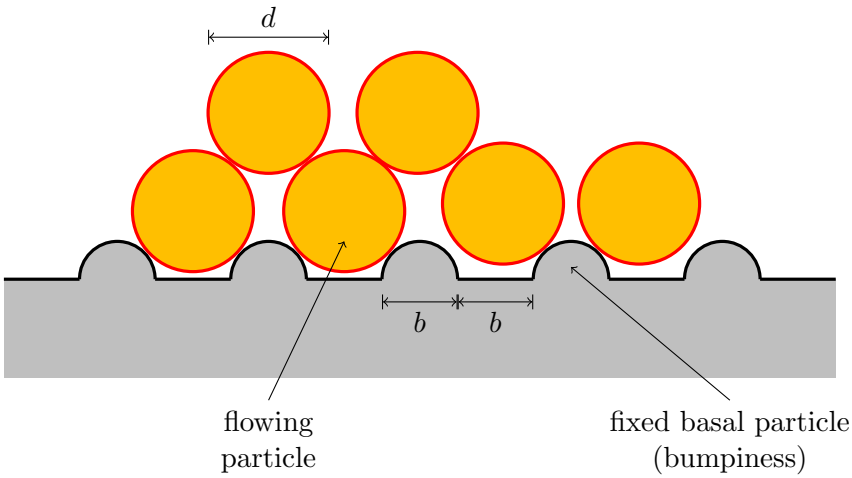

Figure 8.6.: Basal bumpiness may be modelled by lining the basal wall using fixed particles (grey). The fixed particles are semicircular and have diameter b, and they are spaced out, separated by distances b.

8.5. Walls

In the language of discrete particle modelling, while 'boundary' refers to regions of special behaviour, the term 'wall' refers to a fixed object that interacts with particles according to the same contact models that govern inter-particle interactions (Chapter 7), with no extra effects. In particular, surfaces, including the base that a current flows over, are walls.

We must make a distinction here between walls in continuum models and walls in DPM, and how they relate to real surfaces. As we mentioned in §7.4, no real surface is perfectly smooth; all surfaces contain asperities to some level. When these asperities are small compared to the grain size, as we saw in figure 7.2, a DPM treats such a surface as geometrically smooth, with the effects of asperities incorporated through tangential forces in a contact model. But if the bumpiness of the surface is over lengthscales comparable to the particle diameter, then this approach does not capture the geometric effects of the base on the flow.

On the other hand, in a continuum model, the base is taken simply to be a surface $z = 0$, and no thought is given to the particular details of the bumpiness such as the amplitude, except through the choice of a dynamic boundary condition (§4.2.2). In particular, the no-slip condition (4.6) can be used when the bumpiness prevents any motion whatsoever, while the more general Knudsen condition (4.8) may be used for surfaces that allow some slip.

In a DPM, one way of making a surface bumpy is to line it with 'frozen particles', as shown in figure 8.6. In our simulations, the bumpiness shall be generated using semicircular frozen particles of diameter b, spaced out as shown, separated by gaps also of size b. The ratio $\beta = b/d$ shall be referred to as the *relative basal roughness*.[10] The bumpiness created by frozen particles in the arrangement shown in figure 8.6 is just one way of creating a rough base (O'Sullivan 2014). Frozen particles could also be arranged in a random configuration of 'a few layers of fixed larged particles' frozen particles (Denissen et al. 2019, §C.4 and figure 9). Jing et al. (2016) showed, empirically, that the effects of a frozen particle base can be characterised using a number, which

[10]More generally, one could take the frozen particles to have diameter b_1 and the gaps to be of size b_2.

they call R_a, that is a function of the amplitude (analogous to our β) and configuration, such as the spacing, of the particles; in their simulations, they found that '[t]he transition of slip and nonslip conditions is well indicated by changes in the value of R_a'. Instead of using frozen particles, it is also possible to use a curved wall that is geometrically smooth at the particle level: Bharathraj and Kumaran (2017) studied the response of flows to different types of rough bases, including frozen-particle bases in various configurations, or from a geometrically smooth but sinusoidally-curved wall, and found little qualitative difference in the flow profile except 'in a region of height 5–10 particle diameters at the base, [where] there are significant and counterintuitive changes in the flow within this basal layer as the base topography is changed' (Bharathraj and Kumaran 2017, §4.3). Neither of these two studies are satisfactorily applicable to the present work: unlike us, they work in three dimensions and use frictional particles, so that dissipation is not provided purely by inelasticity.

But although there have been these empirical studies on the effects of different types of basal roughness on the properties of a flow, the precise relationship between the two are still poorly understood, and no rule is known for selecting a boundary condition in a continuum model, given a precise description of a rough base. Such a relationship is unlikely to exist for basal roughnesses comparable to particle size, $\beta = O(1)$, since the continuum approximation is necessarily violated at these lengthscales. Moreover, as we shall see in Chapter 11, when there is an abrupt change in the basal roughness, the inertia of an incoming flow allows it to briefly maintain the velocity profile that it previously had (§11.4.3). For an increase in basal roughness, this means that a flow locally exhibits slip over a base that would otherwise be rough enough to create a no-slip flow.

8.6. Free surfaces

As has already been mentioned (§§2.3, 3.1,), the notion of a 'free surface' is a construction of a continuum model that assumes that a material completely occupies a region with a well-defined boundary. No such surface exists in a real flow or in a DPM, because there is no strict cutoff between a collection of discrete particles and the space around it: for example, a current may lie below a thin layer of dissociated saltating particles, as in figure 1.1.[11]

Thus, it is incorrect to talk about 'free surface boundary conditions' in the context of discrete particle models. However, when we try to relate the results of DPM simulations using the language of continuum models, we shall need to define the position of a free surface. This definition shall be given in §9.1.2, but it must be remembered that any such definition is arbitrary, and that one cannot expect the continuum free surface boundary conditions (Chapter 4) to be satisfied exactly.

* * *

Having stated the shapes of particles (§6.2), the contact laws between particles (Chapter 7), and the initial and boundary conditions, we can now proceed to integrate the equations of motion (6.1a, 6.1b) to obtain the particles' positions and velocities. The computational aspects of the numerical integration are outlined in Appendix A.

[11] This is a manifestation of the sorites paradox (see §1.1). Even for classical fluids, it is impossible to identify a distinct free surface at the molecular level.

We must now return to the question of choosing the parameters of a contact model. As with boundary conditions in a DPM, contact laws and boundary conditions are all specified in terms of microscopic, particle-level parameters; the macroscopic, rheological properties of the material cannot be set directly but must be measured. The next chapter discusses the relationship between microscopic parameters and macroscopic properties.

9. Calibration of discrete particle models

> 'Come, let us build ourselves a city and a tower with its top in the heavens, and let us make a name for ourselves, lest we be dispersed over the face of the whole earth.'
>
> Genesis 11

The direct output of a DPM simulation is the positions and velocities of the individual particles, and the positions, magnitudes and directions of inter-particle interactions. However, this detailed information is of little value by itself, given that particles in a DPM do not correspond directly to real grains, especially in a 2D model (Deluzarche and Cambou 2006). For example, the contact model between two particles does not necessarily realistically describe the interaction between two physical grains (§7.5), and a large particle with a low coefficient of restitution may represent a number of grains (§7.5.2). In order to relate a DPM to the predictions of a continuum model or to measurements of a real flow, we must calculate statistical quantities about the bulk behaviour of the flow.

The first section of this chapter will discuss the relationship between discrete particle models and continuum descriptions. We mentioned in Chapter 2 that continuum fields such as $\rho(\boldsymbol{x}, t)$ and $\boldsymbol{u}(\boldsymbol{x}, t)$ represent local statistical properties of particles. The precise definitions of these fields, which were formulated extensively by Weinhart et al. (2012, 2013), will be stated in §9.1.

Defining the position of a free surface s, or equivalently, the depth h of a current, from discrete data merits particular discussion. As mentioned already in §8.6, at the level of individual particles there is no strict cutoff between a current and the empty space above it. There are several ways of defining the position of a free surface, which we describe in §9.1.2.

Having introduced these ideas, we then talk about the procedure for calibrating a DPM against the $\mu(I)$ rheology: in particular, the behaviour of the function $\mu(I)$ must be found for a given species of particles in a model. The procedure for this is described in §9.2; it is analogous to to the experimental setup that is used for real grains (§2.3) We then conduct this calibration test on a number of particle species, varying the coefficient of restitution (§9.3), particle size (§9.4), basal roughness (§9.5) and intrinsic friction (§9.6) and investigating the results of each of these on the function $\mu(I)$. We shall conclude this chapter in §9.7 with a summary of these results.

9.1. Continuum fields from discrete data

When Newton's equations (6.1a) and (6.1b) are integrated, one obtains the positions, velocities and angular velocities of the particles as functions of time. A DPM simulation outputs the value of these functions sampled at a sequence of points in time. To compare between continuum models and DPM simulations, we must convert this output into continuum fields, which represent local averages of particle properties. This process is known as *coarse-graining* and is described in detail in Weinhart et al. (2012, 2013). We recount the main ideas in this section.

Given the particle positions $\boldsymbol{x}_i$ and masses m_i, one defines the localised density field as

$$\rho_{\text{loc}}(\boldsymbol{x}, t) = \sum_i m_i \delta(\boldsymbol{x} - \boldsymbol{x}_i), \tag{9.1}$$

where δ is the Dirac delta function; recall that $\boldsymbol{x}_i = \boldsymbol{x}_i(t)$. The coarse-grained density field is then defined as a convolution

$$\rho(\boldsymbol{x}, t) = \sum_i m_i W(\boldsymbol{x} - \boldsymbol{x}_i), \tag{9.2}$$

where W is a kernel function for the convolution. We take the packing fraction as $\phi(\boldsymbol{x}, t) = \rho(\boldsymbol{x}, t)/\rho_*$. Similarly, we can define a velocity field,

$$\boldsymbol{u}(\boldsymbol{x}, t) = \frac{1}{\rho(\boldsymbol{x}, t)} \sum_i m_i \boldsymbol{u}_i W(\boldsymbol{x} - \boldsymbol{x}_i), \tag{9.3}$$

as the weighted local average of particle velocities. In the absence of any particles, $\rho = 0$ and we say that $\boldsymbol{u}$ is undefined, not zero.

Under these definitions of the density and momentum fields, the mass conservation equation (2.1a) is satisfied exactly. The validity of the incompressibility assumption (2.2) may be checked by taking the divergence of (9.3).

The fields $\rho(\boldsymbol{x}, t)$ and $\boldsymbol{u}(\boldsymbol{x}, t)$ are local averages of particles' masses, positions and velocities, but carry no information about the forces and interactions between particles. It is also possible to define coarse-grained fields for the stress (and in particular the pressure) within a flow by taking local averages of these interaction forces, and the relevant formulae are given in Weinhart et al. (2013). However, limitations on storage space meant that we were not able to record and store information about particle interactions.

9.1.1. The kernel function

The kernel function W must satisfy the normalisation condition that $\int_{\mathbb{R}^n} W(\boldsymbol{r})\,\mathrm{d}\boldsymbol{r} = 1$, where n is the number of dimensions. The kernel will usually be isotropic, so that $W(\boldsymbol{r}) = W(r)$ depends only on the magnitude $r = |\boldsymbol{r}|$. The normalisation condition on an isotropic kernel is therefore $2\pi \int_0^\infty sW(r)\,\mathrm{d}r = 1$ in two dimensions, while the analogous condition in three dimensions is $4\pi \int_0^\infty r^2 W(r)\,\mathrm{d}r = 1$. Otherwise, the choice of W is somewhat arbitrary, although it is usually desirable to take W as having finite support, decreasing in r, and having at least two continuous derivatives (Weinhart et al. 2013).[1, 2] For our two-dimensional simulations, we choose the kernel function to be the quartic formula

$$W(r) = \begin{cases} \dfrac{3}{\pi c^2}\left(1 - (r/c)^2\right)^2, & r < c, \\ 0, & r \geq c, \end{cases} \tag{9.4}$$

[1] Choosing W to have finite support and to be continuously differentiable produces continuum fields that are smooth, resilient to noise, and localised.

[2] Having calculated a field, we shall usually not use it directly, but instead perform further averaging over time or space. The central limit theorem (Grimmett and Welsh 2014) suggests that the averaged fields should have weak dependence on the choice of W. The calculation of §5.3 give us an estimate on the sensitivity of the shape factor to the choice of W.

where c is the coarse-graining range. The choice of the coarse-graining range is again arbitrary, subject to the condition that it be proportional to the particle size; throughout the present work, we take $c = 2d$.[3] A larger value of c would produce a smoother field but one that has less resolution: a sensible choice of c therefore also depends on the resolution at which we wish to evaluate these continuum fields. There is little value in taking very small values of c, as the notion of a continuum is inappropriate over lengthscales comparable to or smaller than d. If a simulation has a large variation in particle diameters d_i, it may be necessary to use a different coarse-graining range for each particle. For example, (9.2) may need to be replaced by

$$\rho(\boldsymbol{x}, t) = \sum_i m_i W(|\boldsymbol{x} - \boldsymbol{x}_i|/d_i), \tag{9.5}$$

so that a larger particle influences a larger region around it. We neglect this correction for the nominally monodisperse flows of the present work.

9.1.2. The position of the free surface

The free surface $z = s(x, t)$ plays an important role in continuum models, but is not fundamentally defined in a DPM (§8.6). There is some arbitrariness in the definition of the free surface position, which cannot be placed more precisely than over an $O(d)$ lengthscale. Also, the continuum boundary conditions (§§4.1, 4.2.1) cannot be satisfied exactly, whatever definition one uses for the free surface position $s(x, t)$. This is because the velocity fields u and w are ill-defined near this free surface, given that ρ in the denominator of (9.3) is close to zero.

One definition of the free surface position is to take $s(x, t)$ as a high percentile, say the 99th percentile, of the z-positions of particles near that position in x. An alternative definition is to take s as the value of z at which the value of the packing fraction ϕ drops below a certain threshold, say 0.2. Since the latter definition calculates s from the coarse-grained field ϕ, it is guaranteed to be smooth. However, the first definition more directly matches the measurement that would be reported by an experimental apparatus (§2.3), and also avoids the costly process of evaluating the coarse-grained field ϕ. We therefore resort to the first definition. In practice, the difference between the two definitions is within the particle diameter; likewise, s was found to be insensitive to the percentile or threshold taken. Under either definition, there may be particles that appear to be above the free surface position.

9.2. Calibration tests

Having established the definitions of continuum fields from discrete particle data, the rest of this chapter focuses on determining the effects of different contact model parameters on the rheological properties of a flow. In particular, this requires determining the function $\mu(I)$.

The simulation procedure for finding $\mu(I)$ is very similar to the experimental procedure described in §2.3. A flow is initiated and allowed to settle until it reaches a steady uniform state. The flow depth and flow rate are then measured, and from these the inertial number may be calculated

[3] Since particles have some size dispersity (10% in the present work), one could alternatively use a larger coarse-graining range for larger particles.

e	Jop fit (2.16)			power-law fit (2.17)			cutoff/°
	$\arctan\mu_1/^\circ$	$\arctan\mu_2/^\circ$	I_0	$\arctan\mu_s/^\circ$	m	α	
0.01	9.6	44.7	0.93	5.5	0.49	0.48	35
0.1	9.4	43.4	0.95	5.0	0.47	0.46	34
0.25	8.9	39.1	0.79	4.3	0.44	0.43	31
0.5	8.1	31.1	0.49	2.5	0.41	0.35	25
0.9	7.4	15.5	0.11	5.8	0.24	0.40	12

Table 9.1.: Fitting parameters for the function $\mu(I)$ for the data shown in figure 9.4, along with the maximum angle for which steady flow was attained.

using the experimental formula

$$I = \frac{5dq}{2(gh^5\cos\theta)^{1/2}}. \tag{2.15}$$

As in §2.3, this test is conducted at a range of slope angles θ.

An important difference from the experimental procedure is that calibration tests in DPM are conducted on periodic domains, not on finite-length domains (§8.1). Therefore, if $\tan\theta$ is greater than the range of μ, the flow is remains statistically uniform, but would not settle to a steady state; it would instead accelerate indefinitely.

From these tests, we also obtain information about the packing fraction ϕ, which we plot against I, using the assumption that ϕ may be a function of I (§3.1). This allows us to estimate the compressibility of a flow. Additionally, we calculate the shape factor χ of the steady flow that develops, which allows us to judge whether the developed flow is indeed Bagnoldian, with $\chi = 5/4$; a higher value of χ would indicate that the velocity profile is affected by nonlocal effects (§3.3).

9.3. The effects of the coefficient of restitution

In figure 9.1, we present results from our own DPM simulations of particles with varying values of the coefficient of friction. In each case, the particle size ratio is $\delta = d/\mathcal{H} = 1/50$, and the basal roughness parameter is $\beta = 1$. There is no intrinsic friction between particles.

Our results show the same qualitative behaviour as those of figure 8 in da Cruz et al. (2005), which were produced from a shear cell test rather than a chute flow. Our results also verify the finding of Rajchenbach (2005) that the coefficient of restitution has no effect on $h_{\text{stop}}(\theta)$, or equivalently, on the dynamic angle of repose: we see that $\mu(0)$ is approximately similar between the different cases. Rajchenbach (2005) further reported that 'the rheological behaviour is found to be *insensitive* to the value of the restitution coefficient', arguing that the number of contacts between grains in a dense state is so high that energy is dissipated very quickly, regardless of how dissipative each individual contact may be. However, the results in figure 9.1(a) indicate that this is not the case at higher slopes or higher inertial numbers. Rather, for the more elastic collisions, the upper bound for the slope θ at which a steady flow no longer becomes possible is lower. (Notably, for $e = 0.9$ the range of angles for which a steady flow is possible is only about 3°.)

We understand this discrepancy to arise from the fact that, at higher slopes, the particles become

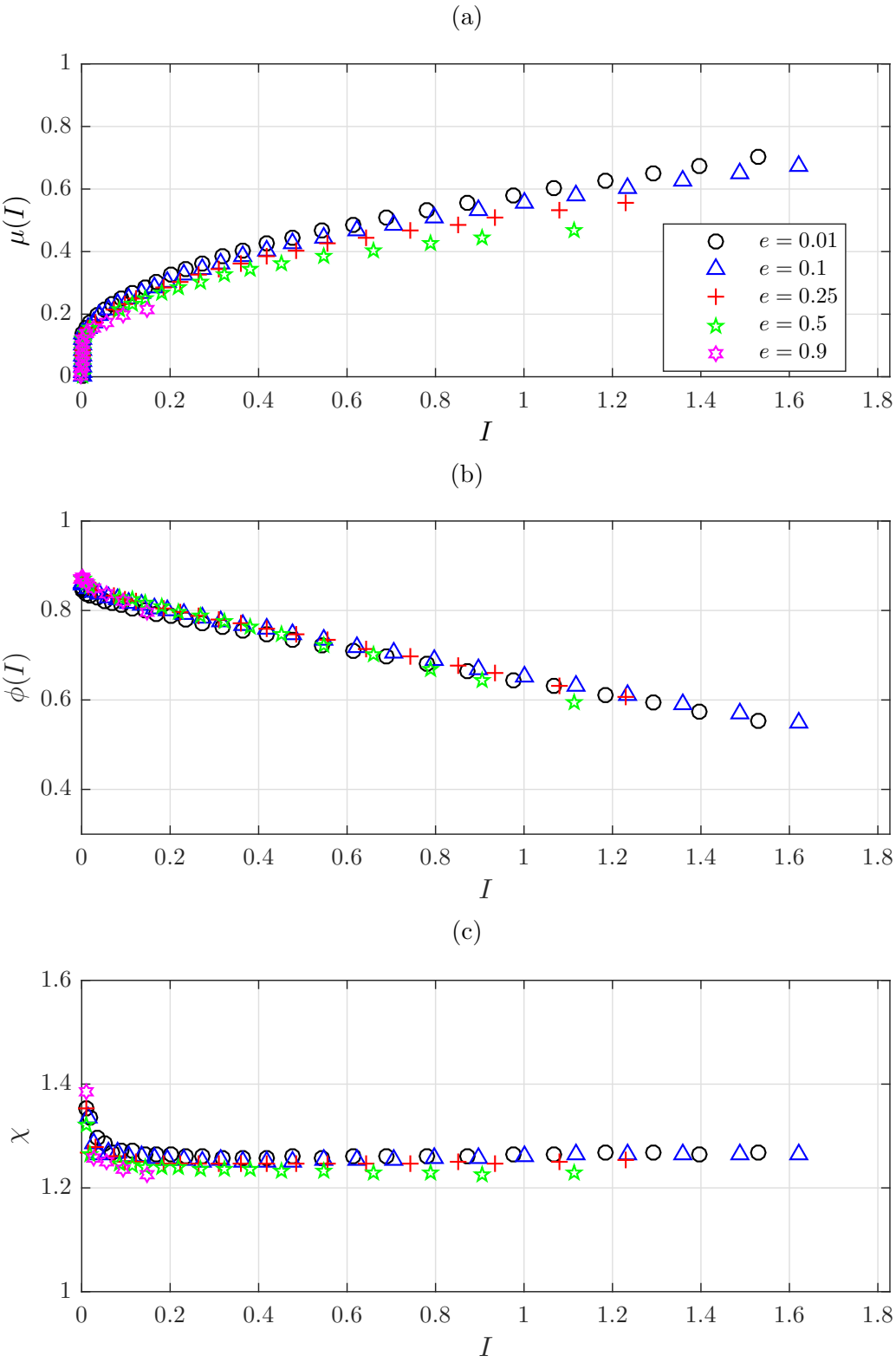

Figure 9.1.: Results from periodic chute flow calibration tests for different values of the coefficient of restitution e, showing (a) the bulk friction coefficient $\mu = \tan\theta$, (b) the packing fraction ϕ, and (c) the shape factor of the flow, all plotted against I, calculated by the experimental formula (2.15).

δ	Jop fit (2.16)			power-law fit (2.17)			cutoff/°
	$\arctan\mu_1/°$	$\arctan\mu_2/°$	I_0	$\arctan\mu_s/°$	m	α	
1/10	15.0	38.4	0.73	3.7	0.51	0.28	32
1/20	11.1	39.7	0.73	2.0	0.52	0.28	32
1/30	10.2	41.2	0.82	3.5	0.50	0.38	33
1/40	9.4	41.4	0.81	4.9	0.47	0.44	33
1/50	9.4	43.4	0.96	5.1	0.47	0.46	34
1/60	9.3	44.2	1.03	5.1	0.47	0.48	34

Table 9.2.: Fitting parameters for the function $\mu(I)$ for the data shown in figure 9.4, along with the maximum angle for which steady flow was attained.

increasingly dissociated, as evident from the packing fraction in panel (b). The particles enter into a collisional regime (§3.2), governed by binary interactions. The rate of energy dissipation is then dependent on the elasticity between individual collisions. On the other hand, the data in panel (a) agree with each other well at lower values of I. The agreement at low inertial numbers supports the claim of Rajchenbach (2005) that, when particles are densely packed and in multiple sustained contacts with each other, the rheology of the material is influenced by the geometry and particles and their base, as well as the frictional force between particles, rather than the dynamics of normal interactions.

9.4. The effects of particle size

Now we consider the effect of particle size on the rheological behaviour of the bulk flow. Figure 9.2 shows the function $\mu(I)$ in panel (a), together with the behaviour of the packing fraction $\phi(I)$ (panel (b)) and the shape factor $\chi(I)$ (panel (c)). The particles in each simulation are frictionless and have fixed coefficient of restitution $e = 0.1$, and the relative basal roughness coefficient in each case is $\beta = 1$, meaning that the frozen particles that constitute the rough base have the same diameter as the flowing particles.

In figure 9.2(a), we see that the function $\mu(I)$ has little dependence on δ: the data from the samples $\delta \leq 1/20$ collapse onto the same curve. For $\delta \leq 1/20$, the fact that the curves $\mu(I)$ agree indicates that the particle size therefore affects the flow rate only through the factor of $1/d$ that appears in (2.15) and (2.13).

The results for $\delta = 1/10$ do not collapse very well onto the same curve as the others. The difference between the $\delta = 1/10$ case and all the others is most pronounced for small values of I; this is not surprising, as we shall note below. More curious, however, is that the behaviour at higher slopes θ and therefore higher I appears to have little dependence on δ. The maximum value of θ for which a steady flow is possible is approximately the same for each sample.

Figure 9.2(b) shows that smaller particles tend to have a marginally higher packing fraction ϕ, with the difference being most profound at larger inertial numbers. This is likely to be a geometrical effect due to the confinement to a periodic domain of finite length; we expect that the difference in ϕ would be less pronounced in a longer domain. At high I and lower ϕ, the flow may be entering into a collisional regime (§3.2).

Investigating the shape factor χ of the chute flow, shown in figure 9.2(c), makes it very clear

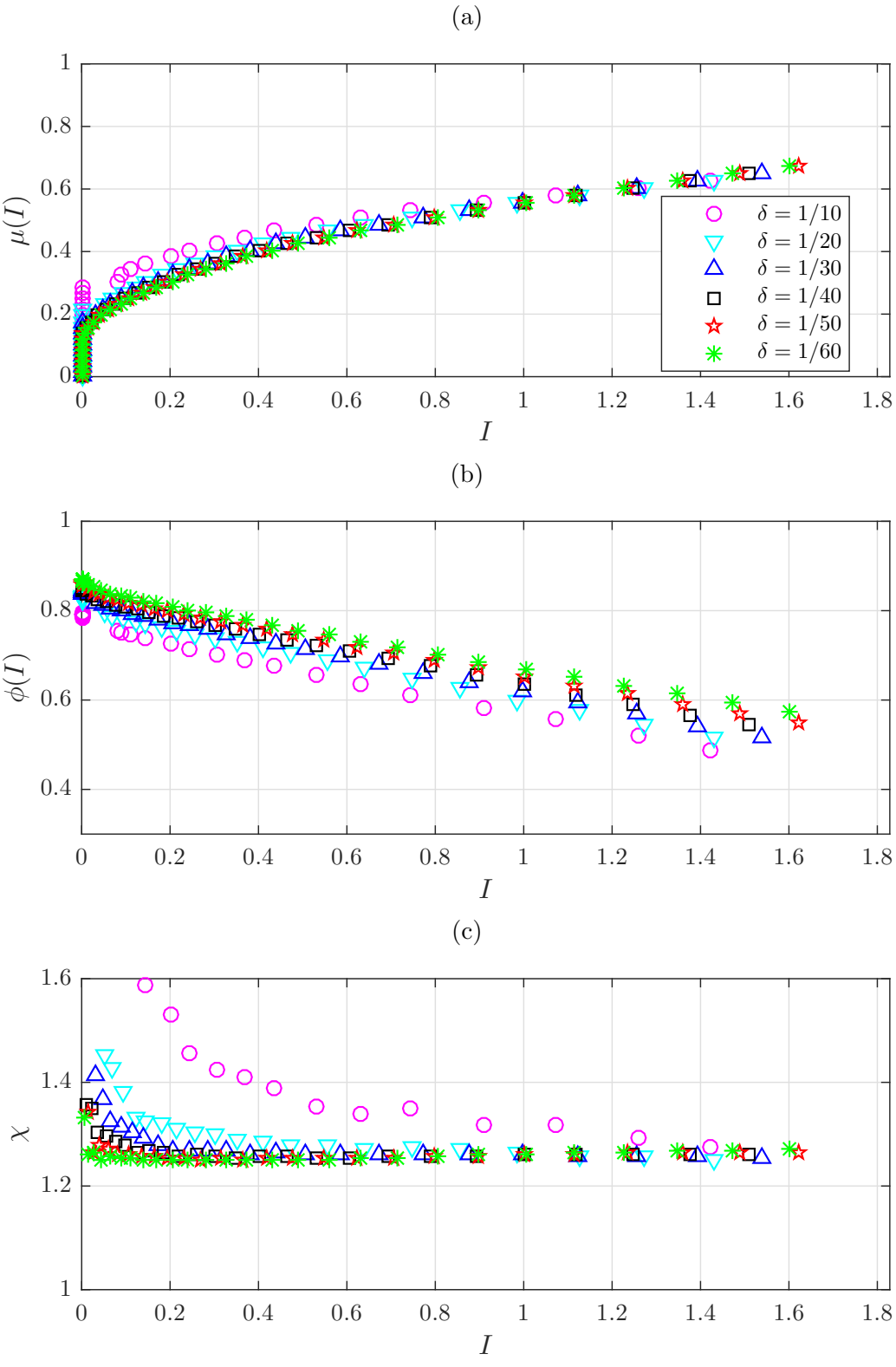

Figure 9.2.: Results from periodic chute flow calibration tests for different particle sizes $\delta = d/\mathcal{H}$, showing (a) the bulk friction coefficient $\mu = \tan\theta$, (b) the packing fraction ϕ, and (c) the shape factor of the flow, all plotted against I, calculated by the experimental formula (2.15).

β	Jop fit (2.16)			power-law fit (2.17)			cutoff/°
	$\arctan \mu_1$/°	$\arctan \mu_2$/°	I_0	$\arctan \mu_s$/°	m	α	
1/2	8.5	30.7	0.45	7.6	0.43	0.65	17
1	9.4	43.4	0.96	5.1	0.47	0.46	34
2	n/a	n/a	n/a	n/a	n/a	n/a	n/a

Table 9.3.: Fitting parameters for the function $\mu(I)$ for the data shown in figure 9.4, along with the maximum angle for which steady flow was attained. The fitting parameters were not obtained for $\beta = 2$ (see text).

that the most notable effect of particle size is at low inertial numbers. For small θ, the depth of this flow is only just larger than $h_{\text{stop}}(\theta)$; in other words, the gravitational acceleration is only just above the yield stress. It is known that nonlocal effects, which we discussed in §3.3, are dominant at low inertial numbers (Kamrin and Henann 2015), and that nonlocal effects produce velocity profiles that have higher values of χ, as shown in figure 3.1. At higher I, the shape factors converge towards the Bagnoldian value 5/4, as nonlocal effects become less important.

9.5. The effects of basal roughness

The previous section showed that the ratio $\delta = d/\mathcal{H}$ has little effect on the bulk behaviour $\mu(I)$. In other words, when the particle diameter is reduced relative to a fixed depth, the Bagnold velocity (2.13) increases as $1/d$, but the increased shear rate which balances against the factor of d that appears in the inertial number (2.6), so that the inertial number remains the same. In the previous section, however, we took the size b of the basal particles to be equal to d, so that the ratio $\beta = b/d = 1$. We now study the effects of varying β, with $\delta = 1/50$ fixed; the coefficient of restitution is $e = 0.1$ and there is no intrinsic friction.

Figure 9.3 and table 9.3 present data from calibration tests for $\beta = 1/2$, $\beta = 1$ and $\beta = 2$. The $\beta = 1$ case behaves very similarly to previously observed results (subject to noise). While all three curves have similar values of $\mu(0)$, the range of slopes for which a sustained is possible varies dramatically: for $\beta = 1/2$, the range is less than half of that of $\beta = 1$. As for $\beta = 2$, steady flows were observed up to $\theta = 45°$, the maximum value of θ for which we conducted these calibration tests.[4] As such, we could not meaningfully apply fits to these data. It is also notable that, for $\beta = 2$, the shape factor approximates 5/4 but does not decrease monotonically with I, unlike all of the other examples presented in this chapter.

Although the data in figure 9.3 appear to converge towards a steady state as $t \to \infty$, so that the flow for $\beta = 2$ is indeed steady, it is notable that, in the case $\beta = 2$, at high inertial numbers the packing fraction ϕ is very low. This, together with the unexpected behaviour for χ, suggest that the flow may have entered into a kinetic regime without causing any discernible discontinuity in the function μ. Contrasting between $\beta = 1/2$ and $\beta = 1$, it is reasonable that, with less basal bumpiness, a current may more easily develop into an unsteady acceleration.

Where they are defined, all three curves agree well with each other, suggesting (as in §§9.3) 9.4 that β controls whether a material attains a steady dense state, but has only a weak influence on a flow that is already in that state.

[4] Coefficients of friction exceeding 1 are not uncommon (Engineering Toolbox 2004).

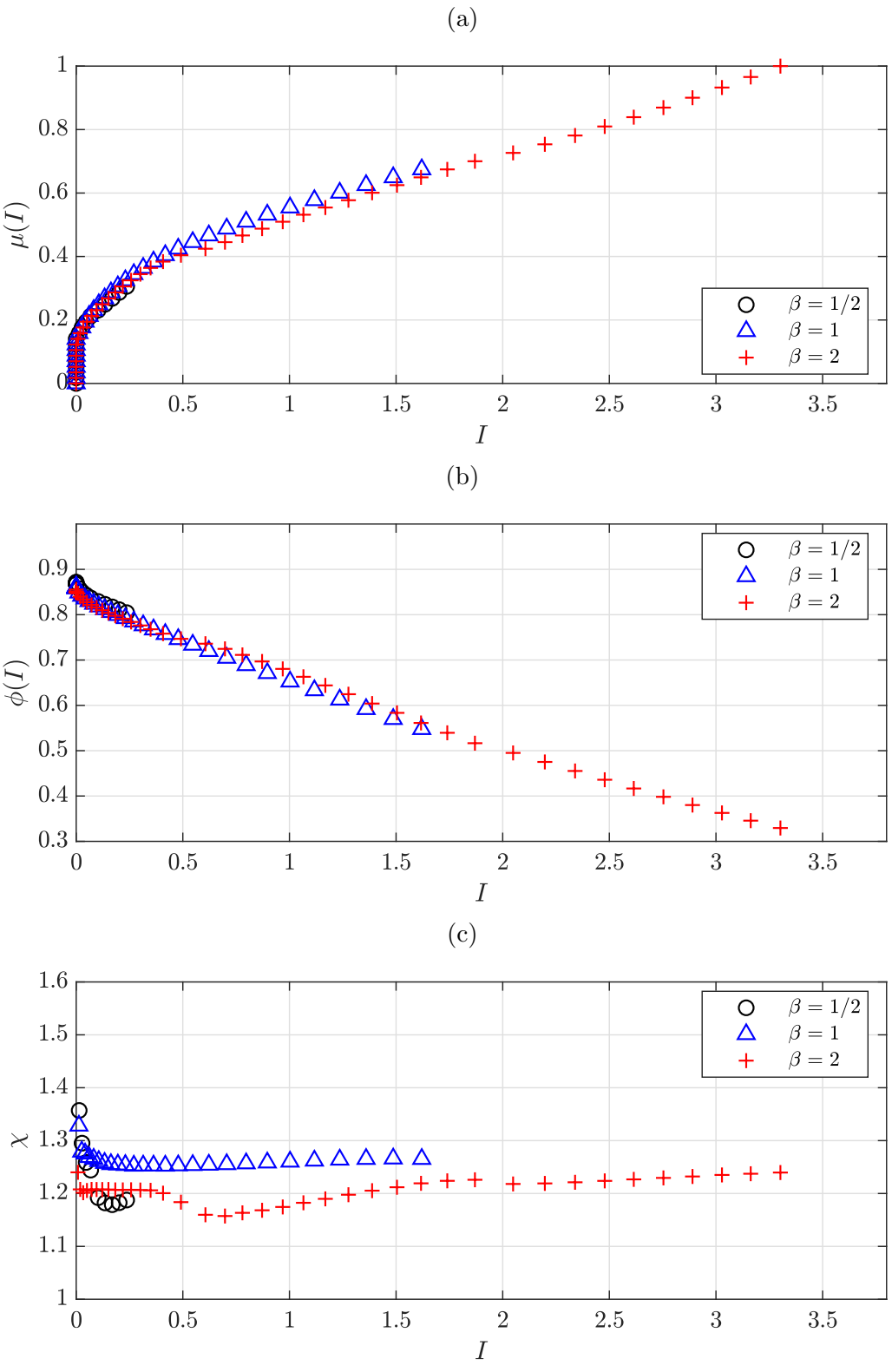

Figure 9.3.: Results from periodic chute flow calibration tests for different values of the basal roughness β. These plots show (a) the bulk friction coefficient $\mu = \tan\theta$, (b) the packing fraction ϕ, and (c) the shape factor of the flow, all plotted against I, calculated by the experimental formula (2.15).

$\arctan\mu_{\mathrm{sl}}/^\circ$	Jop fit (2.16)			power-law fit (2.17)			cutoff/$^\circ$
	$\arctan\mu_1/^\circ$	$\arctan\mu_2/^\circ$	I_0	$\arctan\mu_s/^\circ$	m	α	
0	9.4	43.4	0.96	5.2	0.47	0.47	34
5	11.8	44.1	0.81	6.5	0.52	0.44	34
10	12.7	44.4	0.71	5.9	0.57	0.42	34
20	13.5	44.1	0.60	9.5	0.56	0.49	33

Table 9.4.: Fitting parameters for the function $\mu(I)$ for the data shown in figure 9.4, along with the maximum angle for which steady flow was attained.

Some care should be taken in interpreting these results about β when comparing against experimental data. A series of experiments using different types of grains would have different values for d and therefore of δ between the experiments, but if the experiments all use the same chute lined with the same bumpiness, then b remains the same between experiments, so that $\beta = b/d$ is not kept constant.

9.6. The effects of intrinsic friction

In each of the preceding sections, inter-particle contacts have had zero intrinsic friction. In this section, we study the response of the function $\mu(I)$ to an intrinsic sliding friction (§7.4.1), with zero rolling friction. Figure 9.4 shows the behaviours of μ, ϕ and χ for three different species, with $\mu_{\mathrm{sl}} = \tan 0^\circ, \tan 10^\circ$ and $\tan 20^\circ$. In each case, the nondimensionalised particle size and basal roughness are $\delta = 1/50$ and $\beta = 1$, and the coefficient of restitution is $e = 0.1$. The fitting parameters to the functional forms (2.16) and (2.17) for $\mu(I)$ are given in table 9.4.

The most obvious effect of μ_{sl} is seen in panel (a), where the curve $\mu(I)$ clearly shifts upwards when μ_s is increased. There is a great difference between the curves for $\mu_{\mathrm{sl}} = \tan 0^\circ$ and $\mu_{\mathrm{sl}} = \tan 10^\circ$, while the curves for $\mu_{\mathrm{sl}} = \tan 10^\circ$ and $\mu_{\mathrm{sl}} = \tan 20^\circ$ are relatively similar. Notably, the value of $\mu(0)$ (and correspondingly the dynamic angle of repose $\arctan\mu(0)$) is much higher in the presence of intrinsic friction than in the case $\mu_{\mathrm{sl}} = \tan 0^\circ$.

We also observe that in panel (a), all three curves cut off at approximately the same value of μ, or equivalently, of θ. In other words, the angle beyond which a steady uniform chute flow fails to develop appears to be independent of intrinsic friction. This is reasonable, because at high inertial numbers the flow is beginning to transition into the kinetic regime; there are fewer sustained inter-particle contacts and so the tractional dissipation between them becomes less important.

Panels (b) and (c) in figure 9.4 suggest that the packing fraction and shape factor are mostly independent of μ_{sl}. In panel (b), the packing fraction has a small inverse relationship with μ_s; we hypothesise that this is because intrinsic friction allows particles to pile higher, leaving gaps between them. The similarity between the three cases in panel (c) suggests that intrinsic friction has very little effect on the velocity profile; provided that $I \geq 0.2$, the shape factor $\chi \approx 5/4$, as expected for a Bagnold profile. From this, we infer that intrinsic friction does not influence the magnitude of nonlocal effects, except through increasing the minimum threshold for θ before flow occur. Friction helps to sustain the structure of a static material, but once the material begins to flow, friction may help to increase the contact time between particles,

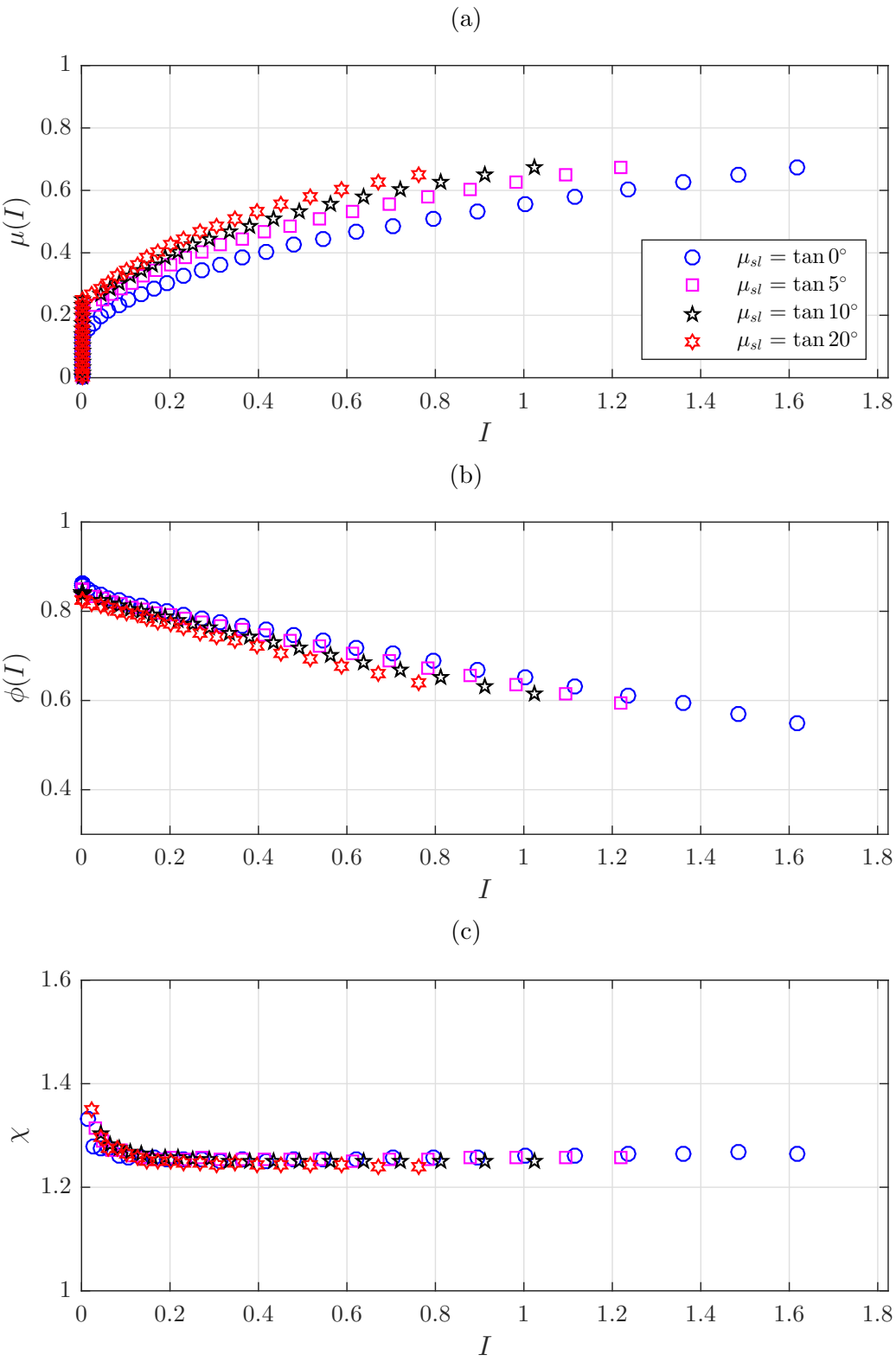

Figure 9.4.: Results from periodic chute flow calibration tests for different values of the intrinsic coefficient of sliding friction, with no rolling friction. These plots show (a) the bulk friction coefficient $\mu = \tan\theta$, (b) the packing fraction ϕ, and (c) the shape factor of the flow, all plotted against I, calculated by the experimental formula (2.15).

but does not affect the length of force chains. This is in contrast to the geometric effects of the particle size.

9.7. Summary and closing remarks

In this chapter, we have performed calibration tests to explore the response the bulk friction properties of a particle species to different values of the coefficient of restitution e (§9.3), the relative particle size $\delta = d/\mathcal{H}$ (§9.4), the relative basal roughness $\beta = b/d$ (§9.5) and the intrinsic friction μ_s between particles (§9.6). The calibration procedure is analogous to those of lab experiments (§2.3).

We found that for frictionless particles, neither e nor δ had much effect on the function $\mu(I)$, provided that the particles were in a dense flow regime of intermediate inertial numbers and that $\delta \leq 1/20$ so that the continuum assumption and the local rheology are applicable. However, these parameters have important effects at very high or very low inertial numbers, or equivalently, at more extreme values of θ: they determine whether particles do in fact settle into a steady dense flow regime. For example, with a high coefficient of restitution, the packing fraction ϕ is low even at moderate values of θ, as particles bounce off each other almost elastically and little energy is dissipated in each contact, so that the flow is in fact in a kinetic regime rather than a dense flow regime. This is in accordance with simulations by Reddy and Kumaran (2007) and Reddy and Kumaran (2010), who investigated systems of nearly elastic particles ($e = 0.9$) and showed that such particles form a 'gaseous' state characterised by binary interactions and governed by kinetic theory (§3.2).[5] However, at lower values of e, the assumption of binary interactions becomes unjustified as particles collapse together[6]; the particles instead form a dense flow.

The main effect of the particle size δ is at low inertial numbers, where a larger value of δ increases the threshold slope θ before any flow becomes possible. The effect of δ is most pronounced for $\delta \gtrsim 1/10$ but is negligible for $\delta \leq 1/20$. This is consistent with the result that a granular current's stopping depth h_{stop} is proportional to the grain size, and the notion that the local rheology applies only in the small grain limit (§3.3).

We conclude therefore that the rheological behaviour of a dense flow is largely governed by the intrinsic friction between particles, and partially by the basal geometry β, but does not depend strongly on the properties of the normal interaction such as e, or from the geometric effects of δ. However, the parameters of e and δ are responsible for determining whether a flow is in fact in the dense regime (in which there are many particle-to-particle contacts), or in a stopped or kinetic regime. The result that parameters such as e, δ and β have only a weak effect on a flow except to determine its phase is a useful one. Provided that the correct qualitative behaviours (in particular, the dense flow regime and the correct basal condition) are attained, it is not necessary to choose particularly precise values for these parameters. This means that there is some freedom in choosing our contact models: we use this freedom to improve the computational efficiency of simulations by using the techniques described in §7.5.

[5] Kinetic theoretical models take the limit $1 - e^2 \ll 1$. However, Jenkins and Berzi (2012) consider values of e as low as 0.6, so that $1 - e^2 = 0.64$, to be acceptable.

[6] 'For a fluid of elastic particles, it is well known that the kinetic theory calculations are valid only in the dilute limit, and they become invalid at higher densities due to the effect of correlations' (Reddy and Kumaran 2010).

(a)

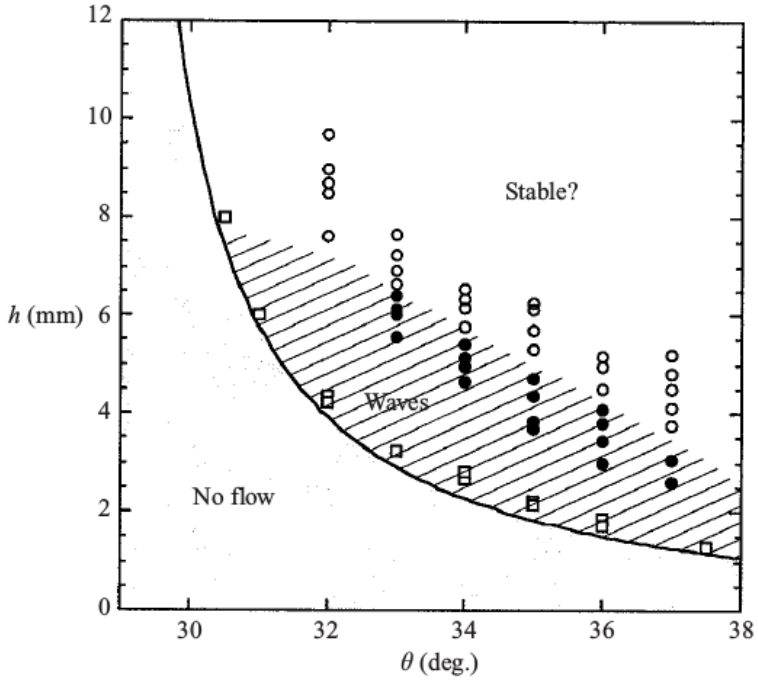

(b)

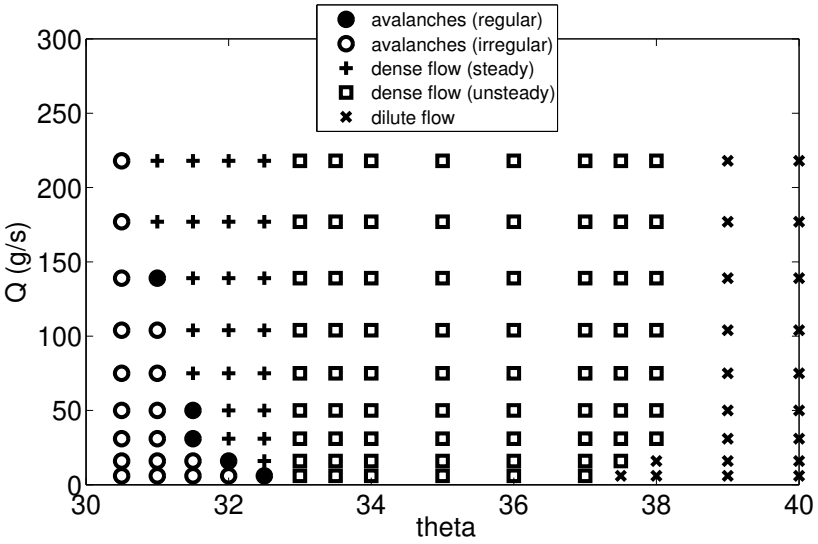

Figure 9.5.: (a) Experimental results on chute flows of sand by Forterre and Pouliquen (2003, figure 2), showing that the minimum threshold for flow depends both on the flow depth h and the slope angle θ. (b) Experimental results by Takagi et al. (2011, figure 2), which also show a minimum threshold for flow, and furthermore the transition from dense to dilute flow at large θ. In (b), the vertical axis shows the flow rate Q, which cannot be directly related to the depth h since the experiments of Takagi et al. (2011) have variable width.

As expected, for each species there is a range of inclinations θ between which a steady dense flow is able to develop; this observation is well-documented experimentally (GDR MiDi 2004, Forterre and Pouliquen 2003, Takagi et al. 2011). Flow does not occur if h is below a certain threshold $h_{\mathrm{stop}}(\theta)$, which depends inversely on θ. This was demonstrated in §9.4 (in terms of the inverse depth $\delta = d/h$), and was also observed by Forterre and Pouliquen (2003), whose results are reproduced here in figure 9.5(a). From figure 9.2(a), we see that the value of $\mu(0)$ decreases with decreasing δ, with an apparent convergence towards a nonzero value as $\delta \to 0$. Figure 9.2(b) shows, unsurprisingly, that smaller particles can be packed more densely into a rectangular domain of a given size. The most dramatic effect of δ is on the measured shape factor, plotted in figure 9.2(c). For larger particles, the shape factor is much larger than the Bagnoldian value 5/4, indicating a severe departure from the Bagnold velocity profile: the larger particle size causes nonlocal effects (§3.3) to become important, invalidating the $\mu(I)$ rheology. Although all species show some deviation from $\chi = 5/4$ at small inertial numbers, for θ just above $\arctan \mu(0)$, the results in figure 9.2(c) are surprising because they show that χ is much larger than 5/4 even for moderate values of I. Intrinsic friction between particles, if present, also increases the threshold (§9.6).

At large θ, we observed a transition away from the dense flow regime and into an unsteady or dilute flow regime; this transition was also observed by Takagi et al. (2011), whose results are shown here in figure 9.5(b).[7] Their results suggest that, for their material ('non-spherical sand grains'), the maximum angle for which steady flow is possible is about 32°; this is consistent with most of our results except at high coefficients of restitution — it is notable that this result from a 3D experiment should be paralleled by DPM simulations in 2D. Takagi et al. (2011) also report that '[a]ll experiments conducted using glass beads resulted in unsteady flow', and 'speculate that shallow flows of glass beads are unstable because they are subcritical, meaning that disturbances move faster than the beads on the surface and hence can propagate upstream'. In light of the present work, we propose instead that the unsteadiness results from flow dissociation that occurs because of a difference in the effective coefficient of restitution e between sand grains and glass beads, the latter having a much higher value of e.[8] Flow dissociation and the entry into a kinetic regime would also be consistent with their observation that the surface velocity of a flow of glass beads fluctuates dramatically.

We noted in Chapter 2 that although experimental data on the function μ from calibration tests (§2.3) can be fitted to the form

$$\mu(I) = \mu_1 + \frac{\mu_2 - \mu_1}{I_0/I + 1}, \tag{2.16}$$

this form should be regarded only as an interpolation for the experimental data for which a steady uniform flow does develop; it has 'not been tested for large values of the inertial number I' (Forterre and Pouliquen 2008), and experimental data (*e.g.* of Pouliquen et al. (2006, figure 1)) and the results of simulations (in the present chapter) do not necessarily support it. In

[7] Note, however, that the experiments of Takagi et al. (2011) cannot be directly compared either to our simulations or to the experiments of Forterre and Pouliquen (2003). The flows of Takagi et al. (2011) are three-dimensional; thus, when they vary the flow rate q, it is the *width* of their flows, not the depth, that varies. In contrast, in our simulations and the experiments of Forterre and Pouliquen (2003), the flow takes place in a channel of fixed width. The vertical axis in figure 9.5(b), showing flow rate q, therefore cannot be related to the flow depth h, which is plotted on the vertical axis of 9.5(a).

[8] Sand and glass may be chemically similar, and therefore have similar intrinsic material properties, but the angularity of sand grains and their larger size dispersity allows them to be packed more tightly. This increases the number of contacts between particles, and therefore the rate of dissipation per unit volume, accounting for the difference in their coefficients of restitution.

particular, although the parameter $\theta_2 = \arctan \mu_2$ is usually interpreted as the maximum slope angle at which a steady uniform flow can develop, we contend that the failure to develop a steady uniform flow arises from a phase transition; θ_2 (or equivalently μ_2) should be interpreted only as a fitting constant, not as the actual maximum value of θ for which steady flow ceases to be possible. Indeed, it is also evident (from tables 9.1–9.4) that the fitted values of θ_2 are much higher than the cutoff angle for a dense flow, and from the figures that the curve of $\mu(I)$ appears to be rising at the cutoff angle, rather than approaching an asymptote.

A useful feature of discrete particle models is that we may vary the individual microscopic parameters independently to understand their effects on the bulk rheological behaviour, as we have done in this chapter. It is important to remember that the same is difficult to achieve in experiments on real grains: one usually has to vary multiple parameters at the same time. In order not to cloud the results of the DPM simulations by exploring an excessive number of parameters, we opted to investigate only the microscopic parameters e, δ, β and μ_s, and the macroscopic outputs μ, ϕ and χ. A true granular flow has many more parameters besides these. Microscopic parameters that we have not explored include the size dispersity (which we fixed at 10%), the coefficient of rolling friction (which we set to 0), and the structure of a rough base (which we took to be that of figure 8.6). DPM in three dimensions have additional parameters, such as the coefficient of torsional friction (§7.4). Macroscopically, we have used μ, ϕ and χ to describe the properties of particles in simple chute flows. The behaviour of μ is enough to fully close the $\mu(I)$ rheology; the function ϕ allows a description of the compressible 'coupled-ϕ rheology (§3.1); while χ gives a partial reflection of nonlocal effects on a current and therefore the deviation from the $\mu(I)$ rheology (§3.3).

For example, the value of χ measured from simulation results describes the velocity profile; at low inertial numbers, χ exceeds the Bagnoldian value 5/4 as the value of $\delta = d/\mathcal{H}$ is increased, reflecting the distortion of velocity profiles by increasingly important nonlocal effects (§9.4). However, the simple chute flow test overlooks other effects of nonlocality, such as the stopping height $h_{\text{stop}}(\theta)$, the depth threshold below which a current does not flow (Pouliquen 1999, Jop 2015); or the onset of the jamming transition for flows in confined spaces (as opposed to the present thesis' free surface flows), such as shear cells or hoppers (Kamrin and Henann 2015, Cates et al. 1998, To et al. 2001). We also noted that at steep angles θ, a steady uniform flow can fail to develop, owing to the dissociation of a flow at high I and the phase transition towards a kinetic regime.

An extension of the present chapter would calculate the rheological behaviour of particle species beyond their manifestation through the quantities μ, ϕ and χ, especially the behaviours at very low and very high values of I near the phase transitions. It is expected that the phase diagram should qualitatively resemble the results of Forterre and Pouliquen (2003) and Takagi et al. (2011), shown here in figure 9.5.

Extending the tests of this chapter to study the relationships between the numerous microscopic and macroscopic properties is an important aspect of discrete particle modelling. The eventual, if ambitious, goal of a comprehensive survey of the relationship between microscopic and macroscopic properties of particles in DPM should be to construct a 'library' of particle species, so that, given some macroscopic properties of a real species of grains, one could find appropriate values for microscopic parameters for a DPM that reproduce these macroscopic properties.[9]

[9]Such a programme was proposed by Andrew Bayly at the September 2017 meeting of the Special Interest Group on 'Granular flows in the environment and industry'.

The present non-existence of such a library is likely due to the heavy computational cost that its construction would involve, although with suitable collaboration this would be possible.

When designing such a library, its scope must be defined and restricted. For example, relaxing the assumption that particles be circular, or working in three dimensions instead of two, would allow the creation of particle species with a wider range of rheological properties, but also introduces a number of additional fitting parameters. Computational limitations must also be taken into account: the contact detection problem between non-circular particles is much more difficult than that between circular particles. Therefore, an important first step should be to identify the microscopic and macroscopic parameters of interest.

Part III.

Applications

Having developed the methods for modelling granular flows, we now apply them to particular examples of granular chute flows interacting with topography. As noted in Chapter 1, we use the term 'topography' to refer to any inhomogeneity in the flow in general, not just a spatial or geometric effect.

We shall devote the majority of our attention to the setup sketched in figure 1.4(a), in which a current flows over a chute whose base is smooth upstream and rough downstream, so that the current experiences an increase in the resistance that it faces. As such, this setup may be viewed as a prototypical example of topography acting adversely against a current. We study this problem using three different continuum models. In Chapter 10, we further develop the depth-averaged models described in Chapter 5, and use these to make predictions about the evolution of the current. In Chapter 11 we propose an adaptation of the $\mu(I)$ rheology (Chapter 2), which we then apply to this problem. We show that the adapted model makes predictions about the internal velocity profile that match closely the results from DPM simulations. Finally, in Chapter 12, we consider the effects of time-dependence in the $\mu(I)$ rheology, and discuss whether the present spatially-dependent problem may be treated instead as a time-dependent problem.

Throughout, an important quantity for describing a current is its Froude number,

$$\mathrm{Fr} = \frac{\mathcal{U}}{(g\mathcal{H})^{1/2}}, \tag{9.6}$$

where $\mathcal{U}$ is a typical velocity scale and $\mathcal{H}$ is a characteristic depth of a current. The Froude number can be interpreted as the ratio between the inertia of a current, and the acceleration due to gravity; alternatively, Fr^2 could be interpreted as the ratio between kinetic and potential energy. When $\mathrm{Fr} < 1$, $\mathrm{Fr} = 1$, or $\mathrm{Fr} > 1$, we say that the flow is subcritical, critical, or supercritical, respectively.

We shall often work in the limit of high Froude number: this limit is relevant for modelling snow avalanches (Hákonardóttir 2004, Hogg and Jóhannesson 2016). Granular flows at high Froude numbers have proven difficult to implement in laboratory experiments, since it is necessary to have a large material at hand in order to maintain a fast steady flow (the mechanism described in Holyoake (2011) and Holyoake and McElwaine (2012) being a notable example of an experimental setup that can achieve $\mathrm{Fr} \approx 25$, albeit with a relatively shallow current). DPM simulations also face difficulties at high Froude numbers, because such flows contain high-speed collisions that must be resolved using a very low collision time and therefore a small time step.

As well as the setup of figure 1.4(a), the machinery developed in this part of the thesis could also be applied to other examples of spatial or temporal topography. For example, we consider also the kinked chute shown in figure 1.4(b), and describe how the depth-averaged model could be applied to such a setup, as well as an analogous time-dependent flow in which the magnitude or direction of gravity changes abruptly.

10. Depth-averaged modelling of topographical effects

Our eventual aim in this chapter shall be to apply the depth-averaged model (5.4) to examples of steady flows over topographical features, including the setups shown in figure 1.4. Before this is possible, we need to establish some properties of (5.4) in the steady case. Of importance is the observation that, over long distances and far from boundaries or transitions, a flow tends to adjust towards the Bagnold equilibrium state (§10.1.3): this establishes the fact that, sufficiently far away from topographical features and from the ends of a chute, a flow has no 'memory' of its interactions with distant features. We shall also need to introduce the boundary conditions on (5.4) that govern a steady flow.

We begin by deleting the $\partial/\partial t$ terms from (5.4). Since the flow is then steady, by (5.4a) the flow rate $q = h\overline{u}$ is conserved along the flow, where h is the depth of the current and $\overline{u}$ is the depth-averaged velocity. Next, (5.4b) becomes a second-order *ordinary* differential equation, which may be written as a pair of first-order equations. By defining

$$\frac{\mathrm{d}h}{\mathrm{d}x} = k, \tag{10.1a}$$

we obtain

$$\frac{\mathrm{d}k}{\mathrm{d}x} = \frac{\mathrm{d}^2h}{\mathrm{d}x^2} = \frac{k^2}{2h} + \frac{g\cos\theta}{q\nu}\left(\tan\theta - M(h;q) - b'(x)\right)h^{3/2} + \frac{1}{q\nu}\left(\frac{\chi q^2}{h^2} - gh\cos\theta\right)h^{1/2}k, \tag{10.1b}$$

where we define $M(h;q) = \overline{\mu}(h, q/h)$ as the depth-averaged coefficient of friction, expressed as a function of h and q rather than h and $\overline{u}$. The system (10.1) governs the evolution of the depth $h(x)$. We treat the flow rate q, which is fixed along the current, as an external parameter (determined by inflow conditions) rather than a dynamical quantity. Note that $M(h;q)$ is monotonically decreasing in h; therefore, if $\tan\theta$ is in the range of $M(h;q)$ then the inverse $M^{-1}(\tan\theta;q)$ exists and is unique. Note also that the (total) derivative

$$M'(h;q) = \frac{\mathrm{d}M}{\mathrm{d}h} = \left(\frac{\partial\overline{\mu}}{\partial h}\right)_{\overline{u}} - \frac{q}{h^2}\left(\frac{\partial\overline{\mu}}{\partial\overline{u}}\right)_h$$

is distinct from the partial derivative $(\partial\overline{\mu}/\partial h)_{\overline{u}}$.

10.1. Homogeneous chutes of finite length

10.1.1. Phase-portrait analysis

The system (10.1) contains the terms $\overline{\mu}(h, q/h)$ (or $M(h;q)$), ν and χ, which are externally specified and are usually taken as constants along a chute (Gray and Edwards 2014). When

(streamwise) topographical features are present, we propose that M, ν and χ could be allowed to depend on x. In particular, if the basal roughness is varying, then M should be interpreted as a characterisation of the friction on the current by the 'local' roughness.

However, before we introduce any such topography, we first consider the case of a finite-length chute $x_{\min} < x < x_{\max}$ that is otherwise homogeneous, so that $b'(x) = 0$ and the other external terms are constants. We do this to motivate a discussion of the boundary conditions on h at $x_{\min}$ or $x_{\max}$.

For a given flow rate q, a streamwise-independent solution to (10.1) could be given by solving the equation $M(h; q) = \tan\theta$ for $h(x) = h^* = M^{-1}(\tan\theta; q)$, if this inversion be possible. However, such a solution could be incompatible with the (as yet unspecified) boundary conditions. Therefore, in the case of a finite-length chute, $h(x)$ in general will not be constant. We can investigate the dynamics of (10.1) more thoroughly using a phase-portrait analysis (see *e.g.* Strogatz (2018)), in which we trace the trajectories of solutions to (10.1) in the (h, k)-plane. Figure 10.1(a) shows an example of the phase portrait of (10.1). A trajectory in the upper-half (resp. lower-half) plane indicates a current of locally growing (resp. decreasing) depth as x increases. The equilibrium state $(h, k) = (h^*, 0)$ is marked on the $k = 0$ axis, and the trajectories in red and blue, going through the equilibrium state, are the unstable and stable manifolds (separatrices) of that state. The sketches in figure 10.1(b) show the shapes of the currents, that is, the evolution of $h(x)$ in real space, corresponding to three trajectories on the phase portrait (§10.1.2).

The system (10.1) is singular at $h = 0$, and the shapes of trajectories near $h = 0$ depend on the asymptotic properties of $\mu(I)$ for large I. According to the Jop fit (2.16), $\mu(I)$ is bounded as $I \to \infty$, and so $M(h; q)$ is bounded as $h \to 0$. Under this assumption, it can be shown that the trajectories near $h = 0$ satisfy either $k \lesssim h^3$ in the upper-half plane, or $k \lesssim -h^{-1/2}$ in the lower-half plane. These include respectively the stable and unstable manifolds of the saddle point, highlighted respectively as blue and red in figure 10.1(a).

10.1.2. Boundary conditions

To select a particular trajectory on figure 10.1(a), we must now specify boundary conditions. We take the downstream boundary condition as $h(x_{\max}) = 0$, to represent the flow off the end of the chute. Since (10.1) is singular near $h = 0$, we must check whether one can attain $h = 0$ for a finite value of x. For example, if $M(0; q)$ is finite, then the trajectories around the unstable manifold have asymptotic shape $k = h'(x) \lesssim -h(x)^{-1/2}$. Therefore, h decays superexponentially, and reaches 0 at a finite value of x. Note, however, that the shallowness assumption (5.1) becomes violated when $|h'| \gg 1$ and so (10.1) ceases to be physically applicable in a region around $x = x_{\max}$.[1]

The downstream condition $h(x_{\max}) = 0$ precludes those trajectories in the shaded region. Even outside of the shaded region, the initial values of h and k at $x = x_{\min}$ cannot be freely chosen: there is the additional constraint that the length of the chute is fixed. There is therefore a

[1] The boundary condition $h(x_{\max}) = 0$ appears to be overspecialised: for example, figure 8.5 showed different behaviours that a current could take in a DPM when a deletion boundary is used at the end of a chute. However, the qualitative dynamics of (10.1) are not affected if we instead allow $h(x_{\max})$ to take a small positive value, because the topological features of the phase portrait remain the same, especially around the equilibrium and away from the endpoints.

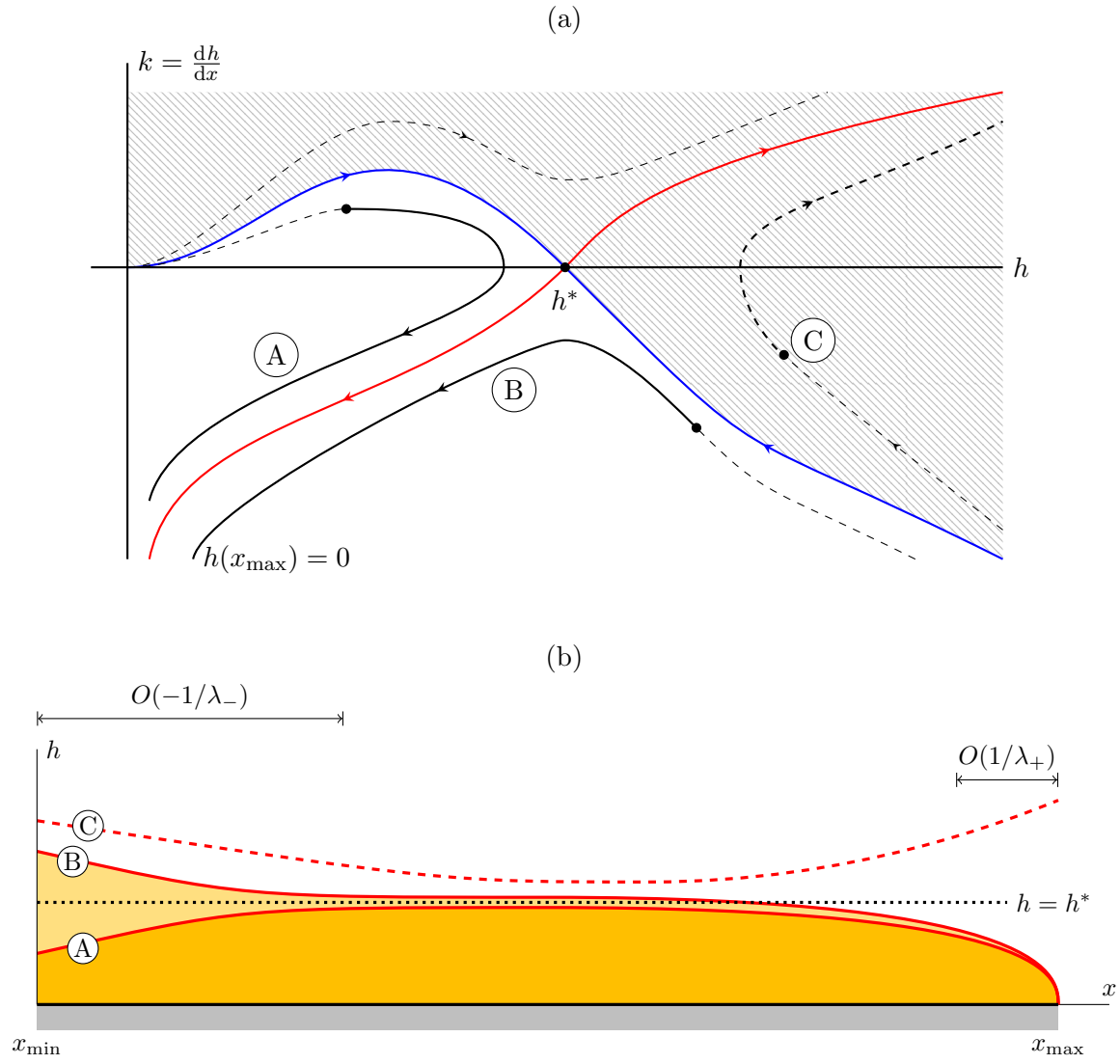

Figure 10.1.: (a) Part of the phase portrait of (10.1) for a fixed value of q, in the case that $\mu(0) < \tan\theta < \mu(\infty)$, so that an equilibrium state $h = h^* = M^{-1}(\tan\theta; q)$ exists. The red (resp. blue) trajectories are the unstable (resp. stable) manifolds of the equilibrium state. Two possible trajectories, with different inflow conditions, are marked in black: trajectories A and B correspond respectively to shallow and deep inflows. Trajectories A and B both satisfy the downstream boundary condition $h(x_{\max}) = 0$. Trajectories in the shaded region, such as trajectory C (dashed), do not satisfy the downstream boundary condition and are not permitted. (b) Sketches of the shapes of $z = h(x)$ corresponding to the three trajectories (§10.1.2), together with the equilibrium depth (dotted). We mark also the adjustment lengthscales (§10.1.3).

one-parameter family of solutions to (10.1) satisfying the downstream boundary condition.[2] Informally, we may choose which trajectory to follow, but not where to start along a given trajectory.

Two possible trajectories, A and B, are marked in black on figure 10.1(a), together with their initial states at $x = x_{\min}$. Trajectory A represents a flow with a shallow incident depth, while trajectory B represents one that is deep upstream. We also mark trajectory C (dashed), an example of a prohibited trajectory that does not satisfy the downstream boundary condition. The current shapes to which the trajectories correspond are shown in 10.1(b).

10.1.3. Adjustment towards the equilibrium state

Trajectories A and B both approach and spend a long distance near the saddle point along a stable manifold, before departing along the unstable manifold. This behaviour represents the tendency for a current to approximate the equilibrium state $h = h^* = M^{-1}(\tan\theta; q)$, which occurs provided that the chute is sufficiently long. The inflow depth of trajectory A is less than the equilibrium depth, so the current initially rises towards the equilibrium, before eventually decreasing again near the end of the chute. On the other hand, the inflow depth of trajectory B is higher than the equilibrium depth, so h decreases monotonically. Noting that the flow rate q is the same for all trajectories on figure 10.1(a), we interpret trajectory A as having an excess of kinetic energy at the inflow, and trajectory B as having an excess of potential energy: in both cases, energy is converted until the equilibrium is attained.

The distance over which a flow adjusts towards or away from the equilibrium can be estimated by calculating the Jacobian matrix $\boldsymbol{J}$ of (10.1) after linearising about $(h^*, 0)$. We find that

$$\boldsymbol{J} = \begin{pmatrix} 0 & 1 \\ Ja & Jb \end{pmatrix}, \tag{10.2}$$

where

$$Ja = \frac{-g\cos\theta}{q\nu}(h^*)^{3/2}M'(h^*), \quad Jb = \frac{1}{q\nu}\left(\frac{\chi q^2}{(h^*)^2} - gh^*\cos\theta\right)(h^*)^{1/2},$$

and $M'(h; q)$ is the (total) derivative of M with respect to h, keeping the parameter q fixed. The eigenvalues $\lambda_\pm$ of the Jacobian are given by

$$\lambda_\pm = \frac{Jb}{2} \pm \sqrt{\frac{Jb^2}{4} + Ja}. \tag{10.3}$$

Now, $Ja > 0$ because M decreases with h, and so both eigenvalues are real, one eigenvalue is positive, and the other is negative. This is to be expected as $(h, k) = (h^*, 0)$ is a saddle point. The positive eigenvalue λ_+ is associated with the unstable manifold, and the negative eigenvalue λ_- with the stable manifold. The lengthscales over which the current adjusts towards and away from the equilibrium are $O(-1/\lambda_-)$ and $O(1/\lambda_+)$ respectively.

[2] This may be more obvious by considering (10.1) as an initial value problem instead: having specified h at $x = x_{\min}$, there is one corresponding value of k that produces the correct value of h at $x = x_{\max}$; this value of k can be found using the shooting method (see *e.g.* Press et al. (1992)).

For illustration, consider a flow with high flow rate q. Correspondingly, the equilibrium depth h^* is small, and so the Froude number $\mathrm{Fr} = (gh^*)^{-1/2}\overline{u} = (g^{1/2}(h^*)^{3/2})^{-1}q \gg 1$. Then,

$$Jb = \frac{q}{\nu(h^*)^{3/2}}\left(\chi - \mathrm{Fr}^{-2}\cos\theta\right) \sim \frac{\chi q}{\nu(h^*)^{3/2}},$$

and $Jb^2 \gg Ja$. The two eigenvalues are therefore

$$\lambda_+ \sim Jb, \qquad \lambda_- \sim -Ja/Jb.$$

Correspondingly, the lengthscales for adjusting towards and away from equilibrium are

$$\frac{1}{-\lambda_-} = \frac{Jb}{Ja} \sim \frac{\chi}{-M'(h;q)}\mathrm{Fr}^2, \qquad \frac{1}{\lambda_+} \sim \frac{\nu}{\chi g^{1/2}}\mathrm{Fr}^{-1}, \tag{10.4}$$

respectively. In other words, a very supercritical flow takes a long $O(\mathrm{Fr}^2)$ distance to adjust towards equilibrium, owing to the large amount of inertia carried by the incident flow: indeed, the Froude number quantifies the ratio between the inertia of a flow and the magnitude of gravitational acceleration.

This $O(\mathrm{Fr}^2)$ adjustment lengthscale, over which a balance between gravitational acceleration and friction develops, shall be seen again in Chapters 11 and 12. In those chapters, we shall see that this lengthscale shall be supplemented by a second lengthscale that governs changes in the internal profile of a flow, which are neglected by the present depth-averaged model.

10.1.4. A note on causality

Phase portraits are usually used to study initial value problems, with the dynamical systems thought of as evolving in time. However, the system (10.1) is instead a boundary value problem and x is a spatial coordinate; the actual trajectory that is followed by a system is affected by the downstream boundary condition. Moreover, although the point $h = h^* = M^{-1}(\tan\theta; q)$ is a saddle point and we shall refer to its 'unstable' and 'stable manifolds', these terms are unrelated to the temporal stability of the time-dependent equations (5.4): the steady states being studied in this chapter are assumed to be temporally stable, and are attained by allowing a flow to develop for a long time.[3]

At first, it may have seemed teleological to impose a boundary condition on the outflow at $x = x_{\max}$, but this apparent paradox is averted by recalling that we are studying a steady flow that has developed over a long time. The flow is initially introduced at $x = x_{\min}$ and takes time to reach $x = x_{\max}$; when this happens, the boundary condition at $x = x_{\max}$ sends an influence back upstream.[4]

While an infinitely (or semi-infinitely) long chute $\mathcal{L} = x_{\max} - x_{\min} = \infty$ may be a useful abstraction, a steady flow on such a chute cannot be understood as having evolved from an upstream introduction (as this evolution would take an infinite amount of time). However, in the limit $\mathcal{L} \to \infty$, the steady state depth $h(x)$ at each fixed value of x converges pointwise towards some limiting value: for homogeneous flows, $h(x) \to h^*$. The convergence is not uniform (Burkill 2002) due to endpoint effects, but we understand an infinitely long chute to represent the double limit $t \to \infty$, $\mathcal{L} \to \infty$, *taken in that order*.

[3] The assumption that a flow governed by (5.4) does indeed settle towards a steady state can be violated by the development of instabilities (§14.2.3).

[4] This may be formalised in terms of the characteristics (Billingham and King 2001, Evans 2010) of the time-dependent system (5.4) (but see footnote 5).

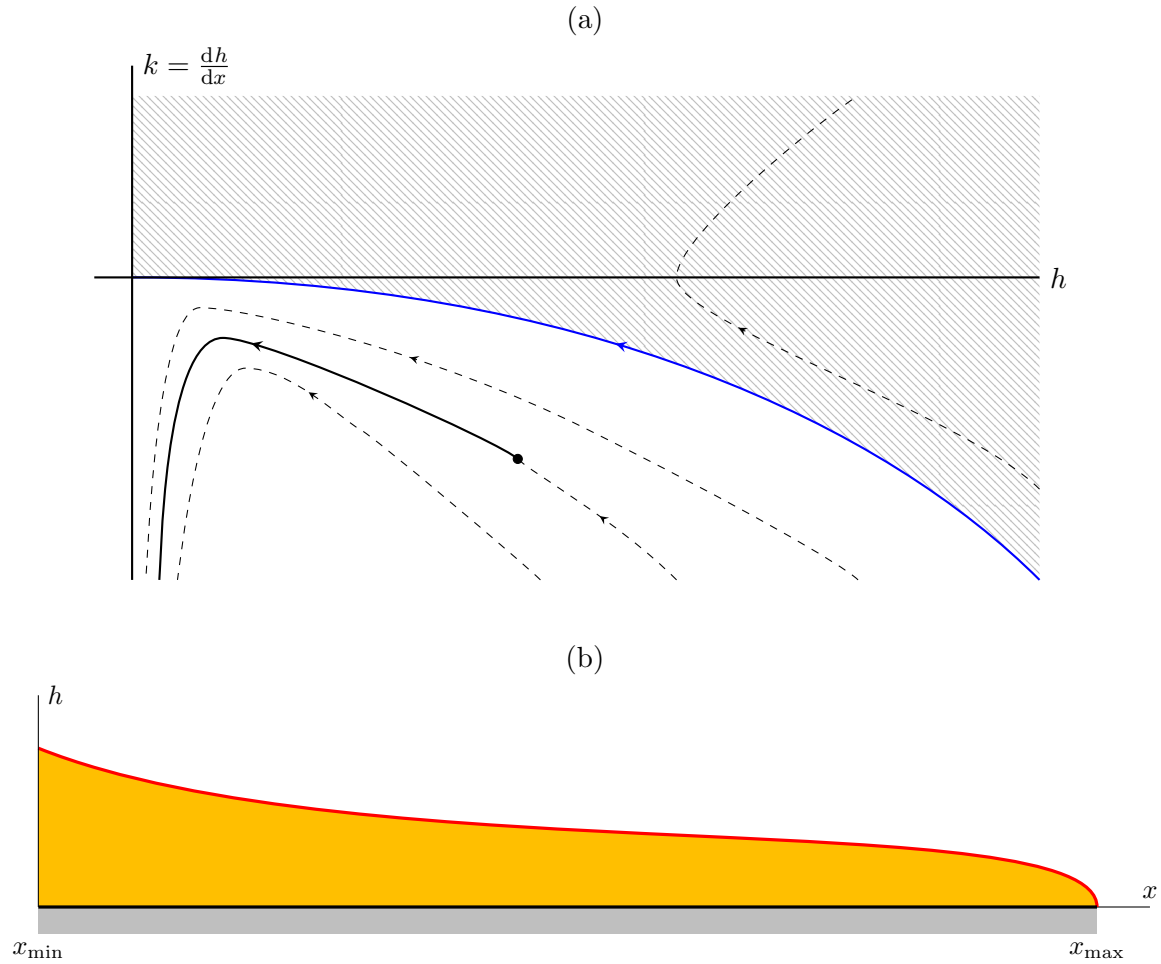

Figure 10.2.: (a) Phase portrait of (10.1) when $\tan\theta > \sup_h M(h;q)$, so that no equilibrium depth exists. As in figure 10.1(a), trajectories in the shaded region do not satisfy the downstream boundary condition $h(x_{\max}) = 0$; this region is bounded by the blue trajectory. (b) Corresponding shape of the current $h(x)$ in real space.

10.1.5. When an equilibrium does not exist

In the discussion so far and the phase portrait in figure 10.1(a), we have assumed that the equilibrium depth $h^* = M^{-1}(\tan\theta; q)$ exists. This will not be the case if θ is too large or too small, so that $\tan\theta$ falls outside the range of M, if M is bounded above or below.

As θ is increased, the equilibrium depth h^* decreases (because $M'(h;q) < 0$); if M is bounded above, then a bifurcation occurs when $\tan\theta$ exceeds the maximum value of M; the equilibrium h^* becomes absorbed into the singularity at $h = 0$. Such a high value of θ represents a slope inclined so steeply that the friction cannot balance the streamwise gravitational acceleration: the flow h decreases monotonically towards 0, regardless of the initial condition. The phase portrait in this case, and an example trajectory, is shown in figure 10.2(a), and the corresponding shape of the current $h(x)$ in real space is shown in panel (b).

On the other hand, if $\tan\theta < \inf_h(M;q)$ then the chute is not inclined sufficiently to maintain a steady uniform flow. On a long chute, the depth may increase to a very high amount before

decreasing again towards the end.

For the rest of this chapter we shall assume that θ and M are always such that equilibria exist, and that chutes are sufficiently long so that these equilibria are approached.

10.2. A sudden increase in basal roughness

Having discussed the boundary conditions on the depth-averaged model (10.1), we may now return to applying this model to spatial topography. We consider a chute that has a sudden change in basal roughness, as shown in figure 1.4(a). The friction function M, shape factor χ and (nonlinear) diffusivity ν are constant on either side of the transition, but change discontinuously at a transition point $x_T \in (x_{\min}, x_{\max})$. In the upstream region, the dynamics of (h, k) follow trajectories of (10.1) using the upstream values M_1, χ_1 and ν_1, while in the downstream region, (h, k) follows the trajectories using the downstream values M_2, χ_2 and ν_2.

10.2.1. Phase-portrait analysis

We can visualise these dynamics by superimposing the upstream and downstream phase portraits, as in figure 10.3. The dotted lines are the trajectories of the system (10.1) using the upstream values $M_1(h; q)$, χ_1 and ν_1, while the dashed lines are for the downstream region. The most obvious difference between the two phase portraits is the positions of the equilibria $h_1^* = M_1^{-1}(\tan\theta)$ and $h_2^* = M_2^{-1}(\tan\theta)$: the downstream equilibrium depth is thicker than the upstream equilibrium, because of the increased friction in the rougher region. The changes in the values of χ and ν affect the precise shapes of the trajectories, but not the qualitative topology of figure 10.3, so we defer discussion of these effects until §10.2.2.

Figure 10.3 shows an example of an actual trajectory (black), together with five locations of interest. The trajectory can be broken into several parts:

- The trajectory begins at point 1, some point on the (h, k) plane, corresponding to the point $x = x_{\min}$. The values of h and k are determined by the boundary conditions.
- Between points 1 and 2, the trajectory follows the upstream dynamics towards the upstream equilibrium $h = h_1^*$, approaching along a stable manifold of that state (blue dotted).
- The system stays near the upstream equilibrium $h = h_1^*$ for much of the region between $x = x_{\min}$ and $x = x_T$ (point 2).
- Just upstream of the transition point, between points 2 and 3, the trajectory leaves $h = h_1^*$ along one of its unstable manifolds (red dotted).
- At the transition point $x = x_T$ itself (point 3), the trajectory switches from upstream dynamics (dotted) to downstream dynamics (dashed).
- Between points 3 and 4, the trajectory heads towards the downstream equilibrium $h = h_2^*$ along one of that state's stable manifolds (blue dashed).
- The system stays near the downstream equilibrium $h = h_2^*$ (point 4) for much of the region between $x = x_T$ and $x = x_{\max}$.

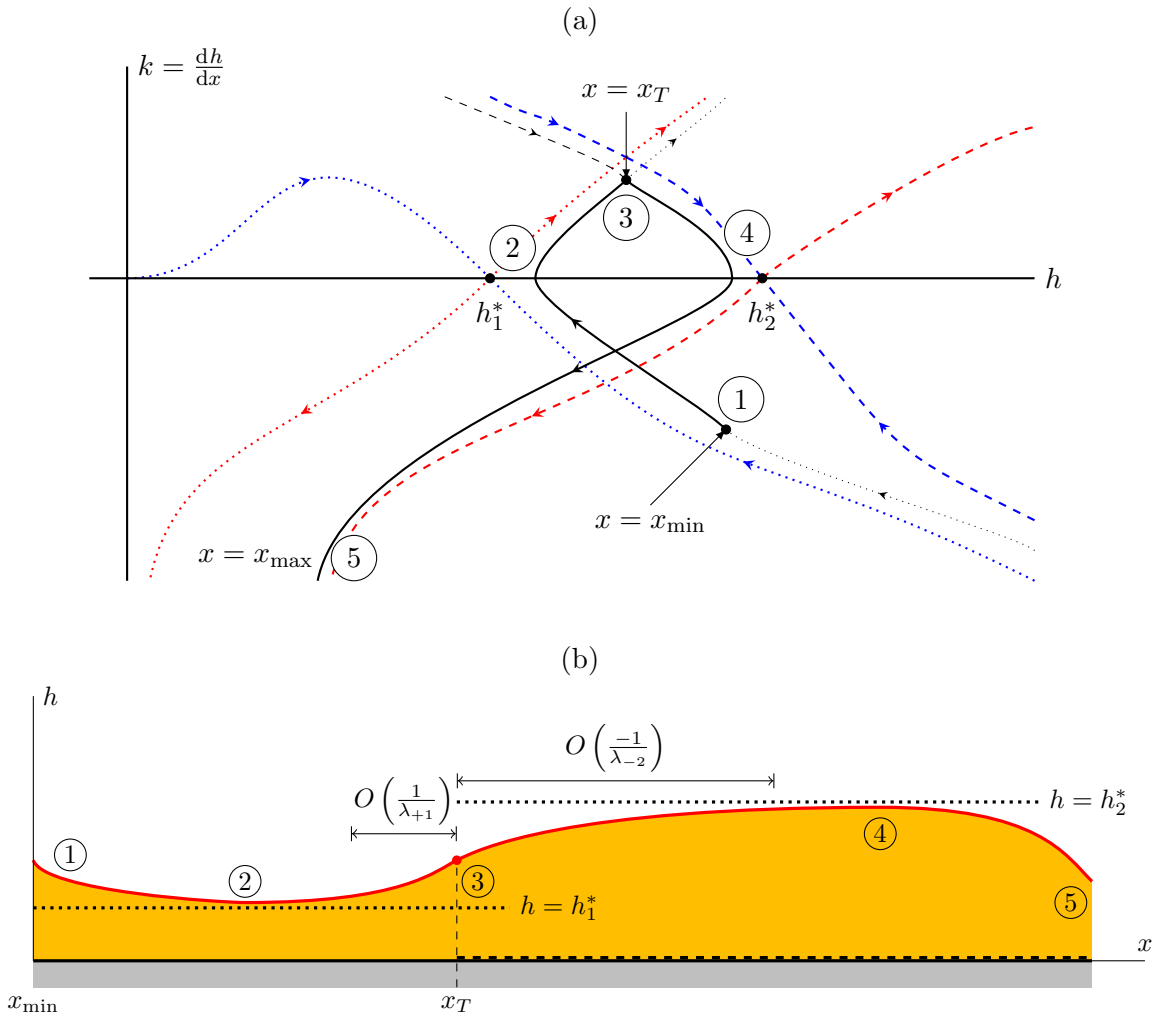

Figure 10.3.: (a) Part of the phase portrait of (10.1) for a fixed value of q, when the friction function M changes discontinuously at some value of x, as in §10.2.1. This portrait assumes that both M_1 and M_2 are invertible at $\tan\theta$, so that the equilibria $h_1^* = M_1^{-1}(\tan\theta)$ and $h_2^* = M_2^{-1}(\tan\theta)$ both exist. The separatrices of the upstream equilibrium are dotted, while those of the downstream equilibrium are dashed. An example trajectory and five locations of interest are marked (see text). (b) Corresponding shape of the current $h(x)$ in real space.

- Near the endpoint $x = x_{\max}$, the system leaves the downstream equilibrium and heads towards $h = 0$, following an unstable manifold (red dashed), as in the homogeneous case, to match onto the downstream boundary condition (point 5).

The position of the initial point on the (h, k)-plane where the trajectory starts (point 1), and the position of the transition (point 3), are both determined by the downstream requirement that $h = 0$ at $x_{\max}$ and that (h, k) should be continuous at $x = x_T$. The apparent teleology of imposing an downstream condition to determine the upstream dynamics was discussed in §10.1.4. The example shown in figure 10.3 assumes that the chute extends sufficiently long on either side of the transition. If not, then the flow may not be able to reach the equilibria, so that the trajectory does not form a very tight loop around points 2 and 4.

The trajectory in figure 10.3 also supposes that the incident flow is deeper than the upstream equilibrium h_1^*. In contrast, figure 10.4 shows a trajectory with a fast incoming flow. Here, the trajectory monotonically increases in depth up to point 4, and only thins out towards the end of the chute at $x = x_{\max}$. However, the dynamics of the two systems are not very particularly different between points 2 and 4, that is, the part of the system around the transition $x = x_T$. The difference between the two systems is only important in the initial convergence of the flow towards the upstream equilibrium. Between points 2 and 4, both trajectories follow the upstream unstable manifold (red dotted) and then the downstream stable manifold (blue dashed), transitioning at point 3.

10.2.2. The transition lengthscales

The phase-portrait analysis in §10.2.1 established the qualitative dynamics of (10.1) around the transition point $x = x_T$. We next use the stability analysis from §10.1.3 to estimate the lengthscales on either side of $x = x_T$ that are influenced by the topographical transition. As previously noted, the values of χ and ν did not affect the overall shape of the trajectories, but they shall affect the following quantitative discussion.

When both the upstream and downstream equilibria have high Froude numbers, the lengthscales of upstream and downstream influence were given in (10.4); note that the downstream equilibrium has a lower Froude number Fr_2 than that of the upstream equilibrium Fr_1. Supposing that $\mathrm{Fr}_1, \mathrm{Fr}_2 \gg 1$, (10.4) states that the transition creates a downstream disturbance over a long $-1/\lambda_{-2} = O(\mathrm{Fr}_2^2)$ distance, while the upstream disturbance is small and localised to a $1/\lambda_{+1} = O(\mathrm{Fr}_1^{-1})$ distance. This asymmetry is related to the supercriticality of flows at high Froude number (Billingham and King 2001).[5]

[5]Supercriticality in the context of the shallow water equations (5.3) refers to the fact that if $\mathrm{Fr} > 1$, then both characteristics of the PDE point in the forwards direction, so that downstream boundary conditions do not propagate information upstream (Evans 2010). Strictly speaking, the notions of characteristics and supercriticality do not directly apply to the granular depth-averaged model (5.4), which is a parabolic rather than hyperbolic system of PDE. The diffusivity term in (5.4b) allows some upstream influence, which is reflected in the proportionality of $1/\lambda_{+1}$ to the diffusivity coefficient ν. Assuming that ν is small, then we can informally apply the notions of characteristics and criticality to (5.4), remembering that the 'Riemann invariants' are not perfectly conserved.

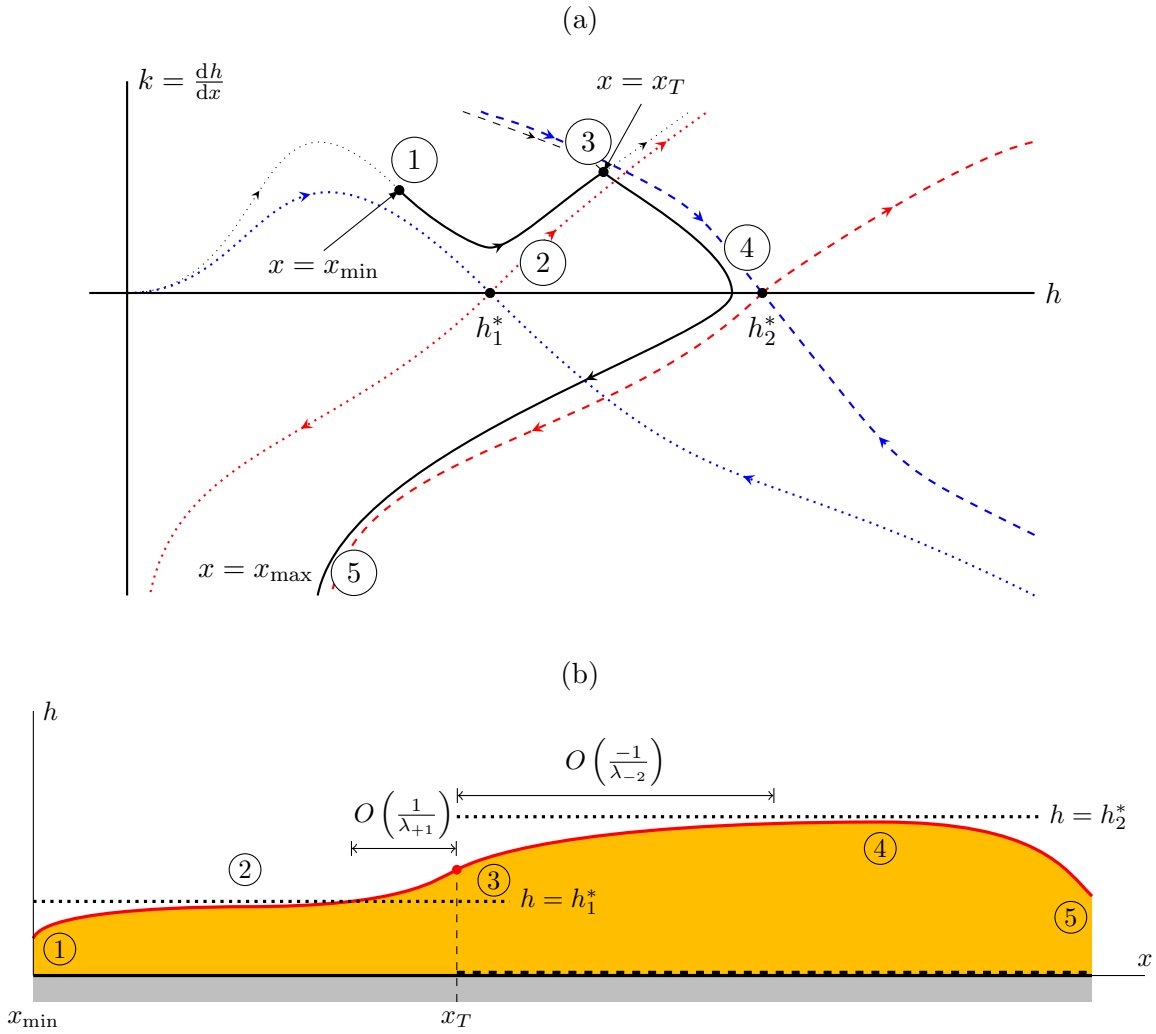

Figure 10.4.: (a) Part of the phase portrait of (10.1) for a fixed value of q and a sudden change in M. In this diagram, the incident flow is shallower than the upstream equilibrium h_1^*. See figure 10.3 and text for caption. (b) Corresponding shape of the current $h(x)$ in real space.

10.3. Further applications of (5.4)

The analyses of §10.2 could also be applied to chutes with other examples of topographical features, if M is allowed to vary with x in some other way than a step increase, or if $b'(x)$ takes nonzero values. As before, changes in M represent variation in the basal roughness along the chute, while changes in $b'(x)$ represent changes in the slope: step changes in $b'(x)$ represent kinks, while continuous changes represent curvature.

10.3.1. Rough-to-smooth transition

A first example is the reverse case of figure 1.4(a), so that the transition is an abrupt decrease in roughness. Again assuming that equilibria exist in both regions, the equilibria are reversed, so that $h_2^* < h_1^*$. An example phase portrait illustrating the corresponding dynamics are shown in figure 10.5. As before, the trajectory shown supposes that the incident flow is deeper than the upstream equilibrium, and that the trajectory does in fact approach each saddle point. Again, the latter condition assumes that the chute is long enough so that the flow can settle down to the local equilibrium.

10.3.2. Multiple abrupt transitions

The discussion in §10.2 could be extended to flows that have multiple abrupt changes of topography. Although the phase portraits in figures 10.3 and 10.4 would become cluttered, the basic concepts are the same. Away from a transition, the flow depth follows the dynamics of the local topography, which has an equilibrium that is represented as a saddle point on the phase portrait. Near each transition, a flow adjusts between the two equilibria, with the adjustment lengthscales as in §10.2.2: for $\mathrm{Fr} \gg 1$, the lengthscale is short on the upstream side and long on the downstream side. Moreover, near the ends of the chute there are adjustments away from the equilibria to accommodate the boundary conditions. As before, the choice of the trajectory and the shape of the current over the entire domain $(x_{\min}, x_{\max})$ are determined by the boundary conditions; the reason for this was discussed in §10.1.4.

If two transition points x_{T1} and x_{T2} are close to each other, then the adjustment regions around each transition may 'overlap' with each other. In this case, although the trajectory follows the local dynamics within the small region $x_{T1} < x < x_{T2}$, it does not necessarily approach the local equilibrium. (In fact, depending on the boundary conditions and the dynamics outside this region, the trajectory may even be travelling away from the local equilibrium.)

10.3.3. Kinked chutes

The discussion so far has been on the effect of basal roughness, rather than on basal shape. That is, we have allowed the coefficient of friction M to vary along the chute (albeit stepwise and not continuously), but taken $b'(x) = 0$ in (10.1).

Suppose instead that M be constant, but that

$$b'(x) = \big(\tan\theta - \tan(\theta + \Delta\theta)\big)\, H(x - x_T),$$

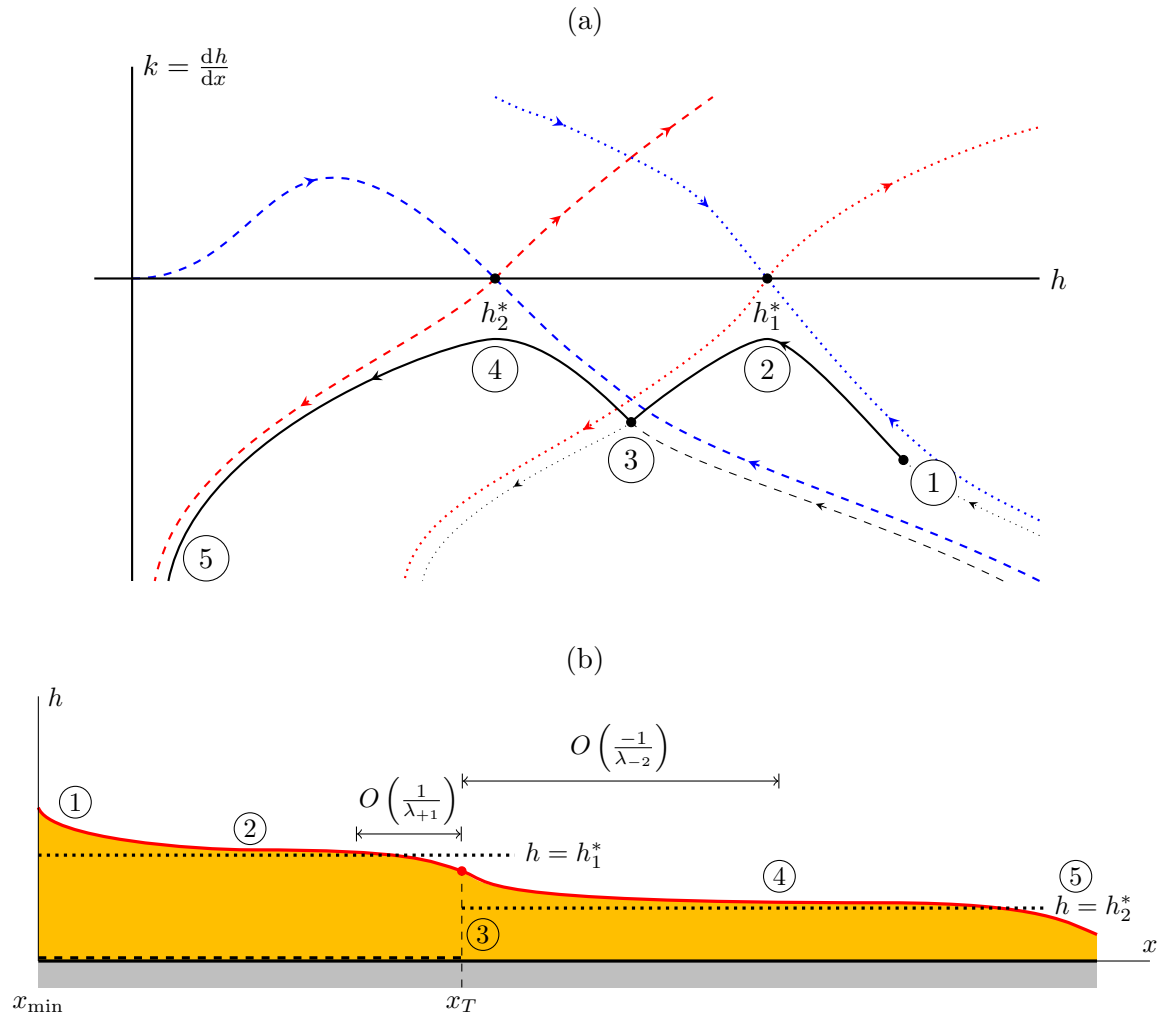

Figure 10.5.: (a) The dynamics of (10.1) with an abrupt transition such that the downstream equilibrium is more shallow than the upstream equilibrium. This applies to a rough-to-smooth transition (§10.3.1), as shown in panel (b), or a downward-kinked chute (§10.3.3). (b) Corresponding shape of the current $h(x)$ in real space.

where H is the Heaviside step function, so that b has a jump discontinuity: this represents a chute with a kink (figure 1.4(b)), with $\Delta\theta$ being the increase in the slope (in figure 1.4(b), $\Delta\theta < 0$). The resulting dynamics of (10.1) are very similar to those described in §10.2: away from the transition point and from endpoint effects, a flow's depth is approximately given by the local equilibria, which are

$$h^* = \begin{cases} M^{-1}(\tan\theta; q) & \text{upstream,} \\ M^{-1}(\tan(\theta + \Delta\theta); q) & \text{downstream.} \end{cases}$$

For $\Delta\theta < 0$, the flow trajectory is similar to those shown in figure 10.3 or 10.4 (depending on inflow conditions); if $\Delta\theta > 0$, so that the second equilibrium is more shallow than the first, then the trajectory is similar to that of figure 10.5.

10.3.4. Gradual transitions and curved chutes

All the discussion so far has focused on abrupt transitions in topography, the system (10.1) can also be applied to problems in which $b'(x)$ or M are allowed to vary continuously with x, representing a curved chute, or a chute whose base has varying roughness, respectively. For the present subsection, we consider the first case, taking M to be independent of x but considering variations in $b'(x)$. For definiteness, suppose that $b'(x) = s(X)$, introducing the 'slow' variable $X = \epsilon x$.[6] We also neglect endpoint effects, and assume that b' (or s) is localised. Then, to leading order in the 'slowness' parameter ϵ, the depth $h(x)$ is given by

$$h(x) \sim h_0(X) = M^{-1}(\tan\theta - s(X); q), \qquad k(x) = O(\epsilon),$$

which we term the *local slope approximation*. This leading-order approximation is the equilibrium depth for the slope at a given point, supposing that the chute had no curvature.

Improvements to the local slope approximation may be found using the method of multiple scales (Hinch 1991). Having introduced the slow variable, one posits a perturbation series solution,

$$\begin{aligned} h(x) &\sim h_0(x, X) + \epsilon h_1(x, X) + \dots, \\ k(x) &\sim k_0(x, X) + \epsilon k_1(x, X) + \dots. \end{aligned}$$

One also replaces the total derivative operator $\mathrm{d}/\mathrm{d}x$ with the new operator $\partial/\partial x + \epsilon\partial/\partial X$. Assuming that, in the far field, $h(x) \sim M^{-1}(\tan\theta; q)$, then, as expected, $h_0 = M^{-1}(\tan\theta - s(X); q)$, and $k_0 = 0$. It can be shown that the $O(\epsilon)$ correction h_1 satisfies the linear equation

$$\begin{aligned} \frac{\partial^2 h_1}{\partial x^2} - \frac{h_0^{1/2}}{q\nu}\left(\frac{\chi q^2}{h_0^2} - g h_0 \cos\theta\right)\frac{\partial h_1}{\partial x} + \frac{g\cos\theta}{q\nu} M'(h_0; q) h_0^{3/2} h_1 \\ = \frac{-s'(X) h_0^{1/2}}{q\nu M'(h_0; q)}\left(\frac{\chi q^2}{h_0^2} - g h_0 \cos\theta\right). \end{aligned} \tag{10.5}$$

[6] Note the notation for derivatives:

$$b''(x) = \frac{\mathrm{d}b'}{\mathrm{d}x} = \epsilon\,\frac{\mathrm{d}s}{\mathrm{d}X}, \quad \text{but} \quad s'(X) = \frac{\mathrm{d}s}{\mathrm{d}X}.$$

The $s'(X)$ in the forcing term on the right-hand side of (10.5) is responsible for h_1 being nonzero: this reflects $s'(X) \propto b''(x)$ being proportional to the curvature of the chute. Indeed, the particular solution from the forcing term gives

$$h_1 = \frac{-s'(X)}{M'^2}\left[\frac{\chi}{\cos\theta}\mathrm{Fr}^2 - 1\right], \qquad \mathrm{Fr} = \frac{q}{g^{1/2}h^{3/2}} = \frac{\overline{u}}{g^{1/2}h^{1/2}}.$$

Note that this solution is again independent of x, except through the slow variable X. The general solution to (10.5) also contains complementary functions, which are exponentials in x. In this case, the complementary functions vanish, since h_1 must be vanish if $s'(X) = 0$.

Now, $M' < 0$, but $M'^2 > 0$, so h_1 has the opposite sign to s'. Thus, for a high Froude number flow $\mathrm{Fr}^2 > \cos\theta/\chi$, an upwards curvature ($s'(X) > 0$) causes a flow to be more shallow than the local slope approximation would predict, while a downwards curvature would produce a deeper flow: a supercritical flow has plenty of inertia, so that the actual depth of the flow at a point reflects the equilibrium from the slope angle upstream of that point. On the other hand, at low Froude number, a flow is affected by the downstream slope angle: as previously noted (§10.1.4), this reflects the influence of downstream boundary conditions on a subcritical flow.

The higher-order corrections $h_2, h_3, \ldots$ satisfy similar linear problems (each of which is nonlinear in the previously determined corrections), although the derivation of these equations would be intractable.

10.4. Limitations of the depth-averaged approach

Fundamental to the derivation of the depth-averaged model (5.4) from the $\mu(I)$ equations (2.10) is the shallowness assumption (5.1), which is needed for the scalings (5.5), which state that the flow is predominantly streamwise and the pressure is approximately hydrostatic. Therefore, the depth-averaged approach is not valid for flows with variation over lengthscales $\mathcal{L}$ comparable to or smaller than the typical depth $\mathcal{H}$ of the flow. This limitation is in common with the shallow water equations (5.3) and their derivation from the Euler equations.

We note two shortcomings in the analysis of §10.2.2 concerning the current on either side of an abrupt transition. Firstly, the upstream side of a transition is predicted to have a short adjustment lengthscale $\mathcal{L} = O(\mathrm{Fr}^{-1})$ on the upstream side of an abrupt transition, in the case of high Froude number. The depth-averaged equations (5.4), and therefore (10.1), omit terms corresponding to perpendicular accelerations or non-hydrostatic pressure.

The second issue with the work of §10.2.2 concerns the much longer downstream adjustment region, which is $O(\mathrm{Fr}^2)$ at high Froude numbers. Even though this is much longer than the typical depth $\mathcal{H}$ (assuming that $M'(h;q) = O(1)$), we shall see that the depth-averaged approach is not entirely satisfactory. A change in basal condition does not affect a current uniformly across its depth, but most strongly affects the base of the current. This depthwise detail cannot be captured by a depth-averaged model, except through the shape factor χ that would need to be specified *a priori*.

The shallowness assumption also requires that any basal slope $b'(x)$ should be small, and that it should have small derivative (that is, small curvature). This is demonstrated in the experiment studied by Viroulet et al. (2017), who studied the flow of grains over a bump. In that work, the

bump is rather steep[7]; consequently, the current does not stay attached to the base but 'takes off and forms a granular jet when moving over the bump' (Viroulet et al. 2017). The flow on an abruptly kinked chute (§10.3.3), with b' a step function and $b''(x_T) = \infty$, therefore cannot fully be described by the depth-averaged model (5.4), until the jet reattaches to the base.

* * *

The following two chapters are dedicated to exploring the $\mu(I)$ rheology and the response of the internal velocity profile, and therefore of the shape factor, in response to an abrupt transition. Chapter 11 will analyse a spatial problem similar to the one studied here, and give the results of DPM simulations on such a flow. Chapter 12 will consider a related time-dependent problem, with similar dynamics albeit a different interpretation of causality (§10.1.4).

[7] '[A] smooth bump [...] with a maximum height of 4.75 cm and [...] '$\sim$ 90% of its amplitude change occurs over a downstream distance of 12 cm' (Viroulet et al. 2017), suggesting that $b'(x) \approx 2/3$.

11. Boundary layer formation and growth: the granular Blasius problem

All conditioned things are transient.

Buddhist concept of *anicca*

11.1. Problem description

In this chapter, we again consider the roughness transition problem first sketched in figure 1.4(a). However, we now consider the evolution of the internal profile, and therefore the shape factor, near the transition point more carefully. To this end, we use the $\mu(I)$ rheology instead of the depth-averaged model (5.4), and we compare the predictions of the rheology against the results of DPM simulations.[1]

The problem is sketched in more detail in figure 11.1(a). A steady flow of particles is introduced onto a chute of varying roughness. The chute has a transition point $x = 0$. In the upstream region $x < 0$, the chute is smooth; in the downstream region $x > 0$, the chute is made bumpy as illustrated in figure 8.6, with $b = d$ so that the relative basal roughness is $\beta = 1$. The chute and particles are all intrinsically frictionless, and all contacts have a restitution coefficient $e = 0.1$; the bulk flow is therefore frictional from this inelasticity (see §9.3 for a discussion of the relationship between inelasticity and bulk friction). Since there is no basal bumpiness or intrinsic friction, the flow in $x < 0$ slips freely against the base, and takes a plug flow profile, $\chi = 1$. The chute is inclined at an angle θ chosen such that the bumpiness and dissipation are sufficient to impose a no-slip condition in $x > 0$. This must be verified empirically, and in practice, this condition does not apply in the immediate vicinity of $x = 0$; as we discussed in §4.2.2, there is no immediate relationship between basal bumpiness and the slip velocity. However, the region in $x > 0$ over which the no-slip condition is violated is small compared to the distance over which the velocity profile evolves, so we shall assume the condition in our continuum model.

Initially, the inertia of the incident flow allows the top part of the current to carry on travelling at the incident speed, and the no-slip condition affects only a thin boundary layer at the bottom of the current. The (bulk) friction causes the effect of the no-slip condition to spread, so that this region grows in size. This is similar to the growth of the boundary layer in the classical Blasius problem for flow over an airfoil (Schlichting and Gersten 2017), which is why we term the present problem as the *granular Blasius problem*.

There are three major differences between the classical problem and the continuum limit of the granular Blasius problem. Firstly, the classical Blasius problem assumes that the blade is

[1] The work in this chapter is an adaptation of a manuscript 'The granular Blasius problem' under consideration for publication in *Journal of Fluid Mechanics* (Tsang et al. 2019).

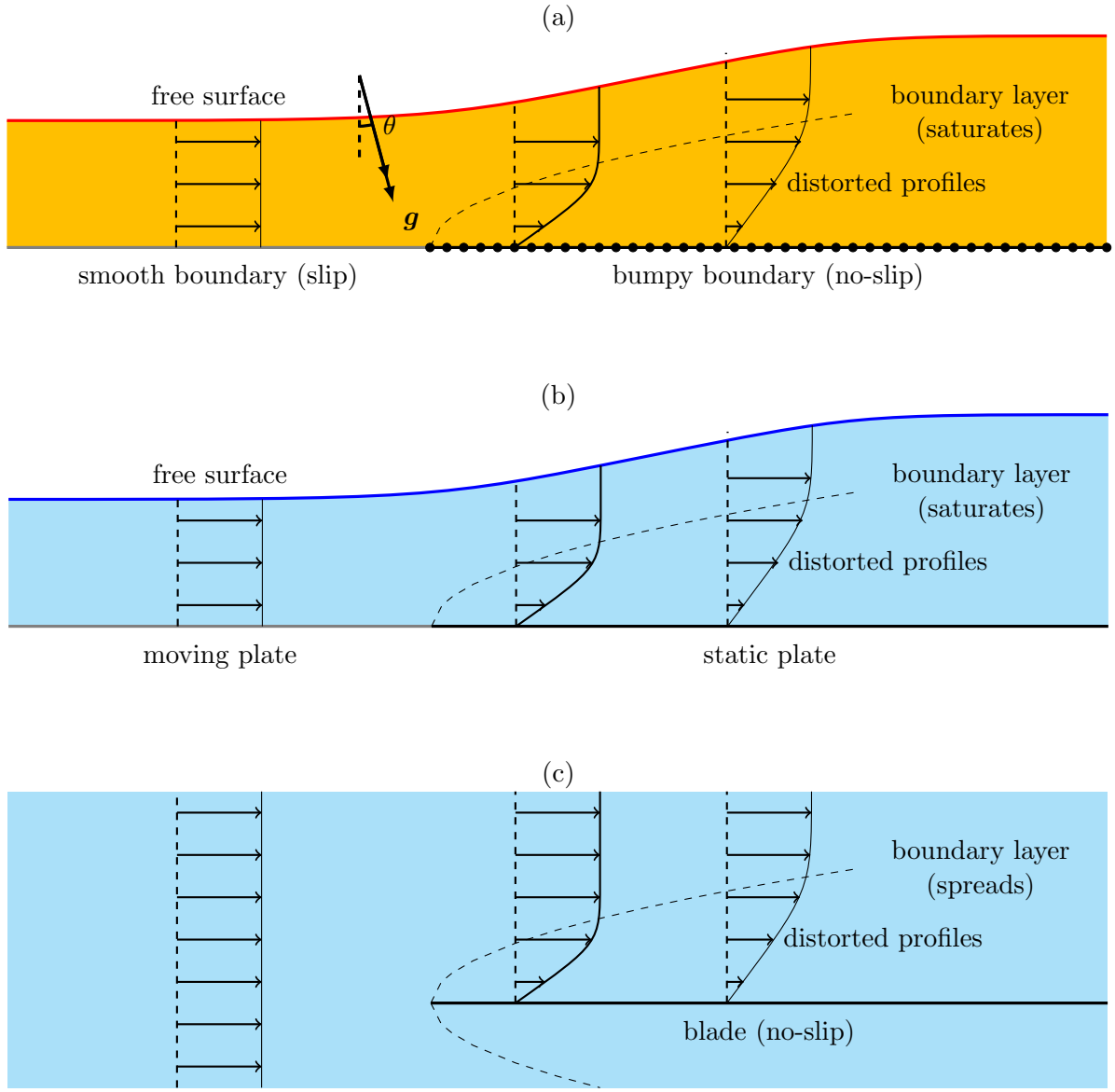

Figure 11.1.: (a) The granular Blasius problem. (b) The free-surface hydrofoil boundary layer problem studied in Tsang et al. (2018). (c) The classical Blasius problem.

immersed in an infinite volume of fluid, but the present problem concerns a current of finite depth, and so a free surface is present, as sketched in figure 11.1(b). The development of the boundary layer has an effect on the outer flow, displacing the free surface upwards and introducing a perturbation to the outer flow, which in turn feeds back on the boundary layer (Tsang et al. 2018). A second difference between the two problems is that the entire system in the granular problem is inclined at an angle $\theta > 0$. Gravity therefore drives the flow forwards and opposes the basal drag. The boundary layer does not grow indefinitely but 'saturates' when its thickness becomes comparable to that of the current, after which point the current is governed by a balance between gravity and drag, with the incident inertia having been spent. Finally, the Navier–Stokes equations, which govern the classical problem with Newtonian fluids, must be replaced with the equations of a rheological model of dense granular flows, such as the $\mu(I)$ rheology.

In §11.3, we shall see that the $\mu(I)$ equations can be analysed using an approach similar to that of Prandtl (1905), which was used for solving the classical Blasius problem. However, this analysis will be successful only if the function $\mu(I)$ takes a particular form. We shall compare the solutions predicted by the $\mu(I)$ equations against the results of DPM simulations in §11.4.

11.2. Analysis for a Newtonian fluid

Before we proceed with analysing the $\mu(I)$ equations, it is illustrative to first study the problem in figure 11.1(b), in which a current of a Newtonian fluid at high Reynolds number is incident onto a static plate. This problem shares many features with the granular Blasius problem, but has the advantage that it will be possible to find analytical solutions to the perturbation to the outer flow (Tsang et al. 2018). The classical Blasius boundary layer problem and its extensions have been extensively studied to model flow around an aerofoil, taken to be an infinitesimally thin blade. With the presence of a free surface, the present problem may be regarded as a 'hydrofoil' problem: that is, a blade cutting through water just below a free surface. In both cases, a boundary layer forms on the blade, but here the boundary layer interacts with the free surface.

In the context of this chapter, the purpose of this hydrofoil problem is to explore the effect of the boundary layer on the pressure in the outer flow. The imposition of the no-slip condition causes the flow near the base to slow down; by conservation of flux, the depth of the current increases along the streamwise direction. The thickening of the current creates a pressure gradient against the flow in the boundary layer. If this adverse pressure gradient is sufficiently strong, then there is a strong coupling between the boundary layer and the outer layer, and the two problems must be treated together. This is in contrast to the classical Blasius problem, where the outer flow is assumed to occupy an infinite area and the boundary layer does not result in a pressure gradient in the outer flow.

Similar problems have been studied in the context of channel flows experiencing sudden changes in basal conditions, and experimental results on turbulent channel flows are outlined in Chow (1959, Chapter 8). Nelson et al. (1995) also consider the boundary layer formed on a free-surface flow over a flat plate; their flow is driven by a shear stress due to a uniform wind blowing above the current, rather than driving by the bottom plate. Our problem has the advantage of being analytically tractable, and allows asymptotic expressions for the velocity profile in terms of special functions.

11.2.1. Mathematical statement of problem

Let $\mathcal{H}$ and $\mathcal{U}$ denote respectively the depth and velocity of the uniform inflow. We define a Reynolds number $\mathrm{Re} = \mathcal{U}\mathcal{H}/\nu$ and a Froude number $\mathrm{Fr} = \mathcal{U}/\sqrt{g\mathcal{H}}$ based on the depth and velocity of the incident flow. In this section, we shall work in units such that $\mathcal{U} = 1$ and $\mathcal{H} = 1$; the magnitudes of gravity g and kinematic viscosity ν are to be encapsulated by Re and Fr. In these units, the flow rate $q = \mathcal{H}\mathcal{U} = 1$. We also take the density as $\rho = 1$, and assume that the air above the liquid has negligible density and viscosity. In the analysis of the granular problem in §11.3, we shall revert to dimensional units.

Both the outer flow and the boundary layer flow are governed by the incompressible Navier–Stokes equations, which in these nondimensional quantities read

$$\frac{\partial u}{\partial x} + \frac{\partial w}{\partial z} = 0, \tag{11.1a}$$

$$\mathrm{Fr}^2\left[\frac{\partial u}{\partial t} + u\,\frac{\partial u}{\partial x} + w\,\frac{\partial u}{\partial z}\right] = -\frac{\partial p}{\partial x} + \frac{\mathrm{Fr}^2}{\mathrm{Re}}\left[\frac{\partial^2 u}{\partial x^2} + \frac{\partial^2 u}{\partial z^2}\right], \tag{11.1b}$$

$$\mathrm{Fr}^2\left[\frac{\partial w}{\partial t} + u\,\frac{\partial w}{\partial x} + w\,\frac{\partial w}{\partial z}\right] = -1 - \frac{\partial p}{\partial z} + \frac{\mathrm{Fr}^2}{\mathrm{Re}}\left[\frac{\partial^2 w}{\partial x^2} + \frac{\partial^2 w}{\partial z^2}\right]. \tag{11.1c}$$

These are supplemented by the boundary conditions

$$u = 1 \text{ and } w = 0 \quad \text{on } z = 0 \text{ for } x < 0, \tag{11.2a}$$

$$u = w = 0 \quad \text{on } z = 0 \text{ for } x > 0, \tag{11.2b}$$

$$w = \partial h/\partial t + u\,\partial h/\partial x \quad \text{on } z = h, \tag{11.2c}$$

$$p = O(\mathrm{Fr}^2/\mathrm{Re}) \quad \text{on } z = h. \tag{11.2d}$$

The final condition is the dynamic boundary condition at the free surface. It comes from the more general condition that the stress component $\boldsymbol{n}\cdot\boldsymbol{\sigma}\cdot\boldsymbol{n} = 0$ should vanish at the free surface in the absence of surface tension (Batchelor 2000). For an inviscid fluid, this condition is equivalent to $p = 0$ at the free surface, but in general, the fluid's viscosity offers a contribution of $O(\mathrm{Fr}^2/\mathrm{Re})$ to $\boldsymbol{n}\cdot\boldsymbol{\sigma}\cdot\boldsymbol{n}$. We are about to consider the case $\mathrm{Re} \gg 1$, and we shall calculate perturbations of size $O(\mathrm{Re}^{-1/2})$, so the $O(\mathrm{Fr}^2/\mathrm{Re})$ contributions are sufficiently small that they need not be considered at this order.

11.2.2. Perturbation analysis for $\mathrm{Re} \gg 1$

Working in the limit of high Reynolds number $\mathrm{Re} \gg 1$, and taking Froude number $\mathrm{Fr} > 1$ fixed so that the incident flow is supercritical, our analysis shall proceed as follows. We first assume that the boundary layer is identical to that which is predicted by the classical problem with no pressure gradient. This boundary layer has an $O(\mathrm{Re}^{-1/2})$ thickness, and the perturbation flow in the outer layer may then be assumed to be $O(\mathrm{Re}^{-1/2})$. Linearising the Navier–Stokes equations in the outer layer about the base state shows that the perturbation flow is governed by Laplace's equation. The boundary conditions on the perturbation flow come from linearising the free surface boundary conditions, and by calculating the perpendicular displacement velocity caused by the boundary layer. We next find the perturbation flow in the form of a Fourier

integral. From this, the perturbation pressure, and therefore the pressure gradient, may be calculated. We shall then examine the magnitude of this pressure gradient in terms of Re and Fr, and consider whether it is sufficiently small that our original assumption is valid.

Leading-order outer solution

In the inviscid limit $\mathrm{Re} = \infty$, the change in basal conditions at $x = 0$ has no effect on the flow, since the no-slip condition may not be applied in the absence of viscosity. The flow merely maintains its upstream values, and the leading-order outer solution is given by

$$h \sim h^{(0)} = 1, \quad u \sim u^{(0)} = 1, \quad w \sim w^{(0)} = 0, \quad p \sim p^{(0)} = h^{(0)} - z.$$

Corrections to this flow field, which are induced by the boundary layer displacement, will be of magnitude $O(\mathrm{Re}^{-1/2})$. We shall find these after describing the boundary layer.

Leading-order boundary layer solution

The leading-order outer solution does not satisfy the no-slip condition at $z = 0$. This condition is enforced by viscous effects confined to a boundary layer of thickness $O(\mathrm{Re}^{-1/2})$ near the base, in which the streamwise velocity adjusts from zero to the outer solution's 'slip velocity'. To leading order, the boundary layer velocity and pressure are given by the Blasius solution (Prandtl 1905, Acheson 1990, Schlichting and Gersten 2017). Below, we recount its derivation.

We begin by writing $z = \epsilon\tilde{z}$, where $\tilde{z}$ is a rescaled perpendicular coordinate, and ϵ is the boundary layer thickness scale: we focus on the region $\tilde{z} = O(1)$. By incompressibility (2.2), the perpendicular velocity $w = O(\epsilon)$ in this region, and so we also rescale $w = \epsilon\tilde{w}$, so that $\tilde{w} = O(1)$. The Navier–Stokes equations (11.1) become

$$\mathrm{Fr}^2\left[\frac{\partial u}{\partial t} + u\,\frac{\partial u}{\partial x} + \tilde{w}\,\frac{\partial u}{\partial \tilde{z}}\right] = -\frac{\partial p}{\partial x} + \frac{\mathrm{Fr}^2}{\epsilon^2\mathrm{Re}}\,\frac{\partial^2 u}{\partial \tilde{z}^2} + \frac{\mathrm{Fr}^2}{\mathrm{Re}}\,\frac{\partial^2 u}{\partial x^2}\,, \tag{11.3a}$$

$$\epsilon\mathrm{Fr}^2\left[\frac{\partial \tilde{w}}{\partial t} + u\,\frac{\partial \tilde{w}}{\partial x} + \tilde{w}\,\frac{\partial \tilde{w}}{\partial \tilde{z}}\right] = -1 - \frac{1}{\epsilon}\,\frac{\partial p}{\partial \tilde{z}} + \frac{\mathrm{Fr}^2}{\epsilon\mathrm{Re}}\,\frac{\partial^2 \tilde{w}}{\partial \tilde{z}^2} + \frac{\mathrm{Fr}^2\epsilon}{\mathrm{Re}}\,\frac{\partial^2 \tilde{w}}{\partial x^2}\,. \tag{11.3b}$$

The inner solution must satisfy the no-slip and no-penetration conditions $u = \tilde{w} = 0$ at $\tilde{z} = 0$. It must also match with the outer solution. To leading order, this matching condition may be expressed as van Dyke's rule (Hinch 1991),

$$\lim_{\tilde{z}\to\infty} u_{(0)} = \lim_{z\to 0} u^{(0)}, \quad \text{and} \quad \lim_{\tilde{z}\to\infty} p_{(0)} = \lim_{z\to 0} p^{(0)}, \tag{11.4}$$

where the lower index indicates the boundary layer solution.

First, the boundary layer thickness scale ϵ can be found by considering (11.3a): the balance between the $O(\mathrm{Fr}^2)$ inertia terms on the left and the $O(\mathrm{Fr}^2/(\epsilon^2\mathrm{Re}))$ depthwise viscous term on the right is attained by taking $\epsilon = \mathrm{Re}^{-1/2}$. Next, the $O(\mathrm{Re}^{1/2})$ pressure gradient term in (11.3b) is unbalanced and must be zero at leading order, indicating that the pressure is approximately constant across the thickness of a boundary layer. By the matching condition (11.4), $p_{(0)} = 1$, and so the pressure gradient term in (11.3a) vanishes. The final term in (11.3a) is $O(\mathrm{Fr}^2/\mathrm{Re})$,

and can also be dropped as they are subdominant compared to the $O(\mathrm{Fr}^2)$ terms, since $\mathrm{Re} \gg 1$. The remaining terms in (11.3a) balance each other, so that, in the steady state, the leading-order boundary layer velocities $u_{(0)}, \tilde{w}_{(0)}$ satisfy

$$\frac{\partial u_{(0)}}{\partial x} + \frac{\partial \tilde{w}_{(0)}}{\partial \tilde{z}} = 0, \qquad u_{(0)} \frac{\partial u_{(0)}}{\partial x} + \tilde{w}_{(0)} \frac{\partial u_{(0)}}{\partial \tilde{z}} = \frac{\partial^2 u_{(0)}}{\partial \tilde{z}^2}\,. \tag{11.5}$$

A similarity solution is found by introducing a streamfunction, such that

$$u \sim u_{(0)} = B'(s), \quad \tilde{w} \sim \tilde{w}_{(0)} = \left(\frac{\partial}{\partial x}\right)_{\tilde{z}} (2x)^{1/2} B(s), \quad p \sim p_{(0)} = 1, \tag{11.6}$$

where, $s = \tilde{z}/(2x)^{1/2}$ is a similarity variable, and B is the unique solution to the system

$$B''' + \frac{1}{2} B B'' = 0, \quad B(0) = B'(0) = 0, \quad \lim_{s\to\infty} B'(s) = 1. \tag{11.7}$$

The two boundary conditions at $s = 0$ correspond to the no-penetration and no-slip conditions, while the condition $\lim_{s\to\infty} B'(s) = 1$ corresponds to the matching condition (11.4).

From this solution, we define the thickness of the boundary layer up to an arbitrary constant of proportionality. The *nominal thickness*,

$$\Lambda(x) = \mathrm{Re}^{-1/2}(2x)^{1/2} = \epsilon(2x)^{1/2},$$

is the value of z such that $\tilde{x} = 1$; and the *displacement thickness* is $s_{\mathrm{disp}}\Lambda(x)$, where

$$s_{\mathrm{disp}} = \lim_{s\to\infty} \big(s - B(s)\big)\,.$$

Here, we have introduced $\epsilon = \mathrm{Re}^{-1/2}$ as the *boundary layer thickness scale*.

First-order correction to the outer flow

In the derivation of (11.6), we made the assumption that the pressure gradient $\partial p/\partial x$ may be dropped from (11.3a). Although the leading-order outer flow has no streamwise pressure gradient, the induced flow does provide a pressure gradient. The assumption that this may be dropped holds provided that the magnitude of this pressure gradient is less than $O(\mathrm{Fr}^2)$. We now calculate the induced flow and the induced pressure gradient, and consider the dependence of its magnitude on Fr.

Although the leading-order outer solution has $w^{(0)} = 0$, the boundary layer solution asserts that

$$\tilde{w}_{(0)} \to c(2x)^{-1/2} \quad \text{as } \tilde{z} \to \infty,$$

where

$$c = \lim_{s\to\infty} (sB' - B) \approx 1.72 \tag{11.8}$$

is the displacement thickness of the Blasius boundary layer from (11.7). In other words, the outer flow experiences a 'displacement velocity' perpendicular to the base, owing to the base slowing the flow down in the streamwise direction. Reverting to the unscaled variable $w = \mathrm{Re}^{-1/2}\tilde{w}$,

the displacement velocity is $O(\mathrm{Re}^{-1/2})$, which does not affect the leading-order outer solution, but suggests that the outer flow must have an $O(\mathrm{Re}^{-1/2})$ correction.

We find this correction by proposing the asymptotic expansions

$$h \sim h^{(0)} + \mathrm{Re}^{-1/2} h^{(1)} = 1 + \mathrm{Re}^{-1/2} h^{(1)}, \tag{11.9a}$$

$$u \sim u^{(0)} + \mathrm{Re}^{-1/2} u^{(1)} = 1 + \mathrm{Re}^{-1/2} u^{(1)}, \tag{11.9b}$$

$$w \sim w^{(0)} + \mathrm{Re}^{-1/2} w^{(1)} = \mathrm{Re}^{-1/2} w^{(1)}, \tag{11.9c}$$

$$p \sim p^{(0)} + \mathrm{Re}^{-1/2} p^{(1)} = 1 - z + \mathrm{Re}^{-1/2} p^{(1)}, \tag{11.9d}$$

and then expanding the governing equations (11.1) and boundary conditions (11.2) to $O(\mathrm{Re}^{-1/2})$, treating Fr as a constant. The viscosity terms are $O(\mathrm{Fr}^2/\mathrm{Re})$ and still do not affect the outer solution at this order.

Assuming a steady state $\partial/\partial t = 0$, the equations of motion become

$$\frac{\partial u^{(1)}}{\partial x} + \frac{\partial w^{(1)}}{\partial z} = 0, \tag{11.10a}$$

$$\mathrm{Fr}^2 \frac{\partial u^{(1)}}{\partial x} = -\frac{\partial p^{(1)}}{\partial x}, \tag{11.10b}$$

$$\mathrm{Fr}^2 \frac{\partial w^{(1)}}{\partial x} = -\frac{\partial p^{(1)}}{\partial z}. \tag{11.10c}$$

Cross-differentiating (11.10b, 11.10c) and subtracting eliminates $p^{(1)}$, and shows that $w^{(1)}$ satisfies Laplace's equation

$$\frac{\partial^2 w^{(1)}}{\partial x^2} + \frac{\partial^2 w^{(1)}}{\partial z^2} = 0. \tag{11.11a}$$

Boundary conditions at the free surface may be found by linearising the exact conditions, applying them at $z = h^{(0)} = 1$ instead of $z = h(x)$. These give

$$w^{(1)} = \frac{\mathrm{d}h^{(1)}}{\mathrm{d}x} \quad \text{and} \quad p^{(1)} = h^{(1)} \quad \text{on } z = 1,$$

which may be combined with (11.10a, 11.10b) to give a Robin boundary condition on $w^{(1)}$:

$$w^{(1)} = \mathrm{Fr}^2 \frac{\partial w^{(1)}}{\partial z} \quad \text{on } z = 1. \tag{11.11b}$$

Meanwhile, the boundary condition on $w^{(1)}$ at $z = 0$ for $x > 0$ comes from matching with the displacement velocity from the boundary layer solution, while there is no displacement velocity for $x < 0$. Hence

$$w^{(1)} = c(2xH(x))^{-1/2} \quad \text{on } z = 0, \tag{11.11c}$$

where $H(x)$ is the Heaviside step function.[2] Note that this boundary condition implies that $w^{(1)}$ is large near $x = 0$, violating the asymptoticity of the expansion when $w^{(1)} = O(\mathrm{Re}^{1/2})$. We propose a resolution of this issue in §11.2.3.

[2] Rather than imposing this condition on $w^{(1)}$ at $z = 0$, we could instead choose to impose the condition at the boundary layer 'displacement thickness' $z = c\mathrm{Re}^{-1/2}(2x)^{1/2}$, and then linearise to turn this into a mixed boundary condition at $z = 0$. For a fixed value of x, this extra term is subdominant in the limit $\mathrm{Re} \to \infty$, and does not change the $O(\mathrm{Re}^{-1/2})$ analysis that follows. However, that term is not negligible for $x = O(\mathrm{Re})$, when the boundary layer saturates (§11.2.3).

Having stated the boundary conditions, the linear system (11.11) for $w^{(1)}$, the perpendicular component of the perturbation velocity, may now be solved using Fourier methods (Riley et al. 2006). Let us first write $f(x) = c(2x)^{-1/2}H(x)$, where the constant c was defined in (11.8). The Fourier transform of f is given by

$$\tilde{f}(k) = \int_{-\infty}^{\infty} \mathrm{e}^{-\mathrm{i}kx} f(x)\,\mathrm{d}x = \frac{1}{2}c\pi^{1/2}\left(1 - \mathrm{i}\,\mathrm{sgn}(k)\right)|k|^{-1/2}, \tag{11.12}$$

and the solution for $w^{(1)}$ can be written in integral form, as an inverse Fourier transform,

$$\begin{aligned} w^{(1)} &= \frac{1}{2\pi}\int_{-\infty}^{\infty} \mathrm{e}^{\mathrm{i}kx}\tilde{f}(k)\frac{\mathrm{Fr}^2 k\cosh(k(1-z)) - \sinh(k(1-z))}{\mathrm{Fr}^2 k\cosh k - \sinh k}\,\mathrm{d}k \\ &= \frac{c\mathrm{e}^{-\mathrm{i}\pi/4}}{(2\pi)^{1/2}}\int_0^{\infty} \mathrm{e}^{\mathrm{i}kx}k^{-1/2}\frac{\mathrm{Fr}^2 k\cosh(k(1-z)) - \sinh(k(1-z))}{\mathrm{Fr}^2 k\cosh k - \sinh k}\,\mathrm{d}k, \end{aligned} \tag{11.13}$$

the real part understood. Note that for $\mathrm{Fr} > 1$, the integrand's singularity at $k = 0$ is integrable, and (11.13) is convergent for all x and all $0 \le z \le 1$, except at the point $x = z = 0$. However, for $\mathrm{Fr} < 1$ the integrand has a non-integrable pole at the positive solution to the equation $\mathrm{Fr}^2 k = \tanh k$. This results from the ill-posedness of the formulation of the problem if $\mathrm{Fr} < 1$.

Pressure gradient induced by correction

The leading-order Blasius boundary layer solution (11.6) assumes that the pressure in the boundary layer is constant, since the leading-order outer solution predicts a constant pressure on $z = 0$. However, the perturbation flow (11.13) induces a pressure gradient. We now calculate the size of this pressure gradient and, in particular, determine whether it is comparable to the $O(\mathrm{Fr}^2)$ inertia terms in (11.3).

The value of this pressure gradient may be evaluated using (11.10):

$$\begin{aligned} \left.\frac{\partial p}{\partial x}\right|_{z=0} &= \mathrm{Re}^{-1/2}\left.\frac{\partial p^{(1)}}{\partial x}\right|_{z=0} = \mathrm{Re}^{-1/2}\mathrm{Fr}^2\left.\frac{\partial w^{(1)}}{\partial z}\right|_{z=0} \\ &= -\frac{\mathrm{Fr}^2 c}{\mathrm{Re}^{1/2}(2\pi)^{1/2}}\int_0^{\infty} \mathrm{e}^{-\mathrm{i}\pi/4}\mathrm{e}^{\mathrm{i}kx}k^{1/2}\frac{\mathrm{Fr}^2 k\sinh k - \cosh k}{\mathrm{Fr}^2 k\cosh k - \sinh k}\,\mathrm{d}k \\ &= -\frac{\mathrm{Fr}^2 c}{\mathrm{Re}^{1/2}(2\pi)^{1/2}}I(x,\mathrm{Fr}^2), \end{aligned} \tag{11.14}$$

where the real part is to be taken throughout. In the last line, the phase $\mathrm{e}^{-\mathrm{i}\pi/4}$ has been absorbed into the integral I: this absorption is useful, because now the real part of $\partial p/\partial x$ is proportional to that of I, except through a minus sign.[3] Now, the integrand of $I(x,\mathrm{Fr}^2)$ has magnitude $O(k^{1/2})$ and is unbounded as $k \to \infty$, but the integral is nonetheless convergent for $x \neq 0$, owing to the oscillatory nature of $\mathrm{e}^{\mathrm{i}kx}$. To see this, we separate the integrand into two

[3] This is different from the notation in Tsang et al. (2018), in which the phase was not absorbed into I.

parts, writing

$$\begin{aligned}
\mathrm{e}^{\mathrm{i}\pi/4} I(x,\mathrm{Fr}^2) &= \int_0^\infty \mathrm{e}^{\mathrm{i}kx} k^{1/2}\,\mathrm{d}k + \int_0^\infty \mathrm{e}^{\mathrm{i}kx} k^{1/2} \left\{ \frac{\mathrm{Fr}^2 k\sinh k - \cosh k}{\mathrm{Fr}^2 k\cosh k - \sinh k} - 1 \right\} \mathrm{d}k \\
&= \frac{\pi^{1/2}}{2} \mathrm{e}^{3\mathrm{i}\,\mathrm{sgn}(x)\pi/4} |x|^{-3/2} - \int_0^\infty \mathrm{e}^{\mathrm{i}kx} k^{1/2} \frac{(\mathrm{Fr}^2 k+1)(\cosh k - \sinh k)}{\mathrm{Fr}^2 k\cosh k - \sinh k}\,\mathrm{d}k \\
&= \frac{\pi^{1/2}}{2} \mathrm{e}^{3\mathrm{i}\,\mathrm{sgn}(x)\pi/4} |x|^{-3/2} - J(x,\mathrm{Fr}^2), \\
I(x,\mathrm{Fr}^2) &= \frac{\pi^{1/2}}{2} \mathrm{e}^{(3\,\mathrm{sgn}(x)-1)\mathrm{i}\pi/4} |x|^{-3/2} - \mathrm{e}^{-\mathrm{i}\pi/4} J(x,\mathrm{Fr}^2), \qquad (11.15)
\end{aligned}$$

where the first term has been evaluated using complex analytical methods (Ablowitz and Fokas 2003). When the real part is taken, this term contributes nothing to $\partial p^{(1)}/\partial x$ for $x > 0$, but is nonzero for $x < 0$, and results in a singularity as $x \to 0^-$, which will be discussed later. In the second term, the integrand of $J(x,\mathrm{Fr}^2)$ has a single $O(k^{-1/2})$ singularity at $k = 0$, which is integrable, and has magnitude $O(k^{1/2}\mathrm{e}^{-k})$ as $k \to \infty$. The integral J is therefore convergent and nonsingular even for $x = 0$.

It is not possible to make further progress on evaluating I (or J) analytically, but we may examine the behaviour of I in two limiting cases for Fr.[4] Firstly, in the limit $\mathrm{Fr} \gg 1$ with $x = O(1)$ fixed, we have the asymptotic approximation

$$I(x,\mathrm{Fr}^2) = I(x,\infty) + O(\mathrm{Fr}^{-2}), \qquad (11.16)$$

$$I(x,\infty) = \mathrm{e}^{-\mathrm{i}\pi/4} \int_0^\infty \mathrm{e}^{\mathrm{i}kx} k^{1/2} \tanh k\,\mathrm{d}k \qquad (11.17)$$

$$\begin{aligned}
&= \frac{\pi^{1/2}}{2} \mathrm{e}^{(3\,\mathrm{sgn}\,x-1)\mathrm{i}\pi/4} |x|^{-3/2} \\
&\quad + \frac{\pi^{1/2}}{8} \mathrm{e}^{-\mathrm{i}\pi/4} \left[\zeta\left(\frac{3}{2}, 1 - \frac{\mathrm{i}x}{4}\right) - \zeta\left(\frac{3}{2}, \frac{1}{2} - \frac{\mathrm{i}x}{4}\right) \right], \qquad (11.18)
\end{aligned}$$

the real part understood throughout.[5] When the real part is taken, the second term of (11.18) vanishes for $x > 0$, but is present for $x < 0$ and produces a singularity as $x \to 0^-$. In the first term, $\zeta(s,a)$ is the Hurwitz zeta function, or generalised Riemann zeta function (Abramowitz et al. 1988, Weisstein 2018).[6]

[4] Tsang et al. (2018) gave an asymptotic analysis for J, but it is actually easier to analyse I, to avoid introducing terms that eventually cancel.

[5] The derivation requires the calculation of $x^{-3/2}$ for both $x < 0$ and $x > 0$. We write $x = |x|\,\mathrm{sgn}\,x$, and then use the identity $\mathrm{sgn}\,x = \mathrm{e}^{(1-\mathrm{sgn}\,x)\mathrm{i}\pi/2}$, so that $(\mathrm{sgn}\,x)^{-3/2} = \mathrm{e}^{-3(1-\mathrm{sgn}\,x)\mathrm{i}\pi/4}$. Note the choice of branch cut: we could instead have chosen $\mathrm{sgn}\,x = \mathrm{e}^{-(1-\mathrm{sgn}\,x)\mathrm{i}\pi/2}$. Doing so would change the $-1 + 3\,\mathrm{sgn}\,x$ into $5 - 3\,\mathrm{sgn}\,x$ in (11.18). This flips the sign of the real part for $x < 0$, incorrectly predicting a negative (favourable) pressure gradient in $x < 0$.

[6] For $\Re s > 1$, the Hurwitz zeta function is defined as

$$\zeta(s,a) = \sum_{k=0}^{\infty} (k+a)^{-s},$$

excluding the term $k = -a$ if a is a nonpositive integer. For $s \neq 1$, $\zeta(s,a)$ is defined by analytic continuation. If a is not a nonpositive integer, then the Hurwitz zeta function satisfies the identity

$$\zeta(s,a-1) = \zeta(s,a) + (a-1)^{-s}.$$

It then follows that for $\mathrm{Fr} \gg 1$, the pressure gradient in $x > 0$ is bounded and has magnitude

$$\left.\frac{\partial p}{\partial x}\right|_{z=0} = \mathrm{Re}^{-1/2} \left.\frac{\partial p^{(1)}}{\partial x}\right|_{z=0} = O(\mathrm{Fr}^2 \mathrm{Re}^{-1/2}).$$

Since $\mathrm{Re} \gg 1$, this pressure gradient is small compared to the $O(\mathrm{Fr}^2)$ inertia and viscosity terms in the boundary layer equation (11.3).

The other limit concerns a flow that is only just supercritical, with $\epsilon = \mathrm{Fr}^2 - 1 \ll 1$. For $\epsilon = 0$, the integrand of I has a non-integrable singularity at $k = 0$, suggesting that for $0 < \epsilon \ll 1$ the integral is dominated by a contribution near $k = 0$. The denominator of the integrand has a distinguished scaling (Hinch 1991) for $k = O(\epsilon^{1/2})$, and

$$\begin{aligned} \mathrm{e}^{\mathrm{i}\pi/4} I(x, 1+\epsilon) &\sim -\epsilon^{-3/4} \int_0^\infty \frac{s^{1/2}}{s + s^3/3} \,\mathrm{d}s \\ &= -\frac{3^{1/4}\pi}{2^{1/2}\epsilon^{3/4}}, \end{aligned} \tag{11.19}$$

evaluating the integral using complex analytical methods (Ablowitz and Fokas 2003). Therefore, I has real part

$$\Re(I) = -3^{1/4}\pi\epsilon^{-3/4} \approx -4.13\epsilon^{-3/4},$$

and no dependence on x.[7] The pressure gradient in this limit is *positive* (adverse), due to the minus sign in (11.15), and has magnitude

$$\left.\frac{\partial p}{\partial x}\right|_{z=0} = O(\mathrm{Re}^{-1/2}(\mathrm{Fr}^2 - 1)^{-3/4}), \tag{11.20}$$

which becomes comparable to the inertia and viscosity terms appearing in (11.3) in the distinguished limit

$$\mathrm{Fr}^2 = 1 + O(\mathrm{Re}^{-2/3}). \tag{11.21}$$

The above discussion is summarised by the plot of $\partial p/\partial x$ in figure 11.2. The induced pressure gradient is always positive and adverse. In the limit $\mathrm{Re} \to \infty$ with $\mathrm{Fr} > 1$ fixed, the induced pressure gradient is bounded for all $x > 0$ and does not affect the leading-order boundary layer solution. But this behaviour is not uniform in Fr, and in the distinguished limit (11.21), the pressure gradient is large and comparable to the inertia and viscosity terms.

11.2.3. Discussion

Summary of results

The purpose of this work was to determine whether the boundary layer produced by an abrupt change in basal conditions, as shown in figure 11.1(b), could be treated independently of the free surface: that is, assuming that there is no two-way coupling between the free surface and the boundary layer behaviour. If this decoupling is possible, then in the limit $\mathrm{Re} \to \infty$, the boundary layer grows according to the classical Blasius solution (11.6) (Prandtl 1905, Schlichting and Gersten 2017, Acheson 1990), until the region $x = O(\mathrm{Re})$ when the boundary layer thickness

[7] That is, $\Re(I)$ does not depend on x in the present transitional region for x, before boundary layer saturation.

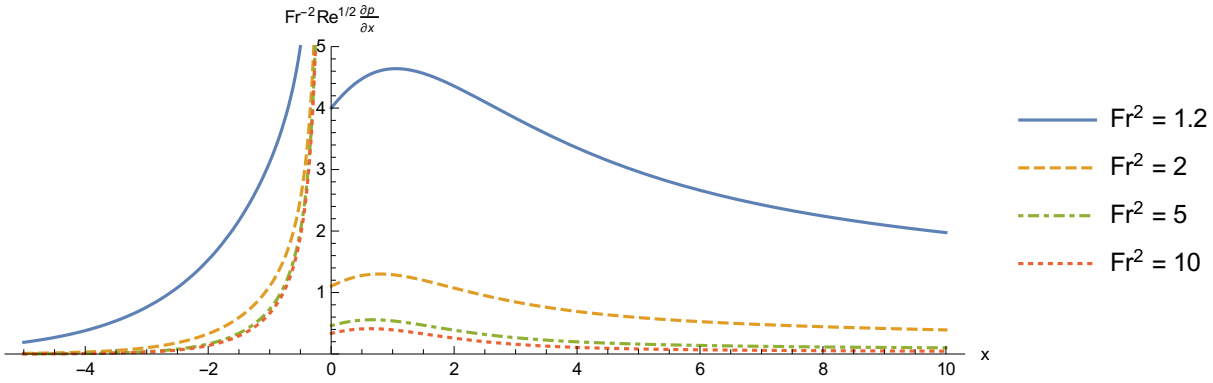

Figure 11.2.: Plots of $\mathrm{Fr}^{-2}\partial p^{(1)}/\partial x$ against x for $\mathrm{Fr}^2 = 1.2, 2, 5, 10$, from the real part of (11.15). Note that dividing by Fr^2 allows a comparison with the inertia and viscosity terms in (11.3).

$(2\mathcal{H}x/\mathrm{Re})^{1/2}$ becomes $O(\mathcal{H})$: that is, when the effects of viscosity have spread so much that the boundary layer thickness may no longer be assumed to be small compared to the depth.

Throughout, we made the assumption that the incident flow is supercritical: that is, that the Froude number $\mathrm{Fr} = \mathcal{U}/\sqrt{g\mathcal{H}} > 1$. Indeed, we saw that the limit $\mathrm{Fr}^2 - 1 \ll 1$ was singular. The supercriticality assumption is required given the formulation of the problem: that is, we are prescribing a particular depth $\mathcal{H}$ and velocity $\mathcal{U}$ far upstream, and assuming that the flow reaches a steady state. By considering the characteristics (Evans 2010) of the shallow water equations (5.3), it can be shown that these requirements on $\mathcal{H}$ and $\mathcal{U}$ on a steady state are compatible only if $\mathcal{U} > \sqrt{g\mathcal{H}}$.

We saw that the value of the Froude number, relative to the Reynolds number, is important in determining the magnitude of the induced pressure gradient, and whether this is comparable to the inertial and viscous terms in (11.3a). For $\mathrm{Re} \to \infty$ with $\mathrm{Fr} > 1$ fixed, the induced pressure gradient is small enough that the classical Blasius behaviour still holds in the boundary layer. On the other hand, if $\mathrm{Re} \gg 1$ but the incident flow is only just supercritical, as in (11.21), then the pressure gradient term in (11.3a) is comparable to the other terms, violating the asymptoticity of the expansions (11.9). In this latter case, there is a full coupling between the boundary layer and the outer layer problems.

These results may be understood by interpreting the square of the Froude number as

$$\mathrm{Fr}^2 = \frac{\rho\mathcal{H}\mathcal{U}^2/2}{\rho g\mathcal{H}^2/2} = \frac{\text{inertia}}{\text{gravitational energy}}.$$

An incident flow with large Fr has plenty of inertia. Although the bottom of this flow is slowed down by the change in basal condition, the main body of the flow will continue unaffected by this retardation; although the surface would rise, the relative weakness of gravity would not create a large pressure gradient. The classical Blasius problem may be regarded as the limiting case $\mathrm{Fr} = \infty$. In the classical problem, though the depth $\mathcal{H}$ of the incident flow be infinite, the gravitational acceleration g is also equal to zero. In other words, the boundary layer still displaces the flow away from the base, which causes the free surface to 'rise', but this does not induce a pressure gradient. In the case $\mathrm{Fr} = \infty$, the induced pressure gradient is not at all comparable to the inertia and viscosity terms.

Domain of validity

The perturbation analysis in §11.2.2 holds for $1 \ll x \ll \mathrm{Re}$, but the problem, as it has been formulated, is ill-posed around $x = 0$ and for x beyond $O(\mathrm{Re})$.

At the leading edge $x = 0$, the sudden change in the basal boundary condition for u, from $u = \mathcal{U}$ in $x < 0$ to $u = 0$ in $x > 0$, is incompatible with the incompressibility assumption (2.2) or (11.1). This unphysicality is present in the classical problem in the absence of a free surface, and will also be an issue in the granular problem. In the classical and hydrofoil cases, the unphysical behaviour arises from treating the aerofoil or hydrofoil as having infinitesimal thickness.

There are also issues downstream, beyond $x = O(\mathrm{Re})$, which require more subtle treatment. As the problem has been stated, the fluid enters the region $x > 0$ with inertia, but as the fluid progresses downstream this inertia is dissipated due to viscous drag from the base. By compressibility, the depth of the current must increase indefinitely as $x \to \infty$.

The $O(\mathrm{Re}^{-1/2})$ analysis above does not predict this downstream problem. Instead, it asserts that the displacement velocity (11.11c) vanishes as $x \to \infty$, as do the perturbation quantities $w^{(1)}$ and $\partial p^{(1)}/\partial x$, according to the Riemann–Lebesgue lemma (Burkill 2002) for Fourier integrals such as (11.13) and (11.15). The error comes from the assumption that the flow can be broken down into an outer layer and a boundary layer, with the latter being thin: for $x = O(\mathrm{Re})$, the boundary layer thickness $c\mathrm{Re}^{-1/2}(2x)^{1/2}$ can no longer be assumed to be small.

The unphysical behaviour at $x = O(\mathrm{Re})$ and beyond can be averted by replacing the present system with slightly different setups, shown in figures 11.3 and 11.4. One resolution, shown in figure 11.3, is to replace the infinite downstream plate with one of finite length L, such that $1 \ll L \ll \mathrm{Re}$. If the flow remains supercritical at $x = L$, then the finite length and the details at the trailing edge do not affect the behaviour in $x = O(1)$, which is still governed by the analysis given earlier in this section.

An alternative resolution, which is more directly relevant to the granular case, is to incline the system at an angle θ. Doing so introduces a favourable acceleration that eventually balances against viscous resistance. Provided that $\theta < O(1/\mathrm{Re})$, then, in the transitional region, the streamwise gravitational is subdominant to the inertia and the viscosity, so that the previous analysis continues to be relevant. The flow far downstream converges towards a Nusselt (semi-Poiseuille) velocity profile,

$$u_{\mathrm{Nus}}(z) = \frac{g\sin\theta}{\nu}\left(h_{\mathrm{Nus}}z - z^2/2\right), \tag{11.22}$$

and by conservation of flux, the depth h converges towards the Nusselt depth,

$$\left(\frac{h_{\mathrm{Nus}}}{\mathcal{H}}\right)^3 = \frac{3\mathrm{Fr}^2}{\mathrm{Re}\sin\theta}, \tag{11.23}$$

where $\mathcal{H}$, Re and Fr are the depth, Reynolds number and Froude number of the *incident* flow. The profile (11.22) is the velocity profile of a Newtonian fluid film with an exact balance between gravitational driving $g\sin\theta$ and viscous resistance: at far-downstream positions, the inertia of the incident flow is spent. When we study the granular case in the next section, the far-downstream Nusselt profile shall be replaced by its granular analogue, the Bagnold profile. This convergence towards an equilibrium profile far away from a topographical feature has already been seen in Chapter 5, and will be seen again in Chapter 12.

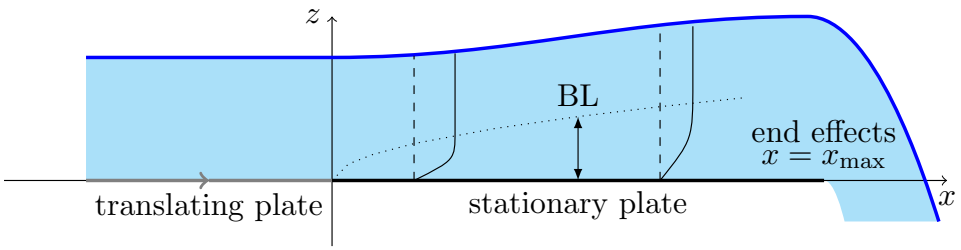

Figure 11.3.: A plate of finite length $1 \ll L \ll \mathrm{Re}$. The perturbation solution found in §11.2.2 applies to the region $x = O(1)$, but breaks down for $x = O(L)$ when end effects become important.

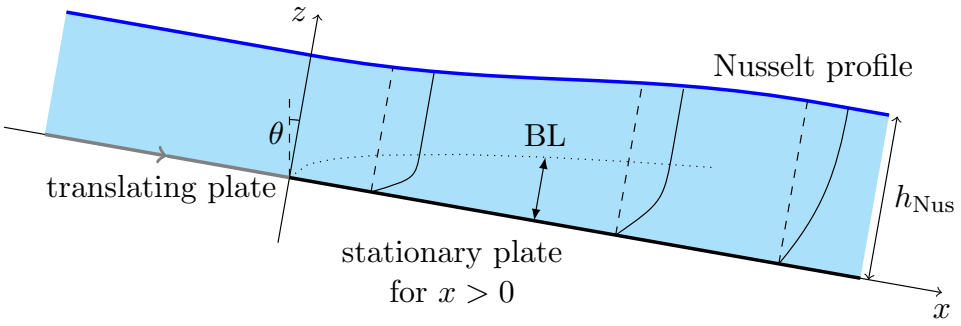

Figure 11.4.: A plate inclined at an angle θ. The effect of streamwise gravity is subdominant for $x = O(1)$ provided that $\theta \ll 1$, so that the perturbation solution is valid there. Gravity eventually becomes important and the flow develops into a Nusselt film, with velocity given by (11.22) and depth h_{Nus} given by (11.23).

The domain of validity might also be limited by downstream flow instabilities. We have restricted our attention to steady and laminar solutions to the Navier–Stokes equations; in reality, the flow may develop instabilities and transition towards turbulence. The downstream distance over which an instability would develop can be predicted by considering when the streamwise Reynolds number Ux/ν exceeds certain critical values for the Reynolds number (Drazin and Reid 2004).

11.3. Analysis of the granular Blasius problem under the $\mu(I)$ rheology

We now return to the case of a granular material, which we assume to be governed by the incompressible $\mu(I)$ rheology (2.10). In this section, we shall derive an equation (11.25b) that governs a granular boundary layer, just as (11.3a) governs that of a classical boundary layer. We shall then give solutions to this equation for particular cases of the function $\mu(I)$.

The hydrofoil problem of §11.2 and the granular Blasius problem have in common the presence of a free surface. In both cases, the deceleration of the flow in the boundary layer causes a perturbation flow in the outer flow, displacing the free surface upwards, creating a pressure gradient that may in turn affect the boundary layer. The work of §11.2 suggests that this induced pressure gradient may be considered small provided that the Froude number of the incident flow is sufficiently high.

We shall proceed by making the assumption that the same is true of the granular case. However, for a granular flow governed by the $\mu(I)$ equations, it is not possible to repeat the methods of §11.2 to calculate the perturbation to the outer flow; the analogous linearised equations, which are given in §B.3 in the appendix, are much more complicated than the simple Laplace equation (11.11a); they are only semilinear and cannot be solved analytically. Therefore, although the assumption is reasonable on the physical grounds given in §11.2.3, we have not been able to justify it mathematically.

The setup studied in §11.2 was on a flat surface, with gravity pointing straight down and having no streamwise components. We discussed in §11.2.3 that a slope θ must be introduced to provide a streamwise acceleration that eventually balances the viscous resistance, to produce a Nusselt film. The same is true of the granular case: for a steady flow to be sustained over an indefinite length, the slope θ should be nonzero, and furthermore such that $\mu^{-1}(\tan\theta)$ exists. In the hydrofoil case, we noted that if $\theta \ll \mathrm{Re}^{-1}$ then the streamwise acceleration is negligible compared to the balance between inertia and viscosity, at least up to $x = O(\mathrm{Re})$. We shall assume that the same is true of the granular problem; as we shall see, it remains the case that the boundary layer is a region of high shear rate, and that the associated shear stress dominates the streamwise acceleration due to gravity (§11.3.3).

In the hydrofoil problem, there were two nondimensional parameters, Re and Fr; the inverses Re^{-1} and Fr^{-1} expressed, respectively, the magnitudes of viscosity and gravitational acceleration relative to the inertia of the incident flow. The analysis in §11.2 concerned the limit $\mathrm{Re} \gg 1$ with Fr fixed, and the boundary layer thickness scaling was $\epsilon = \mathrm{Re}^{-1/2} \ll 1$. For the present granular problem, the (Newtonian) viscosity is replaced by the friction function $\mu(I)$; we fix this function and work in the limit $\mathrm{Fr} \gg 1$. There are a number of additional nondimensional parameters, including the grain size $\delta = d/\mathcal{H}$ and the slope θ. It is not immediately clear how

the boundary layer thickness scale ϵ should depend on these parameters, but we shall find it by again balancing the magnitudes of inertial and frictional terms, eventually obtaining the formula (11.27) for ϵ.

11.3.1. Preliminaries

We define $\mathcal{H}$ and $\mathcal{U}$ as, respectively, the depth and mean velocity of the incident flow; the flow rate is $q = \mathcal{H}\mathcal{U}$. We define the Froude number based on that of the incident flow, $\mathrm{Fr} = \mathcal{U}/(g\mathcal{H})^{1/2}$. We shall work in the limit $\mathrm{Fr} \gg 1$: this approximation allows analytical progress to be made; as explained in the preface to Part III, the limit $\mathrm{Fr} \gg 1$ is of interest to avalanche modelling.

We work with the incompressible $\mu(I)$ equations,

$$\boldsymbol{\nabla} \cdot \boldsymbol{u} = 0, \tag{2.2}$$

$$\rho \left(\frac{\partial \boldsymbol{u}}{\partial t} + \boldsymbol{u} \cdot \boldsymbol{\nabla}\, \boldsymbol{u} \right) = \rho \boldsymbol{g} - \boldsymbol{\nabla}\, p + \boldsymbol{\nabla} \cdot \left(\mu(I) p \boldsymbol{s} \right), \tag{2.10}$$

not yet making any statements about the function $\mu(I)$. We assume the flow is steady, so that $\partial/\partial t = 0$; and that the packing fraction ϕ, and therefore the density ρ, are constants.

We supplement (2.10) with basal boundary conditions on $z = 0$, taking the no-penetration condition $w = 0$, the no-slip condition $u = 0$ on $x > 0$, and allowing slip for $x < 0$. The problem as it has been stated is locally ill-posed at $x = z = 0$ due to the infinite velocity gradient $|\partial u/\partial x| = \infty$ there. We have already discussed the applicability of the no-slip condition in a continuum model (§4.2.2), noting that it is an empirical condition and not one that directly arises from the fundamental behaviour of grains, and we shall return to this issue in §11.5.1. For now, we shall note that the DPM simulations in §11.4 satisfy the no-slip condition in $x > 0$, except within a short transition region, in which the slip velocity decays but does not immediately vanish, as illustrated in figure 11.9.

The incident flow takes the Bagnold-with-slip velocity profile (2.12). In the limit $\mathrm{Fr} \gg 1$, the Bagnold-with-slip profile is approximately a plug flow. Meanwhile, the far-downstream flow is Bagnoldian (without slip). The depth-averaged analysis (§10.2.2) suggests that the adjustment towards the far-downstream profile takes place over an $O(\mathrm{Fr}^2)$ lengthscale, while the disturbance just upstream of $x = 0$ is confined to a short region of length $O(\mathrm{Fr}^{-1})$. We therefore neglect this upstream disturbance, and assume that the velocity profile at $x = 0$ is a plug flow, $u \sim \mathcal{U}$, to leading order in the limit $\mathrm{Fr} \gg 1$.

11.3.2. Boundary layer scalings: The granular Blasius equation

We next consider the transitional region $0 < x \ll \mathrm{Fr}^2\mathcal{H}$, in which the current adjusts between its upstream and downstream equilibria, and in which the internal velocity profile is distorted by the formation and development of the basal boundary layer. Our approach to analysing the boundary layer using the $\mu(I)$ rheology shall be similar to the technique of Prandtl (1905) for deriving the classical Blasius boundary layer from the Navier–Stokes equations (see *e.g.* Acheson (1990), Schlichting and Gersten (2017)).

In the following, we use a different notation from that of §11.2 for nondimensionalisation. In the boundary layer, we again introduce rescalings for the perpendicular coordinate and velocity component,

$$z = \epsilon \mathcal{H} \tilde{z}, \quad w = \epsilon \mathcal{U} \tilde{w}, \tag{11.24}$$

where ϵ is a scaling for the boundary layer thickness at $x = \mathcal{H}$, which is to be determined. The actual boundary layer thickness $\Lambda(x)$ will be proportional to ϵ but grows with x. We also nondimensionalise $x = \mathcal{H}\tilde{x}$ and $u = \mathcal{U}\tilde{u}$, not scaling them by ϵ.

When these substitutions are made, incompressibility (2.2) reads

$$\frac{\partial \tilde{u}}{\partial \tilde{x}} + \frac{\partial \tilde{w}}{\partial \tilde{z}} = 0, \tag{11.25a}$$

the streamwise component of the granular momentum equation (2.10) gives

$$\mathrm{Fr}^2 \left(\tilde{u} \frac{\partial \tilde{u}}{\partial \tilde{x}} + \tilde{w} \frac{\partial \tilde{u}}{\partial \tilde{z}} \right) \sim \sin\theta + \frac{1}{\epsilon} \frac{\partial \tilde{p}}{\partial \tilde{z}} \left(\mu - \frac{1}{2} \frac{\mathrm{d}\mu}{\mathrm{d}I} I \right) + \frac{1}{\epsilon} \tilde{p} \frac{\mathrm{d}\mu}{\mathrm{d}I} I \frac{\partial^2 \tilde{u}/\partial \tilde{z}^2}{\partial \tilde{u}/\partial \tilde{z}}, \tag{11.25b}$$

and the inertial number is

$$I \sim \frac{1}{\epsilon} \frac{\delta \mathrm{Fr}}{\tilde{p}^{1/2}} \frac{\partial \tilde{u}}{\partial \tilde{z}} \,. \tag{11.25c}$$

Details of the derivation of (11.25b) are given in the appendix (§B.1). In the above, we have dropped a number of subdominant terms; in particular, the pressure may be treated as being approximately constant across the boundary layer, since $\partial \tilde{p}/\partial \tilde{z} = O(\epsilon)$, so that $\tilde{p} \sim \cos\theta$ is approximately the hydrostatic value from the outer layer.

We shall refer to (11.25b) as the 'granular Blasius equation', governing the velocity in the boundary layer near $z = 0$ in the transition region. This name reflects its similarity to the classical Blasius equation (11.3a), which governs a classical boundary layer (Schlichting and Gersten 2017). The terms on the right-hand side of (11.3a) represent, respectively, the effects of a pressure gradient and of viscosity; comparing with (11.25b), we see that streamwise acceleration $g \sin\theta$ plays the role of a favourable pressure gradient, while the second term, a frictional term, plays that of an adverse pressure gradient. Meanwhile, the final term in (11.25b), which contains the second derivative $\partial^2 \tilde{u}/\partial \tilde{z}^2$, has a similar effect to the viscous term, but is multiplied by a prefactor that is not constant but depends on $\partial \tilde{u}/\partial \tilde{z}$, in general nonlinearly.

In the absence of a rheology, to discriminate between the relative importance of the terms in the general equation (11.25b) we need to retain all the terms in (11.25b). In the next subsection we shall introduce a rheology of the generalised form given in (2.17), under which the first two terms on the right-hand side of (11.25b), corresponding to the pressure gradient, become subdominant. This results in a dominant balance in (11.25b) between the inertial terms on the left and the final, 'viscous' term on the right.

11.3.3. Similarity solutions

When the streamwise pressure gradient term is removed, the classical Blasius equation (11.3a) admits a similarity solution[8] and predicts a boundary layer that grows with thickness $\Lambda(x) \propto$

[8] It is also possible to find similarity solutions when $\tilde{p}$ and $\partial \tilde{p}/\partial \tilde{x}$ have power-law or exponential dependence on x (Acheson 1990).

$(x/\mathrm{Re})^{1/2}$. We now discuss analogous results for the system (11.25), when suitable approximations are made. Of central importance is the observation that, of the terms on the right-hand side of (11.25b), the final 'viscosity' term will be shown to be $O(1/\epsilon)$ larger than the other two terms. We first find the boundary layer thickness scaling ϵ in terms of the other parameters, in such a way that the dominant balance in (11.25b) is between this term and the inertial terms on the left. We do this by considering the sizes of the terms containing μ and $\mathrm{d}\mu/\,\mathrm{d}I$.

To make any progress, we must specify the function $\mu(I)$ to be used in (11.25b). It is evident from (11.25c) that the inertial number is large in the boundary layer, on account of the $O(1/\epsilon)$ prefactor. This reflects the high shear rate in that layer: the dimensional velocity must adjust from zero at the no-slip boundary to the outer flow's $O(\mathcal{U})$ slip velocity, over the short depth $O(\epsilon\mathcal{H})$. The behaviour of solutions to (11.25b) are therefore dependent on the high-I asymptotic behaviour of the function $\mu(I)$.

While several functional forms are possible for $\mu(I)$ (§2.3), we propose the use of the power-law form (2.17). The form (2.17) has the advantage that $\mathrm{d}\mu/\,\mathrm{d}I$ has a power-law dependence on I, which will allow a similarity solution. Moreover, we fit (2.17) only *asymptotically*: in other words, the parameters μ_s, m and α shall be determined only by fitting (2.17) to large values of I. In practice, we shall take $I > 0.5$ as the cutoff.

Substituting (2.17) into (11.25b), writing I out using (11.25c), and dropping the subdominant terms, we obtain

$$\mathrm{Fr}^2\left(\tilde{u}\,\frac{\partial\tilde{u}}{\partial\tilde{x}}+\tilde{w}\,\frac{\partial\tilde{u}}{\partial\tilde{z}}\right)\sim\frac{1}{\epsilon^{1+\alpha}}\alpha m\cos\theta\left[\frac{\delta\mathrm{Fr}}{(\cos\theta)^{1/2}}\right]^{\alpha}\frac{\partial^2\tilde{u}/\partial\tilde{z}^2}{(\partial\tilde{u}/\partial\tilde{z})^{1-\alpha}}. \tag{11.26}$$

The boundary layer thickness ϵ may now be chosen in terms of the other parameters that appear. Taking

$$\epsilon=\left[\frac{\alpha m\cos\theta}{\mathrm{Fr}^2}\left[\frac{\delta\mathrm{Fr}}{(\cos\theta)^{1/2}}\right]^{\alpha}\right]^{1/(1+\alpha)} \tag{11.27}$$

reduces (11.26) to

$$\tilde{u}\,\frac{\partial\tilde{u}}{\partial\tilde{x}}+\tilde{w}\,\frac{\partial\tilde{u}}{\partial\tilde{z}}\sim\frac{\partial^2\tilde{u}/\partial\tilde{z}^2}{(\partial\tilde{u}/\partial\tilde{z})^{1-\alpha}}. \tag{11.28}$$

The derivation of (11.25b), given in §B.1 in the appendix, makes the assumption that $\epsilon\mathrm{Fr}\ll 1$, and we must check *a posteriori* whether this is true of the ϵ given in (11.27), at least for realistic values of δ and Fr if not unconditionally true. Estimations on the size of $\epsilon\mathrm{Fr}$ are given in §B.2 in the appendix. It will be shown that if $\alpha\geq 0$, then $\epsilon\mathrm{Fr}\ll 1$ is satisfied either automatically, or in practice for realistic values of δ and Fr.

The reduced equation (11.28) is analogous to the classical boundary layer equation (11.5), the difference being on the right-hand side, which is now nonlinear, reflecting the fact that the 'granular viscosity' depends on the shear rate. Using the incompressibility condition to relate $\tilde{u}$ and $\tilde{w}$, a similarity solution to (11.28) may be now found, using similar techniques as for the classical Blasius problem. This solution takes the form

$$\tilde{u}=f'(\zeta),\quad \zeta=\tilde{x}^{-1/(1+\alpha)}\tilde{z}, \tag{11.29}$$

where f is the solution to the boundary value problem

$$f'''+\frac{1}{1+\alpha}(f'')^{2-\alpha}f=0,\quad f(0)=f'(0)=0,\quad \lim_{\zeta\to\infty}f'(\zeta)=1, \tag{11.30}$$

α	ζ_{disp}	$\zeta_{\text{disp}} f''(0)$
0	15.30	1.14
1/10	9.86	0.98
1/3	4.51	0.73
1/2	3.10	0.65
1	1.70	0.57

Table 11.1.: Values of ζ_{disp} and $f''(0)$ for solutions to (11.30) with various values of α.

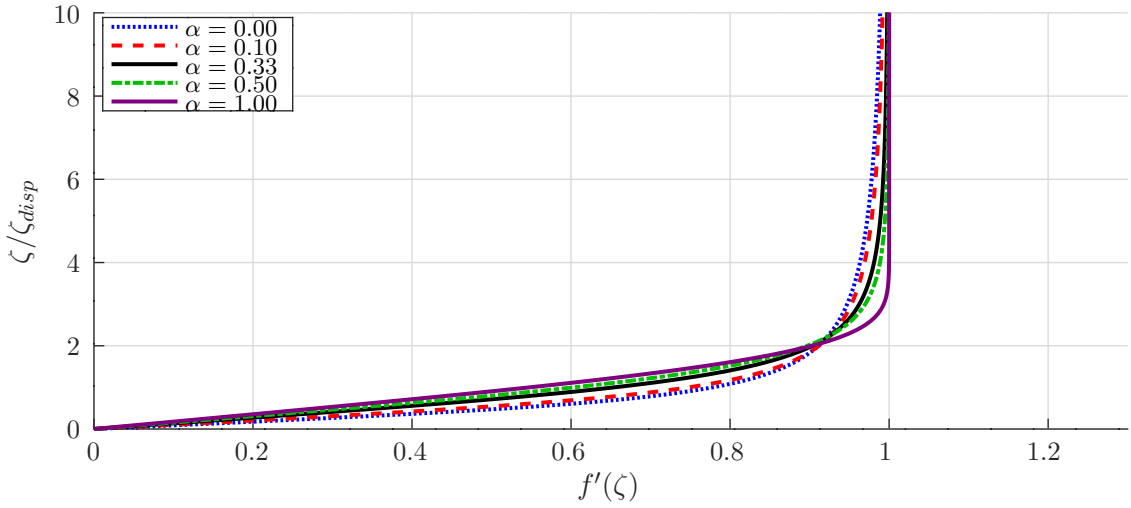

Figure 11.5.: Numerical solution to (11.30) for $\alpha = 0, 1/10, 1/3, 1/2, 1$. In each case, the vertical axis has been rescaled by ζ_{disp} to make visual inspection more convenient. The values for ζ_{disp} and $\zeta_{\text{disp}} f''(0)$ are given in table 11.1. The profile for $\alpha = 1$ is the classical Blasius profile.

with the boundary conditions at $\zeta = 0$ imposing the no-penetration and no-slip conditions, and the condition as $\zeta \to \infty$ ensuring that the matching condition be satisfied. The system (11.30) is solved numerically using a shooting method. Figure 11.5 shows the boundary layer profiles $f'(\zeta)$ for a number of values of α. When visually inspecting the thickness of a boundary layer from simulation or experimental results, it is useful to quote the boundary layer in terms of the 'displacement thickness' (Schlichting and Gersten 2017) $\zeta_{\text{disp}}\Lambda(x)$, where

$$\zeta_{\text{disp}} = \lim_{\zeta \to \infty} \left(\zeta - f(\zeta) \right),$$

which depends on α (see table 11.1). Accordingly, the vertical axis of figure 11.5 has been rescaled by ζ_{disp} in each plot.

Reverting to dimensional quantities, the similarity solution shows that the boundary layer thickness $\Lambda(x)$ is given by

$$\frac{\Lambda(x)}{\mathcal{H}} = \epsilon \left(\frac{x}{\mathcal{H}} \right)^{1/(1+\alpha)}. \tag{11.31}$$

Moreover, from (11.27), we have

$$\epsilon \propto \left(d^{\alpha} g^{1-\alpha/2} \mathcal{H}^{1-3\alpha/2} \mathcal{U}^{-(2-\alpha)} \right)^{1/(1+\alpha)}, \tag{11.32}$$

after dropping $O(1)$ nondimensional constants, and so

$$\Lambda(x) \propto \left(d^{\alpha} (g\mathcal{H})^{1-\alpha/2} \mathcal{U}^{-(2-\alpha)} x \right)^{1/(1+\alpha)}. \tag{11.33}$$

For the species of particles used in the DPM simulations (§11.4), calibration tests showed that the function $\mu(I)$, for $I > 0.5$, can be fitted to a power law form (2.17) with $\alpha = 0.34$ (table 11.2). For now, using the value $\alpha = 1/3$ give rational expressions for the exponents:

$$\Lambda(x) \propto d^{1/4} (g\mathcal{H})^{5/8} \mathcal{U}^{-5/4} x^{3/4}. \tag{11.34}$$

The $\Lambda(x) \propto x^{3/4}$ dependence suggests that the granular boundary layer grows more slowly than the $x^{1/2}$ dependency for a Newtonian fluid.

From (11.31) and (11.27) we can also estimate the lengthscale x downstream of the transition point when boundary layer saturation begins to occur: $\Lambda(x) \sim \mathcal{H}$ when

$$\frac{x}{\mathcal{H}} \sim \epsilon^{-1/(1+\alpha)} \sim \delta^{-\alpha} \mathrm{Fr}^{2-\alpha} = \delta^{-1/3} \mathrm{Fr}^{5/3}. \tag{11.35}$$

This is distinct from the $O(\mathrm{Fr}^2)$ adjustment lengthscale identified by the depth-averaged model (§10.2.2). We attribute this distinction to the presence of two separate processes: on the one hand, the development of the boundary layer is governed by the internal rheological behaviour of the flow; on the other, the adjustment towards the final equilibrium state results from the interaction and eventual balance between gravitational acceleration and friction. Both of these had been neglected in the boundary layer analysis, when we dropped the first two terms on the right-hand side of (11.25b) to obtain (11.28), identifying them as subdominant in the limit of high shear rate.

The lengthscale (11.35) decreases with increasing δ: this is to be expected, since increasing δ is akin to increasing the 'granular viscosity', causing momentum to diffuse within the current more quickly.

11.3.4. Particular cases: $\alpha = 1$ and $\alpha \leq -1$

In this subsection we explore specific cases for the exponent α. As previously mentioned, the value of α is a fitting parameter for empirical data on the behaviour of the function $\mu(I)$. The case $\alpha = 1$ has no special significance and is not necessarily consistent with any real granular material in practice, but we consider it here for demonstration purposes.

If $\alpha = 1$, then $\mu(I)$ takes the affine form $\mu(I) \sim \mu_s + mI$ for large I, and the boundary layer equation (11.28) reduces to exactly the same form as the classical Blasius equation. For $\alpha = 1$, the boundary layer thickness scale is

$$\epsilon = \left[\frac{m(\cos\theta)^{1/2}\delta}{\mathrm{Fr}} \right]^{1/2},$$

and the boundary value problem (11.30) reduces to (11.7), the BVP that gives the profile of a classical Blasius boundary layer in the absence of a pressure gradient. The boundary layer

thickness is given by

$$\frac{\Lambda(x)}{\mathcal{H}} = \epsilon \left(\frac{x}{\mathcal{H}} \right)^{1/2} = \mathrm{Re}_{\mathrm{GB}}^{-1/2} (x/\mathcal{H})^{1/2}, \tag{11.36}$$

where the 'granular Blasius Reynolds number' $\mathrm{Re}_{\mathrm{GB}}$ plays a similar role to the classical Reynolds number, expressing the ratio between inertia and 'viscosity', the latter being the diffusivity of momentum, proportional to the particle size d.

Next, we consider the case $\alpha = -1$, which encompasses the asymptotic behaviour of the Jop fit (2.16). In contrast to the $\alpha = 1$ case described already, the cases $\alpha \leq -1$ imply a physically unreasonable solution for the boundary layer.

With $\alpha = -1$, the exponent of x in the boundary layer thickness (11.33) takes the undefined value $1/0$, and for $\alpha < -1$, the exponent of x is negative, implying a boundary layer thickness that decays with x. This behaviour is qualitatively distinct from the previously mentioned $\alpha = 1$ case, from the results of DPM simulations, and from what we might intuitively expect, in which the boundary layer thickness should grow with x. The fact that $\alpha = -1$ does not give a correct solution may be related to the ill-posedness of the Jop fit (2.16) at high inertial numbers, which Barker et al. (2015) established for steady uniform flows. However, further work, outside the scope of this thesis, would be needed to establish whether or not the $\mu(I)$ rheology is uniformly well-posed for $\alpha > -1$ in this geometry.

The form (2.16) was chosen as a convenient fitting curve for the function $\mu(I)$, and it would seem reasonable that the exact mathematical form of the fitting function should not have an effect on the qualitative behaviour of the flow. However, the present analysis has shown that the asymptotic behaviour of $\mu(I)$ has an important effect on the boundary layer profile, and that the $\alpha = -1$ case is particularly problematic. Informally, the bound $\alpha > -1$ states that either $\mu(I)$ should grow unboundedly as $I \to \infty$, or μ should tend to a constant value but not converge too quickly as $I \to \infty$.

11.3.5. Evolution of the velocity profile

In the preceding subsections, we have given descriptions for the velocity profile throughout the current in the asymptotic case $\mathrm{Fr}^2 \gg 1$, which may be summarised as follows. The incoming flow's velocity profile is Bagnold-with-slip (2.12). For high Fr, the slip velocity is large compared to the Bagnoldian velocity (2.14), and the incident profile is approximately a plug flow, with $\chi \sim 1$. The shape factor increases throughout the transitional regime $0 < x \ll \mathrm{Fr}^2$ as the velocity profile evolves between the far-upstream and far-downstream behaviours. Within this transitional region, the velocity profile may be divided into a boundary layer, in which the basal friction resists the inertia of the incident flow, and an outer layer. Under certain conditions on the mathematical form of the function $\mu(I)$, the boundary layer has a self-similar profile (§11.3.3) with a thickness that grows according to (11.33). The outer layer initially remains plug-like, but experiences a perturbation flow from the growth of the boundary layer; we assume that this perturbation flow is small for $\mathrm{Fr}^2 \gg 1$ and $x \ll \mathrm{Fr}^2$, based on the study on a Newtonian fluid in §11.2. Eventually, the boundary layer saturates as its thickness becomes comparable to that of the whole current, although this saturation is not described by the first-order perturbation theory of §11.2. After saturation, the entire current is then governed by a balance between

basal friction and gravity, with the inertia of the incident flow having been spent. The velocity profile is then Bagnold without slip, and so $\chi \to 5/4$ as $x \to \infty$.

Figures 11.12 and 11.13 demonstrate the evolution of velocity profiles towards the Bagnoldian profile as x progresses.

11.3.6. Evolution of the shape factor

The evolution of the velocity profile may be neatly encapsulated by studying the shape factor χ, defined in (5.6), as a function of x. The evolution of χ can be used in a depth-averaged model (§5.2).

An analytic expression for the growth of the shape factor (to leading-order accuracy in ϵ) cannot be obtained without calculating the perturbation flow $(u^{(1)}, w^{(1)})$ in the outer layer, induced by the boundary layer. This calculation was performed in §11.2 for a Newtonian fluid, for which the perturbation velocity $w^{(1)}$ satisfies the simple equation (11.11a), and the system (11.11) could be solved in terms of Fourier integrals and special functions. The same calculation under the $\mu(I)$ rheology is outside the scope of the present work, as the perturbation variables satisfy a more complicated system of equations, given in the appendix (§B.3). The equations are nonetheless semilinear, and by scaling arguments we may estimate the growth of χ from the approximate solution found in §11.3.3. The boundary layer thickness (11.33) and the incompressibility condition (2.2) together imply that the perpendicular displacement velocity from the boundary layer has magnitude

$$\epsilon w^{(1)} = O\left(\mathcal{U}\Lambda(x)/x\right) = O\left(\epsilon(x/\mathcal{H})^{-\alpha/(1+\alpha)}\right).$$

This displacement velocity is transmitted into the outer flow $w^{(1)}$. Again by incompressibility, the streamwise perturbation flow in the outer layer is of magnitude

$$\epsilon u^{(1)} = O\left(\epsilon w^{(1)} x/\mathcal{H}\right) = O\left(\epsilon(x/\mathcal{H})^{1/(1+\alpha)}\right),$$

this perturbation being negative as the flow is decelerating. The kinematic free surface boundary condition (4.3) implies that

$$h'(x) = O\left(\epsilon(x/\mathcal{H})^{-\alpha/(1+\alpha)}\right), \quad \text{so that} \quad h(x)/\mathcal{H} - 1 \sim \gamma\epsilon(x/\mathcal{H})^{1/(1+\alpha)},$$

for some constant γ. With these scaling laws for $h/\mathcal{H} - 1$ and $u^{(1)}$, it can be shown that

$$\chi - 1 \propto \epsilon(x/\mathcal{H})^{1/(1+\alpha)} = \epsilon(x/\mathcal{H})^{3/4}, \tag{11.37}$$

on setting $\alpha = 1/3$. The incident flow has shape factor approximately 1, assuming that the Froude number is high enough that the slip velocity dominates any internal profile.[9]

The law (11.37) shall be compared to the results of DPM simulations in §11.4.5. It shall indeed be seen that (11.37) is suitable for large Fr, but not as accurate for low Fr.

[9] See §5.3 for an estimate on the magnitude of the relative error of χ resulting from these approximations.

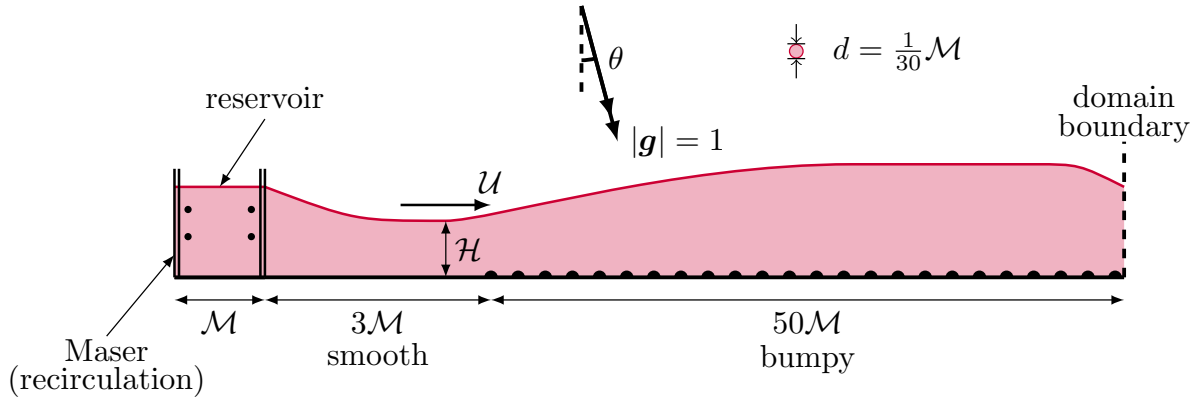

Figure 11.6.: Sketch of the setup for DPM simulations. From Tsang et al. (2019).

11.4. DPM simulations of the granular Blasius problem

Having calculated the velocity profiles and the evolution of χ that the incompressible $\mu(I)$ rheology prescribes, we now realise the granular Blasius problem in DPM simulations, in order to compare between the results of these simulations and the predictions of the continuum model. In §11.4.1 we describe the setup of these simulations, applying the techniques previously described in Part II. The DPM simulations for this work (as for the work in Tsang et al. (2019)) were conducted using the software package MercuryDPM (Weinhart et al. 2017, Thornton et al. 2012, 2013, Weinhart et al. 2012).

11.4.1. Setup of DPM simulations

The setup of the DPM simulations for the granular Blasius problem is shown in figure 11.6. As in Part II, simulations are conducted in two dimensions, and particles are discs. The particles are introduced from a reservoir by means of a Maser (§8.3.3) of length $\mathcal{M}$, which is initially populated using an insertion boundary (§8.2). During a simulation, the speed of the particles inside this reservoir is kept constant by applying a drag force (§8.3.4). The slope θ, the depth of the reservoir and the incident speed can all be varied. The flow behaviour depends on the ratio between d and the reservoir depth, and is insensitive to $\mathcal{M}$, provided that $d \ll \mathcal{M}$.

The reservoir is placed on a smooth boundary at a distance $3\mathcal{M}$ upstream of the transition point $x = 0$. The incident velocity $\mathcal{U}$ is defined as the maximum slip velocity in the region $x < 0$, and the incident depth $\mathcal{H}$ is defined as the depth of the current at this position.[10, 11]

A deletion boundary (§8.4) is placed at the end of the chute, at $x = 50\mathcal{M}$. This distance is chosen to be at least $2.5\mathrm{Fr}^2\mathcal{H}$ for all the cases that we study. Convergence studies show that, provided Fr is sufficiently high, the flow towards the end of the chute is supercritical, so endpoint effects from the deletion boundary are localised (§10.1.3).

[10] The position of a free surface from discrete results cannot be defined exactly (§9.1.2), but through trial and error we managed to control $\mathcal{H}/d$ to within 1 part in 50.

[11] Note that $\mathcal{U}$ and $\mathcal{H}$ are not the same as the speed of particles and the depth of the current within the Maser, because there is some acceleration and thinning in the region $-3\mathcal{M} < x < 0$.

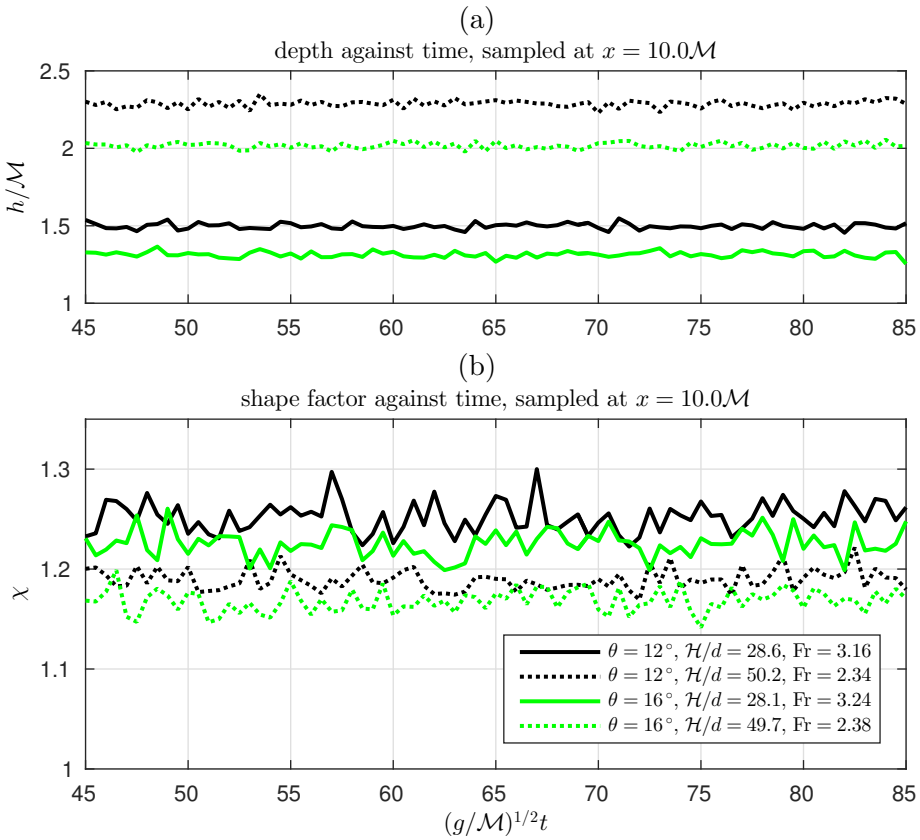

Figure 11.7.: Data from four DPM simulations of the granular Blasius problem, showing the time-variation of (a) the flow depth h and (b) the at the fixed location $x = 10\mathcal{M}$, over the interval $(g/\mathcal{M})^{1/2}t \in [45, 95]$.

In these simulations, $\delta = d/\mathcal{H} \approx 1/50$, which was small enough that the continuum approximation was appropriate[12], while large enough to limit computational costs. A frozen-particle base is used in $x > 0$, and its details are described in §11.4.3.

The simulations reach a quasi-steady state after running for a duration of $T = 45(\mathcal{M}/g)^{1/2}$. They are then allowed to run for a further duration $\Delta T = 40(\mathcal{M}/g)^{1/2}$ in this steady state, during which time-averaged quantities were computed (sampled at intervals of $0.5(\mathcal{M}/g)^{1/2}$). Figure 11.7 shows the time-dependence of the flow depth h and the shape factor χ at a fixed position for four different simulations, and shows that the variations of h and χ are small. The internal velocity profiles also have small variation; the supplementary figure B.2 in Appendix B shows that the variance with time is very small compared to the mean flow, except near $z = 0$ where the mean flow itself is small.

11.4.2. Particle properties

Particle interactions in these simulations are governed by a linear spring-dashpot (viscoelastic) model, with a coefficient of restitution $e = 0.1$. There are no particle-to-particle tangential

[12]The calibration tests on δ in §9.4 showed that the rheological function $\mu(I)$ was largely independent of δ for $\delta \leq 1/20$, while the shape factor χ took its Bagnoldian value 5/4 in a steady uniform state.

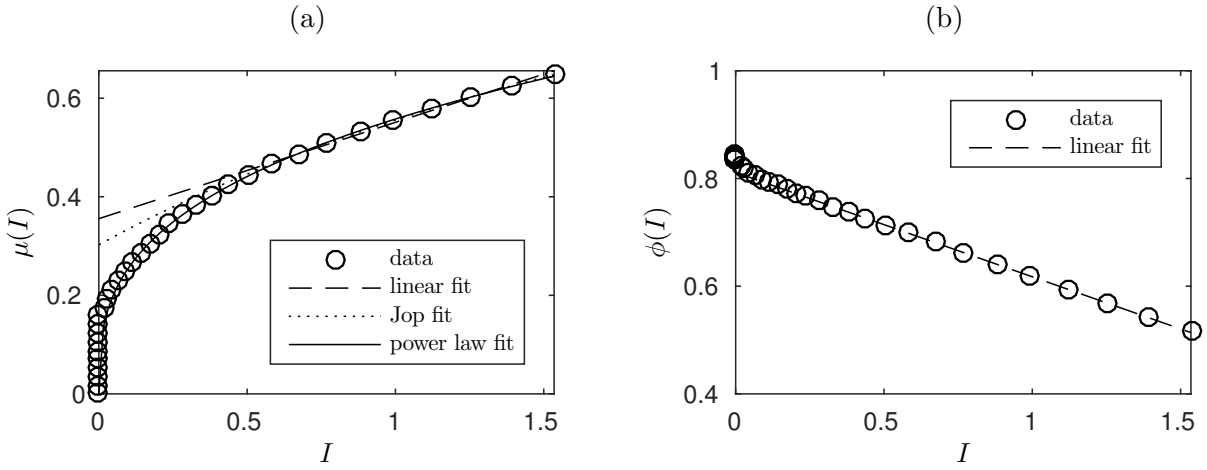

Figure 11.8.: (a) Results from calibration tests for the function $\mu(I)$ used in our DPM simulations for Chapter 11, together with linear, Jop (2.16) and power-law (2.17) fits for $I > 0.5$ The fitting parameters are shown in table (11.2). (b) The packing fraction ϕ against θ, together with the linear best fit $\phi(I) = 0.81 - 0.19I$ for $I > 0.5$.

fit	equation	parameters
Jop	(2.16)	$(\mu_1, \mu_2, I_0) = (\tan 16.83°, \tan 54.08°, 3.25)$
power law	(2.17)	$(\alpha, \mu_s, m) = (0.34, 0, 0.56)$
linear	*	$(\alpha, \mu_s, m) = (1, \tan 19.57°, 0.20)$

Table 11.2.: Fitting parameters for the three fits to the data for $\mu(I)$ shown in figure 11.8(a), in $I > 0.5$. The linear fit is a variation on (2.17), in which we first set $\alpha = 1$ and then fit μ_s and m.

forces: energy is dissipated through the inelasticity of contacts, rather than by friction. The $\mu(I)$ curve was found by periodic chute tests (Chapter 9), and is shown in figure 11.8(a), together with three fitting curves for the region $I > 0.5$. The parameters for these fits are given in table 11.2. The three fits appear to agree with each other well in $I > 0.5$, but the power-law curve has better applicability to lower values of I as well.

We also examined the dependence of the packing fraction ϕ on I in these tests, which is shown in figure 11.8(b). While ϕ decreases with increasing I, the variation of ϕ is comparable to that of da Cruz et al. (2005), so the incompressibility assumption is reasonable (Jop et al. 2006). In practice, the actual depthwise variation of ϕ is even less than suggested by figure 11.8(b), as shown in the supplementary figure B.1 in Appendix B.

11.4.3. Creating a rough base and verifying the no-slip condition

In the simulations, the bumpy base $z = 0$ for $x > 0$ is generated by fixing half-discs, all of diameter $b = \mathcal{M}/30$ and of the same material as the moving discs, to the base. The relative basal roughness coefficient is therefore $\beta = 1$. The jth particle forming the rough base ($j = 1, 2, 3, \dots$) has its centre at

$$(x_j, z_j) = \left(4bj, \frac{b}{2}\left[\tanh(x_j/\mathcal{M}) - 1\right]\right),$$

so that they are spaced equally in the x-direction. The roughness is gradually introduced using a 'mollified tanh' profile, so that the amplitude of the roughness rises slowly.

Although a rough base with $\beta = 1$ would create a no-slip flow if in a periodic domain (§9.5), this is not the case when a transition is present. Incident particles have the inertia to overcome the bumpiness of the base for a short distance. As we previously discussed in §8.5, the presence of basal roughness does not necessarily imply a no-slip condition in the continuum sense. The presence of a slip velocity is related to the ill-posedness at the transition point $x = 0$ and $z = 0$, in common with the classical and hydrofoil problems (§11.2.3). In each case, the sudden imposition of the no-slip condition is incompatible with the incompressibility condition (2.2), because these together predict an infinite shear rate.

The effects of compressibility shall be discussed further in §11.5.1. For now, we find the region in which the no-slip condition is in fact applicable. Figure 11.9 shows u_s, the streamwise component of velocity u at $z = 0$. We verify that slip is present in $x < 0$, and that the no-slip condition is approximately satisfied for $x > 0$ sufficiently downstream of the transition point. Although there is a clear drop in u_s at $x = 0$, a slip velocity persists in a localised region downstream of $x = 0$.

It is not clear how quickly the slip velocity decays, but panel (b) suggests that the no-slip condition begins to apply around $x \approx 0.5\mathrm{Fr}\mathcal{H}$. This suggests that the continuum modelling of §11.3 cannot apply to $0 \leq x \leq 0.5\mathrm{Fr}\mathcal{H}$, since that modelling did not use the proper boundary conditions. Nonetheless, the no-slip condition applies for larger values of x.

11.4.4. Evolution of the velocity profile

In this section and §11.4.5 we give the results of the DPM simulations. We first examine the velocity profiles in the boundary layer region. While there is no definite cutoff between the boundary layer and the outer layer, for the sake of description we focus on the region $\zeta/\zeta_{\mathrm{disp}} = O(1)$; note that $f'(2\zeta_{\mathrm{disp}}) \approx 0.9$ so that $2\zeta_{\mathrm{disp}}$ is the 90th percentile of the velocity. We show these plots in figures 11.10 and 11.11: in each panel of these figures, we plot the scaled velocity $u/\mathcal{U}$ against the similarity variable $\zeta/\zeta_{\mathrm{disp}} = z/(\zeta_{\mathrm{disp}}\Lambda(x))$ at different values of x along the flow, where $\Lambda(x)$ is calculated from (11.33). The different panels correspond to different values of θ and different settings for the incident Froude number Fr. We mark also the predicted similarity profile $f'(\zeta)$ (continuous, black), and emphasise the profiles at $x = 0.5\mathrm{Fr}\mathcal{H}$ (dot-dash, blue) and at $x = \mathrm{Fr}^2\mathcal{H}$ (dotted, blue).

In most of the panels, the profiles at $x = 0.5\mathrm{Fr}\mathcal{H}$ and $x = \mathrm{Fr}^2\mathcal{H}$ collapse very well onto each other, indicating that the boundary layer velocity profiles between these two positions indeed exhibit the predicted self-similarity. In most of the panels, the profiles at $x = 0.5\mathrm{Fr}\mathcal{H}$ align well with the predicted similarity profile $f'(\zeta)$. Subsequent profiles begin to diverge from the black curve, especially after $x = \mathrm{Fr}^2\mathcal{H}$, as the boundary layer thickness grows, and the thitherto subdominant terms in (11.25b) and the perturbation flow to the outer layer begin to be important. Moreover, the velocity profile in the outer layer does not remain constant, but may gradually increase due to streamwise acceleration by gravity. This is most visible in panels (e)–(h) of figure 11.10 and panels (g) and (h) of figure 11.11, where the slope 16° is rather large.

We also consider the evolution of the velocity profile as a whole, including the outer layer. This evolution is shown in figures 11.12 and 11.13, for different settings of the slope θ and the incident Froude number Fr. In these figures, we plot $u/\overline{u}$ against a scaled perpendicular

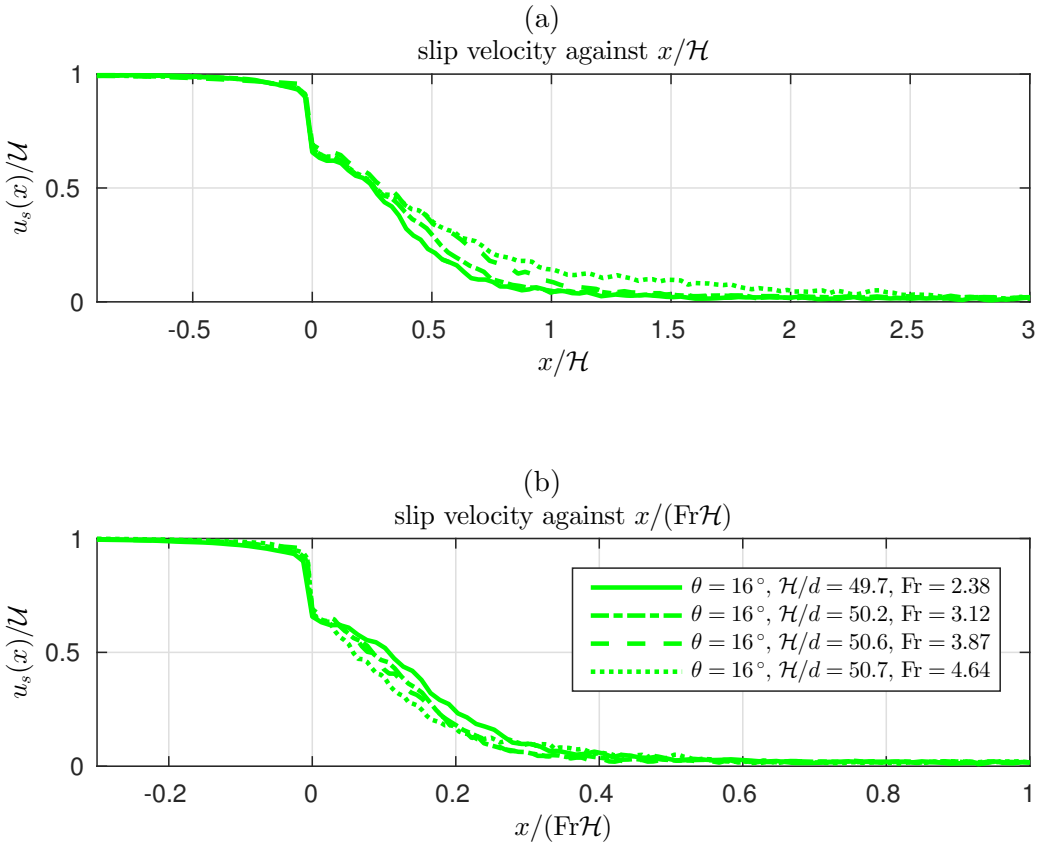

Figure 11.9.: Slip velocity $u_s(x)$ plotted against x, for various values of $\mathcal{U}$ and therefore of Fr. The velocity is scaled against $\mathcal{U}$. The horizontal coordinate x is scaled in (a) against $\mathcal{H}$, and in (b) against $\mathrm{Fr}\mathcal{H}$. See text for discussion.

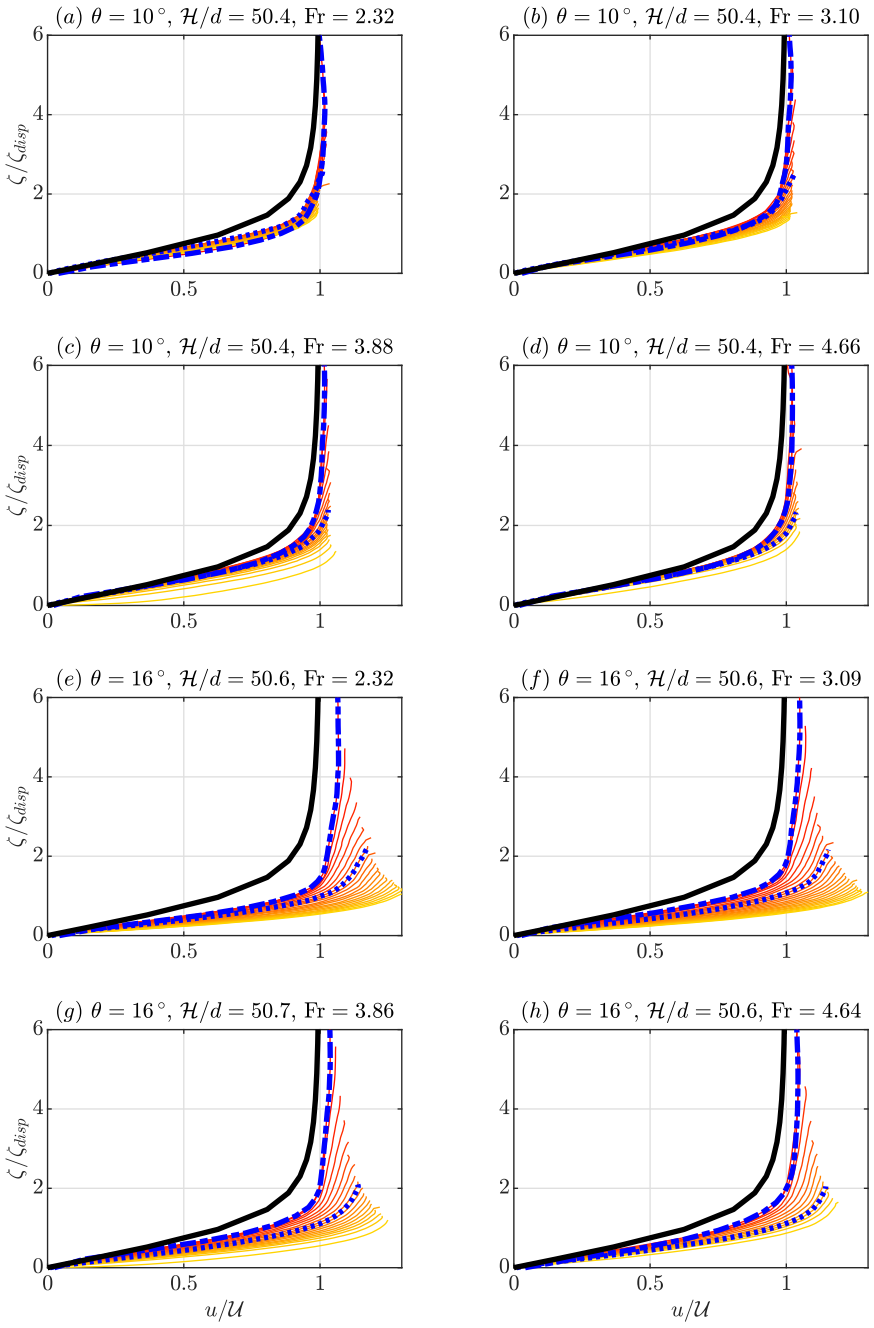

Figure 11.10.: Boundary layer profiles for two settings of θ and four settings for Fr. Each panel shows the nondimensionalised streamwise velocity $u/\mathcal{U}$ (horizontal axis) against the similarity variable $\zeta/\zeta_{\text{disp}} = z/(\zeta_{\text{disp}}\Lambda(x))$ (vertical axis) at various values of x (see text). The thin coloured lines go from $x = 0.5\text{Fr}\mathcal{H}$ (red) to $x = 2.5\text{Fr}^2\mathcal{H}$ (yellow) at intervals of $0.1\text{Fr}^2\mathcal{H}$. Not all panels reach this distance, due to the finite domain length. The blue dot-dashed line shows the profile at $x = 0.5\text{Fr}\mathcal{H}$, and the blue dotted line shows the profile at $x = \text{Fr}^2\mathcal{H}$. The continuous black line indicates the predicted similarity profile $f(\zeta)$.

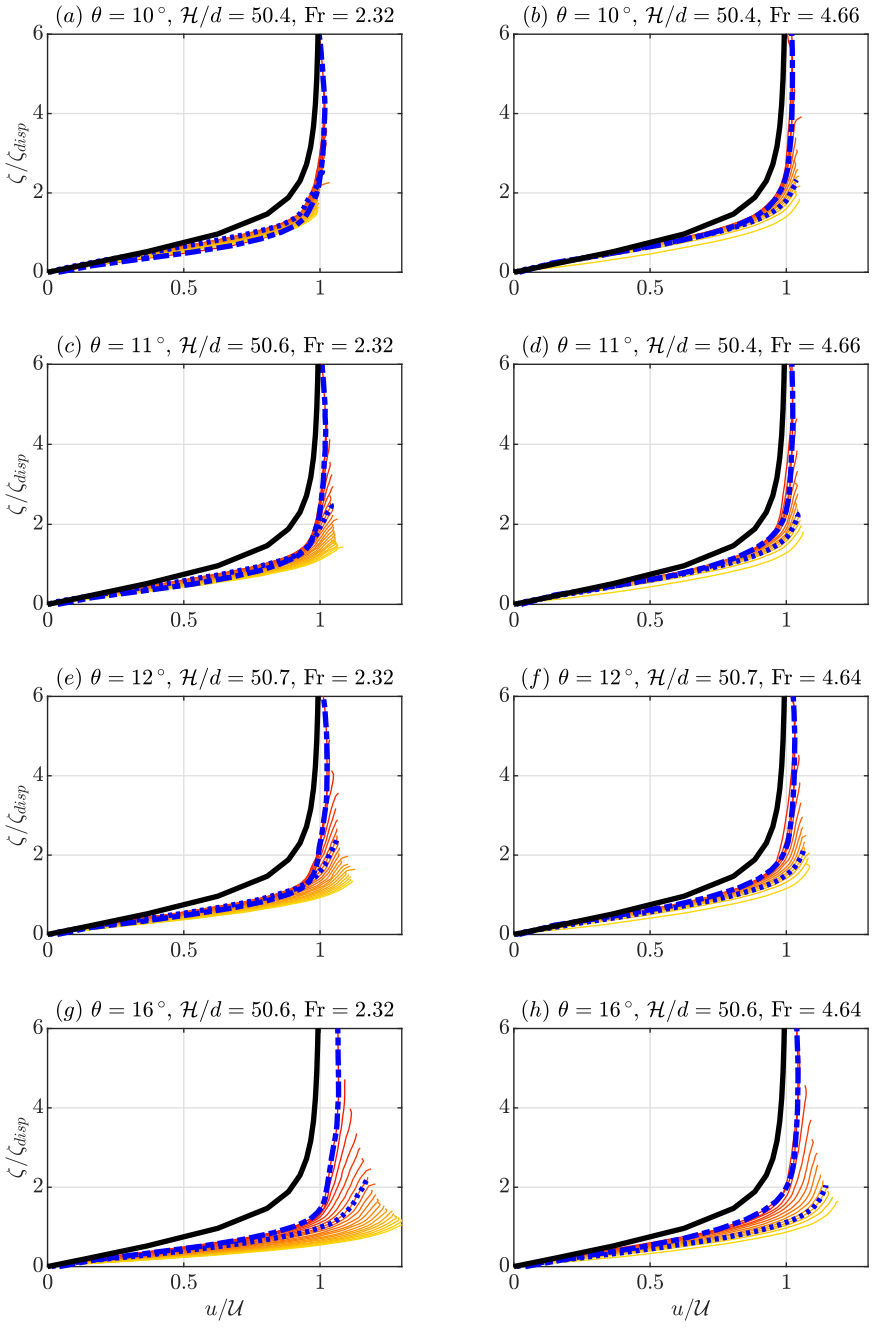

Figure 11.11.: Boundary layer profiles for four settings of θ (rows) and two settings of Fr (columns). See figure 11.10 for plot labels.

colour	θ	Froude number Fr			
		continuous	dashed	dot-dashed	dotted
black	10°	2.32	3.10	3.88	4.66
red	11°	2.32	3.10	3.88	4.66
blue	12°	2.32	3.09	3.87	4.64
green	16°	2.32	3.09	3.86	4.64

Table 11.3.: Values of θ and Fr for DPM simulations in Chapter 11, together with legend for figures in §11.4.5. The nondimensionalised depth δ^{-1} in each case is about 50 (but recall from §9.1.2 that the depth of a current cannot be defined any more precisely).

coordinate $\eta = z/h(x)$.[13] In each panel, the current progresses towards a Bagnold profile (continuous, black) for large x, but this is not reached by the position $x = \mathrm{Fr}^2\mathcal{H}$ or even by $x = 2.5\mathrm{Fr}\mathcal{H}$.

11.4.5. Evolution of the shape factor

Instead of inspecting the evolution of entire velocity profiles as in §11.4.4, it is useful to characterise them using the shape factor χ. The evolution of χ along the current for various simulation parameters is shown in figures 11.14, 11.15, and 11.16, the legend for which are given in table 11.3.

Using the formula (11.27) and noting that $\mathcal{H}$ and d are fixed, (11.37) predicts that

$$\chi - 1 \sim \text{constant} \times \mathrm{Fr}^{(-2+\alpha)/(1+\alpha)}(x/\mathcal{H})^{1/(1+\alpha)}.$$

This can also be expressed as a power-law or a log-log law, *viz.*

$$(\chi - 1)^{1.34} \approx C \times \frac{x}{\mathrm{Fr}^{1.66}\mathcal{H}}, \tag{11.38}$$

$$\log(\chi - 1) \approx 0.75 \log\left(x/\left(\mathrm{Fr}^{1.66}\mathcal{H}\right)\right) + \log C, \tag{11.39}$$

when we set $\alpha = 0.34$. The rescaled-coordinate plots in figures 11.15 and 11.14 show that the curves collapse reasonably well onto each other and match (11.39); indeed, the curves in figure 11.14 are approximately straight lines in the region $0 < x < \mathrm{Fr}^{2-\alpha}\mathcal{H}$. As expected, the worst deviation from a straight line is from the highest value of θ and the lowest value of Fr (continuous green, $\theta = 16°$, $\mathrm{Fr} \approx 2.32$), since the assumption that $\mathrm{Fr} \gg 1$ is not as valid in that case. The constant C in (11.38) may be very crudely approximated as 0.1.

Focusing next on the post-transitional region, figure 11.16 again shows χ against $x/(\mathrm{Fr}^{2-\alpha}\mathcal{H})$, but not as a log-log plot. In most of the cases, the shape factors converge towards $\chi_\infty \approx 5/4$ by the position $x = 4\mathrm{Fr}^{2-\alpha}\mathcal{H}$, and stay there before dropping off near the end of the chute (these localised drops are artefacts from the deletion boundary). The convergence indicates the saturation of the velocity profile in the post-transitional regime: the value of $\chi_\infty \approx 5/4$ is consistent with the saturated profiles being Bagnoldian.

[13] These profiles extend slightly above $\eta = 1$ due to particles that rise above $h(x)$, the time-averaged position of the free surface.

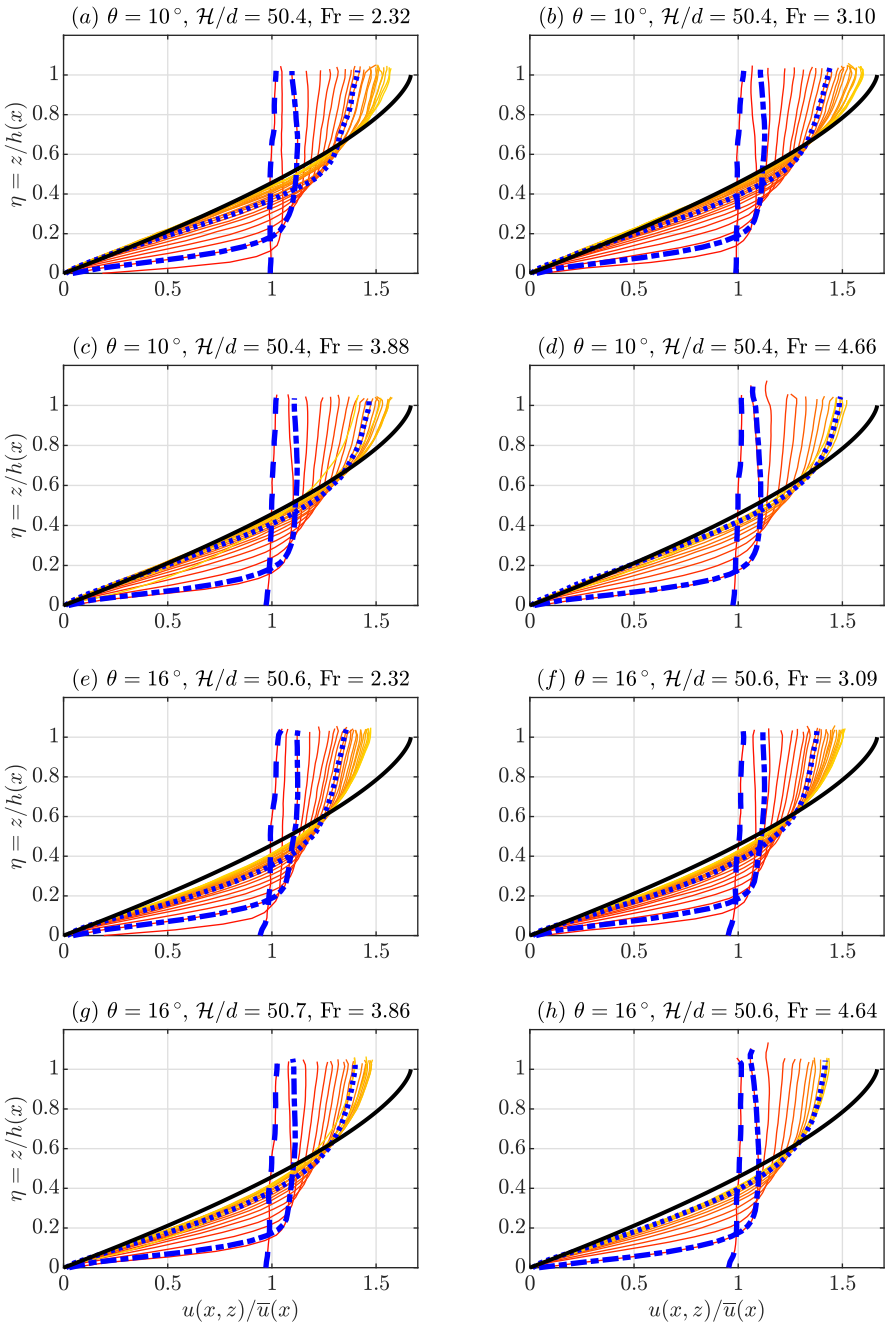

Figure 11.12.: Evolution of the velocity profiles for two settings of θ and four settings of Fr. Each panel shows the nondimensionalised streamwise velocity $u/\mathcal{U}$ (horizontal axis) against a scaled coordinate $\eta = z/h(x)$ at various values of x. The thin coloured lines go from $x = 0$ (red) to $x = 2.5\mathrm{Fr}^2\mathcal{H}$ (yellow) at intervals of $0.1\mathrm{Fr}^2\mathcal{H}$. The blue lines mark the profiles at $x = 0$ (dashed), $x = 0.5\mathrm{Fr}\mathcal{H}$ (dot-dashed) and $x = 2.5\mathrm{Fr}^2\mathcal{H}$ (dotted). The continuous black line indicates the Bagnold profile.

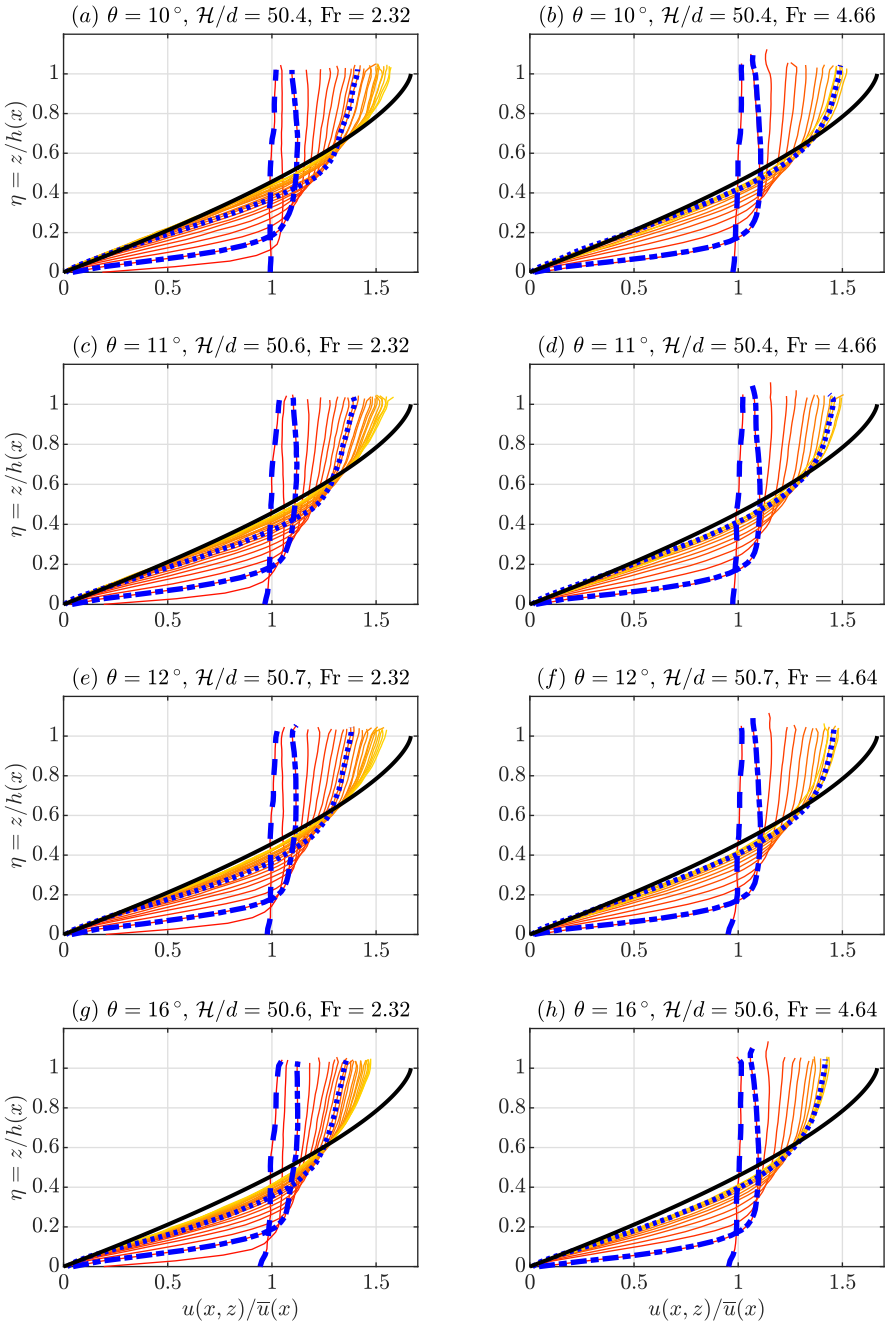

Figure 11.13.: Evolution of the velocity profiles for four settings of θ (rows) and two settings of Fr (columns). See figure 11.12 for plot labels.

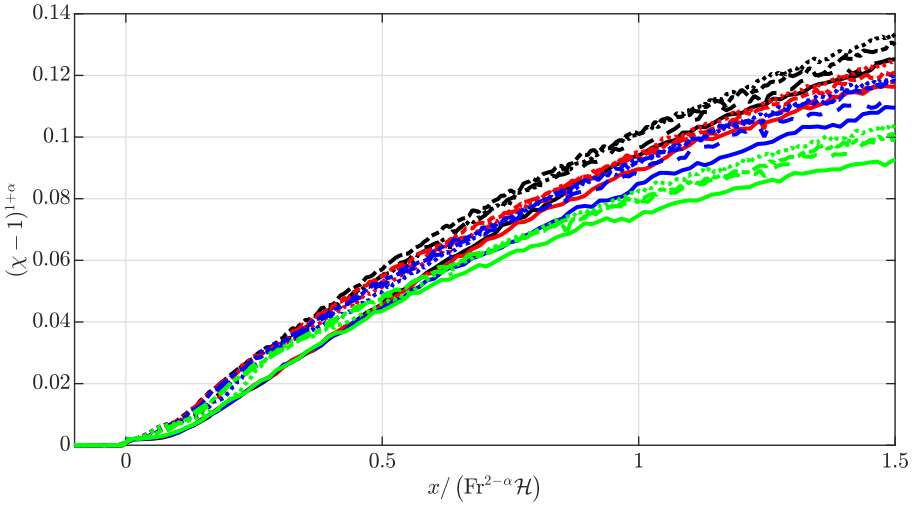

Figure 11.14.: Demonstrating the power-law behaviour (11.37) of $\chi - 1$ against x. Note the rescaled vertical axis; the Bagnoldian value $\chi = 5/4$ corresponds to 0.16 on the vertical axis; this is not attained within the range shown here. The curves correspond to different values of θ and Fr: see table 11.3 for legend.

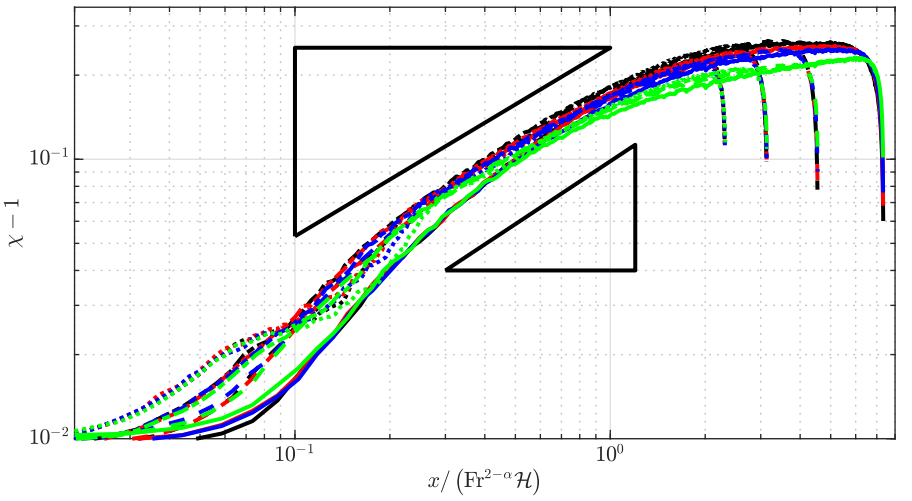

Figure 11.15.: As in figure 11.14, but shown as a log-log plot, together with the slope indicating a $\chi - 1 \propto x^{1/(1+\alpha)}$ dependency. See table 11.3 for legend.

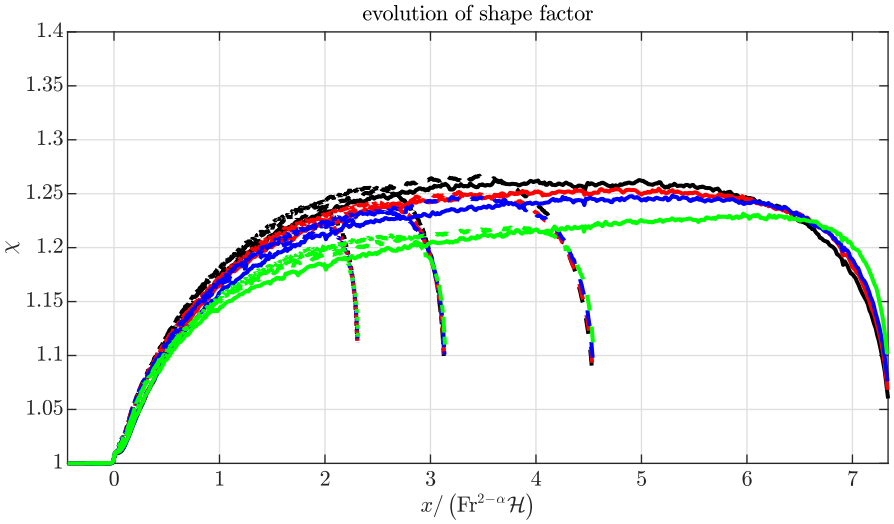

Figure 11.16.: Shape factor χ against the rescaled streamwise coordinate $x/(\mathrm{Fr}^{2-\alpha}\mathcal{H})$. See table 11.3 for legend.

11.5. Discussion

Despite the good agreement between the predicted boundary layer profile and the velocity profiles observed from DPM simulations, there are a number of shortcomings in the analysis of §11.3 that require further consideration.

11.5.1. Compressibility and flow separation at the leading edge

We have made use of the incompressible $\mu(I)$ rheology. However, because the shear rate and the inertial number in the boundary layer is much greater than in the outer layer, we should expect a lower packing fraction ϕ in the boundary layer compared to the outer layer, on account of Reynolds dilatation. Figure 11.17 shows that there is a mild drop in the packing fraction close to the base, but that ϕ nonetheless remains above 0.7 in most cases, and that the change in ϕ is small, suggesting that the flow may nonetheless be treated as an incompressible dense flow. However, this assumption is not valid just downstream of the transition point, where the drop in ϕ at the base is much more pronounced (note in particular the blue dot-dashed line for $x = 0.5\mathrm{Fr}\mathcal{H}$). As in the hydrofoil case, the assumption of incompressibility is incompatible with the sudden imposition of the no-slip boundary condition on u.

Figure 11.18(a) shows the motions of particles near the transition in basal roughness, with particles being coloured according to their speed. Note the fixed basal particles (grey) rising out of the base with a mollified tanh profile (§11.4.3). We see a short region in which particles do not make contact with the base but take ballistic trajectories; flow reattachment eventually occurs when these particles land again.

An analogy may be made with the classical flow at the leading edge of an aerofoil (figure 11.18), which separates and reattaches, with a recirculation bubble in between. However, an important distinction should be made: the fluid in the classical case remains incompressible

and continuous, and the recirculation bubble does contain fluid.[14] Separation in that context refers to the separation of *streamlines* of the flow from the surface of the aerofoil. In contrast, in the granular case, the separated region is devoid of particles.

This analogy motivates our choice of the mollified tanh profile for the rough base, rather than a strictly abrupt transition: the mollification helps to reduce the amount of flow separation, just as a thin aerofoil produces a thinner and shorter wake. Preliminary simulations found that using an abrupt transition produced a longer separation region, without improving the rate at which the slip velocity is brought down.

11.5.2. Downstream behaviour

The boundary layer analysis (§11.3) offers a good agreement with the results from DPM simulations (see *e.g.* figure 11.10), but does not adequately describe the eventual convergence towards a Bagnold profile. As in the Newtonian problem (§11.2), the reason for this is the eventual interaction between the boundary layer and the free surface. Moreover, the streamwise acceleration and friction terms in the granular Blasius equation (11.25b) can no longer be neglected as the boundary layer thickness grows.

The law (11.31) for the boundary layer growth implied that $\Lambda(x) \sim \mathcal{H}$ at the downstream distance (11.35), which is proportional to $\mathrm{Fr}^{2-\alpha}$. In contrast, the eigenvalue analysis of a depth-averaged model (§10.2.2) suggests that the convergence towards a uniform state should occur over an $O(\mathrm{Fr}^2)$ lengthscale. However, the results in figures 11.12 and 11.13 show that the Bagnold profile is not attained by $x = 2.5\mathrm{Fr}^2\mathcal{H}$, suggesting that the inertia of the incident flow is spent more slowly than the depth-averaged model predicts. However, this observation would need to be supported by further DPM simulations at higher speeds and on longer domains.

11.5.3. Alternative rheological models

Our analysis was performed using the incompressibility $\mu(I)$ rheology with the generalisation that the Jop fit (2.16) is replaced with the power-law fit (2.17) in the limit $I \gg 1$. However, this problem could also be studied under different rheological models of dry granular flows. The granular boundary layer equation (11.25b) resembles the classical boundary layer equation (11.5) on account of the second derivative $\partial^2 u/\partial z^2$ in the final terms of both equations. This term appears in (11.25b) because the shear stress term $\sigma_{xz} = \mu(I)ps_{xz}$ has a dependence on $\partial u/\partial z$ through the inertial number I, (and less directly, through the shear direction tensor s_{xz}). We expect a similar structure of equations in any rheology where the shear stress depends on the local strain rate. For such rheologies, it will be possible to perform boundary layer analyses similar to those of §§11.2, 11.3. Most rheological models are strain rate-dependent, with a notable exception being the Mohr–Coulomb rheology (Andreotti et al. 2015), in which $\sigma_{xz} = \mu ps_{xz}$ for a *constant* coefficient of friction μ.

Under a rheology in which the shear stress may depend also on derivatives of the strain rate (or higher derivatives of the velocity), additional boundary layer scalings may be possible. For example, under nonlocal rheologies (§3.3) the stress tensor has additional terms that depend on second derivatives of the inertial number, so that the corresponding equations of motion

[14] For steady flows, streamlines are identical to pathlines and streaklines (Acheson 1990).

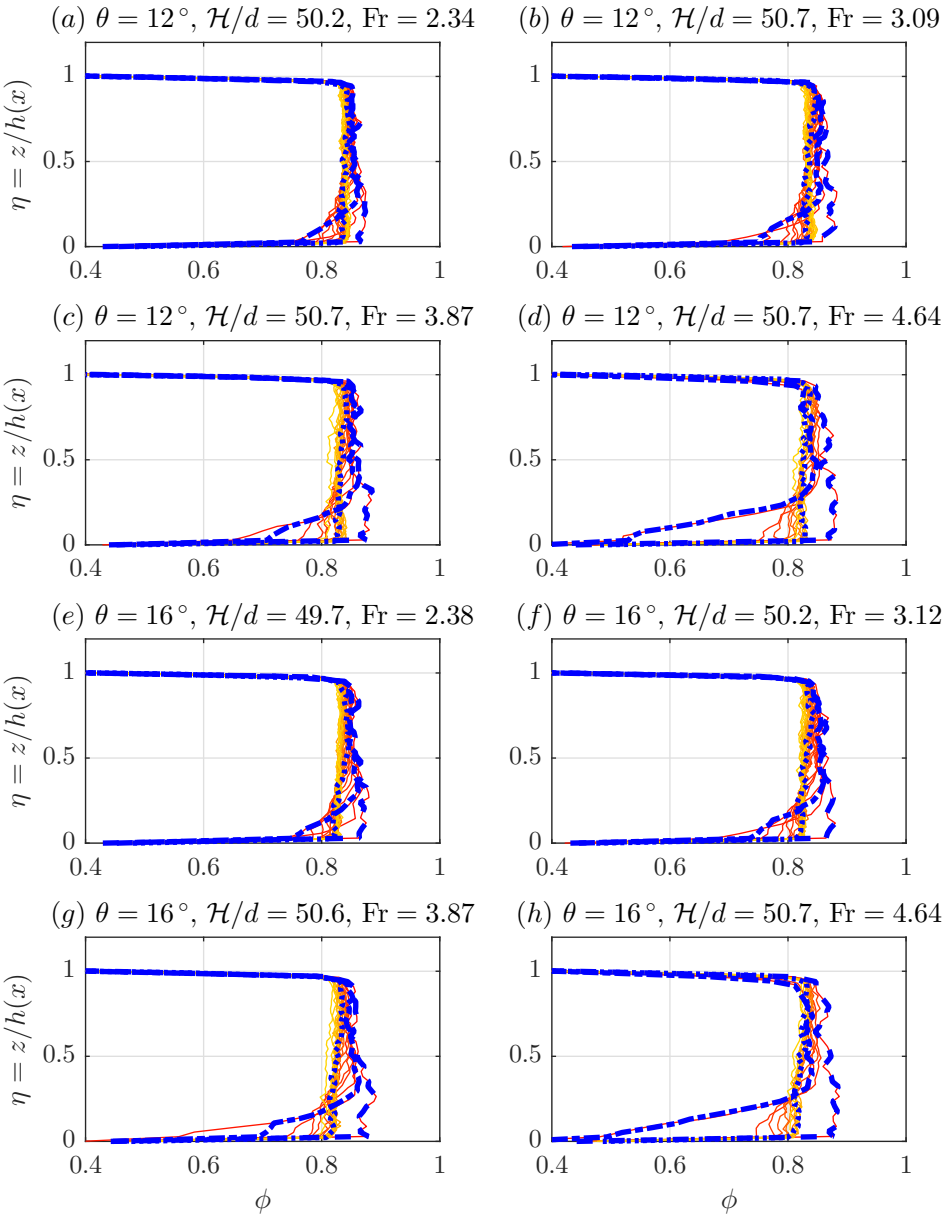

Figure 11.17.: The packing fraction ϕ for the simulations presented in §11.4. The coloured lines are defined in the caption of figure 11.12. The apparent drop to $\phi = 0$ at $z = 0$ is an artefact of the coarse-graining process.

(a)

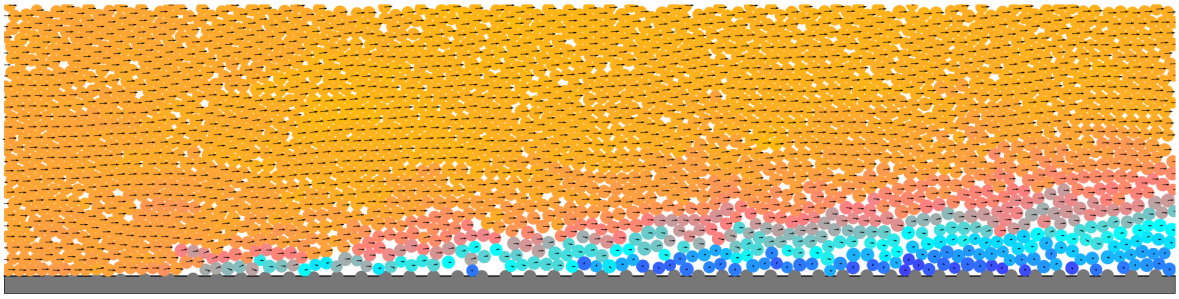

(b)

Figure 11.18.: (a) Flow separation and reattachment in a DPM simulation. Particles are coloured according to their speed, from blue to orange. This picture has been cropped; the free surface is not actually flat. (b) Flow separation at the leading edge of an aerofoil. Photo from Werlé (1974) *Le Tunnel Hydrodynamique au Service de la Recherche Aérospatiale*, Publ. no. 156, ONERA, France, reproduced in Van Dyke (1982).

contain fourth derivatives of the velocity, $\partial^4 u/\partial z^4$, representing nonlocal effects. This term could give rise to an a second boundary layer with a thickness proportional to d, in addition to the boundary layer discussed above.

The aforementioned models all concern dry granular flows, where the medium between grains has no dynamical importance. For mixtures of particles in water, Longo and Valiani (2014) have conducted an experimental study of a similar boundary layer problem, involving a three-dimensional free-surface flow onto a blade that is aligned *vertically* and along the flow. As in the classical and granular Blasius problems, the blade in Longo and Valiani (2014) imposes a no-slip condition that also creates a self-similar boundary layer near the blade. These boundary layers have a different similarity profile from the granular Blasius profile $f'(\zeta)$, owing to the different rheological properties of the suspensions.

11.6. Summary

In this chapter, we have considered a steady granular current flowing down a slope. The base of the smooth is smooth in the upstream region $x < 0$ and bumpy for $x > 0$; in a continuum model, these may be modelled as free-slip and no-slip conditions respectively. This problem is a prototypical example of a short-scale topographical change affecting a granular current. The change in basal boundary condition creates a change in the internal velocity profile, which cannot be captured by a depth-averaged model.

The sudden imposition of a no-slip condition makes this problem analogous to the classical Blasius problem, but the Navier–Stokes equations of the classical problem are replaced by the incompressible $\mu(I)$ rheology for a granular material. The $\mu(I)$ rheology predicts that for a rapid incident flow, the velocity profile is asymptotically plug-like for $x \to -\infty$ and Bagnoldian for $x \to \infty$. As in the classical problem, the no-slip condition for $x > 0$ indicates a distortion in the velocity profile, in a boundary layer initially localised near the base $z = 0$, but whose thickness grows along the streamwise direction.

We began by studying a related problem with a Newtonian fluid to explore whether the finite depth of the flow influences the boundary layer dynamics (§11.2). We found that, provided that the incident flow had a high Froude number Fr, the boundary layer could be studied as though the outer flow were undisturbed. We then proposed that the same would be true of the granular problem.

We have used a Prandtl-like analysis of the $\mu(I)$ equations to study the development of the boundary layer in a transitional region $x \ll \mathrm{Fr}^2\mathcal{H}$ (§11.3). We showed that the boundary layer thickness and velocity profile are determined by the asymptotic behaviour of $\mu(I)$ as $I \to \infty$, and that the Jop fit (2.16) does not yield a valid boundary layer scaling (§11.3.4). However, alternative power-law forms (2.17) for $\mu(I)$ give self-similar solutions for the velocity profile in the boundary layer, and the scalings match well with results from 2D DPM simulations (§11.4).

As we have mentioned, there are various theoretical aspects of this problem that should be considered in the future. In particular, more accurate and precise expressions for χ and $h(x)$ may be obtained by calculating the perturbation to the outer flow induced by the boundary layer. Alternative rheological models incorporating nonlocality (§3.3) could give more accurate expressions for larger values of δ, and the approach taken in the present work could be used to study boundary layers in other non-Newtonian fluids.

12. Time-dependent flows and varying gravitational fields

> And on the pedestal these words appear:
> 'My name is Ozymandias, king of kings;
> Look on my works, ye Mighty, and despair!'
> Nothing beside remains. Round the decay
> Of that colossal wreck, boundless and bare
> The lone and level sands stretch far away.
>
> Percy Shelley, *Ozymandias*

While Chapters 10 and 11 considered the spatial evolution of steady flows, in the present chapter we now study the dynamics of *time-dependent* flows, with no streamwise variation. That is, whereas the previous chapters analysed the incompressible $\mu(I)$ equations (2.10) with the $\partial/\partial t$ terms deleted, we now include those terms but delete the $\partial/\partial x$ terms.

As we remarked back in Chapter 1, in this work, we use the term 'topography' to refer to any externally-imposed inhomogeneities in x or t, causing a flow profile that deviates from the equilibrium profile (§2.2) of steady uniform flows. In this chapter, we consider the response to a flow subject to a sudden change in the basal conditions from free-slip to no-slip (§12.3), and the response of a flow to a time-dependent gravitational field (§§12.4, 12.5). These two problems are time-dependent analogues to the two examples shown in figure 1.4.

An important difference between the spatially-dependent approach of the previous chapters and the present time-dependent approach is that, in the previous chapters, the flow rate q is constant along the current but the depth of the current h was variable. In contrast, under a streamwise-independent model, the flow rate varies with time, but the incompressibility condition implies that there is no perpendicular velocity w, and therefore the free surface position h (defined from DPM data according to §9.1.2) cannot rise or fall.

We begin this chapter by stating the incompressible $\mu(I)$ equations in this geometry (§12.1). Having done so, we first explore the case of constant g and θ: this is the setup used in the DPM calibration tests (Chapter 9). Recall from §2.2 that the Bagnold profile (2.13) is a steady solution to the $\mu(I)$ rheology (provided that the no-slip basal condition holds and that $\mu(I) = \tan\theta$ has a solution): in §12.2, we show that this solution is attractive as $t \to \infty$. This fact is not surprising, and partially justifies our focus on steady-state solutions in Chapters 10 and 11.[1]

In §12.3, we next study the evolution towards the Bagnold profile in the case where the flow at $t = 0$ has a plug flow profile, and is suddenly subject to a no-slip boundary condition. As in Chapter 11, the no-slip condition affects a region of the flow that is initially localised, but spreads through the current: this is a time-dependent version of the granular Blasius problem.

[1] This result applies only to streamwise-independent flows. The uniform Bagnold profile is not necessarily attractive when both time-dependence and streamwise-dependence are permitted (§14.2.

We shall see that although the boundary layer velocity profile and the shape factor both grow initially according to power laws, the boundary layer saturation and towards the Bagnold profile is rather different from the behaviour of the steady, streamwise-dependent problem.

We also study problems in which θ is time-dependent, in the two extreme cases of θ changing discontinuously (§12.4) and changing gradually (§12.5): these are time-dependent analogues of the curved chute problems that we studied using the depth-averaged framework (§§10.3.3, 10.3.4). Again, we shall see that, although there be similarities between these time-dependent problems and the streamwise-dependent cases of Chapter 10, there are also fundamental differences in how a current reacts to streamwise and temporal topographical features.

We shall therefore conclude that caution must be exercised if a chute flow is to be simulated in a DPM using a periodic domain, and spatial topographical features replaced by temporal ones: doing so may be tempting from a computational point of view (§8.1.1), but the resulting problem does not capture the correct physics (§12.6).

12.1. Governing equations under the incompressible $\mu(I)$ rheology

We assume that, statistically, the flow has no x-dependence.[2] We also assume that the flow is incompressible; then $\partial u/\partial x = 0$ implies that $\partial w/\partial z = 0$. Combining this with the kinematic basal boundary condition $w|_{z=0} = 0$ shows that $w = 0$ everywhere. The z-component of the $\mu(I)$ momentum equations (2.10) implies that the pressure is hydrostatic, that is,

$$p = p(z,t) = \rho g(t)\cos\theta(t)(\mathcal{H} - z). \tag{12.1a}$$

The x-component implies that

$$\begin{aligned} u_t &= g\sin\theta + g\cos\theta\left[\mu(I)(\mathcal{H}-z)\right]_z \\ &= -g\cos\theta\left[\left(\tan\theta - \mu(I)\right)(\mathcal{H}-z)\right]_z, \end{aligned} \tag{12.1b}$$

with the inertial number given by

$$I = \frac{du_z}{(g\cos\theta)^{1/2}(\mathcal{H}-z)^{1/2}}, \tag{12.1c}$$

since $||\boldsymbol{D}|| = u_z/2$ for parallel shear flow. The boundary conditions on u are the no-slip basal condition at $z = 0$ and the free surface dynamical boundary condition at $z = \mathcal{H}$,

$$u(0,t) = u_z(\mathcal{H},t) = 0. \tag{12.1d}$$

There is an abuse of notation in (12.1b, 12.1c): strictly speaking, the definition of the inertial number I in (2.6) uses the *absolute value* of u_z, so that $I \geq 0$, and the function $\mu(I)$ is defined

[2] More formally, if

$$\tilde{f} = \frac{1}{\mathcal{L}}\int_0^{\mathcal{L}} f\,\mathrm{d}x$$

denotes the streamwise-average of a quantity f, we assume that $|f - \tilde{f}| \ll \tilde{f}$. This assumption is suitable provided that the initial conditions are streamwise-uniform, and that $\mathcal{L}$ is short enough to prohibit the growth of any instabilities (§14.2). To compare against this model, data from DPM simulations shall first be coarse-grained (§9.1), and then streamwise-averaged.

only for $I \geq 0$. The directionality of the shear rate is accounted for by the shear rate tensor $\boldsymbol{s}$, which appears in (2.10). But for one-dimensional parallel shear flow, it is expedient to define the inertial number as (12.1c), which may become negative, and to extend the definition of the function $\mu(I)$ so that $\mu(-I) = -\mu(I)$. If the original function has $\mu(0) \neq 0$, we treat the extended function as having a jump discontinuity at $I = 0$, and define $\mu(0) = 0$.

A discontinuity of μ at $I = 0$ does not *ipso facto* imply that (12.1) is ill-posed in the sense of Hadamard (Evans 2010), but certainly presents difficulty for numerical solutions. The applications of (12.1) in this chapter shall not encounter any velocity profiles with $u_z < 0$, but, if necessary, one could introduce regularised versions of μ: for example, the Jop form (2.16) could be replaced with the 'mollified' form

$$\mu(I) = \mu_1 \tanh \frac{I}{I_\epsilon} + \frac{\mu_2 - \mu_1}{I_0/I + 1}, \tag{12.2}$$

where the mollification parameter $I_\epsilon \ll I_0$. The form (12.2) has finite $O(1/I_\epsilon)$ derivative at $I = 0$. We solve the system (12.3) numerically using the backwards Euler (BE) scheme, with Newton–Raphson iteration for solving the set of nonlinear implicit equations (see *e.g.* Iserles (2008), Press et al. (1992)). While the BE scheme is only first-order, it is more suitable than the second-order Crank–Nicolson (CN) scheme (see *e.g.* (Iserles 2008)) for the present application, since the BE scheme is more numerically stable for stiff systems.[3, 4]

Assuming that the magnitude of gravity $g(t)$ can be said to take a characteristic value $\mathcal{G}$, the typical velocity scale is given by the Bagnoldian scaling $\mathcal{U}_{\mathrm{Bag}}$, defined previously as

$$\mathcal{U}_{\mathrm{Bag}} = \frac{\sqrt{g\mathcal{H}^3}}{d} = \frac{\sqrt{g\mathcal{H}}}{\delta}, \quad \delta = d/\mathcal{H}. \tag{2.14}$$

We nondimensionalise (12.1) by scaling g by $\mathcal{G}$, z by $\mathcal{H}$, u by $\mathcal{U}_{\mathrm{Bag}}$, and t by the 'diffusive timescale' $\mathcal{T} = \delta^{-1}(\mathcal{H}/\mathcal{G})^{1/2}$, where $\delta = d/\mathcal{H}$. Using tildes to denote nondimensionalised quantities, (12.1b) becomes

$$\begin{aligned} \tilde{u}_{\tilde{t}} &= -\frac{\mathcal{G}\mathcal{T}}{\mathcal{U}_{\mathrm{Bag}}} \tilde{g} \cos\theta \left[\big(\tan\theta - \mu(I)\big)\,(1 - \tilde{z}) \right]_{\tilde{z}}, \\ &= -\tilde{g} \cos\theta \left[\big(\tan\theta - \mu(I)\big)\,(1 - \tilde{z}) \right]_{\tilde{z}}, \end{aligned} \tag{12.3a}$$

with the inertial number given by

$$I = \frac{\tilde{u}_{\tilde{z}}}{(\tilde{g}\cos\theta)^{1/2}(1 - \tilde{z})^{1/2}}. \tag{12.3b}$$

With these scalings, $I = O(1)$ except in regions of high shear, such as boundary layers (§12.3). The boundary conditions simplify to become

$$\tilde{u}(0, \tilde{t}) = \tilde{u}_{\tilde{z}}(1, \tilde{t}) = 0. \tag{12.3c}$$

Under these scalings, the inertial number (12.3b) is $O(1)$. In the remaining sections of this chapter, we shall work with the nondimensionalised system (12.3) rather than (12.1). We shall

[3] The system (12.3) may become stiff if the derivative $\mu'(I)$ becomes large, for example, near $I = 0$ under the mollified Jop fit (12.2).

[4] I thank Karol Bacik (pers. comm., 2018) for suggesting the BE scheme.

also drop the tildes. Note that the definition of $\mathcal{T} = \delta^{-1}(\mathcal{H}/\mathcal{G})^{1/2}$ as a diffusive timescale includes the factor of δ^{-1}: under the $\mu(I)$ rheology, where d appears in the inertial number (2.6), the diffusivity of momentum is inversely proportional to the grain size d, consistent with the notion that grain size acts as a 'granular viscosity' (Barker et al. 2015). Note also that $\mathcal{T}$ is $1/\delta^2$ times larger than the timescale associated with the shear rate $\mathcal{H}/\mathcal{U}_{\mathrm{Bag}}$.

12.2. Relaxation towards the Bagnold profile

As we have seen in §2.2, if g and θ are constant, then a steady-state solution to (12.3) is given by the Bagnold solution (2.13), written in the present chapter's nondimensionalised units as

$$B(z; g, \theta) = \frac{2}{3} I(\theta)(g\cos\theta)^{1/2}\left[1 - (1-z)^{3/2}\right], \qquad I(\theta) = \mu^{-1}(\tan\theta), \tag{12.4}$$

provided that the function $\mu(I)$ has an inverse at $\mu = \tan\theta$. (Recall that $\mu(I)$ must be increasing in I, so if an inverse exists then it must be unique.) If $\tan\theta$ is not within the range of $\mu(I)$, then a steady-state solution to (12.3) does not exist; the flow either accelerates indefinitely or decelerates to a halt. For the rest of this chapter, we shall assume that $I(\theta)$ exists for those values of θ that we shall consider; this is indeed the case in the DPM simulations. We note that (12.4) is appropriate for $-\pi/2 < \theta < 0$, if the definition of the function $\mu(I)$ is extended to negative values of I (§12.1).

If g and θ are constant, then (12.3a) is a parabolic equation for u, governing the relaxation of a velocity profile towards this steady state; the relaxation timescale was defined as $\mathcal{T}$. It is physically reasonable to suppose that (12.4) should be an attractive solution for $u(z,t)$. The convergence can also be established mathematically by considering the function

$$L(t) = \int_0^1 \frac{1}{2}(u-B)^2\,\mathrm{d}z = \frac{1}{2}||u-B||_2^2. \tag{12.5}$$

Now, $L \geq 0$, and $L = 0$ only if $||u-B||_2 = 0$.[5] And for g and θ constant, B is independent of t, so that

$$L'(t) = \int_0^1 (u-B)u_t\,\mathrm{d}z \tag{12.6}$$

$$= -g\cos\theta\int_0^1 (u-B)_z\left(\mu(I) - \tan\theta\right)(1-z)\,\mathrm{d}z, \tag{12.7}$$

after substituting for u_t from (12.3a) and integrating by parts. Now,

$$I = \frac{B_z + (u-B)_z}{(g\cos\theta)^{1/2}(1-z)^{1/2}} \tag{12.8}$$

$$= I(\theta)\left[1 + (u-B)_z/B_z\right], \tag{12.9}$$

so that $I - I(\theta)$ has the same sign as $(u-B)_z$. Writing the above expression for $L'(t)$ out as

$$L'(t) = -g\cos\theta\int_0^1 (u-B)_z\left[\mu\left(I(\theta) + (I - I(\theta))\right) - \mu\left(I(\theta)\right)\right](1-z)\,\mathrm{d}z, \tag{12.10}$$

[5] The equality $||u-B||_2 = 0$ by itself does not imply that $u = B$; one needs the additional that u and B are smooth (Burkill 2002).

it follows that $L'(t) \leq 0$, since $\mu(I)$ increases with I. Moreover, $L'(t) = 0$ if and only if $L = 0$. Therefore, $L(t)$ is a Lyapunov function (Strogatz 2018), and it follows that $u \to B$, under the 2-norm.[6]

The Lyapunov function L quantifies the difference between u and the Bagnoldian profile B. In the present section, with g and θ constant, the decay of L corresponds to the convergence[7] $u \to B$. Although L and the shape factor χ are related statistical measures of the velocity profile (both providing some information about its second moment $\int_0^1 u^2 \, \mathrm{d}z$), χ is more useful for comparing the work of this chapter to the language of Chapters 10 and 11. Note, however, that the convergence $\chi \to 5/4$ is a weaker statement than $L \to 0$; the former does not imply that a flow profile is Bagnoldian.

12.3. Relaxation from a plug flow: the time-dependent granular Blasius problem

We now consider a flow that has a plug flow profile at $t = 0$, but is subject to the no-slip basal condition for $t > 0$. As in Chapter 11, such a flow develops a boundary layer that spreads as time increases, until the boundary layer thickness saturates the depth of the flow. The present problem is therefore a time-dependent analogue of the granular Blasius problem (Chapter 11), and we compare between the time-dependent and spatially-varying problems. The depthwise velocity profile also evolves towards a Bagnoldian profile (§12.2). It shall be shown that these two processes are separate and occur over distinct lengthscales.

Let the initial condition be $u(z, 0) = K$, that is, the flow is K times faster than the Bagnoldian velocity scale (which is $O(1)$ in these units). The Froude number of the initial flow is

$$\mathrm{Fr} = \frac{K\mathcal{U}_{\mathrm{Bag}}}{\sqrt{g\mathcal{H}}} = \frac{1}{\delta}K.$$

We numerically investigate (12.3) for different values of K. For numerical purposes, we use the slightly different initial condition

$$u(z, 0) = K\left(1 - 0.01 \times \frac{2}{\pi} + 0.01 \times \sin\left(\frac{\pi z}{2}\right)\right),$$

introducing a slight velocity gradient to avoid any singular behaviours at $u_z = I = 0$, without changing the flow rate or affecting the free surface boundary condition $u_z(1, 0) = 0$. (The mollification parameter 0.01 is arbitrary and does not strongly affect the results.) For the sake of demonstration, we take the friction coefficient to be

$$\mu(I) = \tan\Theta\left(\frac{2}{5}(\cos\Theta)^{1/2}I\right)^{\alpha} = mI^{\alpha}, \quad \Theta = 15^{\circ}, \quad \alpha = 1/3, \tag{12.11}$$

which is of the power-law form (2.17). The advantage of the form (12.11) is that, on setting $\theta = \Theta$, the inertial number $\mu^{-1}(\tan\Theta) = 5/(2(\cos\Theta)^{1/2})$, so that the flow rate of the Bagnoldian

[6] Colm-cille Caufield (pers. comm., 2018) cautioned that convergence under the 2-norm is a weaker notion of convergence than uniform convergence. But since B is differentiable and $||B'||_2 < \infty$, the uniform convergence $u \to B$ in fact does follow (Daniel Heydecker, pers. comm., 2 January 2019).

[7] See footnote 6.

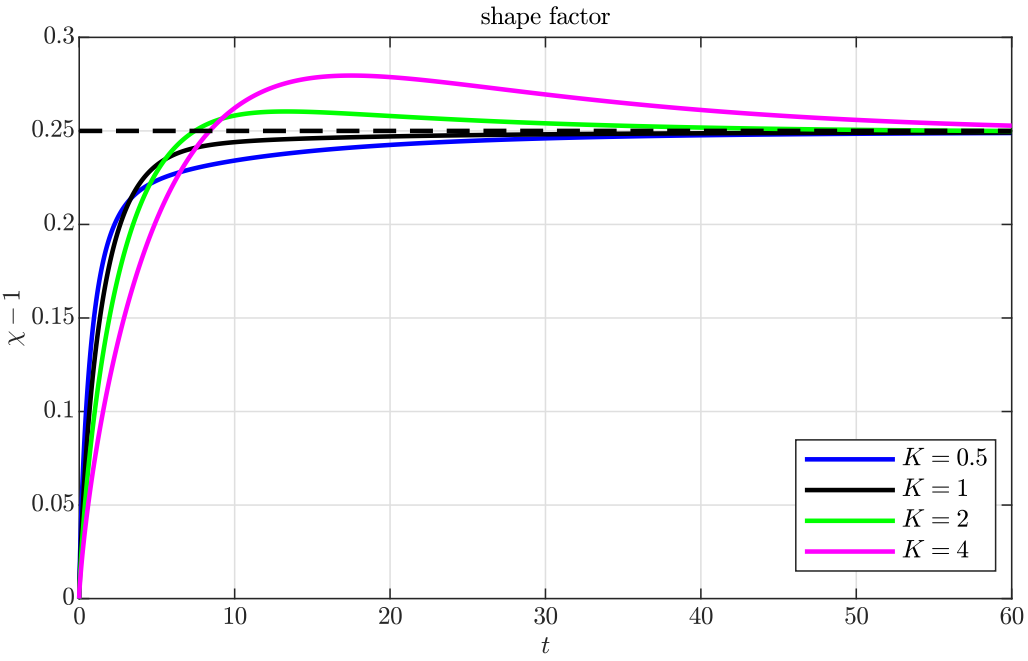

Figure 12.1.: The evolution of the shape factors for the solutions of (12.3), starting from plug-like initial conditions for four different values of K. The dashed line shows the Bagnoldian value $\chi = 5/4$, to which the four curves converge.

profile is $\int_0^1 B \, \mathrm{d}z = 1$. As in Chapter 11, the use of a power law for the function $\mu(I)$ will allow the discovery of similarity solutions. The values $\Theta = 15°$ and $\alpha = 1/3$ are arbitrarily chosen.

From the numerical solutions to (12.3), we calculate the shape factor χ, shown in figure 12.1 for several values of K. Several features stand out from this. Most obviously and to be expected, in each case $\chi \approx 1$ at $t = 0$ (with a slight error from the mollification of the initial profile), and $\chi \to 5/4$ as $t \to \infty$ as the velocity profile becomes Bagnoldian. Secondly, at initial times, $\chi - 1$ has a power-law dependence on t: this is in common with the streamwise-dependent Blasius problem of Chapter 11. As before, the boundary condition at $z = 0$ initially affects only a boundary layer at the bottom of the flow, while the outer layer is unaffected. Taking $z \ll 1$ in the equation of motion (12.3a) produces a nonlinear diffusion equation for the velocity profile in the boundary layer,

$$\frac{\partial u}{\partial t} = \alpha m (g \cos\theta)^{(3-\alpha)/2} \frac{\partial^2 u / \partial z^2}{(\partial u / \partial z)^{1-\alpha}}, \tag{12.12}$$

which is very similar to the equation (11.28) governing a streamwise-spreading boundary layer. As in Chapter 11, a simple scaling argument (Barenblatt 1996) can be used to show that the boundary layer thickness Λ grows with t according to

$$\Lambda(t) \propto \left[\alpha m (g \cos\theta)^{(3-\alpha)/2} K^{\alpha-1} t\right]^{1/(\alpha+1)} \propto \left[\frac{t}{K^{1-\alpha}}\right]^{1/(1+\alpha)}.$$

By arguments similar to those of §11.3.6, the shape factor also grows with a power-law dependency

$$\chi - 1 \propto \left[\frac{t}{K^{1-\alpha}}\right]^{1/(1+\alpha)}, \tag{12.13}$$

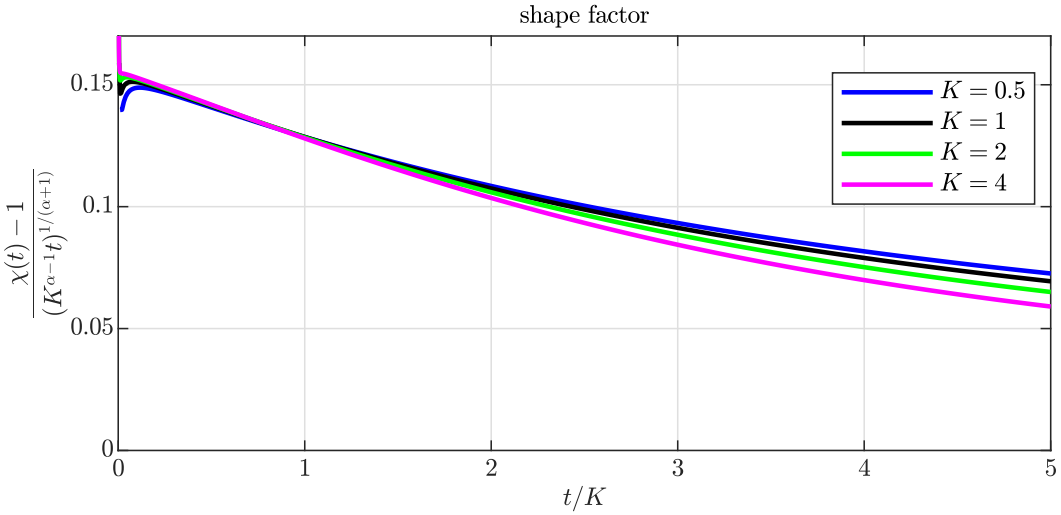

Figure 12.2.: As in figure 12.1, but plotted in rescaled axes: the vertical axis demonstrates the power-law growth for $\chi - 1$, while the horizontal axis t/K indicates the significance of an $O(K)$ timescale (see text). The apparently singular behaviours very near $t = 0$ are numerical artefacts from dividing two small numbers.

which is evident from the rescaled-axis plot in figure 12.2. In that plot, the curves align very well with each other when the horizontal axis has also been scaled to show the variable t/K rather than t: this suggests that the number K, which is the ratio of the initial velocity scale to the Bagnoldian velocity scale, sets a timescale associated with the inertia of the incident flow. Thus, for $t = O(K)$ one has

$$\chi - 1 \sim \left[\frac{t}{K^{1-\alpha}}\right]^{1/(1+\alpha)} C\left(\frac{t}{K}\right),$$

for some function C.

Less expected is the transient behaviour of χ. For the two lower values of K, the shape factor rises monotonically towards 5/4; but for $K = 2$ and $K = 4$, χ grows initially according to the power law (12.13) and in fact exceeds its equilibrium value of 5/4 before settling back down. This overshooting behaviour was not observed in the steady Blasius problem of Chapter 11, where $\chi \to 5/4$ monotonically in all of the DPM simulations. The discrepancy arises from the fact that, in this streamwise-independent problem, the self-similar boundary layer spreading (which drives the power-law growth for χ) is not resisted by an induced flow in the outer layer that causes an adverse pressure gradient (§11.2). Thus, the power-law growth for χ is not interrupted as quickly, and continues until $t = O(K)$ (figure 12.2). The growth in χ is driven both by the flow's retardation at the base, and by its acceleration nearer the free surface: these two act together to increase the variance of the velocity within the current. Moreover, the inability of the free surface to rise implies that any 'excess' kinetic energy in the current (relative to the Bagnoldian equilibrium) cannot be converted into potential energy, but must be dissipated through friction.[8] The decay of a high initial velocity towards the Bagnoldian scale is therefore rather slow.

[8] In practice, the incompressibility assumption must be relaxed: as the flow's shear rate increases, Reynolds dilatation would reduce ϕ and cause the free surface to rise. But we saw in Chapter 9 that the differences in ϕ are rather small, and therefore would not expect compressibility to cause a significant increase in depth.

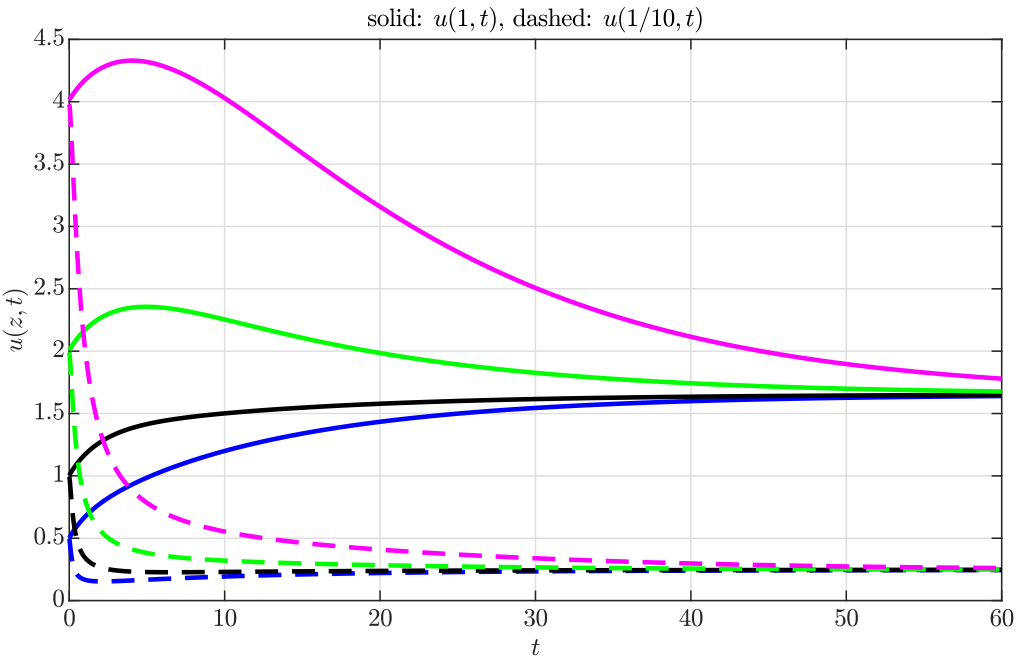

Figure 12.3.: The time-evolution of the velocity u at the two positions $z = 1$ (solid) and $z = 1/10$ (dashed) from plug-like initial conditions for four different values of K. Different colours indicate different values of K (see legend to figure 12.2). In the steady state, $u(1,\infty) = 5/3$ and $u(1/10,\infty) \approx 0.24$ (neither of which are shown).

To illustrate the above discussion, we sketch the time-evolution of the velocity within the current for fixed values of z. Figure 12.3 shows the surface velocity $u(1,t)$ (solid) and the near-base velocity $u(1/10,t)$ (dashed) for the four cases of K shown previously. In all four cases, the velocity at $z = 1/10$ is decreasing at $t = 0$, and monotonically converges towards its equilibrium value $u(1/10,\infty)$.[9] The surface velocity, however, is increasing at $t = 0$: since $u_z \ll 1$ in the initial conditions[10], the inertial number I and the coefficient of friction μ are small there, so that the flow may accelerate, even if this would lead the surface velocity away from its final value of $u(1,\infty) = 5/3$. The slowing down at the base and the acceleration at the top of the flow work together to increase the variance of the velocity and therefore to increase the shape factor. For $K = 2$ and $K = 4$, it is only later that the effects from the basal no-slip condition reduce the surface velocity again.

12.4. Step changes in θ

Now suppose that θ may vary with time, keeping g constant (and $g = 1$ in nondimensionalised units).[11] Suppose also that the flow is Bagnoldian at $t = 0$.

[9] For the chosen value of θ and the chosen function μ, we have $u(1/10,\infty) \approx 0.24$. In all four cases, the initial flow velocity $K > 0.24$.

[10] Recall that we have introduced a slight perturbation to the initial conditions to avoid any singular behaviour with $u_z = 0$.

[11] An increase in g raises both the streamwise force $g\sin\theta$ and the friction force $\mu g\cos\theta$. The two effects approximately cancel each other out, although increasing g also indirectly lowers the coefficient of friction μ

If θ is changed suddenly and then kept constant, the velocity profile can be expected to adjust towards the new Bagnoldian equilibrium, according to the relaxation described in §12.2. Using the previous expression for $\mu(I)$, we consider two cases, for which $g(t) = 1$ and

$$\theta(t) = \Theta \pm 5^\circ H(t), \quad \Theta = 15^\circ,$$

where H is the Heaviside step function. (The angle increment 5° is arbitrary.) The case of an abruptly increasing θ corresponds to a downwards-kinked chute, while decreasing θ corresponds to an upwards kink. Figure 12.4 shows the response of (a) the surface velocity and (b) the shape factor to these two cases. As expected, in both cases $u(1,t)$ adjusts towards their new equilibria, and $\chi \to 5/4$ as $t \to \infty$. The asymmetry between the two cases arises from the concavity of the function form (12.11) for $\mu(I)$, so that $I(\theta) = \mu^{-1}(\tan\theta)$ does not change linearly with θ.

In the present chapter, the initial condition is Bagnoldian and already satisfies the no-slip condition $u(0,0) = 0$. Therefore, unlike the previous section, the evolutions of the velocity profile and of χ are not driven by a growing basal boundary layer. Instead, the relaxations towards the new equilibria are more akin to the transient behaviours in §12.3 after the initial power-law regimes for $\chi - 1$. From figure 12.4(b), we also note that in the case of an downwards kink (corresponding to an increase in θ and therefore an increase in the equilibrium velocity), the shape factor transiently falls below $5/4$; while for the downwards kink the shape factor rises above $5/4$. In any case, however, the variation in χ in figure 12.4(b) is less than $1/20$.

12.5. Gradually varying θ

We also consider the case of θ varying continuously with time, instead of having a step discontinuity.[12] The resulting dynamics depends on the timescale of this variation, and how this timescale compares with the diffusive timescale $\mathcal{T} = \delta^{-1}(\mathcal{H}/\mathcal{G})^{1/2}$, over which momentum diffuses through the current. Suppose that the timescale of variation be $\mathcal{T}/\epsilon$, with the slowness parameter $\epsilon \ll 1$. This slowly-varying case is analogous to the streamwise problem that we studied in §10.3.4: once again, the flow can adjust towards its equilibrium state.

For demonstration, we show numerical solutions for the cases

$$\theta(t) = \Theta + 5^\circ \times \tanh(\epsilon t), \quad \Theta = 15^\circ, \quad \epsilon = \frac{1}{20}, \frac{1}{40}, \frac{1}{60}, \tag{12.14}$$

with θ increasing: figure 12.5 shows the surface velocity (panel (a)) and the shape factor (panel (b)), all plotted against the rescaled variable $\epsilon^{1/2}t$. The collapse of the curves in panel (a) indicate the significance of an $O(\epsilon^{-1/2})$ timescale. The $O(\epsilon^{-1/2})$ scaling for this timescale did not appear to be sensitive to the rheological function $\mu(I)$: specifically, the $O(\epsilon^{-1/2})$ timescale arose irrespective of the value of α in (12.11). As in the previous sections, we understand this to reflect the fact that, because the initial conditions already satisfy the no-slip condition, the velocity profile is not evolving according to a spreading basal boundary layer (whose scalings would depend on α).

It can also be seen, from panel (b), that χ transiently drops below its equilibrium value (as in §12.4), with the reduction in χ being least for the smallest value of ϵ, representing the flow's constant adjustment towards the Bagnoldian state. As in §12.4, the actual variation in χ is not large.

by increasing the pressure and therefore reducing the inertial number.

[12] We could also vary g, but see footnote 11.

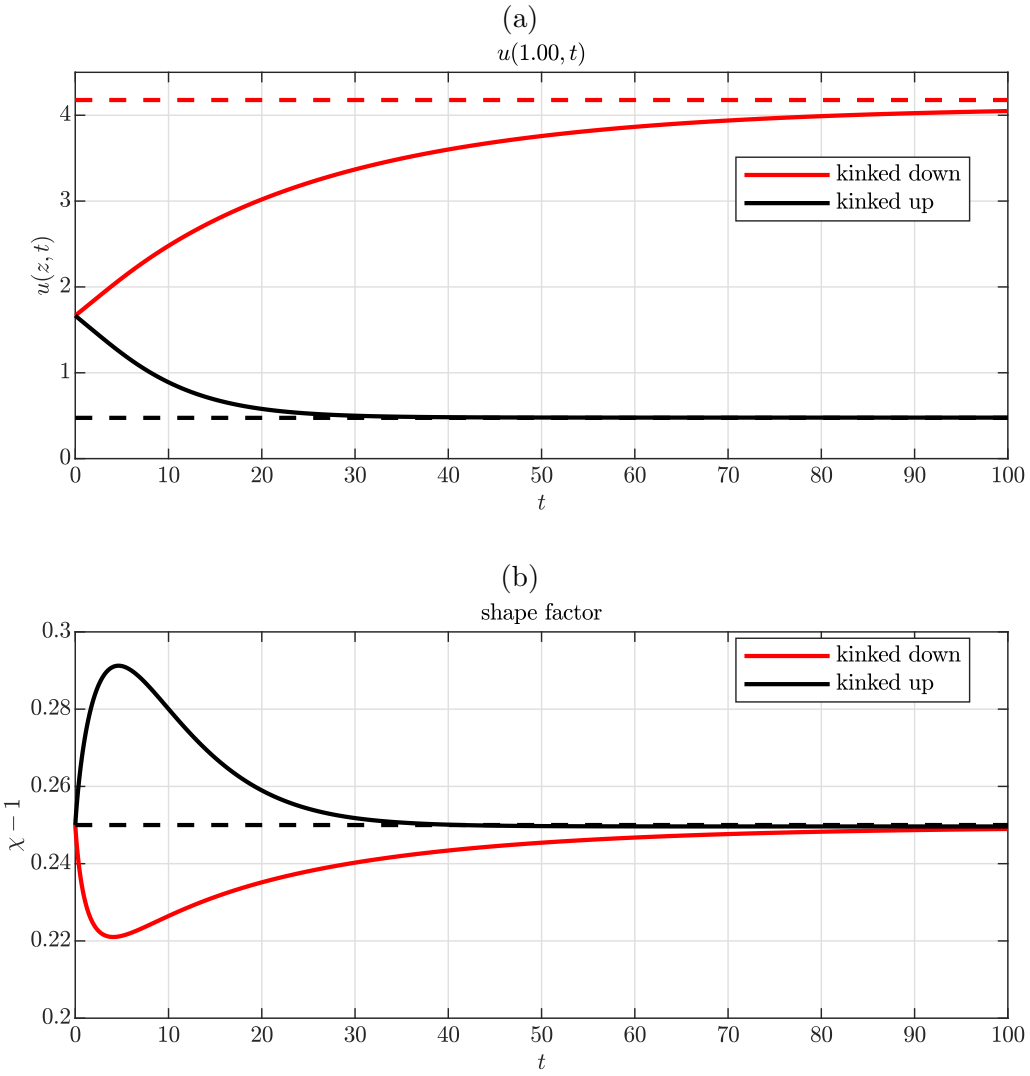

Figure 12.4.: The response of a flow (initially Bagnoldian at 15°) to a sudden change of θ to 20° (red) or to 10° (black). Panel (a) shows the evolution of the surface velocity $u(1, t)$; panel (b) shows the corresponding evolution of the shape factor. The two cases are not symmetrical (see text).

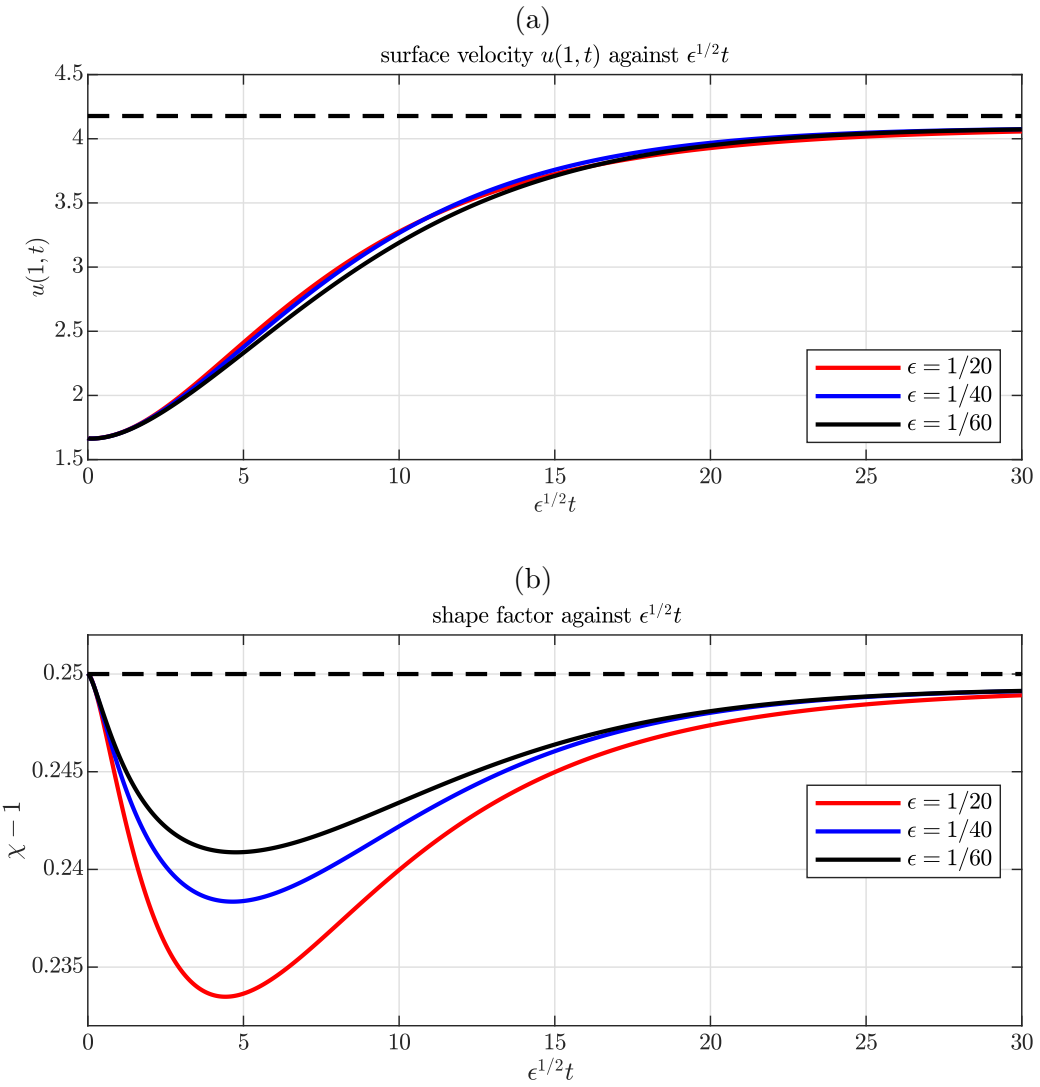

Figure 12.5.: The response of a flow (initially Bagnoldian at 15°) to a gradual increase in θ according to (12.14), with ϵ being a slowness parameter (see text). Panel (a) shows the evolution of the surface velocity $u(1,t)$; panel (b) shows the corresponding evolution of the shape factor. Both are plotted against $\epsilon^{1/2}t$ on the horizontal axis. The behaviour for θ gradually decreasing is reversed but otherwise qualitatively similar: $u(1,t)$ decreases monotonically towards its new equilibrium while χ transiently rises above its equilibrium.

12.6. Applicability towards spatial topography

As in Chapter 11, one motivation for studying the problems in this chapter is to consider the response of the shape factor χ to inhomogeneous topographical features. This information can then be used to inform our choice of χ in a depth-averaged model, beyond the naïve approach, used in Chapter 10, of taking $\chi = 1$ or $\chi = 5/4$ as piecewise constant. In this chapter, the inhomogeneities in basal conditions or the direction of gravity θ were in time, rather than space. We interpreted the step change in basal boundary condition as a temporal version of the setup in figure 1.4(a), and changes in θ as a temporal version of kinked or curved chutes.

Time-dependent basal conditions or gravitational fields ('temporal topography') are difficult to implement in an experiment[13], but they are of relevance to DPM simulations: long chute flows are often simulated using a periodic domain in a DPM (§8.1.1), with the domain taken be a 'representative' portion of the chute. One might attempt to represent a steady flow on a long chute with streamwise features by using a time-dependent flow in a periodic domain that is interpreted as moving along with the flow in a travelling and rotating frame. Therefore, for example, a sudden switch-on of the no-slip condition (§12.3) would represent the point at which this portion crosses a roughness transition.

We noted, however, that a periodic domain cannot validly model a streamwise flow that does not reach an equilibrium, as in figure 8.2: such a flow in a periodic model would instead accelerate indefinitely. We have now also seen that, even when an equilibrium does exist, a streamwise-independent, time-dependent model does not necessarily accurately predict the evolution towards this equilibrium: this was evident from the relaxation of the time-dependent granular Blasius problem (§12.3), where the temporal evolution of the shape factor was qualitatively distinct from the streamwise-dependent problem of Chapter 11. In that problem, the shape factor χ monotonically increased towards its equilibrium value of 5/4; in this chapter, we saw that the transient growth of χ may exceed that value. We have also seen that if the initial velocity profile is already Bagnoldian and therefore satisfies the no-slip condition (and $\chi = 5/4$), then changes in θ, which do not affect this boundary condition, disturb χ from its equilibrium value but only by a very small amount, whether the change in θ be sudden (§12.4) or gradual (§12.4).

We are therefore prompted to identify two separate processes that occur as a flow evolves towards a steady state. The first is the formation and growth of a boundary layer, which arises in response to a change in basal boundary conditions. The second is the adjustment of a velocity profile towards the equilibrium, through the diffusion of momentum, when the profile already has the correct qualitative shape. The first process is responsible for bring the shape factor up from $\chi = 1$ towards $\chi = 5/4$, according to a power law (12.13) whose exponent depends relatively strongly on the rheology of the material, through the exponent α that appears in (12.11). On the other hand, the second process has only a mild effect on χ, acting to accelerate or decelerate the flow uniformly without affecting the overall profile. The inability for the free surface to rise in the present setting also limits the rate of this adjustment.

As for the problems of changing θ (§§12.4, 12.5), care should be taken when directly comparing the behaviour predicted by the streamwise-independent equations (12.3) to that predicted

[13] In a non-inertial frame of reference, the effective body force can be modified by supplementing gravitational acceleration by additional fictitious forces (*cf.* Kollmer et al. (2015, 2016)). In general, these will affect both θ as well as the magnitude g of gravity.

by depth-averaged models (§§10.3.3, 10.3.4), or to the results of DPM simulations. The interpretation of the periodic domain as being in a travelling, rotating frame is not necessarily valid, because it neglects the Coriolis and centrifugal forces that would exist in such a rotating frame. The work of §12.4 may therefore be of limited applicability to modelling flows over kinks (figure 1.4(b)), although the study of the slowly-varying case §12.5 may nonetheless be useful, depending on the size of ϵ (which would control the magnitude of the fictitious forces).

To summarise, although a periodic domain is a tempting option for DPM of chute flow, given its computational simplicity, and although the streamwise-independent problem (12.3) is much more tractable than the full $\mu(I)$ equations, the response to temporal topography when streamwise-dependence is suppressed can be rather different from the response to streamwise topography of a steady flow. The latter is likely to be of more practical significance. Nonetheless, the use of a periodic domain was in the calibration tests of Chapter 9 remains reasonable: in that problem, there were no inhomogeneous topographical features, and we were solely concerned with whether flows reached a steady state and with the properties of that state, not with the transient behaviour.

* * *

Over the last three chapters, we have studied the roughness transition problem (figure 1.4(a)) using three different approaches. The depth-averaged approach (Chapter 10) captured the fact that the depth monotonically increases around the transition point, and identified the $O(\mathrm{Fr}^2)$ lengthscale, while the $\mu(I)$ rheology, which we simplified by setting either $\partial/\partial t = 0$ (Chapter 11) or $\partial/\partial x = 0$ (Chapter 12), gave us information about the internal evolution of the velocity profile.

Part IV.

Discussion and conclusions

We begin the final part of this thesis by summarising the work of the previous three parts (Chapter 13). We next discuss some aspects of granular flows that the models described in this thesis and their applications have neglected (Chapter 14). In particular, we revisit the assumption of two-dimensionality and discuss the interpretation of 2D models, and proposing the extension of these models to three dimensions (§14.1). We also review the possible instabilities that a granular flow may undergo, and suggest how these could interact with topographical features of a chute (§14.2). We close by restating the motivations and conclusions of the thesis (Chapter 15).

13. Summary

This short chapter summarises the contents of this thesis so far. More detailed summaries and discussions can be found throughout the thesis at the ends of parts and chapters.

The motivation for the present work, introduced in Chapter 1, has been to understand how a granular chute flow responds to inhomogeneous features, either streamwise variation along the chute, or time-dependent gravitational acceleration or boundary conditions. We refer to such inhomogeneities as 'topography'. Two examples of streamwise topography are shown in figure 1.4; they are to be contrasted with the uniform chute shown in figure 1.3. There have been numerous experimental studies on steady and uniform granular flows (see *e.g.* Forterre and Pouliquen (2003), GDR MiDi (2004), Takagi et al. (2011), Holyoake (2011)), and models have been validated against these experiments. This thesis seeks to apply these models to more complicated geometries, comparing between the predictions of continuum models (Part I) and the results of discrete particle model simulations (Part II).

Part I discussed continuum models of granular flow, distinguishing between rheological models and depth-averaged models. We reviewed the $\mu(I)$ rheology and its experimental calibration (Chapter 2). The $\mu(I)$ rheology was proposed as a generalisation of a one-dimensional friction law (2.4): the one-dimensional law is consistent with plenty of results from lab experiments and DPM simulations (GDR MiDi 2004, da Cruz et al. 2005); our eventual aim was to apply the tensorial form (2.7) and the equation of motion (2.10) proposed by Jop et al. (2006) to a flow in a more complicated geometry. While the $\mu(I)$ rheology is thought to apply to dense granular flows, it is known that there are many granular phenomena that the $\mu(I)$ rheology is unable to describe. We therefore reviewed some alternative rheological models (Chapter 3): although we made no further use of these other rheologies, we needed their language to describe some of the shortcomings of the $\mu(I)$ rheology. We also discussed the boundary conditions that apply to rheological models (Chapter 4). We noted that these boundary conditions do not arise from first principles, but are empirical and a consequence of the collective motion of individual grains. In particular, while the no-slip boundary condition is widely used in classical fluid dynamics, its applicability to granular flows on a surface depends on the roughness of the surface. We concluded Part I by reviewing the depth-averaged model (5.4), which is based on the $\mu(I)$ rheology (Chapter 5). Depth-averaged models are mathematically and computationally far more tractable than rheological models, especially over very long distances. However, depth-averaged models must make assumptions about the internal profile of a flow, expressed through the shape factor χ, defined in (5.6), which must be externally specified (§5.2). Without any external information, it is usually assumed that χ is constant, so that the velocity profile within a flow is self-similar (5.7). The self-similarity assumption is reasonable in the absence of any external lengthscales that are comparable to the current's depth, but is questionable near abrupt changes in topography that distort the velocity profile.

Part II turned towards discrete particle models (DPM) of granular chute flows. After introducing some fundamental ideas (Chapter 6), we discussed the contact dynamics between particles (Chapter 7), and the initial and boundary conditions that govern a DPM (Chapter 8). We noted

that 'boundaries' in a DPM act on individual particles, unlike boundary conditions in continuum models, which apply to the collective, averaged properties of particles. We emphasised throughout Part II the tradeoff that must be made between physical realism and computational efficiency. In particular, we use two-dimensional simulations: using only one layer of particles in the cross-stream direction allows us to simulate a longer chute or a deeper current, using the same number of particles. One important advantage of discrete particle modelling is the ability to specify freely the microscopic material parameters governing particle-to-particle interactions. We surveyed some of these parameters and studied their effects on the collective rheological behaviour of the flow (Chapter 9). In particular, we saw that the coefficient of restitution between particles controls the maximum value of the slope θ for which a steady uniform flow is possible, while the particle size and intrinsic friction affects the behaviour of the bulk friction function $\mu(I)$ at low inertial numbers.

In Part III we next applied continuum models to predict the response of a flow to changes in basal topography, and in particular to a chute that has an abrupt transition in basal roughness (figure 1.4(a)). For a steady flow responding to an abrupt transition in basal roughness, we analysed the depth-averaged model (5.4), and saw that a current adjusts towards its equilibrium on either side of the transition point, and that the lengthscales over which this adjustment occurs depends on the Froude number $\mathrm{Fr} = \mathcal{U}/(g\mathcal{H})^{1/2}$ (Chapter 10): for $\mathrm{Fr} \gg 1$, the downstream transition lengthscale is $O(\mathrm{Fr}^2)$. However, a transition in basal roughness does not uniformly affect a flow across its depth, but initially influences only a boundary layer near the base. The shape factor therefore does not transition abruptly from $\chi = 1$ (for a plug profile) to $\chi = 5/4$ (for a Bagnoldian profile), but in fact develops gradually. The development of this boundary layer has many similarities to the classical Blasius boundary layer problem. The boundary layer can be predicted by a suitable adaptation of the $\mu(I)$ rheology, with the predicted velocity profiles matching the results of DPM simulations (Chapter 11).

We also applied the $\mu(I)$ rheology to unsteady but streamwise-independent flows, subject to temporally-inhomogeneous topographical features (Chapter 12). Such flows could arise if a DPM in a periodic domain is used to model streamwise topography, supposing that the domain were travelling and rotating. We considered in particular the convergence of a velocity profile towards a Bagnold profile, starting from an initial plug flow (§12.3). As in the streamwise-varying case, the effects of the no-slip condition spread from the base across the depth of the current, again in a self-similar way. However, the subsequent growth and development of the velocity profile, and of the shape factor χ, was different between the time-dependent and the streamwise-dependent problems.

Chapter 14 shall now describe further aspects of granular flows that the present work have neglected, but which would be important for future extensions of the work. Finally, Chapter 15 shall reflect upon the themes and conclusions of the thesis.

14. Further aspects of granular flows

All conditioned things are unsatisfactory.

Buddhist concept of *dukkha*

There are many aspects of granular materials that the models described in this thesis have not captured. In this chapter, we address the effects of three-dimensionality on a granular flow (§14.1), the possibility of flow instabilities (§14.2), and revisit a variety of rheological behaviours that a granular flow may exhibit (§14.3). We also propose how these phenomena can interact with streamwise or time-dependent topography.

14.1. Three-dimensionality

A fundamental assumption that we have made throughout this thesis is that flows can be treated as quasi-two-dimensional.[1] That is, we assumed that there is statistically no velocity component v in the cross-stream direction y, and that the other fields had negligible dependence on y. We now revisit this assumption.

Recall that fields such as the velocity component v are defined by coarse-graining the positions and velocities of individual particles (§9.1). Flows in chutes and channels may be treated as quasi-2D if the typical width $\mathcal{W}$ of a chute is small compared to the length $\mathcal{L}$ and depth $\mathcal{H}$ of the flow, so that particles are constrained in that direction. If $\mathcal{W} \ll \mathcal{H}, \mathcal{L}$, then the incompressibility condition (2.2) in three dimensions offers an extension of the shallowness scaling (5.5), *viz.*

$$\frac{|v|}{\mathcal{W}} \sim \frac{|u|}{\mathcal{L}}, \quad \text{so} \quad |v| \ll |u|,$$

and similarly $|v| \ll |w|$.

However, it is more difficult to justify that the dependence on y of the fields is weak. The validity of this assumption depends on the sidewalls and the shape of the chute. If the sidewalls are perfectly smooth so that grains can slip freely against them, then their presence exerts no stress and therefore no shear in the y direction.[2] But if the sidewalls have some roughness, then the velocity profile is distorted, and the no-slip condition may apply (§4.2.2). The effects of the chute width $\mathcal{W}$ on the velocity profile were studied experimentally by Jop et al. (2005). In their figure 6, Jop et al. (2005) present the cross-stream variation of the surface velocity of flows: as expected, the flow is fastest at the middle and slowest near the sidewalls; the flow is able to slip against the wall, but not freely. A notable result from Jop et al. (2005), in their figure 6(d),

[1] We noted in §6.1 an important distinction between quasi-two-dimensionality in a continuum model, and the 'strict' two-dimensionality of a DPM: a two-dimensional DPM consists of a single layer of particles (figure 6.1) confined to the plane. Our attention in the present section concerns the former notion.

[2] The geometric confinement of the sidewalls affects the packing fraction of the grains, but only weakly so unless $\mathcal{W} \sim d$.

is that although the surface velocity profile in the middle of the chute (away from the walls) is approximately constant, the width of the flow regions retarded by the sidewalls appears to be independent of the flow rate. It is not clear, however, what determines the width of these regions. This width depends on the boundary conditions on the flow at the sidewalls, which from visual inspection take a mixed (Knudsen) form (§4.2.2), allowing partial slip. However, the boundary condition is likely to be specific to the precise material properties of the grains ('glass beads') and of the sidewalls ('smooth [...] glass walls') used in their experiment.

It is tempting instead to interpret a quasi-two-dimensional model as describing the middle portion of the flow on a very *wide* chute, homogeneous in the cross-stream direction. In this context, cross-stream variations caused by sidewall friction are negligible. However, the scaling argument to show that $|v| \ll |u|, |w|$ no longer applies. Moreover, despite the homogeneity of the chute, a flow could nonetheless develop an instability in the cross-stream direction, as will be discussed in §14.2.2.

14.2. Instabilities

While none of the simulations or solutions we have presented have exhibited flow instabilities, we must recognise that granular flows are known to undergo a number of instabilities, three of which we now describe. In polydisperse granular flows, rather than the monodisperse flows studied in this thesis, segregation (§14.2.1) can cause the different species to separate from each other. In three dimensions, granular fingering (§14.2.2) is a secondary instability that occurs in a segregated flow. Finally, the roll-wave instability (§14.2.3) produces flows that are both streamwise-dependent and time-dependent. We shall propose future work to study how these instabilities might be affected by basal roughness, and therefore how they might interact with topography.

14.2.1. Segregation

By construction, the flows that we have considered in this thesis involve grains that are nominally monodisperse. But many important examples of granular flows in nature and industry consist of grains that have huge dispersity in size, shape and material properties. Recall from §6.2 that even a nominally monodisperse sample of grains has some size dispersity, and that a system of perfectly monodisperse particles may exhibit special behaviours such as the formation of regular lattice packings.

A flow consisting of a mixture of grains with a sufficiently large amount of dispersity does not remain homogeneously mixed, but tends to segregate (Andreotti et al. 2015), so that grains with different properties form layers rather than remaining as a mixture. For example, in the case of size dispersity, larger grains tend to rise towards up towards the top of the flow. The top of the segregated current therefore has rather different rheological properties from those at the bottom, and require separate modelling.

Despite the ubiquity of size segregation, the fundamental mechanisms that cause segregation are poorly understood. However, there has been plenty of work on quantifying the size segregation process, at least for bidisperse mixtures (see *e.g.* Gray and Thornton (2005)), and on relating

the rate of segregation to other flow properties. For example, the rate of segregation is known to increase with the shear rate (van der Vaart et al. 2018).

Future work could study how the rate of segregation is affected by topography, and also how segregation affects a flow's response to topography. For example, the fact that the rate of segregation increases with shear rate would suggest that an increase in basal roughness would hasten the segregation process by increasing the shear rate, especially at boundary layers (Chapters 11 and 12). Since the rheology of a bidisperse mixture depends on the local ratio between the two species, it would be interesting to study how the profiles and growth of granular boundary layers are affected by segregation. The methods of Chapter 11 could be useful for studying a segregation model in a context beyond that of steady or uniform flow.

14.2.2. Granular fingering

Granular segregation drives a number of other processes. In three dimensions, these include the granular fingering instability (Pouliquen et al. 1997), in which a bidisperse flow breaks up into fingers in the cross-stream direction, as shown in figure 14.1. There have been many experimental studies on fingering. Baker et al. (2016b) proposed a generalisation of the depth-averaged model (5.4) from Gray and Edwards (2014), with the new model incorporating cross-stream variation and segregation from bidispersity. They calculated numerical solutions to this model, demonstrating that these solutions exhibited granular fingering. More recently, fingering was realised for the first time in three-dimensional DPM simulations (Weinhart et al. 2017).[3]

The fingering instability cannot be created with the two-dimensional models that we have used in this thesis: two-dimensional continuum models suppress any cross-stream variation by setting $\partial/\partial y = 0$, while two-dimensional DPM have only one layer of particles in the cross-stream direction. Nonetheless, we expect that topography should have an important effect on the formation of fingers. As mentioned in §14.2.1, basal roughness can be expected to increase the rate of segregation, which is a necessary preliminary process for fingering; while a transition from rough to smooth basal conditions could suppress segregation but would not destroy any fingers that had already formed by the point of the transition. There is active work into investigating the statistics of finger widths, lengths and positions, both experimentally and using DPM simulations.[4] After these statistics have been established in the basic homogeneous case, then future work could study how these statistics are affected by topographical 'noisiness'. For example, cross-stream inhomogeneities in basal roughness could trigger the formation of a finger, by restricting the flow at some cross-stream positions but not others.

14.2.3. Roll waves

The aim of the present thesis has been to apply continuum models such as the $\mu(I)$ rheology (Chapter 2) and its depth-averaged form (Chapter 5) to time-dependent or spatially-dependent problems, looking at the transient properties of a flow rather than assuming that a flow is always at a quasi-steady and quasi-streamwise-independent state. Chapters 10 and 11 considered

[3] Fingering was first realised in the summer of 2016 in DPM simulations in a collaborative project between JMFT, Binbin Jin and Nathalie Vriend; these simulations were reported in Weinhart et al. (2017).

[4] In a side project, outside the scope of this thesis (footnote 3), we are studying how the fingering instability is affected by simulation parameters; video demonstrations may be found at `https://web.archive.org/web/20190329103404/http://www.damtp.cam.ac.uk/user/jmft2/fingering.html`.

Figure 14.1.: The fingering instability, exhibited by the release of a mixture of fine sand and coarse silicon carbide down a slope.

steady streamwise-dependent flows, while Chapter 12 was concerned with a time-dependent flow independent of x, but we have not considered the interaction between streamwise-dependence and time-dependence.

We have seen that when time-dependence (resp. streamwise-dependence) is suppressed, then the system evolves in the streamwise direction (resp. in time), spending its inertia until it attains the equilibrium state (that is, a Bagnold velocity profile). However, this is not necessarily the case when a flow can depend on both x and t. It is known, for example, that granular flows can be unstable to the roll-wave instability, which is the formation of travelling surface waves (Schonfeld 1996, Razis et al. 2014, Gray and Edwards 2014). The roll-wave instability is also observed in hydraulic flows (Dietze 2016, Cristo et al. 2008), where it is more commonly referred to as the Kapitza instability. In environmental and industrial contexts, 'roll waves possess a tremendous destructive potential' (Schonfeld 1996), because the peak depth and flow rate at the crest of a wave can be higher than those of the mean flow. The convective nature of the roll-wave instability (Drazin and Reid 2004) demonstrates the need for caution when assuming that a flow can be modelled as steady: a flow that appears to be steady at upstream positions may in fact be unsteady downstream.

Gray and Edwards (2014) showed that the depth-averaged $\mu(I)$ equations (§5.1) predict that the steady uniform state can be unstable, with the flow developing away from the steady uniform state and towards a limit cycle solution, which they identified as roll waves. In their stability analysis, Gray and Edwards (2014) took the shape factor as $\chi = 1$, assuming a plug flow profile. However, 'it has long been known that [hydrodynamical] roll waves will not form in the absence of bed friction' (Schonfeld 1996, pg. 9). This appears to be at odds with the assumption $\chi = 1$; basal topography, through its influence on χ, is likely to influence the the growth rate of roll waves. In light of the present thesis, a natural extension of Gray and Edwards (2014) would be to investigate how roll waves interact with topographical features such as the abrupt increase in

roughness encountered in the granular Blasius problem. In Chapter 11, we gave the approximate expression (11.37) for the growth of the shape factor in the transient region, and figure 11.14 showed the actual behaviour of χ from DPM simulations. This behaviour for $\chi = \overline{u^2}/\overline{u}^2$ could now be inserted into the depth-averaged model (5.4) and taken as an externally-specified feature for the base flow, before conducting a stability analysis.

There have been no reports on granular roll waves appearing in DPM simulations. Similarly, we observed no roll waves in the DPM simulations of the granular Blasius problem (§11.4). The position of the free surface had some time-variation, but this could be attributed to the periodicity of the Maser. The lack of roll waves is in spite of the range of slope angles θ and of Froude numbers Fr, with $\mathrm{Fr} > 2$ in each case. While it is unsurprising that frictionless particles moving over a smooth surface should develop no roll waves in $x < 0$, it is less clear why roll waves should be absent in $x > 0$. This may be due to the two-dimensionality of our simulations: since out-of-plane motions are prohibited, particles cannot move around each other as freely, so that overturning motions are restricted.

It is not clear how roll waves would interact with topography, such as an increase in basal roughness. The presence of basal roughness is necessary for the formation of roll waves in a granular flow (Schonfeld 1996). On the other hand, in the $\chi = 1$ case, the amplitude of the limit cycle solution is increasing with Froude number (Gray and Edwards 2014, figure 8(c)), and it is reasonable to assume that this continues to be the case when $\chi \neq 1$. Therefore, the slowing down and thickening of the flow due to the increased roughness might also be expected to decrease the Froude number, weakening the instability.

14.3. Applicability to other fluids

Whenever a rheological model, such as the $\mu(I)$ rheology, is proposed, an elementary problem is to apply it to simple shear flows (which are steady and streamwise-uniform, so that $\partial/\partial x = \partial/\partial t = 0$). These can be produced experimentally in free surface or shear cell geometries (Acheson 1990, GDR MiDi 2004), so they are useful tests for the validity of a rheology. For example, the friction law (2.4) correctly recovers the Bagnold velocity profile for steady uniform free surface flow, provided that the grain size $d \ll \mathcal{H}$. To develop the $\mu(I)$ rheology, Jop et al. (2006) then extrapolated the one-dimensional law (2.4) to the multidimensional tensorial constitutive relation (2.7), and inserted this into the Cauchy momentum equation (2.1b). The validity of this assumption cannot be justified without reintroducing streamwise-dependence or unsteadiness.[5]

The study of a fluid flow's response to inhomogeneous topographical features is therefore useful for testing any proposed rheological model of that fluid, if the problem is analytically tractable. In particular, the methods used to study granular boundary layers in Chapters 11 were directly adapted from Prandtl's classical methods (Prandtl 1905, Schlichting and Gersten 2017, Acheson 1990); for certain forms (2.17) of the function $\mu(I)$ it was even possible to find analytic expressions for the boundary layer profile and the shape factor. As we noted (§11.5.3), a similar

[5]There are parallels to the historical development of classical fluid dynamics (Acheson 1990, Chapter 6). The linear viscosity law $\tau = \eta\dot{\gamma}$ was proposed by Newton in 1687, and was initially applied only to axisymmetric rotational motion (and incorrectly so). A generalisation by Stokes to its full tensorial form $\boldsymbol{\tau} = \eta\boldsymbol{D}$, as used in the Navier–Stokes equations, came only in 1845. Boundary layer theory played an important role in reconciling the theories of inviscid fluids and Stokes flows, which had developed mostly separately.

approach can be performed under any rheological model in which the shear stress depends on the shear rate (to produce higher-order derivatives of the velocity which become dominant in a thin boundary layer).

Future projects could therefore apply these methods to the alternative rheologies of dry granular materials described in Chapter 3: for example, to test whether incorporating compressibility (§3.1) gives a more accurate match with the data from DPM simulations. Another possible project would be to apply this adapted boundary layer analysis to rheologies of granular *suspensions*, attempting to recover the experimentally measured boundary layer profiles of Longo and Valiani (2014).

* * *

Dry granular flows can exhibit a wide variety of behaviours, some of which were discussed in this chapter. While these effects have been studied and modelled mathematically, it is unlikely that any continuum model that fully describes all granular phenomena will ever be produced: for example, the continuum assumption breaks down over lengthscales comparable to the particle size, or when there are strong gradients in packing fraction. Nonetheless, these phenomena should be taken into account when comparing a granular model to experimental data, or when using a model to design an application. While we expect that many of these phenomena would be affected by topographical features, the nature of this relationship is not clear. At present, there is an insufficient mathematical understanding of phenomena such as granular segregation and fingering even in the absence of topography.

Despite the non-existence of a universal model, we have seen in this thesis that existing continuum models such as the $\mu(I)$ rheology are capable of predicting large parts of a flow's behaviour observed in DPM simulations or in experiments. Continuum models therefore remain useful, provided that their limitations can be identified.

15. Conclusions

> Is it not a pleasure, having learned something, to try it out at due intervals?
>
> Confucius, *Analects* 1:1

In this thesis, we have studied the behaviour of dry granular chute flows and their response to inhomogeneous topographical features, paying particular attention to the setup sketched in figure 1.4(a), concerning a flow over a surface that is smooth upstream, but rough downstream. We studied such a flow using several continuum models, and compared their predictions against each other and against the results of discrete particle model (DPM) simulations (Part III).

Modelling the interaction between a granular flow and topographical features on its chute has practical applications, given the importance of granular chute flows in industrial settings. Moreover, we propose that the sudden transition in basal roughness offers a useful model problem for constructing or testing rheological models of granular flows. The problem affords a simple application of a continuum model in which both the inertial and the stress terms are present in the Cauchy momentum equation,

$$\rho\left(\frac{\partial \boldsymbol{u}}{\partial t} + \boldsymbol{u}\cdot\boldsymbol{\nabla}\,\boldsymbol{u}\right) = \rho\boldsymbol{g} + \boldsymbol{\nabla}\cdot\boldsymbol{\sigma}. \tag{2.1b}$$

This is in contrast to steady uniform flow problems, which retain only the stress terms on the right but discard the inertial terms. Indeed, it was the successful study of the Blasius boundary layer that unified classical hydrodynamics by considering the balance between inertial and viscous effects (Acheson 1990, p. 264).[1] The analysis of the boundary layer problem would be useful for studying the rheology of non-Newtonian fluids besides dry granular flows. For example, boundary layers are also known to form in suspensions flowing past a blade (Longo and Valiani 2014). The methods of Chapter 11, in turn based on those of Prandtl (1905), could be adapted to a rheological model of a suspension to find the velocity profile that such a model predicts. Indeed, in each case, the boundary layer is a region of high shear rate, and provided that the stress tensor has a dependence on the shear rate $\partial u/\partial z$, its derivative produces a dominant term proportional to $\partial^2 u/\partial z^2$; when subdominant terms are dropped from the momentum equation (2.1b) one obtains an equation similar to the classical boundary layer equation (11.5).

In the case of the $\mu(I)$ rheology, in which the stress depends on the shear rate nonlinearly through the inertial number I, the boundary layer analysis gave us the granular Blasius equation,

$$\mathrm{Fr}^2\left(\tilde{u}\,\frac{\partial \tilde{u}}{\partial \tilde{x}} + \tilde{w}\,\frac{\partial \tilde{u}}{\partial \tilde{z}}\right) \sim \sin\theta + \frac{1}{\epsilon}\,\frac{\partial \tilde{p}}{\partial \tilde{z}}\left(\mu - \frac{1}{2}\,\frac{\mathrm{d}\mu}{\mathrm{d}I}\,I\right) + \frac{1}{\epsilon}\tilde{p}\,\frac{\mathrm{d}\mu}{\mathrm{d}I}\,I\frac{\partial^2 \tilde{u}/\partial \tilde{z}^2}{\partial \tilde{u}/\partial \tilde{z}}. \tag{11.25b}$$

[1] 'Prior to 1900, ideal flow theory and viscous flow theory had more or less gone their separate ways. [...] [A] major problem remained: that of accounting for the motion of a fluid of small viscosity past a solid body.' (Acheson 1990, p. 264)

When we made the assumption that the rheological function $\mu(I)$ takes the power-law form (2.17), we could make further progress by deleting the first two terms on the right-hand side of (11.25b), and finding a self-similar solution (§11.3.3). However, although the form (2.17) fits data from calibration simulations (see Chapter 9 and figure 11.8), we used (2.17) on the understanding that it no more than a mathematically convenient fit. Likewise, we noted that although the more commonly-used fit

$$\mu(I) = \mu_1 + \frac{\mu_2 - \mu_1}{I_0/I + 1}, \tag{2.16}$$

also fits data from simulations, the value for μ_2 should be regarded only as a fitted parameter, and not be given any physical meaning. While $\arctan \mu_2$ is often identified as the maximum value of θ for steady uniform flow to be possible, we saw that the cutoff angle is in fact smaller than $\arctan \mu_2$ (§9.7).

As mentioned in the introduction (Chapter 1), experimental study of the rheology of granular flows faces several obstacles: in particular, the opaqueness of grains makes it impossible to directly measure the internal velocity profile of a flow. A flow can be measured only through the flow depth $h = s - b$ (where s is the position of the free surface, which can be measured; and b is the position of the base, which we assume to be known), flow rate q, and surface velocity u_{surf}. From h and q, the depth-averaged velocity $\overline{u} = q/h$ can be calculated, but information about the internal velocity profile, such as the shape factor $\chi = \overline{u^2}/\overline{u}^2$, cannot be inferred.[2] Since our interest has been in the internal profile of a flow and its response to basal topography, we resorted to discrete particle model simulations when realising the setup of figure 1.4(a).[3]

A recurrent theme of our discourse on DPM (Part II) has been the trade-off between improving a DPM's resolution at the level of individual particles, and reducing the computational cost of a simulation. By conducting simulations in two dimensions, we were able to simulate flows over long domains, at the expense of detail in the cross-stream dimension.[4] As techniques for improving the computational cost of simulations, working in two dimensions, reducing the number of particles, and reducing the stiffness of contacts are well-established in the DPM literature (O'Sullivan 2014). We extended these techniques by exploring particle-level parameters governing contacts besides stiffness (Chapter 9), and their effects on the bulk, rheological properties of a flow.

An important result was that, although microscopic parameters such as the coefficient of restitution e and the coefficient of sliding friction μ_{sl} have some mild effects on the rheology of a dense flow, their main effect is to determine the boundaries of phase transitions, that is, whether the material does in fact behave as a dense flow. The insensitivity to e and μ_{sl} is useful because it implies that we have some freedom to choose contact properties on the basis of computational criteria. We also found that seemingly unrealistic values for e and μ_{sl} may be taken, especially in a two-dimensional simulation: indeed, we took $e = 0.1$ and $\mu_{\text{sl}} = 0$. For example, the relatively small number of particles in a DPM simulation implies that more energy must be dissipated in each collision, if the volume-integrated total rate of dissipation is to be kept realistic. This is the approach taken by smoothed particle hydrodynamical models (Liu and Liu 2010). On

[2] One can however test whether the measured values of u_{surf} and $\overline{u}$ are consistent with a proposed velocity profile $S(\zeta)$ in (5.7).

[3] This is not to say that no lab experiments are possible: as previously noted (Chapter 6), two-dimensional DPM simulations are similar to experiments on photoelastic discs in their modelling approach.

[4] Two-dimensional simulations also have the advantage of being more directly comparable to experiments on photoelastic discs.

the other hand, intrinsic friction between particles is not necessary for the bulk flow to exhibit friction; as a first attempt, one could set $\mu_{\mathrm{sl}} = 0$.

Together, these results will help guide future researchers constructing DPM of granular flows to choose parameters for their models. Unlike lab experiments, DPM simulations avoid the experimental difficulty that the properties of grains can vary widely between samples and can also change over time. Instead, it is possible to specify material parameters exactly, allowing comparisons between different studies to be drawn. However, in practice, there has been little consensus or standardisation in the DPM literature on the proper values of these parameters; to facilitate comparison, we would therefore encourage future projects using two-dimensional DPM to consider using the parameters taken in this thesis.

While many challenges remain for the modelling of granular flows, it is hoped that the work in this thesis can be used to better understand the behaviour of granular flows, and therefore to assist in the design of chutes and other systems for the transfer of granular materials. Improving the efficiency of such transfer processes will become increasingly important as the economic importance of granular materials continues to grow.

Appendices

A. Implementation of DPM simulations

From all the deceits of the world, the flesh, and the devil, Good Lord, deliver us.
The Litany, from the *Book of Common Prayer*

When contact models (Chapter 7) and initial and boundary conditions (Chapter 8) have all been specified, a simulation may begin, proceeding by time-integrating Newton's equations of motion (6.1a, 6.1b) for each particle and applying boundary conditions on particles when any become applicable. Computationally, this process faces two main difficulties. Firstly, a simulation needs a *contact detection* algorithm to determine which particles are in interaction with each other (§A.1). Secondly, a simulation should use a suitable *integration scheme* that minimises errors from the numerical integration (§A.2).

The simulations conducted in this work were all performed using MercuryDPM, an open-source C++ package for DPM simulations (Thornton et al. 2013, 2012, Weinhart et al. 2012, 2017). In this appendix, we describe existing techniques addressing contact detection and time-integration efficiently, which are implemented in MercuryDPM. In §A.3 we describe the computational resources that were available to us.

A.1. Contact detection algorithm

The contact force $\boldsymbol{f}_{ij}^{\mathrm{c}}$ on particle i by particle j is nonzero only if the particles are in contact with each other: that is, if $|\boldsymbol{x}_i - \boldsymbol{x}_j| < (d_i + d_j)/2$. Since each particle has a limited number of neighbours (§6.1), the number of contacts in a system of N particles, at a given time, is $O(N)$. A good contact detection algorithm keeps track of which particles are near each other, instead of naïvely testing each of the $\binom{N}{2} = O(N^2)$ possible particle pairs for a contact.[1]

MercuryDPM uses a unique 'hierarchical grid' or 'H-grid' method (Thornton et al. 2013, Ogarko and Luding 2012). The simulation domain is divided into a number of grid cells. The algorithm records which particles are in which cells, and checks for contacts only between those particles that are in the same or neighbouring cells. The 'hierarchy' refers to the existence of several layers of grids, similar to the multigrid approach to numerically solving partial differential equations. The hierarchical approach is particularly valuable for systems with large size polydispersity (Ogarko and Luding 2012); contacts involving larger particles are tested for at coarser grids, while contacts between small particles are tested only at finer grids.

[1] This is not possible if particles are allowed to interact over long distances, such as through electrostatic forces.

A.2. Integration scheme

For the numerical integration of Newton's equations (6.1a, 6.1b), MercuryDPM uses the velocity Verlet integration scheme (Verlet 1967, Swope et al. 1982). While this scheme offers only second-order accuracy (as opposed to the common fourth-order RK4 scheme (Iserles 2008)), it is a 'symplectic integrator', and conserves energy when applied to a Hamiltonian system, including non-dissipative contacts, where the dissipation term in (7.3) vanishes (John Hinch, pers. comm., October 2018).[2] As an explicit method, the Verlet scheme is straightforward to implement and not computationally costly.

A.3. Execution

The execution time of a simulation depends not only on the timestep and the number of particles in the system, but also on the speeds of these particles: under the contact detection algorithm described in §A.1, if a particle moves quickly across grid cells then it will be necessary to continually update the grid. There is also a dependence on the size dispersity of the particle, since a variation in particle size will necessitate multiple levels of the H-grid. With our limited 10% size dispersity, the execution time of a simulation of N particles grew approximately as $O(N)$. When there was a significant variance in particle sizes, the execution time was much larger.

To close this appendix, we describe the computational resources that were available to us, as a guide for future work in this environment.[3]

Most of the simulations presented in this work were run on the DAMTP server `beehive`, which has 144 processing units. The server is used by many users, so the real execution time varied greatly depending on the system load from other users' processes. When the system load was at its least, each instance of a simulation took around two weeks to produce the data that we present in Chapter 11. Each simulation contained about 10^5 particles and produced just less than 4GB of output. The parallel execution of multiple instances of MercuryDPM across multiple cores was scheduled using GNU Parallel (Tange 2018).

MercuryDPM provides output about particles' positions and velocities in a `data` file, and about particle-to-particle interaction forces in a `fstat` file, at prescribed intervals during a simulation. Due to constraints on file storage, we were not able to store the `fstat` files for the simulations in Chapter 11.

The coarse-graining process (§9.1) was conducted using `MercuryPostprocessing`, a suite of MATLAB scripts developed for this work.

[2] A generalised notion of symplecticity can be applied to integrators for dissipative systems (Anthony Thornton, pers. comm., April 2018). Such integrators would accurately calculate the rate at which energy is lost.

[3] I would like to thank the Computing Officers for their support and patience with my heavy use of the resources.

B. Further notes on the granular Blasius problem

In this appendix we give some supplementary information about the calculations and results presented in Chapter 11.

B.1. Derivation of the granular Blasius equation

Here we derive (11.25b) from the $\mu(I)$ equations (2.10). Under the scalings (11.24), the strain rate direction tensor $\boldsymbol{s}$ is greatly simplified at leading order in ϵ, with

$$s_{xx} = O(\epsilon), \quad s_{zz} = O(\epsilon), s_{xz} = s_{zx} = 1 + O(\epsilon^2).$$

From this we estimate the size of each term in the z-component of (2.10):

$$\begin{aligned} \epsilon \mathrm{Fr}^2 \left(\tilde{u} \frac{\partial \tilde{w}}{\partial \tilde{x}} + \tilde{w} \frac{\partial \tilde{w}}{\partial \tilde{z}} \right) &= -\cos\theta - \frac{1}{\epsilon} \frac{\partial \tilde{p}}{\partial \tilde{z}} + \frac{\partial (\mu(I) \tilde{p} s_{xz})}{\partial \tilde{x}} + \frac{\partial (\mu(I) \tilde{p} s_{zz})}{\partial \tilde{z}} \\ \implies O(\epsilon^2 \mathrm{Fr}^2) &= -\frac{\partial \tilde{p}}{\partial \tilde{z}} + O(\epsilon). \end{aligned} \tag{B.1}$$

We postulate $\epsilon \mathrm{Fr} \ll 1$, but must later confirm the validity of this assertion (§B.2). The assumption $\mathrm{Fr} \gg 1$ therefore requires $\epsilon \ll 1$. Then (B.1) implies that $|\partial \tilde{p}/\partial \tilde{z}|$ is small in the boundary layer, so that (by the matching condition) the pressure across the boundary layer is given by the pressure from the outer flow, $\tilde{p} = \tilde{h} \cos\theta$. If the depth $\tilde{h}$ is taken to be locally constant (see main text), then $\tilde{p}/\tilde{x}$ vanishes as well, so that $\tilde{p}$ is constant throughout the boundary layer. By definition, the (dimensional) depth of the incident flow is $\mathcal{H}$, so that $\tilde{h} = 1$ and we write $\tilde{p} = \cos\theta$.

We now consider the x-component of (2.10). When the rescalings (11.24) are applied, we obtain

$$\begin{aligned} \mathrm{Fr}^2 \left(\tilde{u} \frac{\partial \tilde{u}}{\partial \tilde{x}} + \tilde{w} \frac{\partial \tilde{u}}{\partial \tilde{z}} \right) &= \sin\theta + \frac{1}{\epsilon} \frac{\partial (\mu(I) \tilde{p})}{\partial \tilde{z}} + O(\epsilon), \\ &= \sin\theta + \frac{1}{\epsilon} \mu(I) \frac{\partial \tilde{p}}{\partial \tilde{z}} + \frac{1}{\epsilon} \tilde{p} \frac{\mathrm{d}\mu}{\mathrm{d}I} \frac{\partial I}{\partial \tilde{z}}, \end{aligned} \tag{B.2}$$

subdominant terms having been omitted. To proceed, we calculate the inertial number. To leading order, the magnitude of the shear rate tensor is

$$||\boldsymbol{D}|| = \frac{1}{2\epsilon} \frac{\partial \tilde{u}}{\partial \tilde{z}} + O(\epsilon),$$

so the inertial number is

$$I \sim \frac{\delta \mathrm{Fr}}{\epsilon \tilde{p}^{1/2}} \frac{\partial \tilde{u}}{\partial \tilde{z}},$$

and

$$\frac{1}{I}\frac{\partial I}{\partial \tilde{z}} \sim -\frac{1}{2\tilde{p}}\frac{\partial \tilde{p}}{\partial \tilde{z}} + \frac{\partial^2 \tilde{u}/\partial \tilde{z}^2}{\partial \tilde{u}/\partial \tilde{z}}.$$

Expanding the derivative on the right-hand side of (B.2) yields

$$\mathrm{Fr}^2\left(\tilde{u}\,\frac{\partial \tilde{u}}{\partial \tilde{x}} + \tilde{w}\,\frac{\partial \tilde{u}}{\partial \tilde{z}}\right) \sim \sin\theta + \frac{1}{\epsilon}\frac{\partial \tilde{p}}{\partial \tilde{z}}\left(\mu - \frac{1}{2}\frac{\mathrm{d}\mu}{\mathrm{d}I}\,I\right) + \frac{1}{\epsilon}\tilde{p}\,\frac{\mathrm{d}\mu}{\mathrm{d}I}\,I\frac{\partial^2 \tilde{u}/\partial \tilde{z}^2}{\partial \tilde{u}/\partial \tilde{z}},$$

which is (11.25b), as required.

B.2. Conditions for $\epsilon\mathrm{Fr} \ll 1$

The derivation of (11.25), given in §B.1, is valid only if the boundary layer thickness scale ϵ satisfies $\epsilon\mathrm{Fr} \ll 1$, which was to be checked *a posteriori*.

The boundary layer thickness scale for ϵ was given in (11.27). When it is stripped of $O(1)$ constants, we have

$$\epsilon \propto \left(\delta^\alpha \mathrm{Fr}^{-(2-\alpha)}\right)^{1/(1+\alpha)},$$

and so

$$\epsilon\mathrm{Fr} \propto \left(\delta^\alpha \mathrm{Fr}^{2\alpha-1}\right)^{1/(1+\alpha)}. \tag{B.3}$$

Assuming that $\alpha > 0$, the required condition for $\epsilon\mathrm{Fr} \ll 1$ is that

$$\delta^\alpha \mathrm{Fr}^{2\alpha-1} \ll 1. \tag{B.4}$$

We note first that (B.4) is satisfied automatically if $\alpha = 0$ or $\alpha = 1/2$, provided that $\delta \ll 1$ and $\mathrm{Fr} \gg 1$. For intermediate values $0 < \alpha < 1/2$, (B.4) becomes

$$\mathrm{Fr} \gg \delta^{\alpha/(1-2\alpha)},$$

which is also automatically satisfied, given that $\delta \ll 1$.

If instead $\alpha > 1/2$, then (B.4) becomes

$$\mathrm{Fr} \ll \delta^{-\alpha/(2\alpha-1)}. \tag{B.5}$$

Our analysis is invalid if Fr is large enough to violate (B.5), but, since $\delta \ll 1$, that upper bound is large and the above condition is almost always satisfied in practice. For example, for $\alpha = 1$, we have $\alpha/(2\alpha - 1) = 1$, and if $\delta = 1/50$ then (B.5) holds up to $\mathrm{Fr} \approx 50$.

We also consider the cases $\alpha < 0$. For $-1 < \alpha < 0$, (B.3) requires that

$$\mathrm{Fr} \gg \delta^{\alpha/(1-2\alpha)}.$$

This is a large *lower* bound on Fr. On the other hand, for $\alpha < -1$, (B.3) is equivalent to

$$\mathrm{Fr} \ll \delta^{\alpha/(1-2\alpha)},$$

which, like (B.4), imposes an upper bound on Fr. Note, however, that the case $\alpha < -1$ predicts an incorrect behaviour for the boundary layer (§11.3.4). Finally, the case $\alpha = -1$ is singular, owing to the power $1/(1 + \alpha)$.

To summarise, the condition $\epsilon\mathrm{Fr} \ll 1$ is automatically satisfied for $0 \leq \alpha \leq 1/2$. For realistic values of δ, the condition is usually satisfied for $\alpha < -1$ or $\alpha > 1/2$, but not for $-1 < \alpha < 0$.

B.3. Perturbation to the outer flow

The perturbation to the outer flow in the granular Blasius problem is $O(\epsilon)$ and, to leading order, satisfy a semilinear system. For simplicity, work in nondimensional units, scaling velocity components u and w bu $\mathcal{U}$, coordinates x and z by $\mathcal{H}$, and pressure p by $\rho g \mathcal{H}$. To leading order in ϵ, let

$$\begin{aligned} u &= u^{(0)}(z) + \epsilon u^{(1)}, & w &= \epsilon w^{(1)}, \\ p &= p^{(0)}(z) + \epsilon p^{(1)}, & h &= 1 + \epsilon h^{(1)}, \end{aligned}$$

where $p^{(0)} = \cos\theta(1-z)$ is the hydrostatic pressure, and $u^{(0)}(z)$ is the Bagnold with slip profile (2.12) of the incident flow. The shear rate tensor has magnitude

$$||\boldsymbol{D}|| = \frac{1}{2}\frac{\mathrm{d}u^{(0)}}{\mathrm{d}z} + \frac{1}{2}\epsilon\left[\frac{\partial u^{(1)}}{\partial z} + \frac{\partial w^{(1)}}{\partial x}\right], \tag{B.6}$$

the shear direction tensor is

$$\boldsymbol{s} = \begin{bmatrix} 2\epsilon\dfrac{\partial u^{(1)}/\partial x}{\mathrm{d}u^{(0)}/\,\mathrm{d}z} & 1 \\ 1 & 2\epsilon\dfrac{\partial w^{(1)}/\partial z}{\mathrm{d}u^{(0)}/\,\mathrm{d}z} \end{bmatrix}, \tag{B.7}$$

the inertial number is given by

$$\frac{I}{\delta \mathrm{Fr}} = \left((p^{(0)})^{-1/2} - \frac{1}{2}\epsilon(p^{(0)})^{-3/2}p^{(1)}\right)\left(\frac{\mathrm{d}u^{(0)}}{\mathrm{d}x} + \frac{1}{2}\epsilon\left[\frac{\partial u^{(1)}}{\partial z} + \frac{\partial w^{(1)}}{\partial x}\right]\right) \tag{B.8}$$

$$= (p^{(0)})^{-1/2}\frac{\mathrm{d}u^{(0)}}{\mathrm{d}z} + \epsilon\left[(p^{(0)})^{-1/2}\left[\frac{\partial u^{(1)}}{\partial z} + \frac{\partial w^{(1)}}{\partial x}\right] - \frac{1}{2}(p^{(0)})^{-3/2}\frac{\mathrm{d}u^{(0)}}{\mathrm{d}z}p^{(1)}\right] \tag{B.9}$$

$$= \frac{1}{\delta \mathrm{Fr}}\left(I^{(0)} + \epsilon I^{(1)}\right), \tag{B.10}$$

and the coefficient of friction is

$$\mu(I) = \mu(I^{(0)}) + \epsilon\mu'(I^{(0)})I^{(1)}, \tag{B.11}$$

$$= \tan\theta + \epsilon\mu'(I^{(0)})I^{(1)}, \tag{B.12}$$

all up to $o(\epsilon)$ error terms.

The equations governing the perturbation variables are the linearised momentum equations

$$\begin{aligned} u^{(0)}\,\frac{\partial u^{(1)}}{\partial x} + \frac{\mathrm{d}u^{(0)}}{\mathrm{d}z}\,w^{(1)} = &-\frac{\partial p^{(1)}}{\partial x} + \tan\theta\,\frac{\partial p^{(1)}}{\partial z} \\ &+ \frac{\partial}{\partial z}\left(\mu'(I^{(0)})p^{(0)}I^{(1)}\right) \\ &+ 2p^{(0)}\tan\theta\frac{\partial^2 u^{(1)}/\partial x^2}{\mathrm{d}u^{(0)}/\,\mathrm{d}z}, \end{aligned} \tag{B.13a}$$

$$\begin{aligned} u^{(0)}\,\frac{\partial w^{(1)}}{\partial x} = &-\frac{\partial p^{(1)}}{\partial z} + \tan\theta\,\frac{\partial p^{(1)}}{\partial x} \\ &+ \mu'(I^{(0)})p^{(0)}\,\frac{\partial I^{(1)}}{\partial x} + 2\,\frac{\partial}{\partial z}\left(\frac{\partial w^{(1)}/\partial z}{\mathrm{d}u^{(0)}/\,\mathrm{d}z}\right), \end{aligned} \tag{B.13b}$$

together with the incompressibility condition

$$\frac{\partial u^{(1)}}{\partial x} + \frac{\partial w^{(1)}}{\partial z} = 0. \tag{B.13c}$$

The linearised boundary conditions at the free surface are that

$$w^{(1)} = \frac{\partial h^{(1)}}{\partial x}\,, \quad \frac{\partial u^{(1)}}{\partial z} = -\,\frac{\partial w^{(1)}}{\partial x}\,, \quad \text{and} \quad p^{(1)} = h^{(1)}\cos\theta \quad \text{at } z = 1, \tag{B.14a}$$

and the basal boundary condition on the perturbation flow is that

$$w^{(1)} = w_{\mathrm{disp}}(x) = \zeta_{\mathrm{disp}}u^{(0)}(0)\Lambda'(x) \quad \text{at } z = 0, \tag{B.14b}$$

where $w_{\mathrm{disp}}(x)$ is the displacement velocity from the boundary layer. Although the system (B.13) and (B.14) is semilinear in the perturbation variables, no further analytical progress is possible, unlike the linear equation $\boldsymbol{\nabla}^2 w^{(1)} = 0$ that arises for a Newtonian fluid, as given in Tsang et al. (2018).

B.4. Density and granular temperature profiles

Figures B.1 and B.2 show the depthwise profiles, along several streamwise positions, for the packing fraction ϕ and the granular temperature T from the simulations whose velocity profiles were presented in figure 11.10.

The granular temperature, a measure of the time-variability of a flow, is defined as the trace of the Reynolds stress tensor,

$$T = \operatorname{trace}\boldsymbol{R}, \quad \boldsymbol{R} = \langle\phi\boldsymbol{u}\boldsymbol{u}\rangle - \frac{\langle\phi\boldsymbol{u}\rangle\langle\phi\boldsymbol{u}\rangle}{\langle\phi\rangle}$$

(Hinze 1975), where angle brackets

$$\langle f\rangle = \frac{1}{t_2 - t_1}\int_{t_1}^{t_2} f\,\mathrm{d}t$$

denote the time-average of a function f. The plots in figure B.2 are normalised by

$$T_0 = \operatorname{trace}\boldsymbol{R}_0, \quad \boldsymbol{R}_0 = \frac{\langle\phi\boldsymbol{u}\rangle\langle\phi\boldsymbol{u}\rangle}{\langle\phi\rangle}.$$

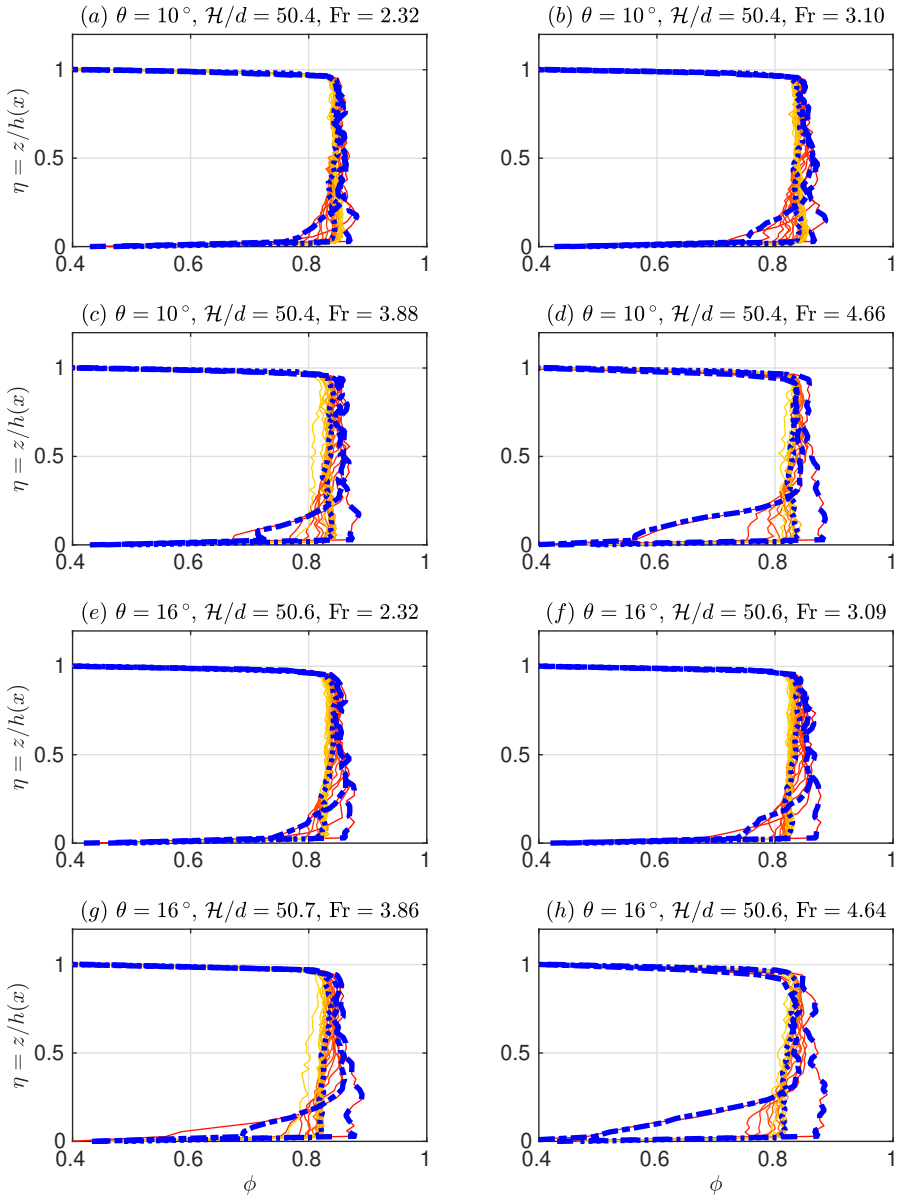

Figure B.1.: Packing fraction profiles for four settings of θ (rows) and two settings of Fr (columns), from the same simulations whose velocity profiles were shown in figure 11.10. See figure 11.10 for plot labels.

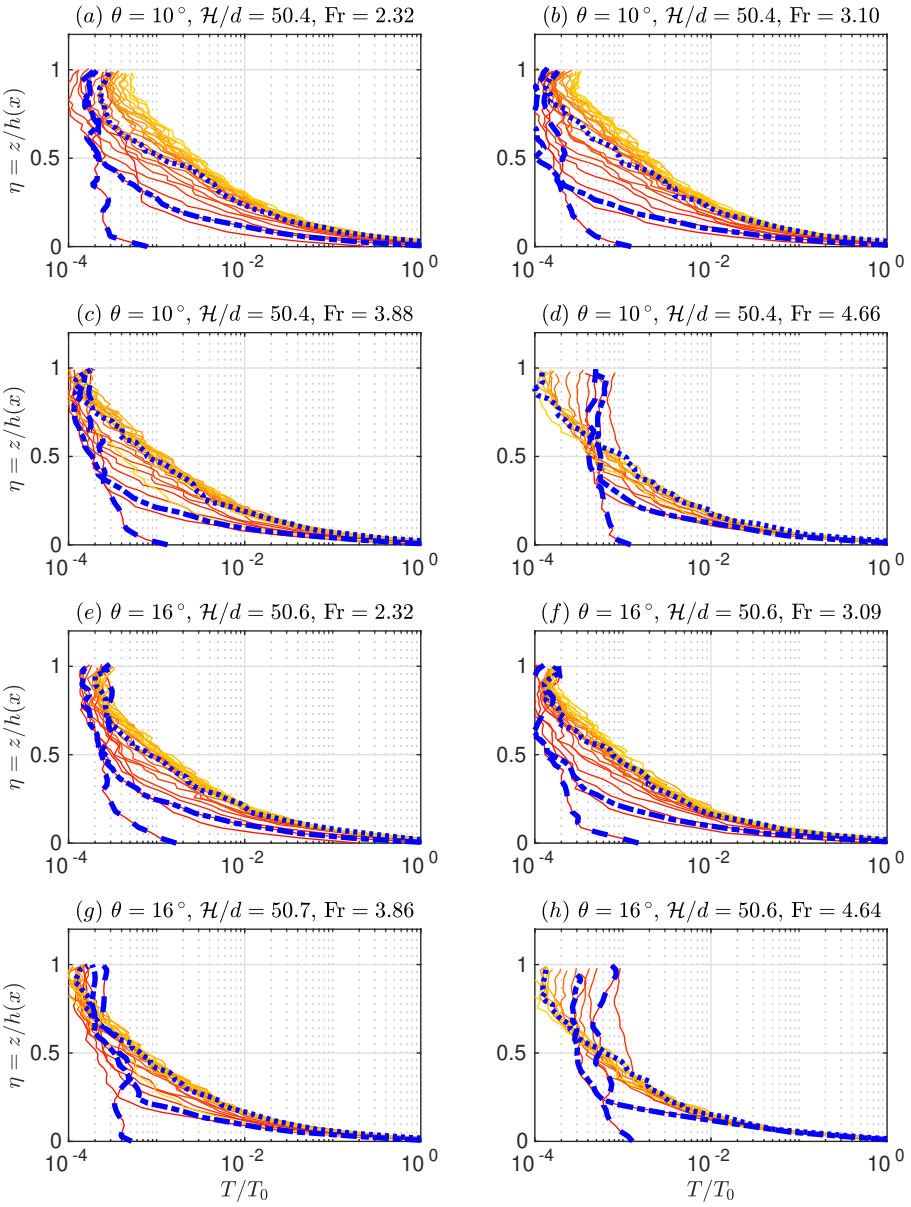

Figure B.2.: Temperature profiles for four settings of θ (rows) and two settings of Fr (columns), from the same simulations whose velocity profiles were shown in figure 11.10. See figure 11.10 for plot labels, and §B.4 for the definition of temperature.

Bibliography

M. J. Ablowitz and A. S. Fokas. *Complex Variables*. Cambridge University Press, 2003. doi: 10.1017/cbo9780511791246.

M. Abramowitz, I. A. Stegun, and R. H. Romer. *Handbook of Mathematical Functions with Formulas, Graphs, and Mathematical Tables*, volume 56. American Association of Physics Teachers (AAPT), oct 1988. doi: 10.1119/1.15378.

D. J. Acheson. *Elementary Fluid Dynamics*. Oxford University Press, 1990. ISBN 0198596790. URL `https://www.ebook.de/de/product/3237798/d_j_acheson_elementary_fluid_dynamics.html`.

B. Andreotti, Y. Forterre, and O. Pouliquen. *Granular Media*. Cambridge University Press, 2015. ISBN 1107034795. URL `https://www.ebook.de/de/product/20339274/bruno_andreotti_yoel_forterre_olivier_pouliquen_granular_media.html`.

D. Antypov and J. A. Elliott. On an analytical solution for the damped Hertzian spring. *EPL (Europhysics Letters)*, 94(5):50004, may 2011. doi: 10.1209/0295-5075/94/50004.

R. Artoni, A. Santomaso, and P. Canu. Effective boundary conditions for dense granular flows. *Phys. Rev. E*, 79:031304, Mar 2009. doi: 10.1103/PhysRevE.79.031304.

J. L. Baker, T. Barker, and J. M. N. T. Gray. A two-dimensional depth-averaged $\mu(I)$-rheology for dense granular avalanches. *Journal of Fluid Mechanics*, 787, January 2016a.

J. L. Baker, C. G. Johnson, and J. M. N. T. Gray. Segregation-induced finger formation in granular free-surface flows. *Journal of Fluid Mechanics*, 809:168–212, nov 2016b. doi: 10.1017/jfm.2016.673.

G. I. Barenblatt. *Scaling, Self-similarity, and Intermediate Asymptotics*. Cambridge University Press, 1996. doi: 10.1017/cbo9781107050242.

T. Barker, D. G. Schaeffer, P. Bohorquez, and J. M. N. T. Gray. Well-posed and ill-posed behaviour of the $\mu(I)$-rheology for granular flow. *Journal of Fluid Mechanics*, 779:794–818, aug 2015. doi: 10.1017/jfm.2015.412.

T. Barker, D. G. Schaeffer, M. Shearer, and J. M. N. T. Gray. Well-posed continuum equations for granular flow with compressibility and $\mu(I)$-rheology. *Proceedings of the Royal Society A: Mathematical, Physical and Engineering Science*, 473(2201):20160846, may 2017. doi: 10.1098/rspa.2016.0846.

G. K. Batchelor. *An Introduction to Fluid Dynamics*. Cambridge University Press, 2000.

Y. Bertho, F. Giorgiutti-Dauphiné, and J.-P. Hulin. Dynamical Janssen Effect on Granular Packing with Moving Walls. *Physical Review Letters*, 90(14), apr 2003. doi: 10.1103/physrevlett.90.144301.

S. Bharathraj and V. Kumaran. Effect of base topography on dynamics and transition in a dense granular flow. *Journal of Fluid Mechanics*, 832:600–640, oct 2017. doi: 10.1017/jfm.2017.683.

J. Billingham and A. C. King. *Wave Motion*. Cambridge University Press, 2001. doi: 10.1017/cbo9780511841033.

G. D. Birkhoff. Proof of the ergodic theorem. *Proceedings of the National Academy of Sciences*, 17(12):656–660, dec 1931. doi: 10.1073/pnas.17.2.656.

M. Bouzid, M. Trulsson, P. Claudin, E. Clément, and B. Andreotti. Nonlocal rheology of granular flows across yield conditions. *Physical Review Letters*, 111(23), dec 2013. doi: 10.1103/physrevlett.111.238301.

H. Burkill. *A Second Course in Mathematical Analysis*. Cambridge University Press, 2002. ISBN 0521523435. URL `https://www.ebook.de/de/product/3265968/h_burkill_a_second_course_in_mathematical_analysis.html`.

M. E. Cates, J. P. Wittmer, J.-P. Bouchaud, and P. Claudin. Jamming, force chains, and fragile matter. *Physical Review Letters*, 81(9):1841–1844, aug 1998. doi: 10.1103/physrevlett.81.1841.

V. T. Chow. *Open-Channel Hydraulics*. The Blackburn Press, 1959.

C. D. Cristo, M. Iervolino, A. Vacca, and B. Zanuttigh. Minimum channel length for roll-wave generation. *Journal of Hydraulic Research*, 46(1):73–79, jan 2008. doi: 10.1080/00221686.2008.9521844.

F. da Cruz, S. Emam, M. Prochnow, J.-N. Roux, and F. Chevoir. Rheophysics of dense granular materials: Discrete simulation of plane shear flows. *Physical Review E*, 72(2), 2005. doi: 10.1103/PhysRevE.72.021309.

R. Deluzarche and B. Cambou. Discrete numerical modelling of rockfill dams. *International Journal for Numerical and Analytical Methods in Geomechanics*, 30(11):1075–1096, 2006. doi: 10.1002/nag.514.

I. F. C. Denissen, T. Weinhart, A. T. Voortwis, S. Luding, J. M. N. T. Gray, and A. R. Thornton. Bulbous head formation in bidispersed shallow granular flow over an inclined plane. *Journal of Fluid Mechanics*, 866:263–297, mar 2019. doi: 10.1017/jfm.2019.63.

G. F. Dietze. On the Kapitza instability and the generation of capillary waves. *Journal of Fluid Mechanics*, 789:368–401, jan 2016. doi: 10.1017/jfm.2015.736.

P. G. Drazin and W. H. Reid. *Hydrodynamic Stability*. Cambridge University Press, 2004. doi: 10.1017/cbo9780511616938.

Engineering Toolbox. Friction and friction coefficients, 2004. URL `https://www.engineeringtoolbox.com/friction-coefficients-d_778.html`.

N. Estrada, E. Azéma, F. Radjai, and A. Taboada. Identification of rolling resistance as a shape parameter in sheared granular media. *Physical Review E*, 84(011306), 2011. doi: 10.1103/physreve.84.011306.

L. Evans. *Partial Differential Equations*. Graduate Series in Mathematics. American Mathematical Society, mar 2010. doi: 10.1090/gsm/019.

Y. Forterre and O. Pouliquen. Long-surface-wave instability in dense granular flows. *Journal of Fluid Mechanics*, 486:21–50, jun 2003. doi: 10.1017/s0022112003004555.

Y. Forterre and O. Pouliquen. Flows of dense granular media. *Annual Review of Fluid Mechanics*, 40(1):1–24, jan 2008. doi: 10.1146/annurev.fluid.40.111406.102142.

P. García-Navarro, P. Brufau, J. Burguete, and J. Murillo. The shallow water equations: An example of hyperbolic system. *Monografías de la Real Academia de Ciencias de Zaragoza*, 31, 01 2008.

GDR MiDi. On dense granular flows. *The European Physical Journal E*, 14(4):341–365, aug 2004. doi: 10.1140/epje/i2003-10153-0.

J. M. N. T. Gray and A. N. Edwards. A depth-averaged $\mu(I)$-rheology for shallow granular free-surface flows. *Journal of Fluid Mechanics*, 755:503–534, aug 2014. doi: 10.1017/jfm.2014.450.

J. M. N. T. Gray and A. R. Thornton. A theory for particle size segregation in shallow granular free-surface flows. *Proceedings of the Royal Society A: Mathematical, Physical and Engineering Sciences*, 461(2057):1447–1473, may 2005. doi: 10.1098/rspa.2004.1420.

G. Grimmett and D. Welsh. *Probability: An Introduction*. Oxford University Press, 2014. ISBN 0198709978. URL `https://www.ebook.de/de/product/23791413/geoffrey_professor_of_mathematical_statistics_university_of_cambridge_grimmett_dominic_professor_of_mathematics_retired_university_of_oxford_welsh_probability.html`.

P. K. Haff. Grain flow as a fluid-mechanical phenomenon. *Journal of Fluid Mechanics*, 134:401, sep 1983. doi: 10.1017/s0022112083003419.

K. M. Hákonardóttir. *The interaction between snow avalanches and dams*. PhD thesis, University of Bristol, 2004.

D. L. Henann and K. Kamrin. A predictive, size-dependent continuum model for dense granular flows. *Proceedings of the National Academy of Sciences*, 110(17):6730–6735, mar 2013. doi: 10.1073/pnas.1219153110.

J. Heyman, R. Delannay, H. Tabuteau, and A. Valance. Compressibility regularizes the $\mu(I)$-rheology for dense granular flows. *Journal of Fluid Mechanics*, 830:553–568, oct 2017. doi: 10.1017/jfm.2017.612.

E. J. Hinch. *Perturbation Methods*. Cambridge University Press, 1991. doi: 10.1017/cbo9781139172189.

J. O. Hinze. *Turbulence (McGraw-Hill series in mechanical engineering)*. McGraw-Hill College, 1975. ISBN 0-07-029037-7. URL `https://www.amazon.com/Turbulence-McGraw-Hill-mechanical-engineering-Hinze/dp/0070290377?SubscriptionId=AKIAIOBINVZYXZQZ2U3A&tag=chimbori05-20&linkCode=xm2&camp=2025&creative=165953&creativeASIN=0070290377`.

A. J. Hogg and T. Jóhannesson. Avalanche Defence Schemes. In *UK Success Stories in Industrial Mathematics*, pages 53–58. Springer International Publishing, Cham, 2016. doi: 10.1007/978-3-319-25454-8_7.

A. J. Hogg and D. Pritchard. The effects of hydraulic resistance on dam-break and other shallow inertial flows. *Journal of Fluid Mechanics*, 501:179–212, feb 2004. doi: 10.1017/s0022112003007468.

A. J. Holyoake. *Rapid Granular Flows in an Inclined Chute*. PhD thesis, University of Cambridge, 2011.

A. J. Holyoake and J. N. McElwaine. High-speed granular chute flows. *Journal of Fluid Mechanics*, 710:35–71, aug 2012. doi: 10.1017/jfm.2012.331.

A. Iserles. *A First Course in the Numerical Analysis of Differential Equations*. Cambridge Texts in Applied Mathematics. Cambridge University Press, 2008. doi: 10.1017/cbo9780511995569.

K. Iwashita and M. Oda. Rolling resistance at contacts in simulation of shear band development by DEM. *Journal of Engineering Mechanics*, 124(3):285–292, mar 1998. doi: 10.1061/(asce)0733-9399(1998)124:3(285).

H. M. Jaeger, S. R. Nagel, and R. P. Behringer. Granular solids, liquids, and gases. *Reviews of Modern Physics*, 68(4):1259–1273, oct 1996. doi: 10.1103/revmodphys.68.1259.

J. T. Jenkins and D. Berzi. Kinetic theory applied to inclined flows. *Granular Matter*, 14(2):79–84, jan 2012. doi: 10.1007/s10035-011-0308-x.

L. Jing, C. Y. Kwok, Y. F. Leung, and Y. D. Sobral. Characterization of base roughness for granular chute flows. *Physical Review E*, 94(5), nov 2016. doi: 10.1103/physreve.94.052901.

K. L. Johnson. *Contact Mechanics*. Cambridge University Press, 1985. doi: 10.1017/cbo9781139171731.

P. Jop. Rheological properties of dense granular flows. *Comptes Rendus Physique*, 16(1):62–72, jan 2015. doi: 10.1016/j.crhy.2014.12.001.

P. Jop, Y. Forterre, and O. Pouliquen. Crucial role of sidewalls in granular surface flows: consequences for the rheology. *Journal of Fluid Mechanics*, 541:167, oct 2005. doi: 10.1017/s0022112005005987.

P. Jop, Y. Forterre, and O. Pouliquen. A constitutive law for dense granular flows. *Nature*, 441(7094):727–730, jun 2006. doi: 10.1038/nature04801.

K. Kamrin and D. L. Henann. Nonlocal modeling of granular flows down inclines. *Soft Matter*, 11(1):179–185, 2015. doi: 10.1039/c4sm01838a.

H. Kaur and R. Singh. Two new species of Myxobolus (Myxozoa: Myxosporea: Bivalvulida) infecting an Indian major carp and a cat fish in wetlands of Punjab, India. *Journal of Parasitic Diseases*, 35(2):169–176, aug 2011. doi: 10.1007/s12639-011-0061-4.

J. Kollmer, S. Lindauer, and K. Daniels. Digging on asteroids: a laboratory model of granular dynamics in microgravity. In *15th Biennial ASCE Conference on Engineering, Science, Construction, and Operations in Challenging Environments*, 04 2016.

J. E. Kollmer, M. Tupy, M. Heckel, A. Sack, and T. Pschel. Absence of subharmonic response in vibrated granular systems under microgravity conditions. *Physical Review Applied*, 3(2), feb 2015. doi: 10.1103/physrevapplied.3.024007.

G. Kuwabara and K. Kono. Restitution coefficient in a collision between two spheres. *Japanese Journal of Applied Physics*, 26(Part 1, No. 8):1230–1233, aug 1987. doi: 10.1143/jjap.26.1230.

E. Lauga and T. M. Squires. Brownian motion near a partial-slip boundary: A local probe of the no-slip condition. *Physics of Fluids*, 17(10):103102, 2005. doi: 10.1063/1.2083748.

M. B. Liu and G. R. Liu. Smoothed particle hydrodynamics (SPH): an overview and recent developments. *Archives of Computational Methods in Engineering*, 17(1):25–76, feb 2010. doi: 10.1007/s11831-010-9040-7.

S. Longo and A. Valiani. Analysis of a boundary layer of a granular mixture flowing past a plate at zero incidence. *European Journal of Mechanics B/Fluids*, 46, 2014.

R. M. Lueptow, A. Akonur, and T. Shinbrot. PIV for granular flows. *Experiments in Fluids*, 28(2):183–186, 2000. ISSN 1432-1114. doi: 10.1007/s003480050023.

C. K. K. Lun. Kinetic theory for granular flow of dense, slightly inelastic, slightly rough spheres. *Journal of Fluid Mechanics*, 233:539, dec 1991. doi: 10.1017/s0022112091000599.

C. K. K. Lun and S. B. Savage. The effects of an impact velocity dependent coefficient of restitution on stresses developed by sheared granular materials. *Acta Mechanica*, 63(1-4): 15–44, nov 1986. doi: 10.1007/bf01182538.

C. K. K. Lun, S. B. Savage, D. J. Jeffrey, and N. Chepurniy. Kinetic theories for granular flow: inelastic particles in Couette flow and slightly inelastic particles in a general flowfield. *Journal of Fluid Mechanics*, 140:223, mar 1984. doi: 10.1017/s0022112084000586.

M. C. Marinack, R. E. Musgrave, and C. F. Higgs. Experimental investigations on the coefficient of restitution of single particles. *Tribology Transactions*, 56(4):572–580, jul 2013. doi: 10.1080/10402004.2012.748233.

J. McElwaine and K. Nishimura. Size segregations in snow avalanches. In *Solid Mechanics and Its Applications*, pages 81–88. Springer Netherlands, 2000. doi: 10.1007/978-94-015-9498-1_7.

D. L. Morris, L. Hannon, and A. L. Garcia. Slip length in a dilute gas. *Phys. Rev. A*, 46: 5279–5281, Oct 1992. doi: 10.1103/PhysRevA.46.5279.

D. M. Mueth, H. M. Jaeger, and S. R. Nagel. Force distribution in a granular medium. *Physical Review E*, 57(3):3164–3169, mar 1998. doi: 10.1103/physreve.57.3164.

J. J. Nelson, A. E. Alving, and D. D. Joseph. Boundary layer flow of air over water on a flat plate. *Journal of Fluid Mechanics*, 284:159–169, feb 1995. doi: 10.1017/s0022112095000309.

V. Ogarko and S. Luding. A fast multilevel algorithm for contact detection of arbitrarily polydisperse objects. *Computer Physics Communications*, 183(4):931–936, apr 2012. doi: 10.1016/j.cpc.2011.12.019.

C. O'Sullivan. *Particulate Discrete Element Modelling: A Geomechanics Perspective*. CRC Press, apr 2014. doi: 10.1201/9781482266498.

E. T. Owens and K. E. Daniels. Sound propagation and force chains in granular materials. *EPL (Europhysics Letters)*, 94(5):54005, may 2011. doi: 10.1209/0295-5075/94/54005.

S. Perkins. Death toll from landslides vastly underestimated. *Nature News*, (doi:10.1038/nature.2012.11140), aug 2012. doi: 10.1038/nature.2012.11140.

J. F. Peters, M. Muthuswamy, J. Wibowo, and A. Tordesillas. Characterization of force chains in granular material. *Physical Review E*, 72(4), oct 2005. doi: 10.1103/physreve.72.041307.

D. Petley. Global patterns of loss of life from landslides. *Geology*, 40(10), 2012. doi: 10.1130/G33217.1.

O. Pouliquen. Scaling laws in granular flows down rough inclined planes. *Physics of Fluids*, 11 (3):542–548, mar 1999. doi: 10.1063/1.869928.

O. Pouliquen, J. Delour, and S. B. Savage. Fingering in granular flows. *Nature*, 386(6627): 816–817, apr 1997. doi: 10.1038/386816a0.

O. Pouliquen, C. Cassar, P. Jop, Y. Forterre, and M. Nicolas. Flow of dense granular material: towards simple constitutive laws. *Journal of Statistical Mechanics: Theory and Experiment*, 2006(07):P07020–P07020, jul 2006. doi: 10.1088/1742-5468/2006/07/p07020.

L. Prandtl. Über Flüssigkeitsbewegung bei sehr kleiner Reibung. In A. Krazer, editor, *Verhandlungen des III Internationalen Mathematiker-Kongresses*, pages 484–491. B. G. Teubner, Leipzig, 1905.

W. H. Press, S. A. Teukolsky, W. T. Vetterling, and B. P. Flannery. *Numerical Recipes in C. The Art of Scientific Computing*. Cambridge University Press, 1992.

J. Rajchenbach. Rheology of dense granular materials: steady, uniform flow and the avalanche regime. *Journal of Physics: Condensed Matter*, 17(24):S2731–S2742, jun 2005. doi: 10.1088/0953-8984/17/24/023.

D. Razis, A. N. Edwards, J. M. N. T. Gray, and K. van der Weele. Arrested coarsening of granular roll waves. *Physics of Fluids*, 26(12):123305, dec 2014. doi: 10.1063/1.4904520.

K. A. Reddy and V. Kumaran. Applicability of constitutive relations from kinetic theory for dense granular flows. *Physical Review E*, 76(6), dec 2007. doi: 10.1103/physreve.76.061305.

K. A. Reddy and V. Kumaran. Dense granular flow down an inclined plane: A comparison between the hard particle model and soft particle simulations. *Physics of Fluids*, 22(11): 113302, nov 2010. doi: 10.1063/1.3504660.

S. Riber, E. Hachem, and R. Valette. Simulations directes d'écroulement de barrage: application aux écoulements de matériaux granulaires. In *22ème Congrès Français de Mécanique*, 2015. URL `http://documents.irevues.inist.fr/bitstream/handle/2042/57314/66044.pdf?sequence=1`.

K. F. Riley, M. P. Hobson, and S. J. Bence. *Mathematical Methods for Physics and Engineering*. Cambridge University Press, 2006. ISBN 0521679710. URL `https://www.ebook.de/de/product/5262416/k_f_riley_m_p_hobson_s_j_bence_kenneth_f_riley_mathematical_methods_for_physics_and_engineering.html`.

D. Roylance. Engineering viscoelasticity, 2001. URL `https://web.archive.org/web/20180218224806/http://web.mit.edu/course/3/3.11/www/modules/visco.pdf`.

Saint-Venant. Théorie du mouvement non permanent des eaux, avec application aux crues de rivières et à l'introduction de marées dans leurs lits. *Comptes rendus de l'Académie des Sciences*, 73:147–154, 237–240, 1871.

H. Schlichting and K. Gersten. *Boundary-Layer Theory*. Springer Berlin Heidelberg, 8th edition, 2017. doi: 10.1007/978-3-662-52919-5.

B. Schonfeld. Roll waves in granular flows and debris flows. Master's thesis, McGill University, 1996. URL `http://digitool.library.mcgill.ca/R/?func=dbin-jump-full&object_id=23756&local_base=GEN01-MCG02`.

A. Shukla. Dynamic photoelastic studies of wave propagation in granular media. *Optics and Lasers in Engineering*, 14(3):165–184, jan 1991. doi: 10.1016/0143-8166(91)90047-w.

J. E. Simpson. *Gravity Currents: In the Environment and the Laboratory*. CAMBRIDGE UNIV PR, 2012. ISBN 0521664012. URL `https://www.ebook.de/de/product/3761146/john_e_simpson_gravity_currents_in_the_environment_and_the_laboratory.html`.

J. T. Staley. Bacteria, their smallest representatives and subcellular structures, and the purported precambrian fossil metallogenium. In *Size Limits of Very Small Microorganisms: Proceedings of a Workshop*, 1999. URL `https://www.ncbi.nlm.nih.gov/books/NBK224752/`.

S. H. Strogatz. *Nonlinear Dynamics and Chaos*. CRC Press, may 2018. doi: 10.1201/9780429492563.

W. C. Swope, H. C. Andersen, P. H. Berens, and K. R. Wilson. A computer simulation method for the calculation of equilibrium constants for the formation of physical clusters of molecules: Application to small water clusters. *The Journal of Chemical Physics*, 76(1):637–649, jan 1982. doi: 10.1063/1.442716.

D. Takagi, J. N. McElwaine, and H. E. Huppert. Shallow granular flows. *Physical Review E*, 83(3), mar 2011. doi: 10.1103/physreve.83.031306.

Z. Tang, T. A. Brzinski, M. Shearer, and K. E. Daniels. Nonlocal rheology of dense granular flow in annular shear experiments. *Soft Matter*, 14(16):3040–3048, 2018. doi: 10.1039/c8sm00047f.

O. Tange. *GNU Parallel 2018*. Zenodo, 2018. doi: 10.5281/zenodo.1146014.

A. L. Thomas and N. M. Vriend. Photoelastic study of dense granular free-surface flows. *accepted for publication in Phys. Rev. E*, 2019.

A. R. Thornton, T. Weinhart, S. Luding, and O. Bokhove. Modeling of particle size segregation: Calibration using the discrete particle method. *International Journal of Modern Physics C*, 23(08):1240014, aug 2012. doi: 10.1142/s0129183112400141.

A. R. Thornton, D. Krijgsman, A. te Voortwis, V. Ogarko, S. Luding, R. Fransen, S. Gonzalez, O. Bokhove, O. Imole, and T. Weinhart. A review of recent work on the discrete particle method at the University of Twente: An introduction to the open-source package MercuryDPM. *DEM6 - International Conference on DEMs*, 2013. URL `https://research.utwente.nl/en/publications/a-review-of-recent-work-on-the-discrete-particle-method-at-the-un`.

C. Thornton. Numerical simulations of deviatoric shear deformation of granular media. *Géotechnique*, 50(1):43–53, feb 2000. doi: 10.1680/geot.2000.50.1.43.

K. To, P.-Y. Lai, and H. K. Pak. Jamming of granular flow in a two-dimensional hopper. *Physical Review Letters*, 86(1):71–74, jan 2001. doi: 10.1103/physrevlett.86.71.

J. M. F. Tsang, S. B. Dalziel, and N. M. Vriend. Interaction between the Blasius boundary layer and a free surface. *Journal of Fluid Mechanics*, 839, jan 2018. doi: 10.1017/jfm.2018.2.

J. M. F. Tsang, S. B. Dalziel, and N. M. Vriend. The granular Blasius problem. *Journal of Fluid Mechanics*, 872:784–817, 2019. doi: 10.1017/jfm.2019.357.

K. van der Vaart, M. P. van Schrojenstein Lantman, T. Weinhart, S. Luding, C. Ancey, and A. R. Thornton. Segregation of large particles in dense granular flows suggests a granular Saffman effect. *Physical Review Fluids*, 3(7), jul 2018. doi: 10.1103/physrevfluids.3.074303.

M. Van Dyke. *An Album of Fluid Motion*. Parabolic Press, Inc., 1982. ISBN 0915760029. doi: 10.1115/1.3241909. URL `https://www.amazon.com/Album-Fluid-Motion-Milton-Dyke/dp/0915760029?SubscriptionId=AKIAIOBINVZYXZQZ2U3A&tag=chimbori05-20&linkCode=xm2&camp=2025&creative=165953&creativeASIN=0915760029`.

L. Verlet. Computer "Experiments" on Classical Fluids. I. Thermodynamical Properties of Lennard-Jones Molecules. *Physical Review*, 159(1):98–103, jul 1967. doi: 10.1103/physrev.159.98.

S. Viroulet, J. L. Baker, A. N. Edwards, C. G. Johnson, C. Gjaltema, P. Clavel, and J. M. N. T. Gray. Multiple solutions for granular flow over a smooth two-dimensional bump. *Journal of Fluid Mechanics*, 815:77–116, feb 2017. doi: 10.1017/jfm.2017.41.

T. Weinhart, A. R. Thornton, S. Luding, and O. Bokhove. From discrete particles to continuum fields near a boundary. *Granular Matter*, 14(2):289–294, feb 2012. doi: 10.1007/s10035-012-0317-4.

T. Weinhart, R. Hartkamp, A. R. Thornton, and S. Luding. Coarse-grained local and objective continuum description of three-dimensional granular flows down an inclined surface. *Physics of Fluids*, 25(7):070605, jul 2013. doi: 10.1063/1.4812809.

T. Weinhart, D. R. Tunuguntla, M. P. v. S. Lantman, I. F. C. Denissen, C. R. Windows-Yule, H. Polman, J. M. F. Tsang, B. Jin, L. Orefice, K. van der Vaart, S. Roy, H. Shi, A. Pagano, W. den Breeijen, B. J. Scheper, A. Jarray, S. Luding, and A. R. Thornton. MercuryDPM: Fast, flexible particle simulations in complex geometries: Part B: Applications. In *V International Conference on Particle-based Methods — Fundamentals and Applications, Particles 2017*, 2017. ISBN 9788494690976. URL `https://research.utwente.nl/en/publications/mercurydpm-fast-flexible-particle-simulations-in-complex-geometri-2`.

E. W. Weisstein. Mathworld — A Wolfram Web Resource, 2018. URL `http://mathworld.wolfram.com/`.